The Multiplicity of T Tauri Stars in the Star Forming Regions Taurus - Auriga and Ophiuchus - Scorpius: A 2.2 μm Speckle Imaging Survey

Thesis by

Andrea Ghez

In Patial Fulfillment of the Requirements

for the Degree of

Doctor of Philosophy

California Institute of Technology

Pasadena, California

1993

(Submitted September 29, 1992)

Acknowledgements

I would like to thank my advisor Gerry Neugebauer for his support and faith in my abilities throughout my graduate studies. I have received much encouragement from and had many useful discussions with James Graham, Susan Kleinmann, Keith Matthews, Anneila Sargent, and Tom Soifer. The staff at Palomar Observatory provided invaluable assistance during every observing run; they are a special group of people who are a pleasure to know. I have benefited from collaborating with Steve Beckwith, Peter Gorham, Chris Haniff, Chris Koresko, Shri Kulkarni, and Mike Simon.

Keith Matthews has provided crucial assistance in adapting the standard infrared system to one appropriate for speckle imaging. Tom Prince and the Caltech Concurrent Supercomputing Facility provided time on the Caltech NCUBE supercomputers which allowed me to analyze the vast amounts of data collected for this thesis project. Fred Walter kindly provided information on T Tauri stars in Ophiuchus - Scorpius prior to publication. I would like to thank Alycia Weinberger for reading my thesis and wish her the best of luck on continuing the work of speckle imaging at Caltech. I acknowledge the financial assistance I have received from the Pacific Telesis Fellowship and Amelia Earhart Fellowship while in graduate school.

I am particularly grateful for the support I have received from Tom LaTourrette through the highs and lows of graduate school.

Dedication

I dedicate this thesis to all the women scientists I have known.

Abstract

We present the results of a magnitude limited (K <= 8.5 mag) multiplicity survey of T Tauri stars (TTS) in two nearby star forming regions (SFR), Taurus-Auriga and Ophiuchus-Scorpius. Each of the 69 stars in the sample was observed at K(2.2 μm) with an infrared array camera on the Hale 5-m Telescope at Palomar Observatory and imaged using two-dimensional speckle interferometric techniques.

Thirty three companion stars were found, of which 15 were new detections. A subset of 64 observations was sensitive to all companion stars in the projected linear range 14 to 225 AU and the magnitude difference range 0.0 to 2.0 mag. We used this subset and region to study the multiplicity of TTS; the frequency of companion stars within this region is 34 ± 9%, independent of SFR. We discovered a distinction between the classical TTS (CTTS) and the weak-lined TTS (WTTS) based on the binary star frequency as a function of separation; *the WTTS dominate the binary star distribution at the closer separations and the CTTS populate the wider separations.* The cross over occurred near 100 AU, the size typically quoted for a circumstellar disk. We suggest that all TTS begin as CTTS and become WTTS when accretion has ceased, and that the nearby companion stars act to shorten the accretion timescale in multiple star systems.

Integrated over all magnitude differences the binary star frequency in the projected linear separation range 14 to 225 AU for TTS (59 ± 16%) is a factor of 3.5 greater than that of the solar-type main sequence stars (17 ± 3%). Given the limited angular separation range that we are sensitive to, i.e., both the spectroscopic and wide binaries are missed, the rate at which binaries are detected suggests that *most, if not all, TTS stars have companions.* We propose that the observed overabundance of companions to TTS with respect to their older counterparts on the main sequence is an evolutionary effect; in this scheme triple and higher order TTS, which are

observed at higher frequencies than for the solar-type main sequence stars, are disrupted by close encounters with another star or system of stars.

Table of Contents

Chapter One

1. Introduction

1.1. Motivation for Studying T Tauri Stars

Understanding the formation of stars like the Sun remains one of the unsolved fundamental problems of astrophysics. Much of the work on this topic has been driven by the desire to explain the origins of our solar system and thus has resulted in scenarios for the production of single stars that, at a young age, are surrounded by a disk of gas and dust from which planets may form.

T Tauri stars are a class of young low mass (0.2 to 3.0 M_O) pre-main sequence stars whose ages are in the range 2×10^5–2×10^7 years (see for example Shu et al. 1987). These stars have just emerged from the deeply embedded phase (i.e., they were previously low luminosity protostars) and are evolving towards the main sequence. Once they reach the main sequence, they will be very much like our Sun. Furthermore, a growing body of observational evidence suggests that many T Tauri stars are surrounded by disks (§1.2). Thus, the study of T Tauri stars is motivated by the desire to understand the early evolution of stars like our Sun and to learn what conditions are necessary to support the formation of a planetary system.

1.2. Identifying T Tauri Stars

The class of T Tauri stars was originally defined by Joy (1945) on the basis of their photometric and spectral properties. These stars were noted for having large and irregular light variations, and optical spectra with strong emission lines, in particular the Balmer series of hydrogen and Fe II lines (e.g., Herbig 1962). Ambartsumian (1947), however, was the first to recognize these objects as low mass pre-main

sequence stars. Today T Tauri stars are identified primarily on the basis of the following spectroscopic and kinematic criteria: (1) strongly enhanced Li I absorption, which indicates the young age of the object and (2) a radial velocity that is consistent with membership in an associated molecular cloud.

The class of T Tauri stars has recently been divided into two, observationally defined, sub-classes, the classical T Tauri stars (CTTS), which have strong H_α emission ($W(H_\alpha) > 10$ A), and the weak-lined T Tauri stars, which have weak H_α emission ($W(H_\alpha) < 10$ A) (e.g., Strom et al. 1989). The physical difference between these stars is believed to be the presence of an active accretion disk in the CTTS and the lack of such a disk in the WTTS (e.g., Basri & Bertout 1989).

One of the first suggestion that many of the T Tauri stars are surrounded by circumstellar disks came from the infrared excess observed in several of these objects (Rucinski 1985; Adams et al. 1987; Kenyon & Hartmann 1987). This excess radiation has been assumed to be from dust, but models in which the dust is distributed in a spherically geometry about the star are irreconcilable with the observed low optical extinction to these sources. Modeling the IR spectrum as an optically thick (but geometrically thin) disk reconciled the two observations. Further evidence for circumstellar disks came from the profiles of forbidden [OI] and [SII] lines. These lines are all blue shifted, which suggested that there is a disk obscuring the red shifted counterpart to these lines (Appenzeller et al. 1984; Edwards et al. 1987). Optical polarization measurements have also been modeled in terms of a disk (e.g., Bastien et al. 1989) Recently, kinematic studies using CO emission have shown direct evidence for the presence of a disk around the CTTS HL Tau (Beckwith et al. 1986; Sargent and Beckwith 1987; Sargent & Beckwith 1991). Most models for these disks suggest that they are roughly 100 AU in size. A sufficient amount of observational and theoretical evidence has been accrued today to make the disk hypothesis generally accepted.

1.3. Motivation for Looking for Companion Stars

Although most evolutionary theories of how T Tauri stars emerge from the deeply embedded protostellar stage and progress toward the main sequence are based on single star scenarios (e.g., Adams et al. 1988), surveys of main sequence stars have already shown that about 2/3 of the solar-type stars are in multiple star systems (Abt & Levy 1976; Abt 1983; Duquennoy & Mayor 1991). So the question arises of how and when these multiple star systems form, for they appear to be the norm as opposed to the exception. The early work of Joy & Van Biesbroeck (1944) showed that 5 of the first 11 known T Tauri stars were binary stars, which suggests that multiple star systems are formed early on in the stars formation process. Since 1944 more than 450 T Tauri stars have been identified (see for example Herbig & Robbin-Bell 1988), but only recently has the question of how many of these stars are in multiple systems been revisited (see §1.4).

If many companion stars are found among the T Tauri stars, then a myriad of questions arise. Are all solar-type multiple star systems formed by the T Tauri star stage of evolution? What controls the formation of multiple star systems in the star forming regions? Does the multiple star formation efficiency vary from region to region just as the overall star forming efficiency does? How do companion stars affect a circumstellar disk?

1.4. Other T Tauri Surveys

Recent surveys, which have begun to reveal T Tauri companion stars, include lunar occultations (Simon 1992a; Simon et al. 1992; Leinert et al. 1991; Chen et al. 1990; Simon et al. 1987), radial velocity measurements (Mathieu 1992; Mathieu et al. 1988), direct imaging work (Simon et al. 1992; Zinnecker et al. 1992), and speckle imaging work (Leinert et al. 1992). Figure 1.1 shows the distribution of solar-type main sequence stars (Duquennoy & Mayor 1991) transcribed to be a function of

angular separation if all the stars were located at 150 pc, the approximate distance to many nearby star forming regions. Each technique is sensitive to a unique limited range of binary separations. Thus the different surveys are complimentary, since a combination of several methods of detection is necessary to deduce what fraction of young stars have companions.

1.5. This Work

This thesis reports the results of a magnitude limited speckle imaging survey of T Tauri stars in the two nearest star forming regions observable from the northern hemisphere, Taurus - Auriga (140pc, Elias 1978) and Ophiuchus - Scorpius (125 pc, de Geuss et al. 1989). If T Tauri stars have the same binary star frequency distribution as their older counterparts on the main sequence (Figure 1.1), then speckle imaging is an ideal technique for finding companion stars because it is sensitive to the peak of the binary star frequency distribution. Furthermore, at the distances of these star forming regions, speckle imaging is capable of detecting companion stars that are separated by less than the predicted circumstellar disk size, ~100 AU (Beckwith & Sargent 1992). Thus by using speckle imaging techniques we are able to study the effects of a companion star on circumstellar disks.

The organization of this thesis is as follows: Chapter Two outlines the technique of speckle imaging and its implementation at the Hale 5-m Telescope. Chapter Three details the speckle imaging search for close companions around T Tauri stars and the results of this survey are discussed in Chapter Four. Appendix A contains the data upon which the results of this survey are based. Also included in Appendix B is a multiple wavelength study of binary star T Tauri, which was published by Ghez et al. 1991, as an example of the importance of finding the companions to these stars.

The principal results of this thesis are the discovery of an overabundance of T Tauri star companions relative to their older counterparts on the main sequence. This implies that most, if not all, T Tauri stars have companion stars. Furthermore, the distributions of the CTTS and WTTS binary stars as a function of separation are significantly different from each other; the WTTS dominate the binary star distribution at the closer separations and the CTTS dominate the distribution at wider separations. We suggest that all T Tauri stars begin as CTTS and become WTTS when accretion has ceased, with the nearby companion stars acting to shorten the accretion timescale in some stars. In this way, the companion stars account for the presence of WTTS that are coeval with many CTTS.

Figure Captions

Figure 1.1: The distribution of solar-type main sequence stars (Duquennoy & Mayor 1991) as a function of angular separation, if all the stars were located at 150 pc, the approximate distance to many nearby star forming regions. Also shown is which region techniques such as spectroscopy, lunar occultations, speckle imaging (at 2.2 μm on a 5 m telescope), and direct imaging are sensitive to.

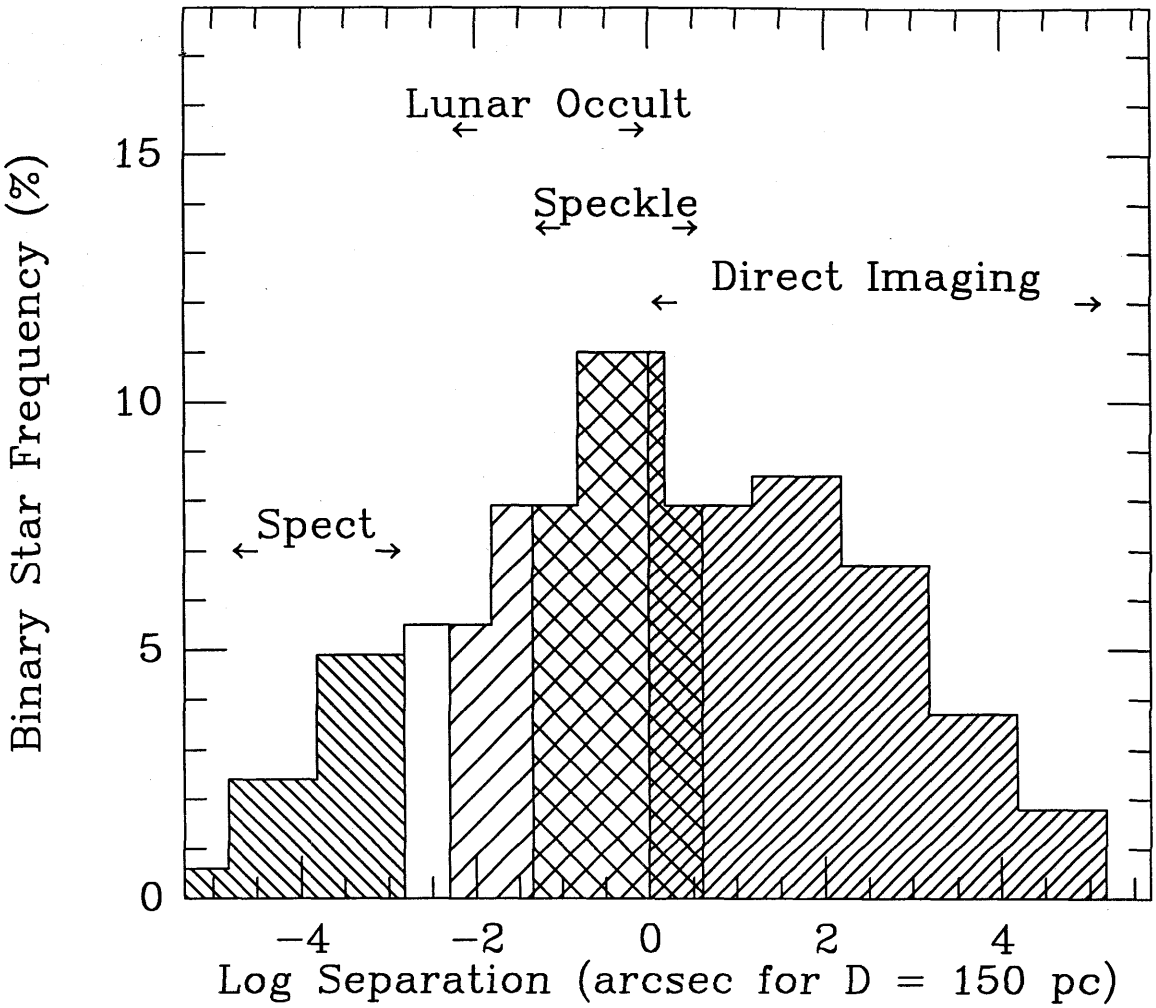
Lunar Occult
Speckle
Direct Imaging
Spect
Binary Star Frequency (%)
0
5
10
15
−4
−2
0
2
4
Log Separation (arcsec for D = 150 pc)

Figure 1.1

Chapter Two

2. Two-Dimensional Infrared Speckle Imaging

2.1. Atmospheric Seeing

Due to the turbulence in the atmosphere, the resolution of images formed by large ground based telescopes is limited not by diffraction but by the inhomogeneities in the atmosphere. Consequently, images obtained with such telescopes depend both on the size and shape of the telescope aperture and the statistics of the wavefront degradation as described in detail elsewhere (e.g. Fried 1979; Dainty 1984; Roddier 1988) Here we describe only what is necessary to understand the purpose and effect of speckle imaging. The "typical" values that we quote here are taken from Chelli (1984).

The inhomogeneities in the atmosphere cause random phase fluctuations of the incoming wavefront. The coherence length of these fluctuations is parameterized by r_o (Fried 1965, 1966), defined as the length over which the phases fluctuate less than 1 radian; r_o depends on both the observing wavelength, λ, and zenith angle, z, $r_o \propto \lambda^{6/5}\ (cosz)^{3/5}$, where the functional dependence is determined assuming a Kolmogrov spectrum of atmospheric turbulence. At 2.2 μm, r_o has a typical value of 60 cm. The phase fluctuations are also time varying. A simple model for their time dependence assumes that the fluctuations are frozen into the atmosphere and therefore act as a phase screen, which drifts past the telescope at a constant speed, v. During a long exposure, the phase screen in front of the telescope changes many times. The resulting image is blurred and has the resolution of a r_o sized telecope.

In contrast to the long exposure images, short-exposure images preserve diffraction-limited information. This is true over a timescale, τ_o, which is short

enough that the phase screen does not change significantly: $\tau_o = \frac{r_o}{v}$, which is typically 60 msec at 2.2 μm. However the resulting image of a point source is not a classic Airy pattern, but rather a speckle pattern, due to the distortions of the incoming wavefront. The speckles result from the interference effects of the r_o sized cells, over which the light is coherent. Each speckle is roughly a diffraction-limited image. The number of speckles a short exposure image breaks into is given by, $N_s \propto (\frac{D}{r_o})^2$, where D is the diameter of the telescope. Thus the number of speckles is proportional to the number of r_o coherence cells that fall within the area of the telescope mirror. For a 5 m telescope and a coherence length of 60 cm the N_s is typically 113. These speckles fall within a certain area forming what is called a speckle cloud. As might be expected, the size of this cloud is roughly the size of a long exposure image, since the effect of the moving phase screen during a long exposure is for the speckles to move around within the area of the speckle cloud. Given the speckled nature of short exposures, they are usually referred to as specklegrams.

An image, whether formed from a long or short exposure ($I(\mathbf{x})$, where $\mathbf{x}$ is the spatial variable), can be described as the true object brightness distribution, $O(\mathbf{x})$, convolved with telescope and atmospheric transfer function, $T(\mathbf{x})$, which depends on the length of the exposure,

$$I(\mathbf{x}) = O(\mathbf{x}) * T(\mathbf{x}), \tag{2.1a}$$

where * denotes convolution. Equivalently in the Fourier domain (Fourier transforms are indicated by tildes) Equation 2.1a becomes,

$$\tilde{I}(\mathbf{u}) = \tilde{O}(\mathbf{u}) \cdot \tilde{T}(\mathbf{u}), \tag{2.1b}$$

where $\mathbf{u}$ is the spatial frequency variable. As mentioned above the transfer function for long exposure images does not allow high resolution information through, and thus $\tilde{T}^{long}(\mathbf{u})$ is ~zero for angular frequencies higher than $\frac{r_o}{\lambda}$; for $\lambda = 2.2\ \mu m$ the

highest nonzero spatial frequency is typically $\mathbf{u}_{\text{lim}}^{long} = 1.32 \frac{cycles}{arcsec}$. For short exposures the transfer function is non-zero out to the limit of the telescope, $\frac{D}{\lambda}$; for $\lambda = 2.2\ \mu m$ and $D = 5\ m$ the highest nonzero spatial frequency is $\mathbf{u}_{\text{lim}}^{short} = 11.02 \frac{cycles}{arcsec}$.

The signal to noise ratio (SNR) in a single short exposure frame of data is poor for most sources. One simple way to increase the SNR in each frame is to slightly increase the exposure time from τ_o. The effect of increasing the exposure time is a uniform depression of $\tilde{T}(\mathbf{u})$ between spatial frequencies $\mathbf{u}_{\text{lim}}^{long}$ and $\mathbf{u}_{\text{lim}}^{short}$ until it reaches zero, i.e., the long exposure limit where no high resolution information remains. Another way to increase the SNR in each frame is to increase the bandwidth, $\Delta\lambda$. However, two effects are introduced when non-monochromatic light is used: (1) a wavelength dependent magnification of the speckle pattern and (2) a loss of coherence due to atmospheric optical path differences. The first effect causes an elongation of the speckles. This is similar to the spread produced by a grating and is a negligible effect if $\frac{\Delta\lambda}{\lambda} < \frac{r_o}{D}$. Otherwise this magnification effectively produces a spatial frequency cutoff at $\sim\frac{r_o}{\lambda}$. The second effect has a similar consequence as the effect of using $\tau > \tau_o$, i.e., it uniformly depresses the high spatial frequencies of the transfer function. This effect is negligible if $\frac{\Delta\lambda}{\lambda} < 2.4 \left[\frac{r_o}{D}\right]^{5/6}$. This criteria is set by considering optical path differences in the atmosphere (Dainty 1984). As a result of these constraints, it is not possible to get significant SNR in an individual speckleogram for most sources. Thus the challenge presented is to recover the high resolution information present in very short exposure images over many integrations.

2.2. Speckle Imaging: Theory

Speckle imaging is one technique for retrieving diffraction-limited images in the presence of a rapidly changing turbulent atmosphere. This is done by analyzing the interference effects observed in short exposures. The analysis of the individual speck-legrams, $I_i(\mathbf{x})$, to recover the true object brightness distribution, $O(\mathbf{x})$, is carried out in the Fourier domain (Equation 2.1b).

Any complex function in the Fourier domain, $\tilde{X}(\mathbf{u})$, can be expressed in terms of its Fourier real and imaginary parts,

$$\tilde{X}(\mathbf{u}) = \mathrm{Re}\,\tilde{X}(\mathbf{u}) + i\ \mathrm{Im}\,\tilde{X}(\mathbf{u}), \tag{2.2a}$$

or its Fourier amplitudes and phases,

$$\tilde{X}(\mathbf{u}) = |\tilde{X}(\mathbf{u})|\ e^{i\,Arg\tilde{X}(\mathbf{u})}, \tag{2.2b}$$

where,

$$|\tilde{X}(\mathbf{u})| = \sqrt{(\mathrm{Re}\,\tilde{X}(\mathbf{u}))^2 + (\mathrm{Im}\,\tilde{X}(\mathbf{u}))^2}, \tag{2.2c}$$

and

$$Arg\tilde{X}(\mathbf{u}) = \tan^{-1}\left[\frac{\mathrm{Im}\,\tilde{X}(\mathbf{u})}{\mathrm{Re}\,\tilde{X}(\mathbf{u})}\right]. \tag{2.2d}$$

Therefore the functions in Equation 2.1b, $\tilde{I}(\mathbf{u})$, $\tilde{O}(\mathbf{u})$, and $\tilde{T}(\mathbf{u})$, can be expressed in terms of their Fourier amplitudes and phases as follows,

$$\tilde{I}(\mathbf{u}) = |\tilde{I}(\mathbf{u})|\ e^{i\theta(\mathbf{u})}, \tag{2.3a}$$

$$\tilde{O}(\mathbf{u}) = |\tilde{O}(\mathbf{u})|\ e^{i\phi(\mathbf{u})}, \tag{2.3b}$$

and

$$\tilde{T}(\mathbf{u}) = |\tilde{T}(\mathbf{u})|\ e^{i\omega(\mathbf{u})}. \tag{2.3c}$$

In the analysis that is described in the following sections, the object's Fourier amplitudes ($|\tilde{O}(\mathbf{u})|$) and phases ($\phi(\mathbf{u})$) are recovered in two separate processes.

2.2.1. Fourier Amplitude Recovery

Labeyrie (1970) was the first to recognize that diffraction-limited Fourier amplitudes of an astronomical object could be retrieved from a series of short exposures. He noted that the high resolution information is not lost if one averages power spectra, as opposed to directly averaging the specklegrams in which case one returns to the long exposure limit (i.e., no high frequency information). Therefore SNR can be built up by calculating the ensemble averaged power spectrum of the specklegrams of an object ($<|\tilde{I}_i(\mathbf{u})|^2>$), which can be expressed in terms of the power spectrum of the true object brightness distribution and the time-varying transfer function.

$$<|\tilde{I}_i(\mathbf{u})|^2> = |O(\mathbf{u})|^2 \cdot <|\tilde{T}_i(\mathbf{u})|^2>. \tag{2.4}$$

Furthermore, he realized that although the transfer function, $\tilde{T}_i(\mathbf{u})$, varies in time, its ensemble averaged power spectrum can be measured by the ensemble averaged power spectrum of a source that is unresolved by the telescope. Thus the Fourier amplitudes of an object are recovered by dividing the ensemble averaged power spectrum of specklegrams of the obj, $<|\tilde{I}_i^{obj}(\mathbf{u})|^2>$, by the ensemble averaged power spectrum of a calibrator, i.e., the unresolved source, $<|\tilde{I}_i^{cal}(\mathbf{u})|^2>$:

$$|\tilde{O}(\mathbf{u})|^2 = \frac{<|\tilde{I}_i^{obj}(\mathbf{u})|^2>}{<|\tilde{I}_i^{cal}(\mathbf{u})|^2>}. \tag{2.5}$$

2.2.2. Fourier Phase Recovery

The object's Fourier phases are recovered via bispectral analysis, originally developed by Weigelt and his collaborators (Weigelt 1977; Lohmann et al. 1983; Bartelt et al. 1984). Other techniques for phase recovery exist, such as the Knox-Thompson algorithm (Knox & Thompson 1974), but are not discussed here. The bispectrum, $B(\mathbf{u},\mathbf{v})$, is a triple product of the Fourier transform of the image measured at three spatial frequencies,

$$\tilde{B}_i(\mathbf{u},\mathbf{v}) = \tilde{I}_i(\mathbf{u})\tilde{I}_i(\mathbf{v})\tilde{I}_i(-\mathbf{u}-\mathbf{v}) \tag{2.6a}$$

Once again this can be expressed in terms of the true object distribution and a transfer function.

$$\tilde{B}_i(\mathbf{u},\mathbf{v}) = \tilde{O}(\mathbf{u})\tilde{O}(\mathbf{v})\tilde{O}(-\mathbf{u}-\mathbf{v})\tilde{T}_i(\mathbf{u})\tilde{T}_i(\mathbf{v})\tilde{T}_i(-\mathbf{u}-\mathbf{v}) \tag{2.6b}$$

The crucial point to note is that the three spatial frequencies sum to zero. The phase of the ensemble averaged bispectrum, $Arg\langle|\tilde{B}_i(\mathbf{u},\mathbf{v})|\rangle = \Phi(\mathbf{u},\mathbf{v})$, is a linear sum of three image Fourier phases,

$$\Phi(\mathbf{u},\mathbf{v}) = \theta(\mathbf{u}) + \theta(\mathbf{v}) + \theta(-\mathbf{u}-\mathbf{v}) \tag{2.7a}$$

or the sum of three object Fourier phases and three transfer function phases

$$\Phi(\mathbf{u},bv) = \phi(\mathbf{u}) + \phi(\mathbf{v}) + \phi(-\mathbf{u}-\mathbf{v}) + \omega(\mathbf{u}) + \omega(\mathbf{v}) + \omega(-\mathbf{u}-\mathbf{v}). \tag{2.7b}$$

The bispectral phase of a symmetric function is zero (e.g., Gorham et al. 1989), and thus in theory the phase of the ensemble averaged bispectrum of the transfer function (assumed to be symmetric on average, but not necessarily instantaneously) contributes nothing to the bispectral phase. Therefore the phase of the ensemble averaged bispectrum is a direct linear combination of the object's Fourier phases,

$$\Phi(\mathbf{u},\mathbf{v}) = \phi(\mathbf{u}) + \phi(\mathbf{v}) + \phi(-\mathbf{u}-\mathbf{v}) \tag{2.8}$$

and is analogous to the closure phase of radio astronomy (Roddier 1986; Cornwell 1987)

Because each bispectrum phase is a linear combination of three object Fourier phases and there are more bispectral points than Fourier phases, the measured bispectrum points define an overdetermined set of linear equations from which the object's Fourier phases can be solved.

2.3. Speckle Imaging: Practice

2.3.1. Observations

2.3.1.1. The Data Acquisition System

The standard Palomar Infrared Cassegrain camera, which contains a Hughes-Santa Barbara Research 58×62 InSb hybrid array, is used to obtain the specklegrams. For direct imaging this camera is mounted at the Cassegrain focus of the Hale 200-inch Telescope on Palomar Mountain with a f/70 Cassegrain secondary mirror. This produces a pixel scale of 0.313 $\frac{arcsec}{pixel}$, which is inadequate for diffraction-limited imaging, i.e., it does not Nyquist sample the 5-m mirror at near infrared wavelengths. The pixel scale is changed by a factor of ~6 with a f/415 Gregorian secondary, designed by Keith Matthews with the intention of Nyquist sampling the 5-m mirror at 2.2 μm. The resulting pixel scale, confirmed by observing and reconstructing (as described below) binary stars found in Sky Catalogue 2000 with well known orbits, is 0."053 ± 0."001, with north aligning with the long axis of the array to $\pm 1^o$.

The array sits on a direct readout multiplexer with two readout amplifiers. The direct readout allows for shutterless operation, because, unlike a CCD, carriers are confined to individual pixels. Each image is read by the two amplifiers simultaneously in a raster fashion (see Figure 2.1) at a rate of 18 $\frac{\mu sec}{pix}$. Thus in time, the array is read out from the bottom left pixel to the upper right pixel, proceeding row by row. Since the "even" pixel in a row is read by one amplifier while the adjacent "odd" pixel is simultaneously read by the other amplifier the time to read an entire frame is 32 msec. The fact that the pixels are reset when read gives an almost 100% duty cycle at the expense of a temporal skew in the frame of 32 msec from upper right to lower left. The system is capable of operating reliably for extended periods

of time with exposure times down to 70 msec. Reading out the array at this rate, regardless of the integration time, consistently produces a Gaussian readout noise level of 450 e^- (rms).

2.3.1.2. Data Collection

The general observing philosophy is to alternate taking a series of specklegrams on the object of interest (OBJ) and a calibrator source (CAL), which is a star that is presumably unresolved by the 200-inch telescope. Since there is no way to guarantee *a priori* that a star is unresolved, several calibrators (usually two, CAL1 and CAL2) are observed. In addition to the OBJ, CAL1, and CAL2, a series of snap shots on a blank portion of sky (SKY) are taken to measure the background and the noise level. A typical observing sequence is as follows: CAL1 SKY CAL2 OBJ OBJ CAL1 SKY CAL2 OBJ OBJ CAL1 SKY CAL2.... This sequence guarantees that we can check the calibrators against each other to make sure they are unresolved. Furthermore, if one is resolved, the other is interspersed evenly so that there is always a calibrator observed close to each object.

The number of exposures on a star obtained at one time is determined by a trade off between: (1) needing enough frames to form an ensemble average for the power spectrum and bispectrum and (2) minimizing the time between observing the object and calibrator, so that the atmospheric conditions do not change significantly between them. Series of 400 frames are usually obtained (see Chapter Three). Each CAL1 SKY CAL2 OBJ (or equivalently OBJ CAL1 SKY CAL2) series is termed a "pair."

2.3.2. Data Analysis

2.3.2.1. Initial Data Reduction

The initial stage of data processing is removing detector induced artifacts; hereafter we refer to this process as "scrubbing." First, an estimate of the images' background level, obtained using median filtered exposures of nearby blank sky (SKY), is subtracted from each the raw data frames. Second, the nonuniformity of the pixels' sensitivity is corrected for by flat fielding. Median filtered long sky exposures, from which median filtered dark frames (obtained with the same integration time) are subtracted, are used as the flat field. The dark exposures are taken with a cold shutter placed in front of the array, thereby measuring the detector's response in the absence of light. Next, the dead pixels in the array, seen as two cracks and a number of individual pixels, and any cosmic ray events are interpolated over using the 8 nearest neighboring pixels. Last, each frame is padded out to a 64×64 data array with zeroes, such that two-dimensional fast Fourier transforms (FFT) can be performed. We refer to the scrubbed data frames as $J_i(\mathbf{x})$. Figure 2.2 shows a frame of data before and after it was scrubbed.

2.3.2.2. Amplitude Recovery

We use two methods for recovering the object's Fourier amplitudes: Fourier deconvolution and CLEAN. The first method is the most commonly used and is described in Equation 2.5. It recovers the object's Fourier amplitudes by division of the ensemble average of the image's power spectra by the ensemble average of the calibrator's power spectra. However, the scrubbed data frames, $J_i^{cal\ or\ obj}(\mathbf{x})$, differ from the image and calibrator frames, $I_i^{cal\ or\ obj}(\mathbf{x})$, of Equation 2.5 by an additive noise term,

$$J_i^{cal\ or\ obj}(\mathbf{x}) = I_i^{cal\ or\ obj}(\mathbf{x}) + N_i(\mathbf{x}). \tag{2.9}$$

The noise, which results mainly from the readout electronics, has a zero mean, but contributes to the power spectrum. Therefore the average power spectra for both the scrubbed image and the scrubbed calibrator have an offset due to the noise, which can be measured by the average power spectra of the sky frames, $<|\tilde{J}_i^{sky}(\mathbf{u})|^2>$. The sky frames are scrubbed in an identical manner to the object and calibrator frames, in particular an average sky frame is subtracted from them, so their mean should be zero. We convert the average power spectra of the scrubbed data into the average power spectra of specklegrams referred to in Equation 2.5 via,

$$<|\tilde{I}_i^{cal\ or\ obj}(\mathbf{u})|^2> = <|\tilde{J}_i^{cal\ or\ obj}(\mathbf{u})|^2> - <|\tilde{J}_i^{sky}(\mathbf{u})|^2>. \tag{2.10}$$

Described in terms of the scrubbed data, Equation 2.5 becomes,

$$|\tilde{O}(\mathbf{u})|^2 = \frac{<|\tilde{J}_i^{obj}(\mathbf{u})|^2> - <|\tilde{J}_i^{sky}(\mathbf{u})|^2>}{<|\tilde{J}_i^{cal}(\mathbf{u})|^2> - <|\tilde{J}_i^{sky}(\mathbf{u})|^2>}. \tag{2.11}$$

The Fourier equivalent to dividing power spectra is deconvolving auto-correlation functions (ACF). This is done using the CLEAN algorithm, which was originally developed for the deconvolution of the effects of irregular array spacings in aperture synthesis radio maps. CLEAN works by subtracting a fraction of the convolution function (the dirty beam) from the maximum point in the measured function (the dirty map), recording separately the position of the maximum and the amount subtracted. The process is repeated until the maxima in the remaining dirty map fall into the noise or begin to appear outside the known region of emission. The list of maxima and their accumulated intensities are then convolved with a restoring "CLEAN" beam, and the residuals are added back into the map. In this application of CLEAN to speckle interferometry, the dirty beam is the Fourier transform of the ensemble averaged calibrator power spectra (i.e., the calibrator ACF) and the dirty map is the Fourier transform of the ensemble averaged image power spectra. CLEAN requires a dirty beam that is twice as large as the dirty map, so we insert our

scrubbed data into a 128×128 data array before calculating the power spectra and then vignette the object's raw ACF back down to a 64×64, before CLEAN'ing. The resulting cleaned map is the true object's ACF, from which the desired Fourier amplitudes are obtained. A more detailed discussion of the use of CLEAN in speckle interferometry can be found in Gorham et al. (1990).

The results of the two methods are shown in Figures 2.3 and 2.4. Figures 2.3e and 2.4c show the calibrated power spectrum and ACF where the structure of a binary star is separated out from the atmospheric and telescope transfer function. Although in theory the two methods are Fourier equivalents, in practice they are not. This results mainly from the systematics of our system. Figure 2.5 shows the average power spectrum of series of sky exposures, which is expected to be flat for purely Gaussian readout noise plus the sky. The spikes, apparently from the camera's electronics, are fairly well localized in the spatial frequency domain. However over time the corrupted frequencies shift in location. This problem is solved by treating these corrupted frequencies in a similar manner to bad pixels in the image domain and interpolating over them using their nearest neighbors. Another systematic problem is aliased frequencies. Most of the observations presented here were obtained at K(2.2 μm), a wavelength at which the pixels are slightly oversized (53 $\frac{mas}{pix}$) for Nyquist sampling the 200-inch mirror (45 $\frac{mas}{pix}$.) Figure 2.6 shows the aliasing effects at a number of wavelength in the spatial frequency domain; 2.2 μm is the most commonly used wavelength. Both of these problems, aliasing and the systemic readout noise, remain localized when dividing power spectra but not when deconvolving ACF's. Nonetheless, CLEAN is very good at finding discrete point sources. Therefore both methods are generally used to interpret a given data set, using CLEAN as a first pass and Fourier deconvolution to model the source in detail while omitting the corrupted and aliased frequencies altogether (see §3.2.1). If many object/calibrator

pairs are obtained then the amplitudes are pairwise calibrated. The resulting Fourier amplitudes are then averaged together to produce a final estimate of the object's diffraction-limited Fourier amplitudes.

2.3.2.3. Phase recovery

The principle for retrieving an object's diffraction-limited Fourier phases is described in §2.2.2. However, as mentioned in the previous section and described in Equation 2.9, the scrubbed data have a random noise contribution that must be accounted for in calculating the bispectrum (Equation 2.6a). Once again this is accomplished by calculating the bispectrum of the sky frames and subtracting this from the ensemble-averaged bispectrum of the scrubbed object frames. In theory the bispectrum of an object does not need to be calibrated, since the closure phase (Equation 2.8) of a point source, i.e., the calibrator, should be zero. However, in practice the bispectrum is found to be in need of calibration (e.g., Haas 1990; Gorham et al. 1989), due to telescope aberrations and detector artifacts. Thus the bispectrum is expressed as follows:

$$<B_i^{obj}(\mathbf{u},\mathbf{v})> = \frac{<\tilde{J}_i^{obj}(\mathbf{u})\tilde{J}_i^{obj}(\mathbf{v})\tilde{J}_i^{obj}(-\mathbf{u}-\mathbf{v})> - <\tilde{J}_i^{sky}(\mathbf{u})\tilde{J}_i^{sky}(\mathbf{v})\tilde{J}_i^{sky}(-\mathbf{u}-\mathbf{v})>}{<\tilde{J}_i^{cal}(\mathbf{u})\tilde{J}_i^{cal}(\mathbf{v})\tilde{J}_i^{cal}(-\mathbf{u}-\mathbf{v})> - <\tilde{J}_i^{sky}(\mathbf{u})\tilde{J}_i^{sky}(\mathbf{v})\tilde{J}_i^{sky}(-\mathbf{u}-\mathbf{v})>}. \quad (2.12)$$

If many pairs are obtained then the bispectrum is pairwise calibrated and then averaged together. Before fitting the final bispectrum phases to derive the object's Fourier phases, we eliminate the bispectrum points that contain the corrupted frequencies for both the object and the calibrator. We also throw out all bispectrum points that have signal to noise ratios less than one. Thus out of the 418,215 unique bispectral points for our system, which are calculated, typically 200,000 bispectrum points remain after calibration.

The remaining ~200,000 bispectrum points still effectively provide an overdetermined set of linear equations from which the object's Fourier phases are solved. The

phases are found by performing a global least squares fit to the bispectrum. An example of the recovered phases is shown in Figure 2.7.

2.3.2.4. Final Image

The Fourier amplitudes and phases of an object are combined by an inverse FFT to form the final reconstructed image. The reconstructed image of LkCa 3 is shown in Figure 2.8. Other speckle images are shown in Figures 3.2 (DD Tau), 3.5 (RW Aur), and B.2 (T Tau). Images of sources with K magnitudes down to 8.5 mag are now routinely being made.

Figure Captions

Figure 2.1: Readout of the 58×62 infrared array camera. The two amplifiers readout pixels simultaneously working from the lower left hand corner up to the upper right hand corner. The exact pattern is shown for the lower 6×6 corner (the crossed region in the upper panel and detailed in the lower panel). Each pixel indicates which amplifier readouts it out (A or B) and the subscript denotes the order in which the pixels are readout; each amplifier reads out 1798 pixels.

Figure 2.2: On top is an example of the raw data before it has been "scrubbed". On bottom is the resulting data frame after being scrubbed , $J_i(\mathbf{x})$, of the star SAO 103106.

Figure 2.3: Fourier deconvolution of LkCa 3's diffraction-limited Fourier amplitudes. (a) the ensemble average power spectrum of the specklegrams on the object, LkCa 3 ($<|\tilde{I}_i^{obj}(\mathbf{u})|^2>$) (b) the logarithm of ($<|\tilde{I}_i^{obj}(\mathbf{u})|^2>$) for illustration only (c) the ensemble average power spectrum of the specklegrams on the calibrator, SAO 76461 ($<|\tilde{I}_i^{cal}(\mathbf{u})|^2>$) (d) the logarithm of ($<|\tilde{I}_i^{cal}(\mathbf{u})|^2>$) for illustration only (e) the recovery Fourier amplitudes of LkCa3 ($|\tilde{O}(\mathbf{u})|^2$), showing the fringe pattern expected for a binary star. The spikes are from the corrupted frequencies.

Figure 2.4: Example of use of CLEAN in speckle interferometry. (a) dirty map (b) dirty beam (c) CLEAN'ed map, the auto correlation of the object's brightness distribution.

Figure 2.5: Ensemble average of the power spectra of scrubbed sky frames, which shows corrupted frequencies.

Figure 2.6: The spatial frequencies at J(1.25 μm), H(1.65 μm), K(2.2 μm) and L'(3.7 μm). The black areas represent aliased frequencies, the gray areas represent frequencies that are beyond the diffraction limit, and the white areas represent frequencies with unaliased information.

Figure 2.7: Recovered Fourier phases for LkCa 3

Figure 2.8: Reconstructed speckle image of LkCa 3

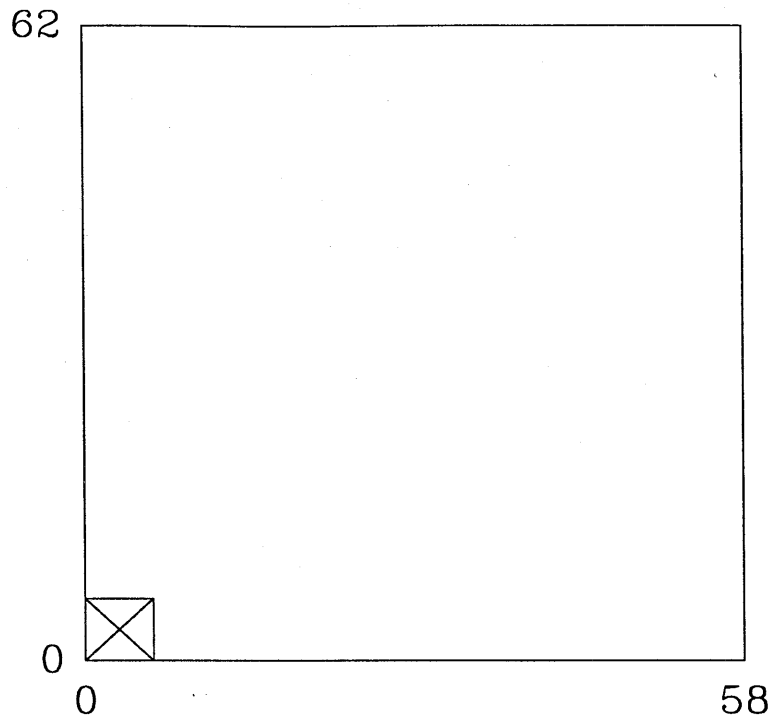

B_{117}	B_{118}	B_{119}	B_{120}	B_{121}	B_{122}
A_{117}	A_{118}	A_{119}	A_{120}	A_{121}	A_{122}
B_{59}	B_{60}	B_{61}	B_{62}	B_{63}	B_{64}
A_{59}	A_{60}	A_{61}	A_{62}	A_{63}	A_{64}
B_1	B_2	B_3	B_4	B_5	B_6
A_1	A_2	A_3	A_4	A_5	A_6

Figure 2.1

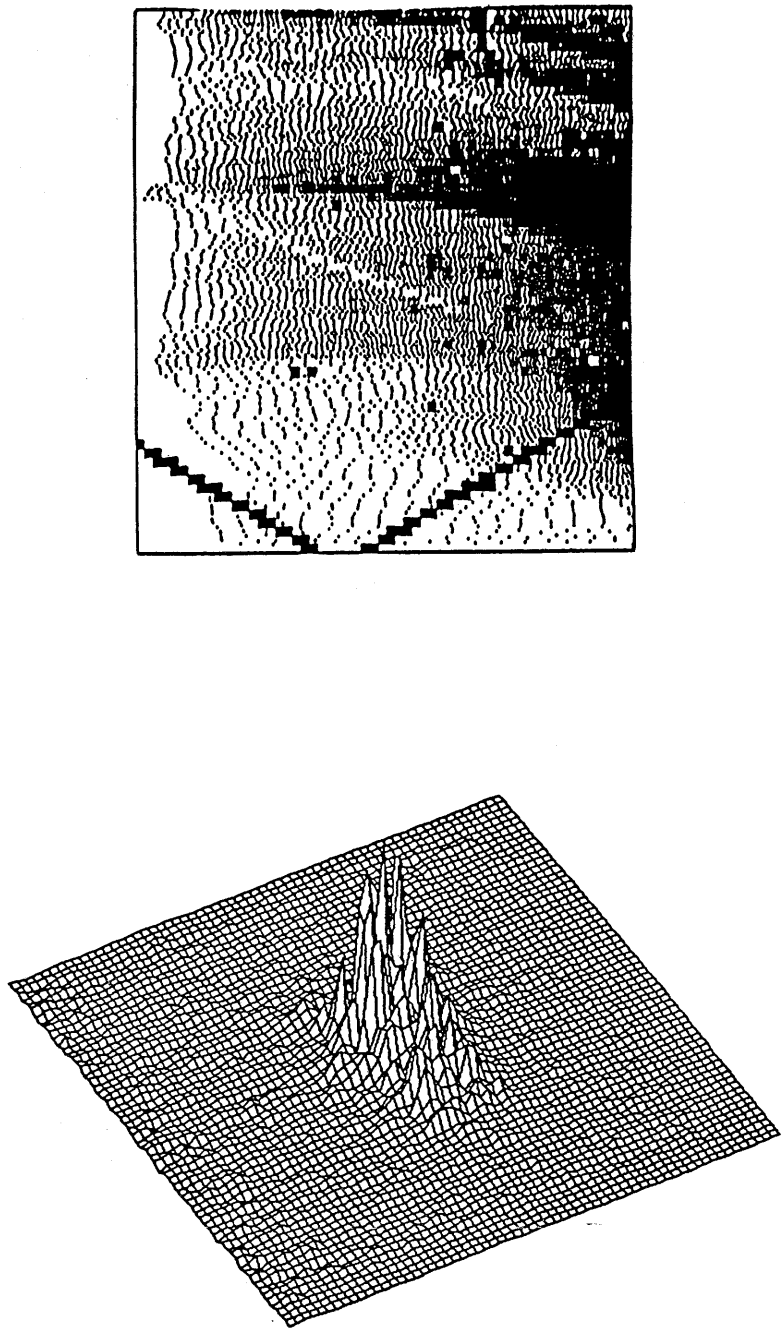

Figure 2.2

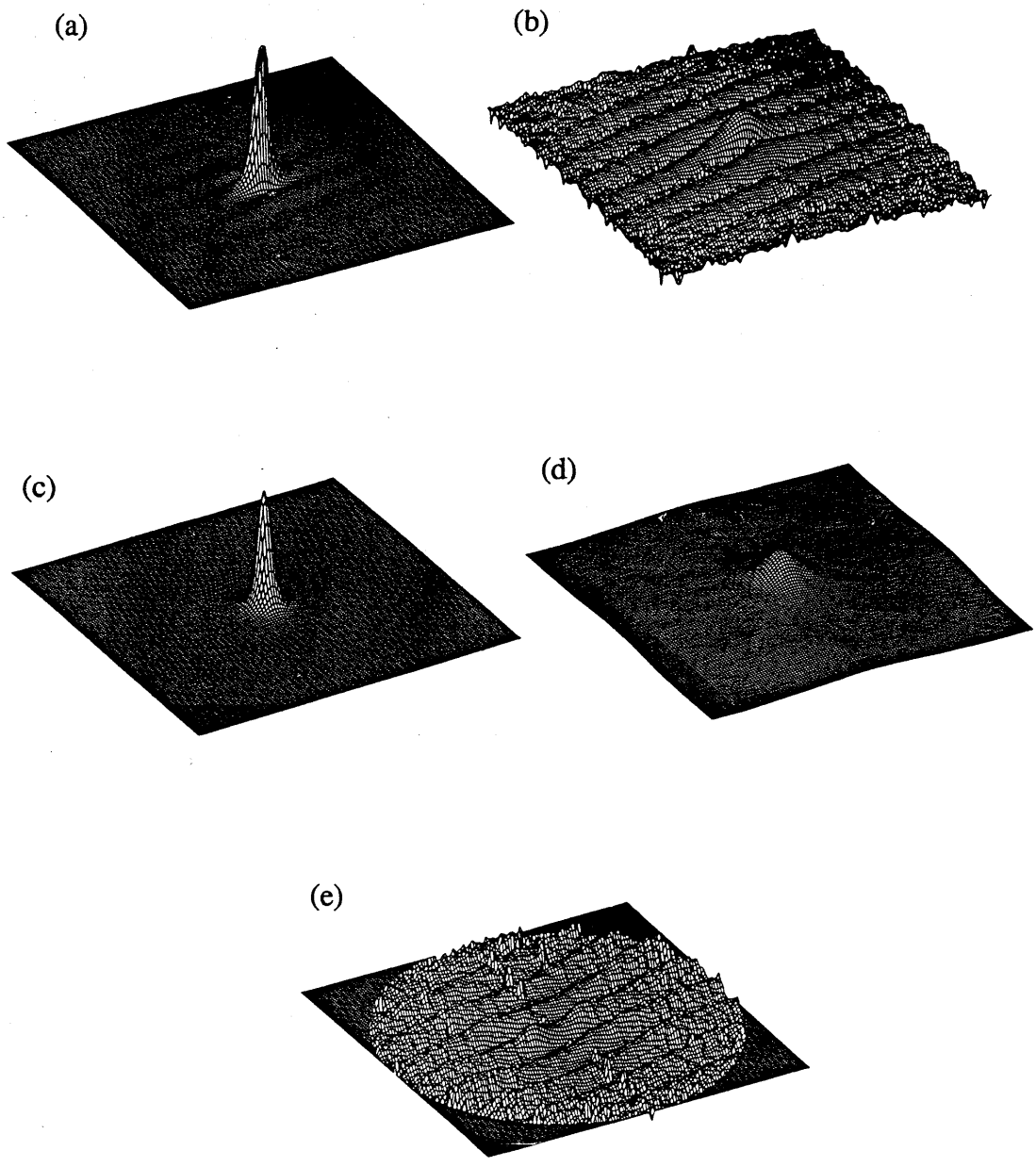

Figure 2.3

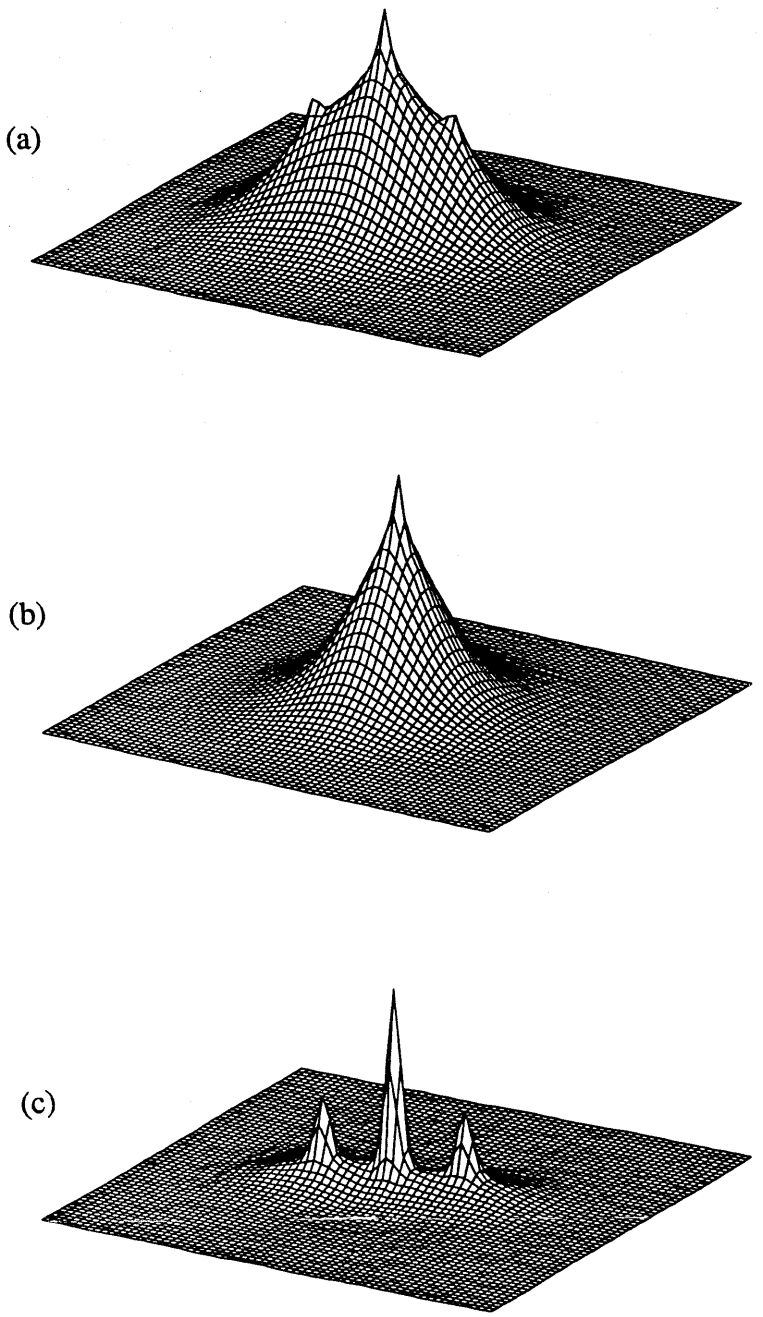

Figure 2.4

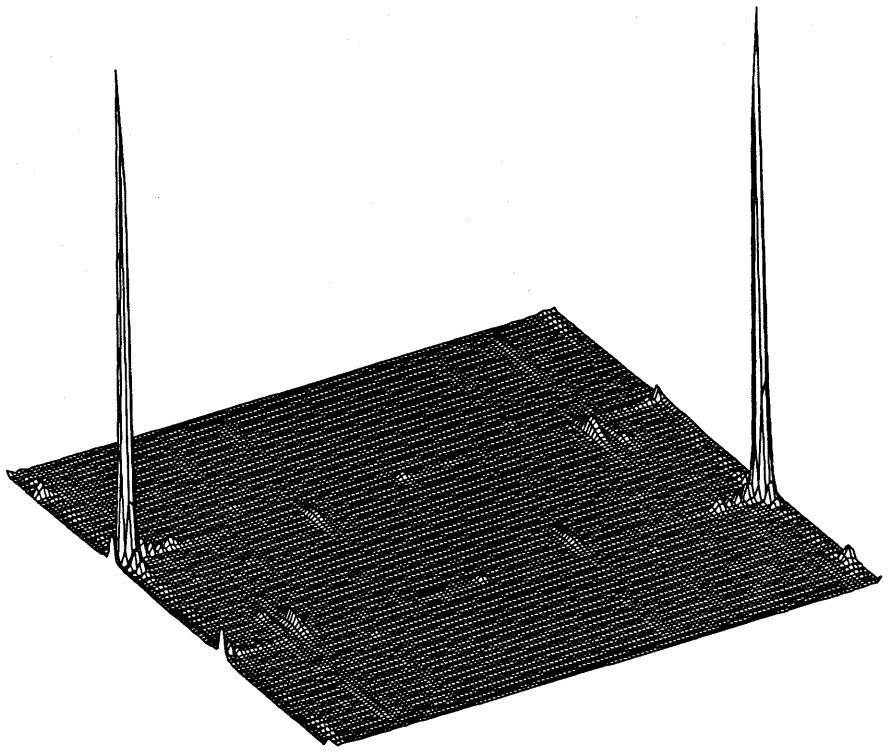

Figure 2.5

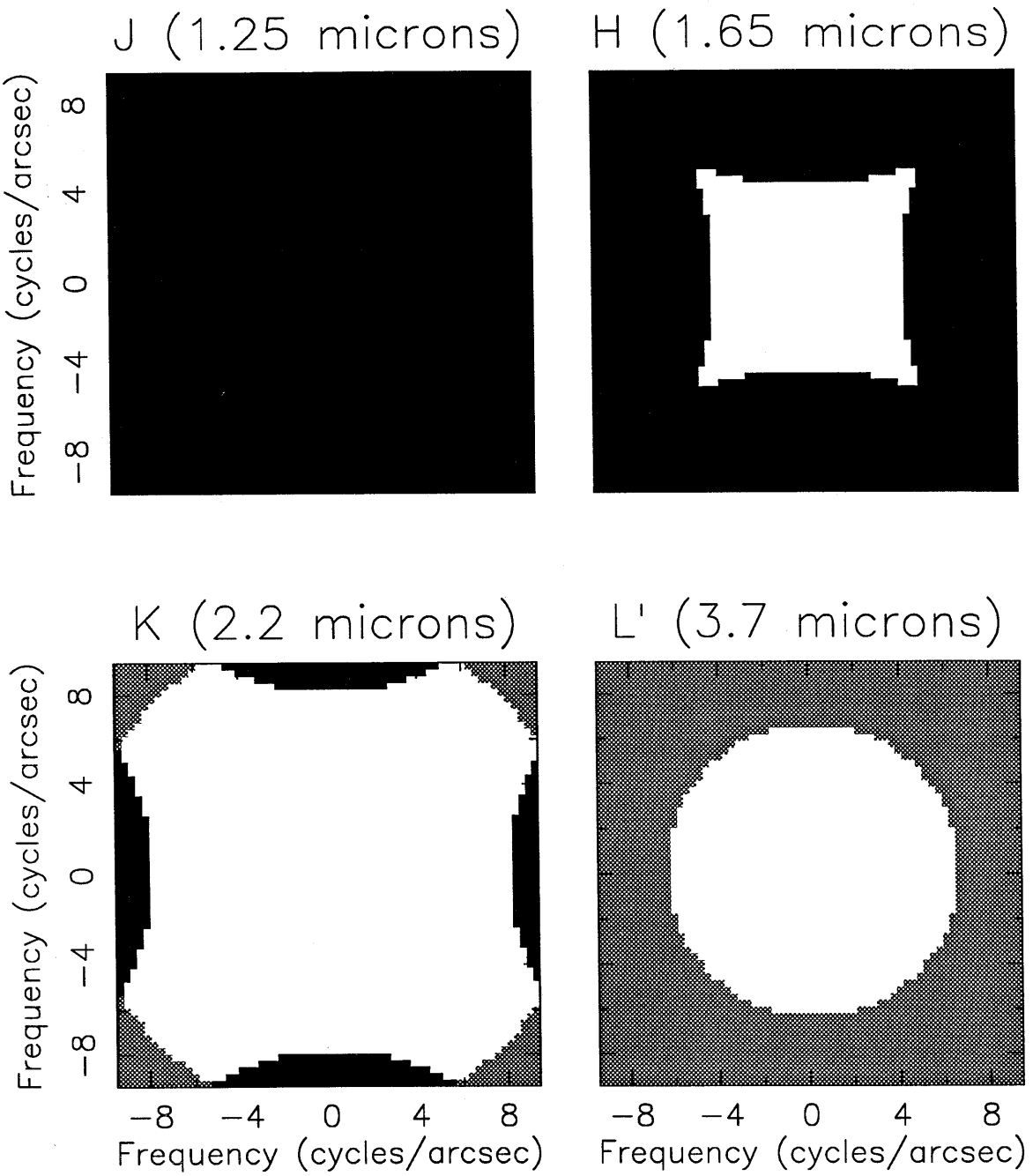
J (1.25 microns)
H (1.65 microns)
K (2.2 microns)
L' (3.7 microns)
Frequency (cycles/arcsec)
8
4
0
−4
−8
−8 −4 0 4 8
Frequency (cycles/arcsec)

Figure 2.6

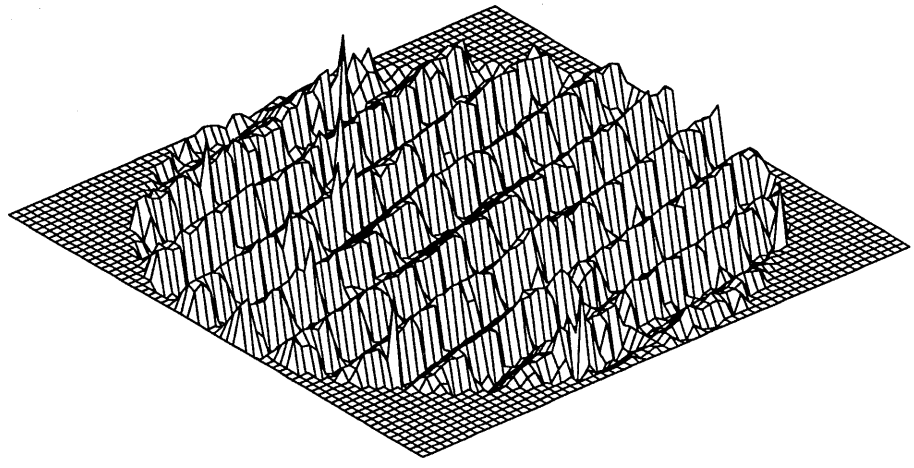

LkCa 3 Fourier Phases

Figure 2.7

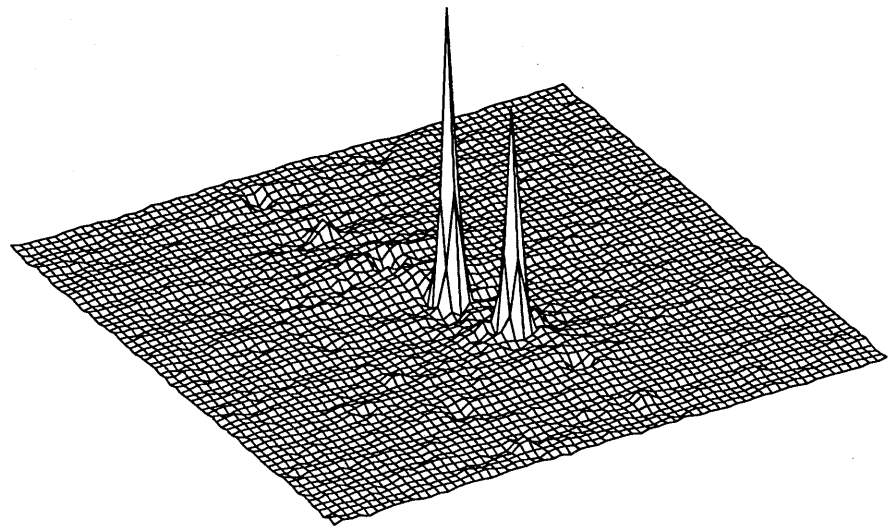

LkCa 3

Figure 2.8

Chapter Three

3. Speckle Imaging Survey of T Tauri Stars

3.1. Sample Definition

3.1.1. Regions

This survey was confined to the two nearest star forming regions observable from the northern hemisphere, Taurus - Auriga (140 pc, Elias 1978) and Ophiuchus - Scorpius (125 pc, de Geus et al. 1989). These regions have many similarities; in particular, they are both sites of active low mass star formation. Nevertheless, they are quite different in their distributions of molecular gas and stellar densities (see discussion in §4.2). Both regions have been extensively studied and a considerable body of literature on both the stellar and cloud properties exists (e.g., Lada et al. 1992; Herbig & Robbin-Bell 1988 and references therein).

3.1.2. Selection Criteria

The compilation of Herbig & Robbin-Bell (1988) and recent X-ray selected source lists (Bouvier & Appenzeller 1991; Walter 1990) were used to identify a total of 143 T Tauri stars in the regions of interest. Based on the Bastian et al. (1983) definition of T Tauri stars, we selected stars that are associated with a region of obscuration and have spectra which display H_α and Ca II H and K lines in emission. The presence of Li I 6707 A absorption was also useful in identifying these young stellar sources. Following the example of many researchers (e.g., Walter 1986; Strom et al. 1989), we sub-divided the sample into classical T Tauri stars (CTTS), which have an equivalent width $W(H_\alpha) > 10$ A, and weak-lined T Tauri stars

(WTTS), which have $W(H_\alpha) < 10$ A (the "naked T Tauri" stars defined by Walter are a subset of the WTTS's).

For speckle imaging of T Tauri stars, the optimum bandpass is K (2.2 μm) due to the following three competing effects: (1) the spectral energy distributions of T Tauri stars peak near 1 μm, (2) the coherence time of the atmosphere, and hence the exposure time used in speckle imaging, increases with $\lambda^{1.2}$, and (3) beyond 3 μm thermal noise dominates the readout noise. The limiting magnitude of our speckle system was K = 8.5 mag. Thus only stars brighter than this were included resulting in a final observing list of 95 T Tauri stars (66% of the identified T Tauri stars). Since the K magnitudes of T Tauri stars occasionally vary unpredictably, we have used the most recent available values; the distribution of K magnitudes is shown in Figure 3.1. Much of the original sample lacked near infrared photometry and were excluded from the final observing list although they may have been bright enough to measure.

3.2. Observations

Over the period 1990 July to 1991 November, we observed 69 of the 95 T Tauri stars at the f/415 Cassegrain focus of the Hale 5-m Telescope of Palomar Observatory using the 58 x 62 InSb array camera in the photometric K(2.2 μm) band. All our sample brighter than K = 7.0 mag were observed; 33 stars with 7.0 < K <= 8.5 mag remain to be measured (see Figure 3.1). Table 3.1 lists the observed stars along with their positions, K magnitudes, and CTTS/WTTS designation.

Table 3.2 is a journal of the observations. For each object, these were carried out in a number of object/calibrator "pairs." A "pair" consists of a series of 400 snapshots (100 msec exposures) on the object of interest followed by a similar series of measurements of a calibrator source. Here the "calibrator" is a source that we expected to be unresolved by the 5 m telescope. Given the unprecedented angular

resolution achieved, two calibrator stars were observed for each target star to ensure that at least one was an unresolved point source. This was checked by calibrating the calibrators against one another. Both calibrators, if point sources, were used in the initial image reconstruction, but in most cases one calibrator was preferred due to the other being either too bright or farther away from the target. Table 3.2 lists the calibrator star that was used in the final data reduction, the number of sets obtained, and the seeing at 2.2 μm. Typical 2.2 μm seeing during these observations, 0."85 ± 0."23, was estimated from the FWHM of integrated calibrator data.

3.3. Survey Data Analysis

The data obtained for each of the 69 target stars observed were reduced using speckle imaging techniques. The details of this process were described in Chapter Two. The Fourier amplitudes were recovered by deconvolving the ensemble averaged autocorrelation function (the Fourier equivalent of the power spectrum) of the target star with that of its calibrator. The Fourier phases for each target were retrieved by calculating the bispectrum of the object and fitting the bispectrum phases using a global least-squares algorithm. A Fourier inversion of these amplitudes and phases produced the final speckle image.

3.3.1. Finding Binary Stars and Fitting for Their Parameters

With speckle imaging, we were able to spatially resolve much closer binary systems than with direct imaging by a factor ~10. Companion stars were initially identified through the CLEAN process of deconvolving the measured object's autocorrelation function (ACF) with that of its calibrator. Secondary sources that were at least 5 σ above the background noise level were identified as companion stars.

Although binary stars were identified in the ACF domain, the flux density ratio, R, and the separation s of these systems were determined in the power spectrum

domain. In general these two quantities, which are Fourier equivalents, are interchangeable but the the systematic readout noise of our detector was most easily identified and eliminated in the power spectrum domain. In both cases there is a 180° ambiguity in the position angle of the binary systems; this was resolved by inspecting the Fourier phases (or equivalently the resulting image).

Figure 3.2a, the calibrated power spectrum for DD Tau, reveals the characteristic fringe pattern of a binary star, $P(\mathbf{f}) = |O(\mathbf{f})|^2 = R^2 + 1 + 2Rcos(2\pi\mathbf{f}\cdot\mathbf{s})$; spikes typical of our readout noise are clearly visible. For brighter targets, the power spectra would dominate the spikes (see Ghez et al. 1991). We estimated the binary system flux density ratio (R) and separation (**s**) by fitting a one-dimensional projection of the power spectrum, $P(\mathbf{f})$, along the separation axis of the two stars. Most of the frequencies corrupted by the readout electronics were excluded from the average performed to obtain this projection by setting minimum and maximum allowed values for the power spectrum. The mask displayed in Figure 3.3 was used to exclude further regions of the power spectrum that contained aliased power due to slightly oversized pixels (see §2.3.2.2) and that were outside the diffraction-limit. The lowest spatial frequencies, $f < 2\ \frac{cycles}{arcsec}$, were also excluded to eliminate the most severe effects of seeing miscalibration (Christou et al. 1985). Figure 3.4 shows the one-dimensional power spectra for DD Tau; the one dimensional power spectra for all the binary stars in the survey along with their model fits are shown in Appendix A. Table 3.3 lists the fitted binary system parameters and their uncertainties.

Two stars warrant special attention: in the case of the widely separated (s > 2") binary, DK Tau, the companion star was detected, but much of its flux was off the edge of the field of view. The binary star parameters were not well determined in these observations and are not entered in Table 3.3.

The triple system, RW Tau, is shown in Figure 3.5. The components are labeled A, B, and C in order of decreasing K flux density. The analysis of this

system was treated in two steps, each of which dealt with the interference effects between a set of components. The two-dimensional power spectrum was first projected along the A-B separation axis and the lower spatial frequencies were fit to obtain the parameters of the wide binary system. This is equivalent to an observation with poorer resolution, which could not resolve component C. The parameters obtained in this first step are for A-(BC) (i.e., the flux density ratio is between star A and the combination of B and C). A projection along the B-C separation axis was then performed to determine the parameters of this close pair.

3.3.2. Limits for Undetected Companion Stars in Individual Observations

Limits for companions that could have gone undetected were determined for stars observed as singles. Similarly, in the cases of binary and triple systems limits were set for additional companion stars. The noise level in the power spectrum determines the largest binary star flux density ratios (primary/secondary) that could have been detected. We used the algorithm originally suggested by Henry (1991) which is based on the minimum values observed in a group of one-dimensional power spectra made from projections of $P(\mathbf{f})$ at different assumed position angles of an undetected binary star. For each target, 36 one-dimensional power spectra, $p(f)$, were produced by projecting the two-dimensional power spectrum, $P(\mathbf{f})$, at angles between 0^o and 175^o, with respect to the sky, at 5^o intervals. The power spectrum is symmetric and therefore the projections between 180^o and 355^o offer no new information. As described in the above section, certain regions are excluded from these projections.

The minimum values found in the projected power spectra determine the limit of the flux density ratio ($\frac{primary}{secondary} \geq 1$) of an undetected binary system. The two-dimensional power spectrum of an unresolved source is completely flat in all directions, $P(\mathbf{f}) = 1$. For a binary star, $P(\mathbf{f})$ varies sinusoidally along an axis parallel to the binary star position angle. The amplitude depends on the flux density ratio of the

system and the period depends on the binary star separation. The one-dimensional power spectra, $p(f)$, obtained from projections at angles near the separation vector of the binary star should reveal this variation. By contrast, at angles perpendicular to the binary axis, $p(f)$ should be close to unity at all spatial frequencies. The power spectra at the spatial frequency where a minimum is expected for a given binary star separation, sets an upper limit to the flux density ratio for an undetected companion. Minima of a normalized power spectra translate into flux density ratio limits by the following relationship

$$flux\ ratio\ limit = \frac{1 + \sqrt{minimum\ power}}{1 - \sqrt{minimum\ power}}. \tag{3.4}$$

Since the noise in the power spectrum increases with spatial frequency, limits at many different binary star separations were set; those at 0."1, 0."2, 0."8 are listed in Table 3.4. Setting these limits corresponds to determining the minimum values at spatial frequencies 5.0, 2.5, and 0.6 $\frac{cycles}{arcsec}$, respectively. The uncertainty quoted for each limit was propagated from an uncertainty in the normalization of the power spectrum. Each projection was normalized by the mean of the projected dc values ($p(0)$) and the variance of these dc levels determined the uncertainty in the normalization. Examples of the projected power spectra of sources, for which no binary component was seen, are shown in Figure 3.6; the entire set of power spectra for sources with no detected companion stars is in Appendix A.

For additional companion limits in multiple star systems, the evidence of the observed companions was first removed by expanding the one-dimensional binary star solution to a two-dimensional function and subtracting it from the original data. The data were then treated as described above for the single star case. Table 3.5 contains these limits for additional components in the multiple star systems and the plots which display the $p(f)$'s for each of these sources are in Appendix A.

3.4. Overall Survery Results

3.4.1. Observed Companions

Among the 69 target objects observed, we detected 31 binary and one triple system (see Table 3.3). Usually the most massive component in a multiple star system is designated the primary star. However, we could not determine masses from the available data; we have therefore designated the components as primary, secondary, or tertiary (A, B, and C) based on their relative K band flux densities at the time of the observation; the brightest component is taken as the primary star. We note that T Tauri stars are known to be variable, so relative brightnesses may well change with time.

The probability that any of the detected double stars are merely chance alignments with a field star is small. Simon et al. (1992) estimated the density of field stars with K magnitudes brighter than 12 mag to be $\approx 4\times10^{-5}\frac{stars}{arcsec^2}$ in the direction of Tau - Aur and $\approx 3\times10^{-4}\frac{stars}{arcsec^2}$ in the direction of Oph - Sco (Simon 1992a). The faintest companion observed has a K = 11 mag (Figure 3.9); these magnitudes were determined by combining the flux density ratios measured with speckle imaging with the photometric measurements obtained from the literature. Each target star was centered in the field of view; as discussed below, the largest angular separation of detected pairs is $\leq$ 2."5. Of our 45 targets in Tau - Aur, 0.04 are therefore expected to show a field star within a radius of 2."5. Likewise, for the 24 targets observed in Oph - Sco, only 0.14 are expected appear as doubles as a result of a chance projection with a field star.

3.4.2. Overall Survey Limits

Before we can address the astrophysical implications of our survey results, it is essential to estimate the completeness. The sensitivity of a particular observation to finding a companion star, determined in §3.2.2, depends on many factors including the binary star's separation, position angle, flux density ratio (or ΔK), as well as the total K magnitude of the system and the atmospheric conditions. Here, we address the sensitivity of the survey as a whole as opposed to that of the individual measurements.

3.4.2.1. Binary Star Separation Range

In theory, the angular separation range of binary stars detectable by this survey should be constrained only by the diffraction limit of the Hale 5 m Telescope and the field of view of the camera. As described earlier the existence of a binary system is revealed in the power spectrum by a sinusoid. At $\lambda = 2.2\ \mu m$, the diffraction limit corresponds to a maximum spatial frequency, f_{max}, of 11.2 $\frac{cycles}{arcsec}$. This frequency corresponds to the first minima in the power spectrum of a binary system with an angular separation of 0."045, the closest binary system resolvable with this system.

The upper limit for the survey's binary star separation range depends on the camera's field of view. Each target star observed was centered on the array and thus any components outside half the field of view (plus half the seeing disk) were not detected. Since the detector is not circular, the maximum binary star separation that could have been observed depends on the position angle and ranges from 1."8 to 2."5, where we considered the effects of the array size and the best seeing conditions of 0."5 (see Table 3.2) to give a conservative upper limit. To eliminate the dependence on position angle, we selected an upper limit of 1."8 for the angular separation range.

3.4.2.2. Overall Sensitivity to Faint Companions

Within the separation range 0."045 to 1."8, the sensitivity to faint companions was not uniform and varied as a function of separation with the sensitivity increasing with distance from the primary star. For each of the speckle measurements, limiting flux density ratios for unobserved companions were determined at a number of separations, as described in §3.2 (see also Tables 3.4 and 3.5). These limits depend on several factors; (1) the total flux density of the target, (2) the "seeing" or the coherence length of the atmosphere (r_o) and its stability, (3) the atmospheric coherence time (τ_o) and its stability, (4) the amount of data accumulated on the target, and (5) the systematic electronic readout noise (the strength of which varied from run to run). Each factor has a different effect on the way the sensitivity varies as a function of separation and most of these factors varied from observation to observation. Thus the sensitivity of each observation to finding a companion star as a function of separation was unique.

We estimated the overall sensitivity for finding faint companion stars by calculating an average limiting flux density ratio for undetected companion stars amongst the 69 observed targets. If observations of the same object were repeated we selected the best measurement. Figure 3.7 shows histograms of the limiting flux density ratios (plotted as ΔK's) at separations of 0."045, 0."055, 0."069, 0."08, 0."1, 0."2, and 0."8, with the mean and the rms value printed in the top right corner of each distribution. The bin farthest to the left in each of the histograms contains observations that have no significant signal at that particular angular resolution, i.e., a $\Delta K = 0$ mag binary star would not have been detected.

The mean values of the distributions in Figure 3.7 were used to construct a typical limiting sensitivity curve for this survey, which is shown in Figure 3.8. The observed magnitude differences of the detected binary stars are also plotted in Figure 3.8 as circles. On average the observations were of sufficient quality to detect binary

stars with magnitude differences of up to 3.1 mag for separations between 0."1 and 1."8. We note that speckle images of individual objects are routinely made with a much higher dynamic range (e.g., Ghez et al. 1991; Koresko et al. 1991) by obtaining larger data set, i.e., more pairs. In the interest of observing many objects we preferred to accept a lower overall sensitivity. The sensitivity curve in Figure 3.8 rolls off between 0."1 and 0."045 as a result of an exposure time that did not always match the atmospheric conditions. For example, when τ_o, the atmospheric coherence time, was less than the exposure time, the highest spatial frequencies were suppressed. For this survey the exposure time was always 100 msec.

We also evaluated the sensitivity of the observations by converting the limiting flux density ratios into limiting K magnitudes for additional companion stars. We combined our flux density ratio limits with K mag of each target found in the literature (Table 3.1). The average sensitivity curve and its uncertainty in Figure 3.9 was constructed similarly to that in Figure 3.8. On average we were sensitive to companion stars brighter than K = 10.6 mag at distances between 0."1 and 1."8 from the target stars. This is consistent with the estimated apparent magnitudes of the detected companion stars, which are also plotted in Figure 3.9.

Table 3.1a: Oph - Sco Sample

HBC	Name	RA (1950)	DEC (1950)	K (mag)	Ref^{K}	Type	Ref^{TTS}
254	AS 205	16 08 37.7	-18 30 43	5.8	5	ctts	1
637	DoAr 21	16 23 01.7	-24 16 50	6.1	4	wtts	2
649	RNO 90	16 31 17.5	-15 42 04	6.5	6	ctts	1
639	DoAr 24 E	16 23 22.0	-24 14 14	6.7	4	wtts	2
	ROXs 43A	16 28 18.1	-24 23 40	6.7	3	wtts	2,3
270	V1121 Oph	16 46 25.2	-14 16 56	6.8	5	ctts	1
264	SR 9	16 24 38.9	-24 15 23	6.9	4	ctts	1, 2
262	SR 24 S	16 23 56.6	-24 38 55	7.1	7	ctts	1
	155203-2338	15 52 02.6	-23 38 29	7.1	3	wtts	3
643	SR 20	16 25 31.2	-24 16 08	7.1	4	ctts	1, 2
	ROXs 42C	16 28 13.6	-24 27 36	7.2	3	wtts	2,3
257	Haro 1-4	16 22 10.6	-23 12 26	7.3	4	ctts	1
268	Haro 1-16	16 28 31.7	-24 21 10	7.5	4	ctts	1,2
	160946-1851	16 09 46.4	-18 51 48	7.5	3	wtts	3
259	SR 4	16 22 54.9	-24 14 02	7.5	4	ctts	1, 2
	160815-1857	16 08 14.7	-18 57 02	7.7	3	wtts	3
267	Haro 1-14	16 28 03.9	-23 58 12	7.8	4	ctts	1
	162218-2420	16 22 18.1	-24 20 01	7.8	3	wtts	3
266	V853 Oph	16 25 43.7	-24 21 42	8.0	4	ctts	1,2
	155913-2233	15 59 12.6	-22 33 09	8.1	3	wtts	3
	160905-1859	16 09 05.1	-18 59 12	8.1	3	wtts	3
638	DoAr 24	16 23 15.8	-24 13 36	8.1	4	ctts	1, 2
	155828-2232	15 58 27.8	-22 32 18	8.5	3	wtts	3
	160827-1813	16 08 27.3	-18 13 11	8.5	3	wtts	3

HBC = Catalogue entry number in Herbig & Robbin-Bell (1988)

(1) Herbig & Robbin-Bell (1988)
(2) Bouvier & Appenzeller (1991)
(3) Walter (1990)
(4) Rydgren et al. (1976)
(5) Glass & Penston (1974)
(6) Herbst & Warner (1981)
(7) Graham (1991)

Table 3.1b: Tau - Aur Sample

HBC	Object	RA (1950)	DEC (1950)	K (mag)	Ref^{K}	Type	Ref^{TTS}
35	T Tau	04 19 04.2	+19 25 05	5.3	6	ctts	1
34	RY Tau	04 18 50.8	+28 19 35	5.7	7	ctts	1
79	SU Aur	04 52 47.8	+30 29 19	6.0	5	wtts	1,14
74	DR Tau	04 44 13.2	+16 53 24	6.4	3	ctts	1
367	V773 Tau	04 11 07.3	+28 04 41	6.5	4	wtts	1
37	DG Tau	04 24 01.0	+25 59 36	6.7	3	ctts	1
36	DF Tau	04 23 59.6	+25 35 41	6.8	2	ctts	1
25	CW Tau	04 11 11.3	+28 03 27	6.9	3	ctts	1
80	RW Aur	05 04 37.7	+30 20 14	6.9	2	ctts	1
380	HDE 283572	04 18 52.5	+28 11 07	6.9	8	wtts	1,14
404	V807 Tau	04 30 05.2	+24 03 39	6.9	11	ctts	1
76	UY Aur	04 48 35.7	+30 42 14	7.0	3	ctts	1
45	DK Tau	04 27 40.5	+25 54 59	7.1	9	ctts	1
49	HL Tau	04 28 44.4	+18 07 36	7.1	3	ctts	1
50	XZ Tau	04 28 46.0	+18 07 35	7.2	3	ctts	1
415	HP Tau/G2	04 32 54.2	+22 48 08	7.3	13	wtts	1,14
52	UZ Tau E	04 29 39.3	+25 46 13	7.3	9	ctts	1
374	Hubble 4	04 15 40.9	+28 12 54	7.3	11	wtts	1
57	GK Tau	04 30 32.8	+24 14 52	7.3	4	ctts	1
66	HP Tau	04 32 52.8	+22 48 18	7.3	13	ctts	1
402	FZ Tau	04 29 30.1	+24 13 44	7.5	8	ctts	1
386	FV Tau	04 23 49.8	+26 00 13	7.5	8	ctts	1
67	DO Tau	04 35 24.2	+26 04 55	7.5	7	ctts	1
54	GG Tau	04 29 37.1	+17 25 22	7.5	13	ctts	1
29	V410 Tau	04 15 24.8	+28 20 02	7.5	4	wtts	1
396	Haro 6-13	04 29 13.6	+24 22 43	7.6	8	ctts	1
368	LkCa 3	04 11 42.8	+27 45 05	7.6	12	wtts	12
56	GI Tau	04 30 32.3	+24 15 03	7.6	4	ctts	1
33	DE Tau	04 18 49.8	+27 48 05	7.7	7	ctts	1
55	GH Tau	04 30 04.8	+24 03 18	7.7	3	ctts	1
61	CI Tau	04 30 52.2	+22 44 17	7.8	7	ctts	1
423	*LkH* α 332/G1	04 39 03.4	+25 17 24	7.8	8	wtts	8
59	IS Tau	04 30 32.7	+26 15 03	8.0	4	ctts	1
30	DD Tau	04 15 25.1	+28 09 15	8.0	3	ctts	1
41	IQ Tau	04 26 47.7	+26 00 16	8.0	3	wtts	1,14
32	BP Tau	04 16 08.6	+28 59 15	8.0	7	ctts	1
398	V928 Tau	04 29 17.2	+24 16 08	8.0	8	wtts	1
44	FX Tau	04 27 27.9	+24 20 18	8.1	3	ctts	1
369	FO Tau	04 11 43.6	+28 05 02	8.1	8	ctts	1
53	UZ Tau W	04 29 39.3	+25 46 13	8.1	9	ctts	1
24	FN Tau	04 11 08.6	+28 20 27	8.2	3	ctts	1
39	DI Tau	04 26 38.0	+26 26 20	8.4	4	wtts	1
388	042417+1744	04 24 17.2	+17 44 03	8.4	8	wtts	1
28	CY Tau	04 14 27.7	+28 13 29	8.4	3	ctts	1
378	V819 Tau	04 16 19.9	+28 19 03	8.5	8	wtts	1

(1) Herbig & Robbin-Bell (1988)
(2) Rydgren et al. (1976)
(3) Rydgren & Vrba (1983)
(4) Rydgren & Vrba (1981)
(5) Warner et al. (1977)
(6) Skrutskie (1992)
(7) Rydgren et al. (1982)

(8) Walter et al. (1988)
(9) Cohen & Kuhi (1979)
(10) Simon et al. (1992)
(11) Elias (1978)
(12) Herbig et al. (1986)
(13) Moneti & Zinnecker (1991)
(14) Strom et al. (1989)

Table 3.2a: Journal of Observations Oph - Sco

Date	Object	Cal (SAO)	Sets	Seeing at K (")
1990 July 7	AS 205	159745	3	0.9
	RNO 90	159948	4	0.7
	V1121 Oph	160116	4	0.8
1990 July 8	155913-2233	183901	5	0.7
	155203-2338	183901	4	0.7
	162218-2420	183901	4	0.6
	ROXs 42C	184549	5	0.8
	ROXs 43A	184549	4	0.7
1990 July 9	DoAr 21	184429	4	0.9
	SR 24 S	184549	4	0.9
	DoAr 24 E	184549	6	0.9
	SR 9	184549	4	0.9
	SR 20	184549	4	0.9
	Haro 1-16	184549	4	1.2
	Haro 1-4	184549	4	0.9
	SR 4	184549	4	1.0
1990 Aug 5	SR 9	184549	5	0.9
	160946-1851	159745	4	0.9
	160815-1857	159745	4	0.9
	160905-1859	159745	4	0.9
1990 Aug 6	Haro 1-16	184549	5	0.9
	160827-1813	159745	6	1.0
1990 Aug 7	SR 4	184549	8	1.0
	V853 Oph	184549	8	0.8
	DoAr 24	184549	6	1.0
	155828-2232	183901	4	1.4
1991 May 3	ROXs 42C	184549	6	1.2
1992 Feb 18	Haro 1-14	184429	6	1.0

Table 3.2b: Journal of Observations Tau - Aur

Date	Object	Cal (SAO)	Sets	Seeing at K (")
1990 Oct 2	RY Tau	76461	8	1.0
	DD Tau	76551	8	1.1
	LkHα 332/G1	76727	4	1.2
1990 Oct 3	V773 Tau	76551	8	1.0
1990 Oct 4	CW Tau	76551	8	0.8
	DD Tau	76551	8	0.7
	RY Tau	76461	8	0.7
	LkHα 332/G1	76727	8	0.7
	SU Aur	57454	10	0.6
1990 Nov 9	DG Tau	76613	9	1.3
	T Tau	98918	7	1.3
	DR Tau	93907	8	1.3
	RW Aur	76876	8	0.9
	DF Tau	76613	5	1.0
1990 Nov 10	HDE 283572	76551	3	1.2
	V807 Tau	76613	8	0.9
	UZ Tau E	76613	8	0.9
	UZ Tau W	76613	8	0.9
	UY Aur	57454	8	1.2
	HL Tau	93907	11	1.2
1991 Oct 18	LkCa 3	76461	2	0.6
	FO Tau	76461	5	0.6
	CY Tau	76461	4	0.6
	V819 Tau	76461	6	0.6
	DI Tau	76727	4	0.6
	FX Tau	76727	2	0.6
	042417+1744	93918	5	0.6
1991 Oct 19	FN Tau	76461	6	0.5
	BP Tau	76461	6	0.5
	IQ Tau	76727	4	0.5
	V928 Tau	76727	6	0.6
	IS Tau	76727	6	0.6
	FZ Tau	76727	6	0.6
	Haro 6-13	76727	6	0.5
	GI Tau	76727	6	0.6
	GH Tau	76727	6	0.6
	CI Tau	76727	4	0.5
1991 Oct 20	V410 Tau	76461	6	0.7
	DE Tau	76485	7	1.1
	Hubble 4	76485	6	0.8
	GK Tau	76727	5	0.8
	FV Tau	76613	6	0.7
	GG Tau	93918	6	0.7
	HP Tau	76727	5	0.8
	HP Tau/G2	76727	5	0.8
	DK Tau	76727	5	0.8
	XZ Tau	93874	5	1.0
1991 Nov 19	DO Tau	76618	5	0.9

Table 3.3a: Double Star Parameters Oph - Sco

OBJECT	Date	Separation *arcsec*	P.A. *deg*	Flux Ratio	Notes
SR 20	1990 July 9	0.071 ± 0.001	225 ± 5	8 ± 1	
ROXs 42C	1990 July 8	0.157 ± 0.003	135 ± 3	4.0 ± 0.3	4a
	1991 May 3	0.152 ± 0.003	139 ± 3	4.7 ± 0.3	
160946-1851	1990 Aug 5	0.208 ± 0.004	164 ± 2	3.99 ± 0.06	
162218-2420	1990 July 8	0.236 ± 0.005	156 ± 2	1.25 ± 0.03	
155913-2233	1990 July 8	0.288 ± 0.005	347 ± 2	2.15 ± 0.03	4a
V853 Oph	1990 Aug 7	0.399 ± 0.008	96 ± 2	4.2 ± 0.5	
SR 9	1990 July 9	0.59 ± 0.01	350 ± 1	11 ± 2	2
	1990 Aug 5	0.59 ± 0.01	350 ± 1	13 ± 2	
Haro 1-4	1990 July 9	0.72 ± 0.01	27 ± 1	4.2 ± 0.2	2
155203-2338	1990 July 8	0.80 ± 0.01	229 ± 1	7.1 ± 0.4	
AS 205	1990 July 7	1.32 ± 0.02	212 ± 1	3.2 ± 0.2	2,3
DoAr 24 E	1990 July 9	2.03 ± 0.04	150 ± 1	5.6 ± 0.9	1

Notes proceeded by an "a" indicate measurements of additional components in these systems that were outside of the separation range of this survey. Otherwise the notes refer to other measurements of the observed binary stars.

(1) Chelli et al. (1988) identified the companion using direct near infrared imaging techniques

(2) Weintraub (1989) detected these binary stars using one-dimensional near-infrared speckle measurements. The discrepancies between these results and the survey presented here are easily accounted for by the limited angular resolution obtained by Weintraub (1989) (f_{max}=0.3–3.6*cycles/arcsec*)

(3) Cohen & Kuhi (1979) identified the secondary component directly at optical wavelengths

(4a) Mathieu et al. (1988) detected both a spectroscopic binary companion in both 162814-2427 (ROXs 42C)and 155913-2233: thus both systems consist of at least three stars.

Table 3.3b: Double Star Parameters Tau - Aur

OBJECT	Date	Separation *arcsec*	P.A. *deg*	Flux Ratio	Notes
DF Tau	1990 Nov 9	0.088 ± 0.002	329 ± 5	2.13 ± 0.02	1
V773 Tau	1990 Oct 3	0.112 ± 0.002	295 ± 4	2.15 ± 0.01	8
DI Tau	1991 Oct 18	0.12 ± 0.01	294 ± 4	8 ± 1	1
V410 Tau	1991 Oct 20	0.123 ± 0.002	218 ± 4	6.2 ± 0.9	
FO Tau	1991 Oct 18	0.166 ± 0.003	182 ± 3	1.53 ± 0.03	8
V928 Tau	1991 Oct 19	0.165 ± 0.003	125 ± 3	1.66 ± 0.02	8
LkH α 332/G1	1990 Oct 4	0.215 ± 0.004	77 ± 2	1.78 ± 0.02	8
	1990 Oct 2	0.201 ± 0.004	261 ± 2	3.4 ± 0.2	
IS Tau	1991 Oct 19	0.221 ± 0.004	92 ± 2	6.3 ± 0.9	1
GG Tau	1991 Oct 20	0.288 ± 0.006	3 ± 2	4.0 ± 0.1	6,10a
XZ Tau	1991 Oct 20	0.311 ± 0.006	153 ± 2	1.96 ± 0.05	7
GH Tau	1991 Oct 19	0.314 ± 0.006	299 ± 2	1.8 ± 0.02	8
UZ Tau W	1990 Nov 10	0.360 ± 0.007	359 ± 1	2.18 ± 0.07	1
V807 Tau	1990 Nov 9	0.375 ± 0.007	330 ± 1	2.69 ± 0.06	11a,8
LkCa 3	1991 Oct 18	0.491 ± 0.009	77 ± 1	1.046 ± 0.005	8
DD Tau	1990 Oct 4	0.56 ± 0.01	186 ± 1	1.92 ± 0.02	
	1990 Oct 2	0.56 ± 0.01	186 ± 1	2.17 ± 0.07	3,8
T Tau	1990 Nov 9	0.71 ± 0.01	176 ± 1	11 ± 1	4
FV Tau	1991 Oct 20	0.73 ± 0.01	92 ± 1	1.56 ± 0.04	1,6,9a
UY Aur	1990 Nov 10	0.88 ± 0.02	227 ± 1	2.86 ± 0.06	5,2,8
FX Tau	1991 Oct 18	0.90 ± 0.02	291 ± 1	1.965 ± 0.001	
RW Aur A-BC	1990 Nov 9	1.39 ± 0.03	256 ± 1	8 ± 1	5,2,8
RW Aur B-C		0.120 ± 0.004	111 ± 3	41 ± 105	
DK Tau	1991 Oct 20	-	-	-	1,2

Notes proceeded by an "a" indicate measurements of additional components in these systems that were outside of the separation range of this survey. Otherwise the notes refer to other measurements of the observed binary stars.

(1) Simon et al.'s (1992) measured the binary systems DF, DI, FV, and UZ Tau E using lunar occultations and DK Tau using direct imaging techniques. Note: Although IS Tau was initially reported as a single star, the companion was detected in the occultation measurements close to the noise level (Simon private communication).

(2) Weintraub (1989) detected these binary stars using one-dimensional near-infrared speckle measurements. The discrepancies between these results and the survey presented here are easily accounted for by the limited angular resolution obtained by Weintraub (1989) (f_{max}=0.3–3.6*cycles/arcsec*)

(3) Bouvier et al. (1992) studied this double star at multiple wavelengths using speckle and direct imaging techniques

(4) This double star was first detected by Dyck et al. (1982) with one-dimensional near-infrared speckle interferometry. Ghez et al. (1991) and references within have also studied this double star using high resolution imaging techniques.

(5) Joy & Van Biesbroeck (1944) resolved the widely separated components of RW Aur and UY Aur directly at optical wavelengths.

(6) Leinert et al. (1991) measured the double star GG Tau using one-dimensional speckle imaging techniques and FV Tau using lunar occultations. speckle, and CCD imaging

(7) Haas et al. (1990) measured this double star using one-dimensional near-infrared speckle imaging techniques

(8) Leinert et al. (1992) measure these double stars using near infrared speckle imaging techniques.

(9a) FV Tau appears to consist of at least four stars. FV Tau/c is located 12" away from FV Tau (Herbig & Robbin-Bell 1988). Both FV Tau (see table) and FV Tau/c have close companions (Simon et al. 1992).

(10a) GG Tau also appears to consist of at least four stars. GG Tau/c is located 10" away from GG Tau (Cohen & Kuhi 1979, Moneti & Zinnecker 1991). Both GG Tau (see table) and GG Tau/c have close companions detected by Leinert et al. (1991).

(11a) Simon (1992b) detected an additional companion with a projected separation of 23 mas from the southern component of the observed binary star V807 Tau (Elias 12). This third component reduces the visibility in our measurements, but no minimum is observed, so the actual separation is between 23 - 45 mas.

Table 3.4a: Limits for Stars Observed Without Companion Stars in Oph - Sco

OBJECT	Date	Flux Ratio Limits			Notes
		0."10	0."20	0."80	
V1121 Oph	1990 July 7	47 ± 13	47 ± 13	47 ± 13	
RNO 90	1990 July 7	27 ± 7	27 ± 7	28 ± 8	
SR 24 S	1990 July 9	23 ± 7	23 ± 7	23 ± 7	1a
Haro 1-16	1990 Aug 6	20 ± 4	20 ± 4	20 ± 4	
	1990 July 9	14 ± 3	14 ± 3	14 ± 3	
160815-1857	1990 Aug 5	17 ± 3	18 ± 4	18 ± 4	3a
SR 4	1990 Aug 7	17 ± 4	22 ± 6	23 ± 6	
	1990 July 9	11 ± 2	11 ± 2	11 ± 2	
DoAr 21	1990 July 9	16 ± 2	16 ± 2	16 ± 2	
ROXs 43A	1990 July 8	14 ± 4	14 ± 4	14 ± 4	2a
160827-1813	1990 Aug 6	11 ± 2	11 ± 2	11 ± 2	
DoAr 24	1990 Aug 7	8.0 ± 0.8	15 ± 3	15 ± 3	
Haro 1-14	1992 Feb 18	8 ± 2	8 ± 2	10 ± 3	
160905-1859	1990 Aug 5	3.2 ± 0.3	5.1 ± 0.7	5.4 ± 0.8	
155828-2232	1990 Aug 7	3.0 ± 0.7	3.0 ± 0.7	3.0 ± 0.7	

Notes proceeded by an "a" indicate measurements of additional components in these systems that were outside of the separation range of this survey.

(1a) Haro & Chavira (1974) noted SR 24 to be a wide (6" at P.A. 60^o) north - south double star. Simon (private communication) found SR 24 S to be associated with an additional close companion star.

(2a) ROXs 43 appears to consist of at least three stars. Bouvier & Appenzeller (1991) identified the widely separated (6" at P.A. 13^o) pair, which they labeled as ROX 43 AB. Mathieu et al. (1988) measured 162819-2423S (ROX 43A) as a spectroscopic binary system.

(3a) Mathieu et al. (1988) discovered a spectroscopic binary in this system.

Table 3.4b: Limits for Stars Observed Without Companions Stars in Tau - Aur

OBJECT	Date	Flux Ratio Limits			Notes
		0."10	0."20	0."80	
DR Tau	1990 Nov 9	43 ± 11	43 ± 11	43 ± 11	
RY Tau	1990 Oct 2	43 ± 12	43 ± 12	45 ± 13	
	1990 Oct 4	27 ± 8	27 ± 8	27 ± 8	
SU Aur	1990 Oct 4	41 ± 14	44 ± 16	44 ± 16	
CW Tau	1990 Oct 4	28 ± 7	34 ± 9	35 ± 10	
BP Tau	1991 Oct 19	26 ± 7	30 ± 10	35 ± 12	
Haro 6-13	1991 Oct 19	25 ± 8	25 ± 8	25 ± 8	
FZ Tau	1991 Oct 19	25 ± 8	25 ± 8	25 ± 8	
DO Tau	1991 Nov 19	24 ± 6	24 ± 6	24 ± 6	
UZ Tau E	1990 Nov 10	22 ± 6	22 ± 6	23 ± 7	
IQ Tau	1991 Oct 19	18 ± 4	18 ± 4	18 ± 4	1a
FN Tau	1991 Oct 19	18 ± 5	18 ± 5	18 ± 5	
HL Tau	1990 Nov 10	16 ± 4	20 ± 6	20 ± 6	
GI Tau	1991 Oct 19	16 ± 6	16 ± 6	16 ± 6	
042417+1744	1991 Oct 18	15 ± 3	16 ± 3	16 ± 3	
DG Tau	1990 Nov 9	14 ± 4	22 ± 7	22 ± 7	
V819 Tau	1991 Oct 18	14 ± 4	14 ± 4	14 ± 4	
CY Tau	1991 Oct 18	14 ± 4	14 ± 4	14 ± 4	
HP Tau	1991 Oct 20	11 ± 2	15 ± 4	16 ± 5	
GK Tau	1991 Oct 20	11 ± 4	11 ± 4	11 ± 4	
CI Tau	1991 Oct 19	10 ± 2	10 ± 2	10 ± 2	
HDE 283572	1990 Nov 10	9 ± 2	9 ± 2	9 ± 2	
HP Tau/G2	1991 Oct 20	9 ± 3	9 ± 3	9 ± 3	2a
Hubble 4	1991 Oct 20	8 ± 2	8 ± 2	8 ± 2	
DE Tau	1991 Oct 20	6 ± 1	8 ± 2	12 ± 4	

Notes proceeded by an "a" indicate measurements of additional components in these systems that were outside of the separation range of this survey.

(1a) Herbig & Robbin-Bell (1988) detected another star separated by 10" from IQ Tau.

(2a) HP Tau/G2 is located 10" away from HP Tau/G3 (Moneti & Zinnecker 1991)

Table 3.5a: Limits for Stars Observed as Multiple Systems in Oph - Sco

OBJECT	Date	Flux Ratio Limits		
		0."10	0."20	0."80
SR 20	1990 July 9	28 ± 5	30 ± 6	30 ± 6
SR 9	1990 Aug 5	24 ± 7	26 ± 8	27 ± 8
	1990 July 9	16 ± 3	16 ± 3	16 ± 3
ROX 42C	1991 May 3	21 ± 4	23 ± 5	23 ± 5
	1990 July 8	13 ± 4	13 ± 4	13 ± 4
Haro 1-4	1990 July 9	21 ± 4	21 ± 4	24 ± 6
160946-1851	1990 Aug 5	19 ± 3	33 ± 9	33 ± 9
162218-2420	1990 July 8	19 ± 4	20 ± 5	20 ± 5
DoAr 24 E	1990 July 9	19 ± 4	19 ± 4	19 ± 4
155293-2338	1990 July 8	9 ± 2	9 ± 2	12 ± 3
AS 205	1990 July 7	7 ± 1	8 ± 1	8 ± 1
V853 Oph	1990 Aug 7	7 ± 1	7 ± 1	8 ± 2
155913-2233	1990 July 8	5.9 ± 0.8	10 ± 2	12 ± 3

Table 3.5b: Limits for Stars Observed as Multiple Systems in Tau - Aur

OBJECT	Date	Flux Ratio Limits		
		0."10	0."20	0."80
T Tau	1990 Nov 9	56 ± 18	56 ± 18	56 ± 18
DD Tau	1990 Oct 4	42 ± 10	42 ± 10	42 ± 10
	1990 Oct 2	20 ± 5	21 ± 6	23 ± 7
RW Aur	1990 Nov 9	41 ± 13	41 ± 13	41 ± 13
UY Aur	1990 Nov 10	33 ± 10	36 ± 12	39 ± 14
V807 Tau	1990 Nov 10	25 ± 4	47 ± 13	47 ± 13
FO Tau	1991 Oct 18	23 ± 5	34 ± 9	34 ± 9
UZ Tau W	1990 Nov 10	23 ± 7	23 ± 7	27 ± 10
V928 Tau	1990 Nov 9	20 ± 6	26 ± 9	26 ± 9
DF Tau	1990 Nov 9	20 ± 5	20 ± 5	20 ± 5
DI Tau	1991 Oct 18	17 ± 4	18 ± 5	19 ± 5
LkHα 332/G1	1990 Oct 4	17 ± 3	59 ± 24	59 ± 24
	1990 Oct 2	7 ± 1	12 ± 3	12 ± 3
XZ Tau	1991 Oct 20	15 ± 4	15 ± 4	15 ± 4
IS Tau	1991 Oct 19	13 ± 3	16 ± 4	17 ± 4
GG Tau	1991 Oct 20	12 ± 3	12 ± 3	13 ± 3
FX Tau	1991 Oct 18	12 ± 3	12 ± 3	12 ± 3
V410 Tau	1991 Oct 20	12 ± 3	16 ± 5	16 ± 5
FV Tau	1991 Oct 20	10 ± 2	15 ± 5	16 ± 5
V773 Tau	1990 Oct 3	10 ± 2	10 ± 2	10 ± 2
LkCa 3	1991 Oct 18	9 ± 2	9 ± 2	9 ± 2
GH Tau	1991 Oct 19	7.8 ± 0.8	7.8 ± 0.8	7.8 ± 0.8
DK Tau	1991 Oct 20	5 ± 2	5 ± 2	5 ± 2

Figure Captions

Figure 3.1: Histogram of identified T Tauri Stars in Tau - Aur and Oph - Sco as a function of the total K magnitude (the outline region). The hatched region corresponds to the distribution of the observed sample.

Figure 3.2: The reconstruction of the binary star DD Tau from 1990 Oct 4 (a) the calibrated power spectrum (b) the Fourier phases, and (c) the final image.

Figure 3.3: The mask used to eliminate frequencies outside the diffraction limit and those that that have aliased power.

Figure 3.4: The one-dimensional power spectrum and model fit for DD Tau.

Figure 3.5: Speckle image of RW Aur (triple star system)

Figure 3.6: The 36 one-dimensional power spectra and companion limits for V1121 Oph, 042417+1744, and Hubble 4. These three examples were chosen to show the range of sensitivity. V1121 Oph is an example of one of the best limits achieved and Hubble 4 is an example of one of the poorest sensitivity observations allowed in the complete sample (4.1).

Figure 3.7: Histograms of the limiting K magnitude differences for unobserved companions at 0."045, 0."055, 0."069, 0."08, 0."1, 0."2, and 0."8. Each histogram contains a total of 69 limits, one for each target. In the cases of multiple observations of a single target the best limits were used.

Figure 3.8: The average sensitivity curve, measured in terms of limiting K magnitude difference, is plotted as a function of separation. Also plotted here are the observed binary star magnitude differences.

Figure 3.9: The average sensitivity curve, measured in terms of limiting apparent K magnitude of a companion star, is plotted as a function of separation. Also plotted here are the observed companion star magnitudes. Secondaries are plotted as squares and the one tertiary is plotted as a triangle.

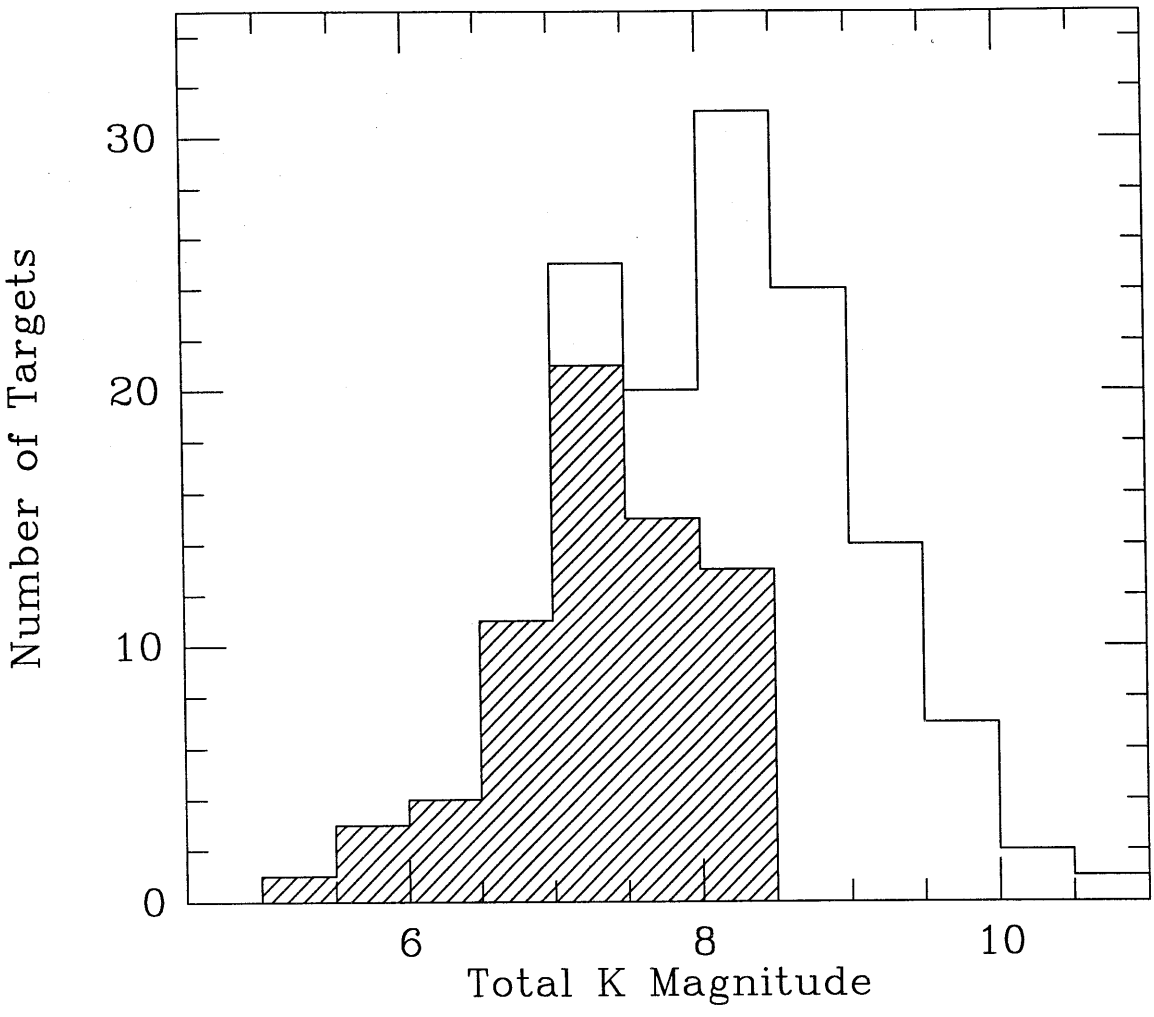

Figure 3.1

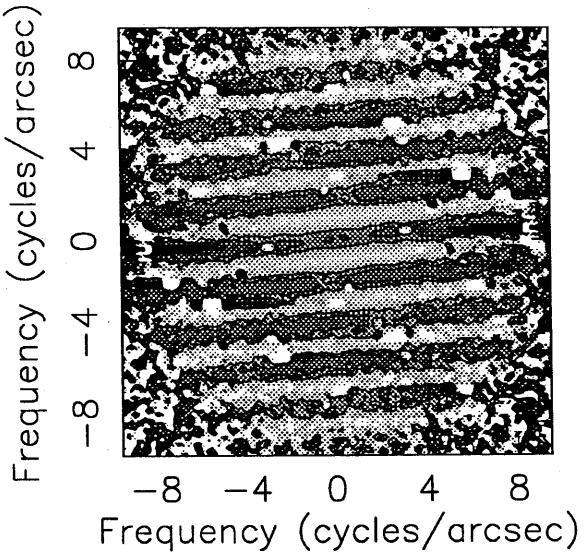
Frequency (cycles/arcsec)
8
4
0
−4
−8
−8 −4 0 4 8
Frequency (cycles/arcsec)

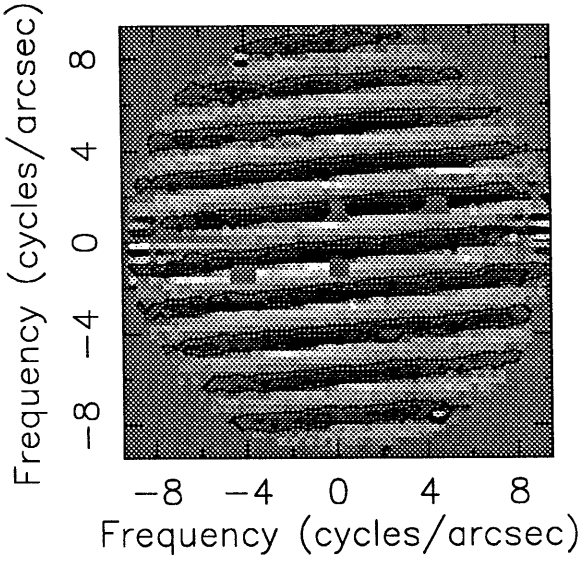
Frequency (cycles/arcsec)
8
4
0
−4
−8
−8 −4 0 4 8
Frequency (cycles/arcsec)

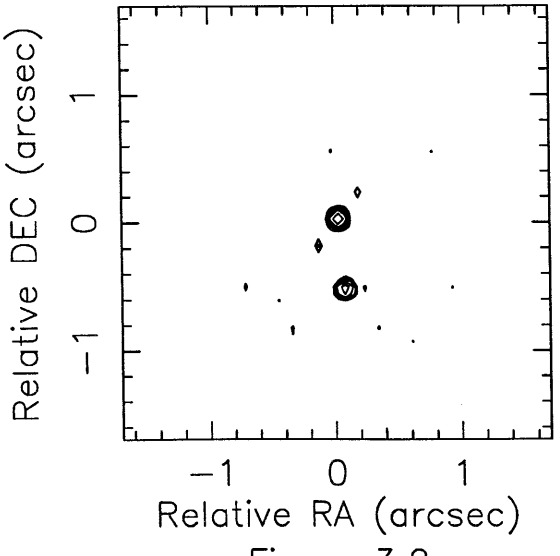
Relative DEC (arcsec)
1
0
−1
−1 0 1
Relative RA (arcsec)

Figure 3.2

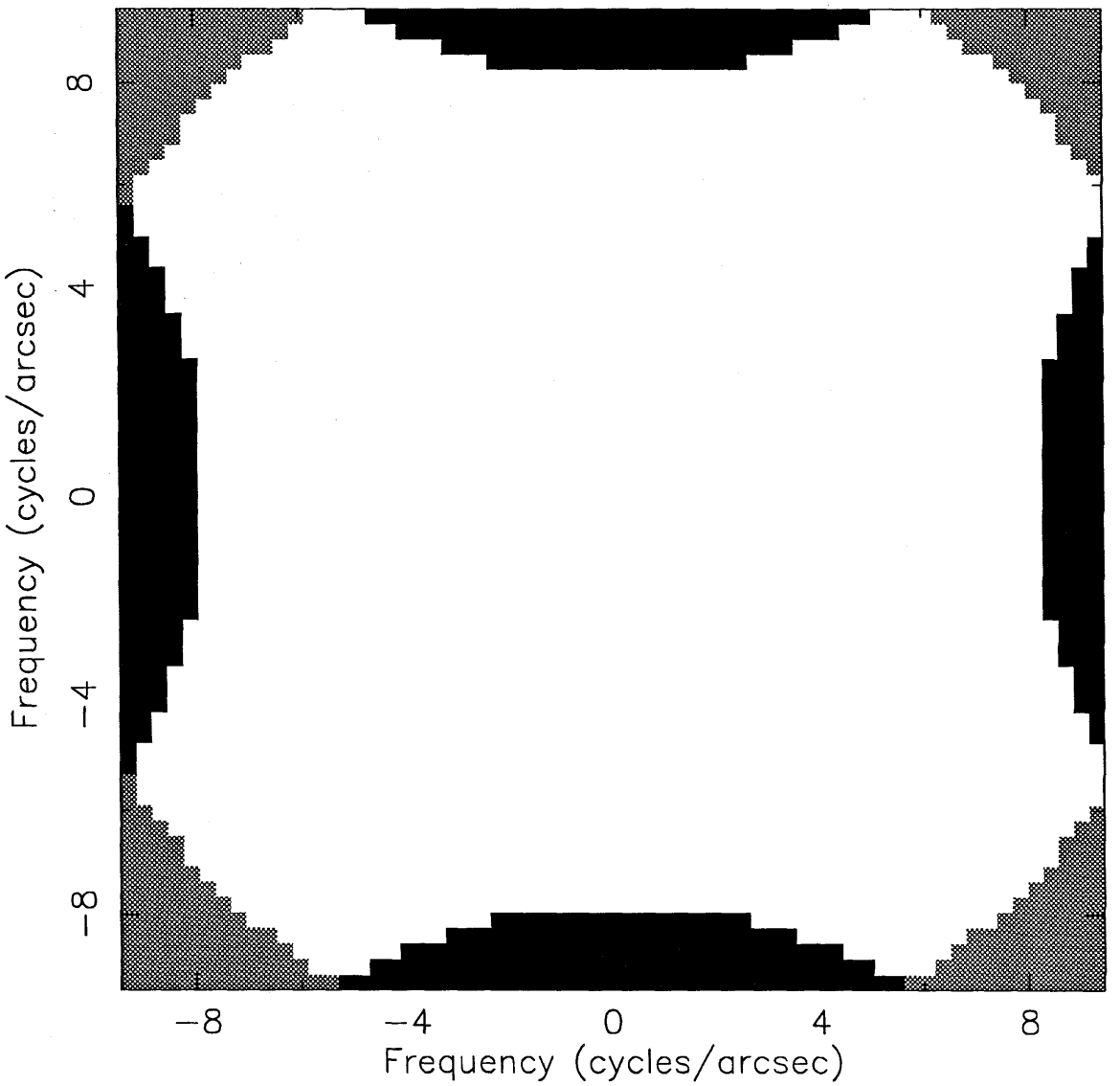
Frequency (cycles/arcsec)
8
4
0
−4
−8
−8
−4
0
4
8
Frequency (cycles/arcsec)

Figure 3.3

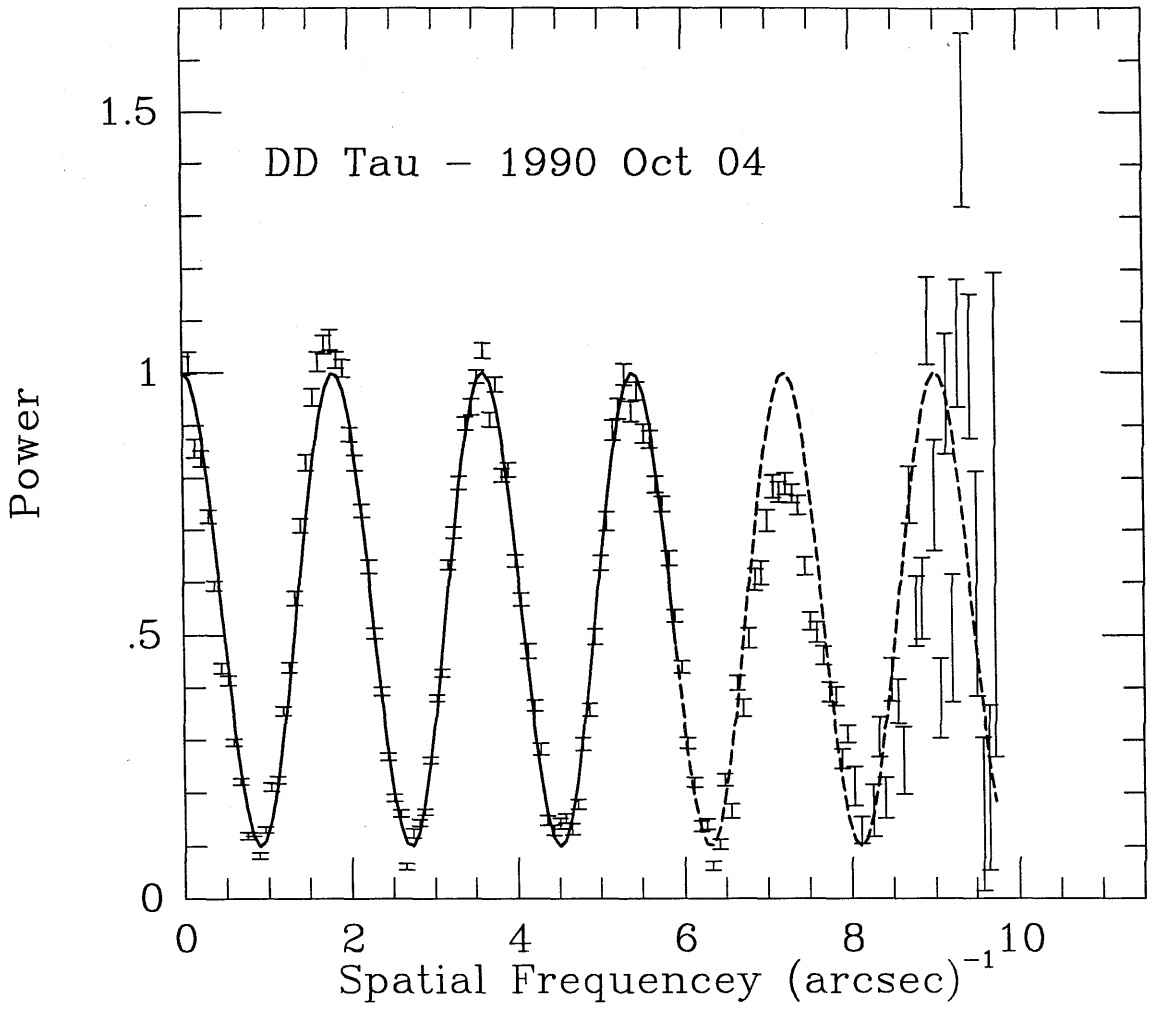
DD Tau – 1990 Oct 04
Power
1.5
1
.5
0
0
2
4
6
8
10
Spatial Frequencey (arcsec)$^{-1}$

Figure 3.4

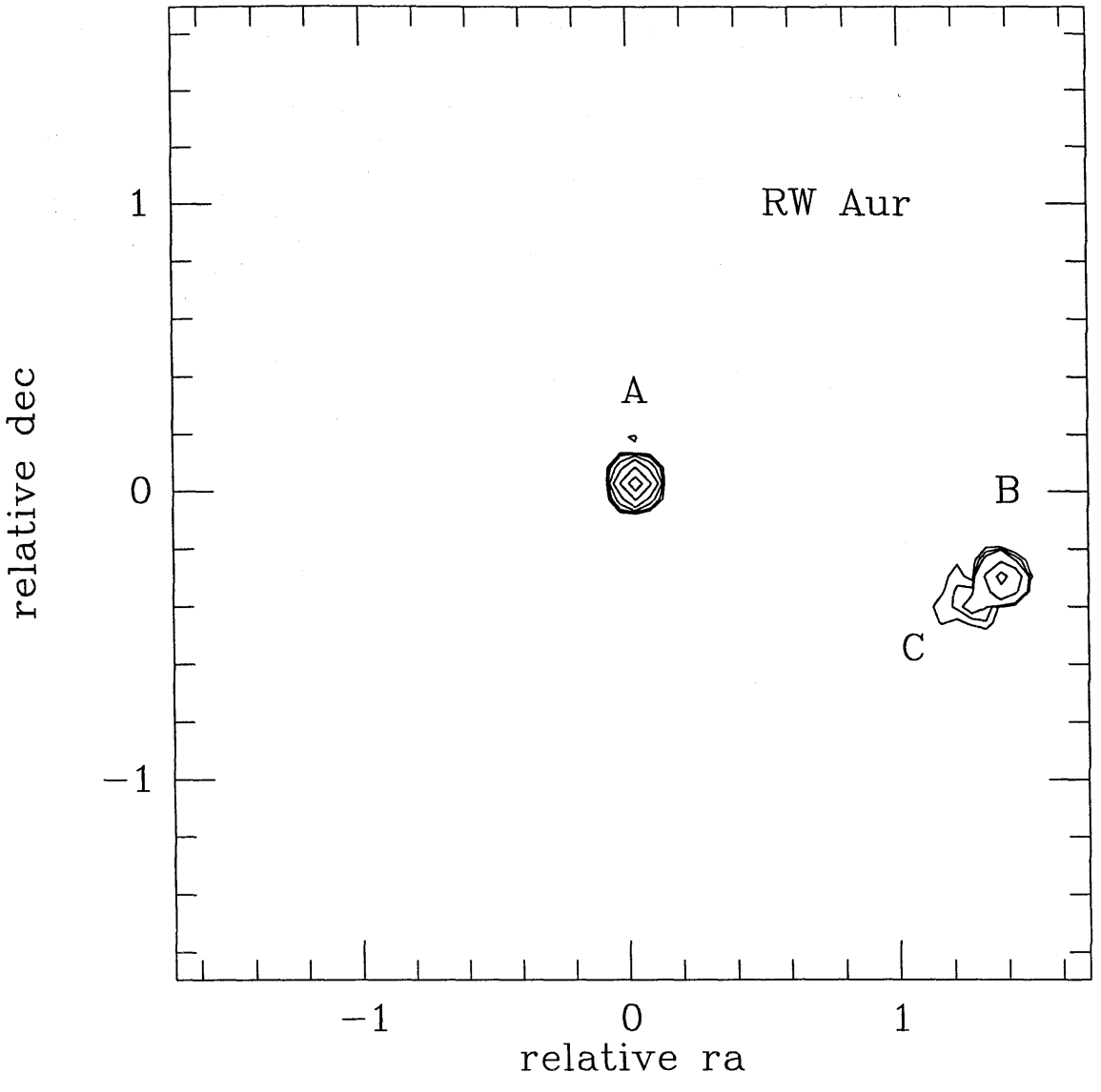

Figure 3.5

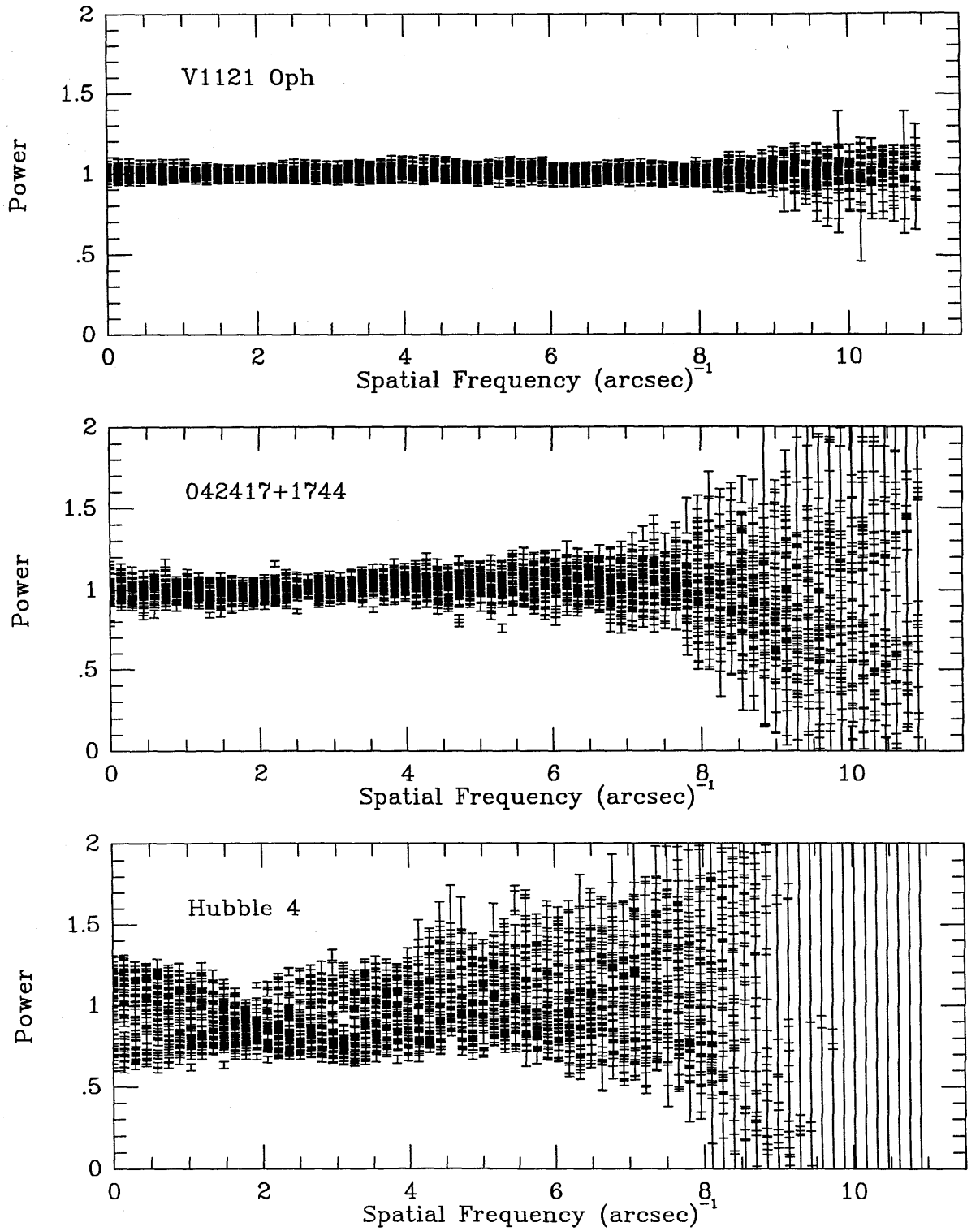
V1121 Oph
042417+1744
Hubble 4
Power
Spatial Frequency (arcsec)$^{-1}$
0
.5
1
1.5
2
0
2
4
6
8
10

Figure 3.6

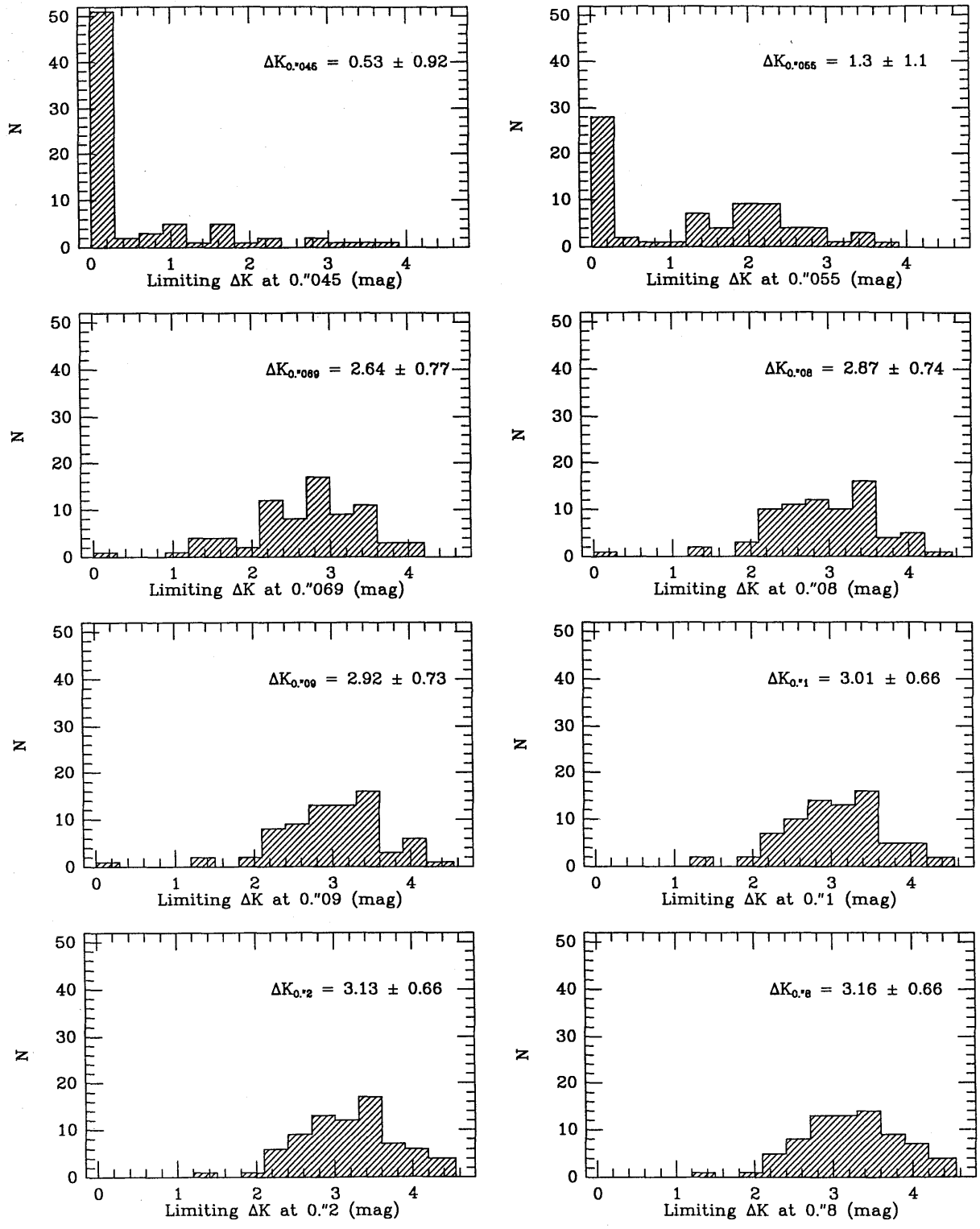
ΔK0.″045 = 0.53 ± 0.92
Limiting ΔK at 0.″045 (mag)
ΔK0.″055 = 1.3 ± 1.1
Limiting ΔK at 0.″055 (mag)
ΔK0.″069 = 2.64 ± 0.77
Limiting ΔK at 0.″069 (mag)
ΔK0.″08 = 2.87 ± 0.74
Limiting ΔK at 0.″08 (mag)
ΔK0.″09 = 2.92 ± 0.73
Limiting ΔK at 0.″09 (mag)
ΔK0.″1 = 3.01 ± 0.66
Limiting ΔK at 0.″1 (mag)
ΔK0.″2 = 3.13 ± 0.66
Limiting ΔK at 0.″2 (mag)
ΔK0.″8 = 3.16 ± 0.66
Limiting ΔK at 0.″8 (mag)
N

Figure 3.7

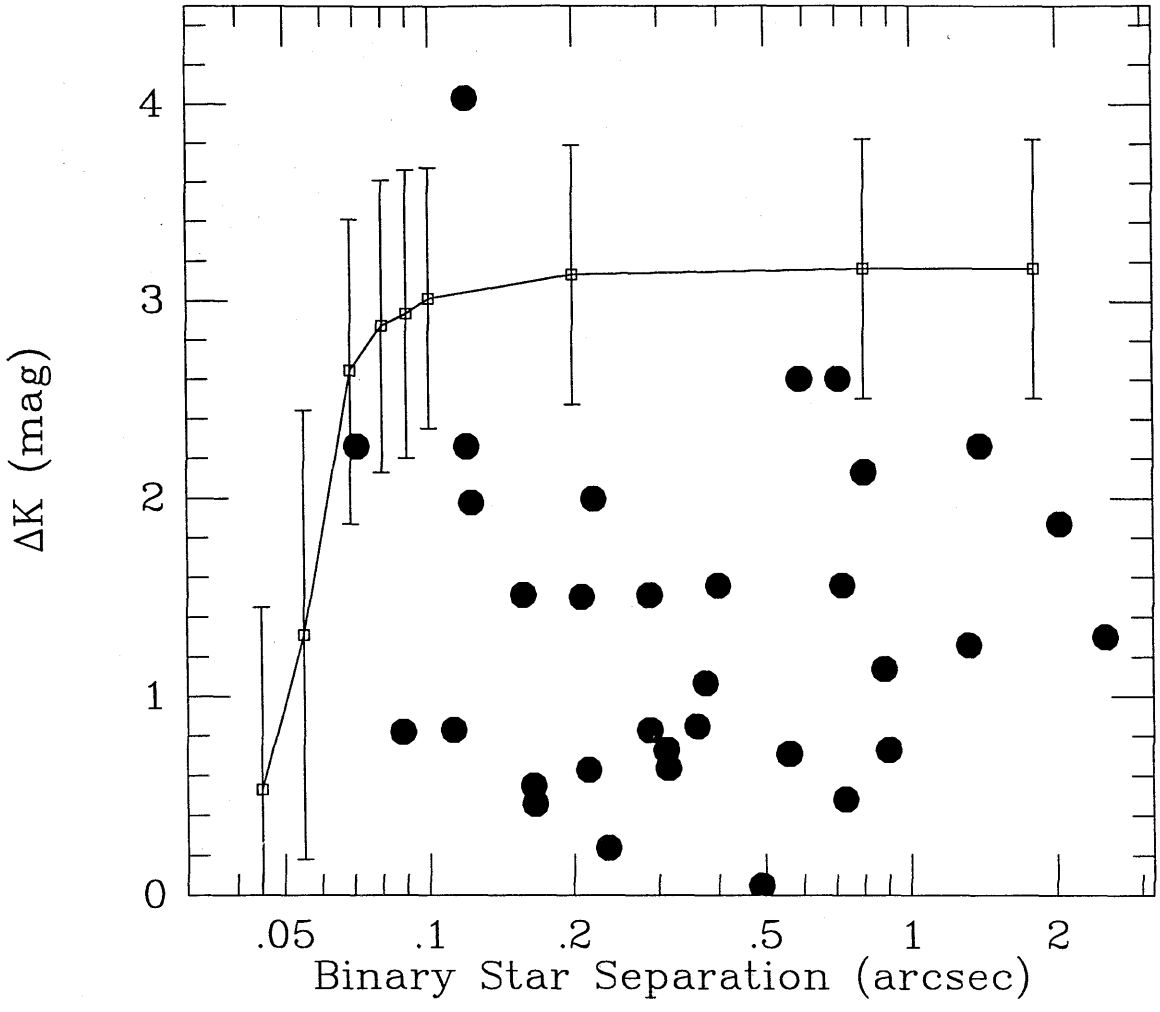

Figure 3.8

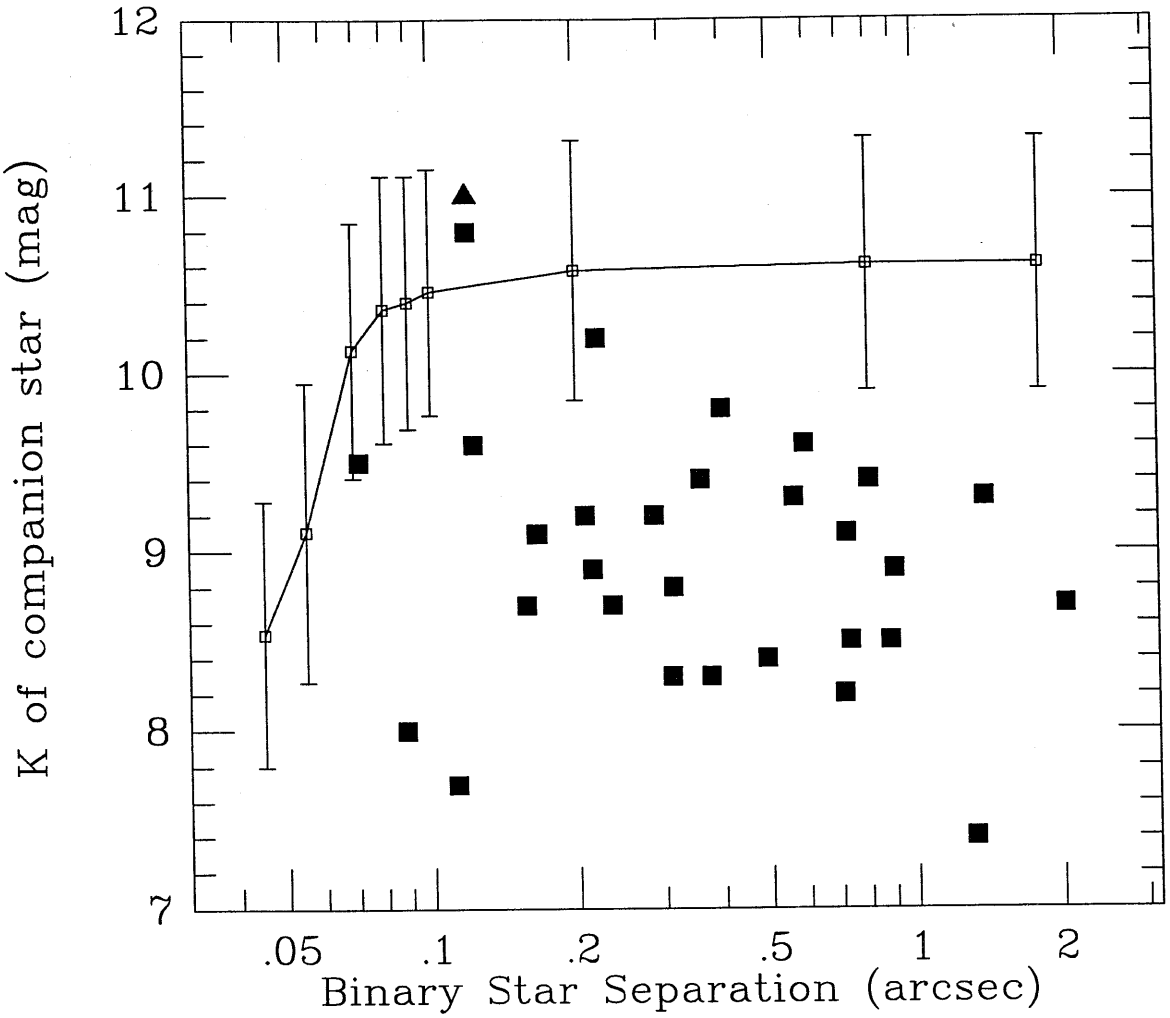
12
11
10
9
8
7
K of companion star (mag)
.05
.1
.2
.5
1
2
Binary Star Separation (arcsec)

Figure 3.9

Chapter Four

4. Discussion

4.1. Completeness and Multiplicity

In the first few sections of this discussion we compare the binary star frequencies of various groups of T Tauri stars to address questions regarding the formation of binary stars. To ensure both completeness and consistency in these comparisons, we define a subset of our survey as the "complete sample." The first step taken to construct this sample was to require each of the included observations, whether or not a companion star was detected, to be sensitive to additional companions within a specified area in the magnitude difference - angular separation phase space. We call this area the completeness region, because we are guaranteeing that all the companion stars with magnitude difference and angular separation within the range of this region were detected. Based on the average sensitivity curve plotted in Figure 3.7, we restricted ourselves to angular separations between 0."1 and 1."8 and magnitude differences from 0.0 to 2.0 mag. As a result, 5 of the 69 targets observed are excluded from the complete sample due to insufficient sensitivity of the observations (155828-2232, 160905-1859, DE Tau, 155913-2233, and DK Tau). Two of the excluded sources were detected as double stars. The second step taken to define the complete sample was to convert the angular separation range to a projected linear separation range, since the two star forming regions studied, Tau-Aur and Oph-Sco, are located at slightly different distances, 140 and 125 pc respectively. The angular separation range of 0."1 to 1."8 corresponds to projected linear separations of 14 to 252 AU and 12 to 225 AU in Tau-Aur and Oph-Sco respectively. Thus for the complete sample we considered only the common range of 14 to 225 AU.

The distribution of detected companions for targets in the complete sample is shown in Figure 4.1. Within the completeness region, we detected 22 companion stars. Outside the boundaries of the completeness region (the outlined area in Figure 4.1), we are no longer confident that all the companion stars, such as those of RW Aur, T Tau, and SR 9, were detected. Companions outside this region were detected, because some observations had better sensitivity than was required to be a member of the complete sample.

For comparisons of subgroups within our sample, we defined a restricted binary star frequency: the ratio of companion stars within the separation range 14 to 225 AU and the magnitude difference range 0.0 to 2.0 mag, i.e., the completeness region, to the number of targets in the complete sample. This restricted binary star frequency (bsf) can be expressed in terms of a differential binary star frequency, $\frac{d\,\mathrm{BSF}}{d\,\mathrm{s}\;d\Delta\mathrm{K}}$,

$$\mathrm{bsf} = \int_0^2 \int_{14}^{225} \frac{d\,\mathrm{BSF}}{d\,\mathrm{s}\;d\Delta\mathrm{K}}\; d\,\mathrm{s}\;d\Delta\mathrm{K}, \tag{4.1}$$

where s is the projected linear separation and ΔK is the K(2.2 μm) magnitude difference. For the 64 included targets, there are 22 companion stars within the completeness region (see Figure 4.1); *thus the restricted binary star frequency is 34 ± 7%.*

The target stars with no companions or companions only outside the completeness region are considered as single stars. Therefore the restricted binary star frequency is a lower limit to the true binary star frequency (BSF), the total number of companion stars with any separation and magnitude difference for a given sample,

$$\mathrm{BSF} = \int_0^\infty \int_0^\infty \frac{d\,\mathrm{BSF}}{d\,\mathrm{s}\;d\Delta\mathrm{K}}\; d\,\mathrm{s}\;d\Delta\mathrm{K}. \tag{4.2}$$

Nonetheless the restricted binary star frequency of this sample is well defined and is therefore useful for the comparisons listed in Table 4.1 and discussed below (§4.2 -

4.4).

4.2. Binary Stars and Star Forming Regions

One of the goals of this study was to investigate the physical processes that control the formation of multiple star systems. The large fraction of T Tauri stars observed with at least one companion star suggests that multiple stars are formed during the process of star formation, as opposed to some later time, e.g. by capture (see also discussion in §4.4). Thus the various physical and environmental conditions of the regions where these stars originate are presumably among the factors that effect binary star formation. In this section, we examine the multiplicity of T Tauri stars as a function of star forming region, in the hope of understanding what environmental factors effect binary star formation.

We used the restricted binary star frequency of the complete sample, defined in §4.1, to compare the binary star frequency between the two star forming regions studied, Tau - Aur and Oph - Sco. Six out of 21 stars in Oph - Sco (29 ± 12%) and 16 out of 43 stars in Tau - Aur (37 ± 9%) have companion stars. We also examined the restricted binary star frequency for the two regions as a function of separation (Figure 4.2); they appear to be quite similar. The result of a Kolmogorov-Smirnov test indicates a 0.95 probability that the two distributions are the same as a function of separation between 14 and 225 AU. *Thus we conclude that there is no statistically significant difference between the binary stars frequencies of the two star forming regions integrated over the projected linear separation range 14 to 225 AU or as a function of projected linear separation.*

Tau - Aur and Oph - Sco are alike in that they are both sites of low mass star formation, contain dark clouds (Lynds 1962), and have a total mass of $\approx 10^4\ M_O$ (de Geus et al. 1989; Ungerechts & Thaddeus 1987). However, one distinct difference between these two regions is the presence of a large centrally condensed core and an

associated high density of young stellar objects in Oph - Sco. This high mass core (the ρ Ophiuchi cloud) appears to have a much higher star forming efficiency (Wilking and Lada 1983; Wilking, Lada, and Young 1989) than the low mass cloud cores, which are distributed throughout both regions and are characterized by much lower stellar densities and overall star formation efficiency (Myers 1985).

It has been suggested, on the basis of the differences noted above, that two modes or environments of star formation exist: isolated, i.e., in the scattered low mass cloud cores, and clustered, i.e., in the high mass cloud cores (Lada et al. 1992). Thus we separated those stars in the high mass cloud core ρ Oph to see if the two putative modes of star formation produce multiple stars systems with different efficiencies as might be expected if different physical processes are at work. In our complete sample, the restricted binary star frequency of the ρ Oph cloud core (44 ± 22%) is not significantly different from that of the remainder of the complete sample (34 ± 8%). We note however that this test was not very sensitive due to the small number of observations in the ρ Oph cloud core.

4.3. Binary Stars and Circumstellar Disks

Another aim of this survey was to examine the physical relationship between the two observationally defined subclasses of the T Tauri stars, the classical T Tauri stars (CTTS) and the weak-lined T Tauri stars (WTTS). These two subgroups are characterized on the basis of their H_α emission: CTTS have strong and broad H_α emission ($W(H_\alpha) > 10$ A) whereas WTTS have weak and narrow H_α emission ($W(H_\alpha) < 10$ A) (e.g., Herbig & Robbin-Bell 1988; Strom et al. 1989). Most researchers agree that the weak H_α emission observed in WTTS probably originates from the chromosphere, whereas many theories have been presented to account for the presence of strong H_α emission in CTTS. A recent and intriguing proposal suggests that the strong H_α emission arises from disk accretion (Basri & Bertout 1989). However,

neither this model nor any of the other proposals for the strong H_α emission provide a satisfactory explanation for the two subclasses, i.e., why some T Tauri stars exhibit strong H_α emission and others do not.

We used the results of this survey to investigate the possibility that the underlying difference between the WTTS and the CTTS is related to the presence of a close secondary star. To make this comparison, we used the restricted binary star frequency of the complete sample (§4.1), and combined the results of the two star forming regions, since they appear to have similar binary star frequencies (§4.2). Fourteen of the 42 CTTS (33 ± 9%) and 8 of the 22 WTTS (36 ± 13%) were detected as double stars with separations ranging from 14 to 225 AU and magnitude differences between 0.0 and 2.0 mag; the binary star frequency appears to be similar in the two subclasses. However, by integrating over 14 - 225 AU, we could have washed out any observable distinction, since circumstellar disks are typically assumed to be roughly 100 AU in size. Figure 4.3 shows the CTTS and WTTS restricted binary star frequency binned as a function of projected linear separation. The figure reveals an apparent difference in their dependence on separation; the WTTS dominate the binary star distribution at the closer separations and the CTTS dominate the distribution at wider separations. To test the significance of this difference, we performed a Kolmogorov-Smirnov test on the unbinned data and found a probability of 0.008 for the two sets being drawn from the same distribution. *Thus we conclude that the distributions of the CTTS and WTTS binary stars as a function of separation are significantly different from each other. The WTTS binary star distribution is enhanced at smaller separations as compared to the CTTS binary star distribution.*

The observed difference between the CTTS and WTTS binary star distributions suggests that close companion stars play a significant role in the differentiation of these two T Tauri star subclasses. We adopt Basri and Bertout's (1989) model, in which the strong H_α emission of the CTTS arises from the boundary layer of an

accretion disk. It has been suggested that all T Tauri stars are formed with an accretion disk (e.g., Shu et al. 1987) and therefore would be initially classified as CTTS; they would eventually be observed as WTTS when their accretion disks are depleted. The distribution of the ages of these stars (Walter et al. 1988), however, implies that the two subclasses are more or less coeval, which seems to contradict this evolutionary theory. It should be noted however, that the very oldest population of T Tauri stars appears as WTTS (Walter et al.). If we also account for the presence of a secondary star located within the circumstellar disk, the stellar age inconsistency may be resolved. A close secondary star can create a gap in the circumstellar disk (Lin & Papaloizou 1992), truncating the amount of material available for accretion. We propose that by reducing the amount of material that can be accreted the effect of a close secondary star is to shorten the accretion timescale in close binary T Tauri stars. In this way those T Tauri stars with close companions would quickly deplete their accretion disks and appear as WTTS at a fairly early age. Presumably, secondary stars outside the circumstellar disk (~100 AU) should be of no consequence to the accretion timescale. This scenario suggests that the accretion timescale should decrease with decreasing binary star separations (for separations less than ~100 AU). We therefore expect the fraction of WTTS to CTTS observed as binary stars to increase with decreasing binary star separations. This is consistent with what we have observed, where the WTTS:CTTS ratios are 6.6, 0.3, and 0.0 in the separation bins centered at 22, 56, and 141 AU respectively (Figure 4.3).

4.4. Binary Stars and Mass

The class of T Tauri stars covers all visible pre-main sequence stars older than $\sim 10^7$ years with masses less than 3 M_O. In this section, we estimate the masses of the observed stars in order (1) to examine the binary star frequency of T Tauri stars as a function of mass and (2) to determine what type of main sequence stars they

will become (see §4.6).

T Tauri stars are expected to evolve to the main sequence along convective-radiative tracks for low mass stars ($M < 3.0\ M_O$) such as those given by Cohen & Kuhi (1979) and reproduced in Figure 4.4. Since the evolutionary tracks for low mass stars are fairly constant in effective temperature, much can be learned from the spectral types of the stars alone. This is fortunate since the measurements of spectral types are generally unaffected by the presence of companion stars. The spectral types of the T Tauri stars in the complete samples are listed in Table 4.2 and their distribution is shown in Figure 4.5a. The restricted binary star frequency, shown in Figure 4.5b, suggests a dependence on spectral type. Since the later spectral types in general correspond to lower masses, the distribution in Figure 4.5b implies that the restricted binary star frequency may depend on mass.

To further investigate this putative dependence, we estimated the masses of these stars from their location in the HR diagram with respect to the evolutionary tracks. To place the stars we needed both their effective temperature, T_{eff}, and stellar luminosity, L. We obtained the effective temperatures of the target stars from their spectral types using the conversion adopted by Cohen & Kuhi (1979). The stellar luminosity for many of the target stars has been estimated from optical and near infrared data. These stellar luminosity (L_*) estimates are listed in Column 6 of Table 4.2. We used these values directly for the target stars observed without companion stars. For those observed with companions, these published luminosities are overestimates due to the unaccounted for secondary stars. We assumed that the brightest component observed at K is the optically identified T Tauri star, for which the spectral type is known, and used the measured K flux density ratio to divide the previously derived stellar luminosity between the components of the system. The primary star luminosity, L_*^{prim}, listed in Column 8 of Table 4.2b is therefore given by

$$L_*^{prim} = \frac{R}{1+R} L_*, \tag{4.3}$$

where R is the flux density ratio ($R \geq 1$).

Figure 4.4 shows the stars in the complete sample in an HR diagram along with the evolutionary tracks from Cohen & Kuhi (1979). The distribution of estimated masses for these T Tauri stars, shown in Figure 4.6, ranges from 0.2 to 2.3 M_O and peaks between 0.5 and 1.5 M_O. The mass dependence on effective temperature, or equivalently spectral type, is shown in Figure 4.7. The correlation between effective temperature and mass holds extremely well for spectral types M5 through K7 or equivalently for masses less than 1 M_O. For earlier spectral types the correlation is not as tight, but the resulting masses are all greater than 1 M_O.

We used this correlation between spectral types and mass to examine the T Tauri binary star frequency as a function of mass. By grouping spectral types M5 through K7 and K6 through G0 together, we compared the restricted binary star frequency for T Tauri stars with masses less than 1 M_O to that of stars with masses greater than or equal to 1 M_O. Thirteen of 32 stars with M < 1 M_O (41 ± 11%) and 9 of 32 stars with M ≥ 1 M_O (28 ± 9%) had companion stars within the completeness region (see §4.1). Although the lower mass stars in our sample have more companion stars in the projected linear separation range 14 to 225 AU and the magnitude difference range 0.0 to 2.0 mag, the difference is not statistically significant. Furthermore, we must be careful in comparing the restricted binary star frequencies of different mass stars. Given the shape of the convective-radiative tracks and the isochrones, magnitude differences most likely reflect mass differences. Thus if the lower mass stars do indeed have a higher restricted binary star frequency, that would most likely indicate that the lower mass stars have more high mass ratio (i.e., $\frac{M_1}{M_2}$ tends toward one) binary systems than the higher mass targets. Such a distinction would provide a strong constraint on star formation mechanisms.

4.5. T Tauri vs. Main Sequence Binary Stars

The results of this survey indicate that a large fraction of T Tauri stars have companion stars. The youth of this population of stars (< ~10^7 years) suggests that multiple star systems are produced during the early stages of star formation. To study in greater detail questions regarding when multiple star systems form and the early evolution of these systems, we compared the multiplicity of the T Tauri stars in this sample with their older counterparts on the main sequence.

To compare the binary star frequency of the T Tauri stars to that of the main sequence stars, we selected multiplicity surveys of main sequence stars that have a mass range similar to that of the T Tauri stars (Figure 4.6). Duquennoy & Mayor (1991) surveyed a sample of nearby solar type main sequence stars with spectral types F7 to G9. This corresponds to a range in main sequence masses of ~0.8 to ~1.3 M_O. Therefore this sample of main sequence stars appears to be an appropriate older counterpart for a large percentage (44%) of the T Tauri sample. Fischer & Marcy (1992) investigated the multiplicity of the nearby main sequence M dwarfs, which have masses between ~0.1 and ~0.5 M_O. This mass range incorporates 28% of the T Tauri stars in the complete sample and therefore Fischer & Marcy's study is also useful for comparison with the T Tauri results.

The main sequence surveys mentioned above combine the results of many detection techniques and therefore cover a much larger binary star separation range than the speckle imaging survey of T Tauri stars. Consequently before a comparison was made between these samples, we calculated the binary star frequency for the main sequence samples in the projected linear separation range 14 to 225 AU, to which the T Tauri survey was sensitive.

4.5.1. Main Sequence Star Surveys

Duquennoy & Mayor (1991) searched a total of 164 nearby solar type main sequence stars for companion stars and found that the number of companion stars as a function of the orbital period, P, could be fit by a Gaussian distribution in log P. Their binned bias corrected data as well as the model fit are reproduced in Figure 4.8a. To compare this work to the T Tauri star sample, we converted their distribution, which is a function of orbital period, to a function of average projected linear separation. This was done in several steps: first, the orbital period was converted to its corresponding semi-major axis using Kepler's law,

$$P_{yrs}^{2} = \frac{A_{AU}^{3}}{M_{M_O}}, \tag{4.4}$$

where A is the semi-major axis, and M is the total mass. This conversion requires an estimate of the total mass in these systems. For this solar type main sequence sample, the average primary star mass is 1 M_O and the average mass ratio, which was calculated from Duquennoy & Mayor's Figure 10, is 0.40. Thus we assumed an average total mass of 1.4 M_O for the conversion of orbital period to semi-major axis. Second, we obtained an average projected linear separation, <a>, from the semi-major axis, A, using a Monte Carlo simulation carried out by Fischer and Marcy (1992), which gave the following relationship

$$A = 1.26 \langle a \rangle. \tag{4.5}$$

Thus we derived the following relationship to convert orbital period to average projected linear separation,

$$\log P_{days} = \log \langle a \rangle_{AU} + 2.64. \tag{4.6}$$

The distribution of solar-type main sequence star companion stars as a function of <a> was then rebinned, using Duquennoy & Mayor's model fit, such that the new bin width matched our separation range ($\Delta \log \langle a \rangle_{AU} = 2.2$). The final step was to

normalize this distribution by the total number of target stars (164) to produce a binary star frequency distribution, which is shown in Figure 4.8b. Integrated over the project linear separation range 14 to 225 AU, the binary star frequency of nearby solar type main sequency stars studied by Duquennoy & Mayor (1991) is 17 ± 3%, where the uncertainty is based on Poisson statistics.

Fischer & Marcy (1992) compiled the results of several M dwarf surveys, which were conducted with different observing techniques, to determine the multiplicity of these low mass main sequence stars. Their results are quoted in terms of the number of companion stars per target per AU for a given range of semi-major axes (their Table 2). We used their semi-major axis to average projected separation relationship (Equation 4.5) to convert these binary star frequencies to a function of projected linear separation. Integrating these values over 14 to 225 AU, we estimated the binary star frequency in this range for the M dwarf to be 13 ± 4%.

4.5.2. Comparison of Surveys

The M dwarf and solar type (F7 to G9) main sequence stars have similar binary star frequencies in the projected linear separation range 14 to 225 AU, 13 ± 4% and 17 ± 3%, respectively. Since these values do not differ significantly and the solar type main sequence stars are the older counterparts to the majority of the T Tauri stars, we used the solar type main sequence binary star frequency in our comparison with the T Tauri binary star frequency.

Since both main sequence results are corrected for detection biases and are therefore estimates of the true main sequence binary star frequency over all magnitude differences, we need an estimate of the true binary star frequency in the projected linear separation range 14 to 225 AU and over all magnitude differences,

$$\mathrm{BSF}' = \int_0^{\infty} \int_{14}^{225} \frac{d\mathrm{BSF}}{ds\, d\Delta\mathrm{K}}\, ds\, d\Delta\mathrm{K}, \qquad (4.7)$$

for the T Tauri stars. We have already evaluated the number of companion stars in the projected linear separation range 14 to 225 AU and magnitude difference range 0.0 to 2.0 mag for the complete sample (§4.1). Thus to estimate BSF', we need to calculate the distribution, in ΔK, of the binary star frequency for $\Delta K > 2.0$ mag. We did this by examining strips in the ΔK - projected linear separation parameter space above $\Delta K = 2.0$ mag. For each ΔK strip, spanning 14 to 225 AU and an interval of 0.5 mag in magnitude difference, we asked how many observations are sensitive to this region and, of these, how many had companion stars that fall within that region (see Table 4.3). There were observations sensitive up to magnitude differences of 4.0 mag; beyond this range we have no way of estimating the binary star frequency. Nonetheless integrating over these results and the completeness region (i.e., $0.0 \leq \Delta K \leq 4.0$mag), we estimated the binary star frequency in the projected linear separation range 14 to 225 AU integrated over all magnitude differences to be 58 ± 16%.

Before we compared the T Tauri star results with the solar-type main sequence results, we made one final adjustment to the T Tauri binary star frequency. The binary star frequency obtained for the solar-type main sequence stars was normalized by the number of targets, where Duquennoy & Mayor's definition of target star differred from ours in the sense of how far another star could be before it was considered to be another target star. For this discussion we adopted a value of 2×10^3AU, the lowest value suggested by Duquennoy & Mayor, for the limiting separation of two stars that are considered to be members of one system. This affected only the way we treated UZ Tau E and W, which were previously counted as two targets and are now viewed as one system. This only slightly changed our value for binary star frequency in the projected linear separation range 14 to 225 AU, which was previously estimated to 58 ± 16% (§4.1.2) and is now taken to be 59 ± 16%. *Thus the T Tauri binary star frequency appears to be greater than that of the*

main sequence stars by a factor of 3. The discrepancy between the two binary star frequencies is a 3σ effect.

The putative discrepancy could be due to a difference in the sensitivity of the two surveys, which would imply that our survey is much more sensitive to companion stars than Duquennoy and Mayor's (1991) survey in the projected linear separation range 14 to 225 AU. However, the solar-type main sequence sample has already been corrected for undetected companion stars down to visual magnitude differences of 7.0 mag. Whereas the T Tauri results were sensitive to companions with magnitude difference of at most 4.0 mag. Although it is difficult to determine how ΔK's for T Tauri stars correspond to ΔV's for main sequence stars, it seems unlikely that the apparent overabundance of companion stars among the T Tauri stars compared to the solar-type main sequence stars is the result of unaccounted for companions in Duquennoy and Mayor's sample.

If the difference in the binary star frequency between the T Tauri stars and their older counterparts on the main sequence is due to an intrinsic difference in their properties (i.e. it depends on their age), then the stars in the current T Tauri star sample will have the same properties as the solar-type main sequence sample once they evolve down to the main sequence. We explored two possible evolutionary scenarios that might explain the putative overabundance of companion stars at the younger stage of evolution in the projected linear separation range 14 to 225 AU.

First, we considered the possibility that T Tauri stars and solar-type main sequence stars have the same number of companion stars integrated over all possible separations. In this case an overabundance of companion stars in the T Tauri sample with respect to the solar-type main sequence sample in the projected linear separation 14 to 225 AU requires a deficiency of T Tauri star companion stars outside this range so that the integrated number of companion stars would be the same for both samples. The observed difference would then be the result of a more peaked distribution

for the T Tauri stars, as opposed to a difference in the overall binary frequency. This implies that the distribution of binary stars as a function of separation would spread or relax as a function of time. Integrated over all separations, the binary star frequency for solar-type main sequence stars is 62 ± 6%. This is comparable to the binary star frequency of T Tauri stars in the limited project linear separation range 14 to 225 AU. If this hypothesis is true, then only 2 (± 11) companion stars should be found in the complete sample outside the separation range 14 to 225 AU. Table 3.3 and 3.4 indicate that 16 companion stars have already been detected outside this separation range, even though the current knowledge of companion stars in the complete sample at all separations is far from complete. It therefore appears that the total number of companion stars is greater at the T Tauri stage of evolution than on the main sequence.

If there is an overabundance of companions stars integrated over all separations among the T Tauri stars as compared to the solar-type main sequence stars, then some of the current T Tauri star pairs must be disrupted by the time they evolve to the main sequence. One possible mechanism is the disruption of young triple or higher order systems, in which the system is "ionized" by close encounters with another star or system of stars.

It is worth stressing again the importance of observing the *same* sample with many *different* techniques. This is necessary to determine the frequency of double, triple, and quadrupole systems, because the various components of a given system will not all be observed with any one technique. The incomplete overlap of our sample with other techniques has already revealed that 14% of the target stars in our sample are members of systems with three or more components, whereas Duquennoy and Mayor (1991) find that only 5% of their solar type main sequence targets are members of these higher order systems. The triples and quadrupoles that have been observed so far are all in hierarchical systems, i.e., the ratio of separations in the

system is large (≥ 10). If disruption occurs, then the more widely separated stars (or pair of stars) would be more likely to break away. Thus one would expect to observe no difference between the T Tauri and the main sequence binary star frequencies at the shortest separation. This is consistent with current spectroscopic measurements of T Tauri stars, which reveal a binary star frequency at the shortest periods (P < 100 days), or equivalently at the smallest separation, that is similar to that of the solar-type main sequence stars (Mathieu et al. 1988; Mathieu 1992). Thus if the 3σ discrepancy between the number of companion stars observed for the T Tauri stars and the solar-type main sequence stars is real, the disruption of triple and quadrupole systems may provide a satisfactory evolutionary scenario.

4.6. Summary

We carried out a magnitude limited (K <= 8.5 mag) multiplicity survey of T Tauri stars in two nearest star forming regions the northern hemisphere, Taurus-Auriga and Ophiuchus-Scorpius. Each of the 69 star in the sample was observed at K(2.2 μm) with an infrared array camera on the Hale 5-m Telescope at Palomar Observatory and imaged using two-dimensional speckle interferometric techniques.

Thirty three companion stars were found, of which 15 are new detections. A subset of 64 observations, the "complete sample," was sensitive to all companion stars in the projected linear range 14 to 225 AU and the magnitude difference range 0.0 to 2.0 mag, the "completeness region." We used this subset and region to study the multiplicity of T Tauri stars; the frequency of companion stars within this region is 34 ± 9%

There appears to be no statistically significant difference between the binary star frequency of Tau - Aur (37 ± 9%) and Oph - Sco (29 ± 12%). Similarly, the binary star frequency in the high mass cloud core ρ Oph (44 ± 22%) compared to that of the remainder of the sample (34 ± 8%) shows no significant difference, although the

small number of stars in ρ Oph renders this comparison fairly insensitive.

We discovered a distinction between the classical T Tauri stars (CTTS) and the weak-lined T Tauri stars (WTTS) based on the binary star frequency as a function of separation; the WTTS binary star distribution is enhanced at the smaller separations compared to the CTTS binary star distribution, which dominates the wider separations. The cross over occurs near 100 AU, the size typically quoted for a circumstellar disk. We suggest that all T Tauri stars begin as CTTS and become WTTS when accretion has ceased, with the nearby companion stars acting to shorten the accretion timescale in multiple star systems.

Integrated over all magnitude differences the binary star frequency in the projected linear separation range 14 to 225 AU for T Tauri stars (59 ± 16%) is a factor of 3.5 greater than that of the solar-type main sequence stars (17 ± 3%). Given the limited angular separation range that we are sensitive to, i.e., both the spectroscopic and wide binaries are missed, the rate at which binaries are detected suggests that most, if not all, T Tauri stars have companions. We propose that the observed overabundance of companions to T Tauri stars with respect to their older counterparts on the main sequence is an evolutionary effect; in this scheme triple and higher order T Tauri systems, which are observed at higher frequencies than for the solar-type main sequence stars, are ionized by close encounters with another star or system of stars.

Table 4.1: Multiplicity of T Tauri Stars in the Complete Sample[a]

Sample	# Targets	# Companions in Completeness Region	bsf[b] (%)	Section
Total	64	22	34 ± 7	4.1
Oph - Sco	21	6	29 ± 12	4.2
Tau - Aur	43	16	37 ± 9	
WTTS	22	8	36 ± 13	4.3
CTTS	42	14	33 ± 9	
M < 1 M_O	32	13	41 ± 11	4.4
M > 1 M_O	32	9	28 ± 9	

(a) The complete sample, discussed in 4.1, includes all observations sensitive to the "completeness region," i.e., that revealed all companion stars within the projected linear separation range 14 to 225 AU and within the magnitude difference range 0 to 2.0 mag.

(b) The restricted binary star frequency (bsf) incorporates only companion stars within the completeness region, and is therefore a lower limit to the true binary star frequency in the separation range 14 to 225 AU. Nonetheless, it is useful for comparisons of various groups of T Tauri stars, which are discussed in the sections listed in Column 5.

Table 4.2: T Tauri Binary Star Frequency

ΔK Range mag	# Obs	# Companions	Freq %
0.0 - 2.0	64	22	34 ± 7
2.0 - 2.5	56	3	5 ± 3
2.5 - 3.0	41	2	5 ± 3
3.0 - 3.5	22	0	0
3.5 - 4.0	7	1	14 ± 14
0.0 - 4.0	-	-	58 ± 16

Table 4.3a: Stars in the Complete Sample Observed Without Companion Stars

HBC	Name	SpT	Ref	log T_{eff} K	L_* L_O	Ref	Mass M_O
259	SR 4	K6	2	3.623	1.4	2	1.1
262	SR 24 S	K2	1	3.695	2.2	1	1.4
267	Haro 1-14	M0	1	3.593	0.8	1	0.7
268	Haro 1-16	K3	1	3.679	1.1	2	1.2
270	V1121 Oph	K5	1	3.643	4.1	1	1.5
637	DoAr 21	K0	2	3.719	17.1	2	2.3
638	DoAr 24	K5	2	3.643	0.9	2	1.15
649	RNO 90	G5	6	3.753	4.4	16	1.5
	160815-1857	K2	17	3.695	1.3	16	1.1
	160827-1813	K5	17	3.643	0.6	16	1.05
	ROXs 43A	G0	2	3.771	2.7	2	1.3
24	FN Tau	M5	1	3.494	1.0	8	0.2
25	CW Tau	K3	1	3.679	2.6	8	1.55
28	CY Tau	M1	1	3.566	0.7	8	0.45
32	BP Tau	K7	1	3.602	1.2	8	0.8
34	RY Tau	K0	3	3.719	7.5	8	1.9
37	DG Tau	K7	3	3.602	1.7	8	0.8
41	IQ Tau	M0.5	1	3.580	0.9	8	0.5
49	HL Tau	K7	3	3.602	0.9	8	0.8
52	UZ Tau E	M0	3	3.593	0.8	13	0.7
56	GI Tau	K7	1	3.602	1.1	7	0.8
57	GK Tau	K7	1	3.602	1.6	8	0.8
61	CI Tau	K6	3	3.623	1.1	7	1.1
66	HP Tau	K3	1	3.679	2.0	8	1.4
67	DO Tau	K7-M0	1	3.598	1.4	8	0.75
74	DR Tau	M0	3	3.593	2.5	8	0.75
79	SU Aur	G2	3	3.761	14.4	8	2.15
374	Hubble 4	K7-M0	1	3.598	2.5	16	0.8
378	V819 Tau	K7	10	3.602	1.0	8	0.8
380	HDE 283572	G5	10	3.753	7.6	13	1.8
388	042417+1744	K1	10	3.708	1.4	13	1.25
396	Haro 6-13	Cont	1	3.590	2.1	8	0.7
402	FZ Tau	Cont	1	3.590	1.8	14	0.7
415	HP Tau/G2	G1	1	3.766	8.0	13	1.8

Table 4.3b: Stars in the Complete Sample Observed with Companion Stars

HBC	Name	SpT	Ref	log T_{eff} K	L_*^{old} L_O	Ref	L_*^{prim} L_O	Mass M_O
254	AS 205*	K2	3	3.695	9.3	1	7.1	1.9
257	Haro 1-4*	K6	1	3.623	2.7	1	2.2	1.15
264	SR 9	K7	1	3.602	0.7	2	0.6	0.75
266	V853 Oph*	M1.5	1	3.555	0.8	1	0.6	0.4
639	DoAr 24 E	K0	2	3.719	8.5	2	7.2	1.8
643	SR 20	G0	2	3.771	10.8	2	9.6	1.9
	155203-2338	G2	17	3.761	2.4	16	2.1	1.2
	160946-1851*	K0	17	3.719	1.6	16	1.3	1.2
	162218-2420*	G8	5	3.736	1.2	16	0.7	1.0
	ROXs 42C*	K6	2	3.623	1.4	2	1.1	1.1
29	V410 Tau*	K2	3	3.695	2.19	8	1.9	1.35
30	DD Tau*	M1	1	3.566	1.0	8	0.7	0.45
35	T Tau	K0	3	3.719	8.8	15	8.8	2.0
36	DF Tau	M2	3	3.544	3.0	8	2.0	0.4
39	DI Tau	M0	1	3.593	0.9	8	0.8	0.7
44	FX Tau*	M1	1	3.566	1.0	8	0.7	0.45
50	XZ Tau*	M3	1	3.526	1.6	8	1.1	0.35
53	UZ Tau W*	M2	3	3.544	0.6	14	0.4	0.4
54	GG Tau*	K7	3	3.602	1.8	7	1.4	0.8
55	GH Tau*	M2	1	3.544	0.9	8	0.6	0.4
59	IS Tau*	K2	1	3.695	3.1	8	2.7	1.5
76	UY Aur*	K7	3	3.602	0.8	7	0.6	0.75
80	RW Aur	K5	3	3.623	3.3	14	2.9	1.4
367	V773 Tau*	K3	9	3.679	7.7	8	5.3	1.8
368	LkCa 3*	M1	11	3.566	1.3	12	0.7	0.45
369	FO Tau*	M2	1	3.544	1.0	14	0.6	0.4
386	FV Tau*	K5	1	3.643	2.0	14	1.2	1.0
398	V928 Tau*	M0.5	1	3.580	1.0	1	0.6	0.5
404	V807 Tau*	K7	4	3.602	3.7	16	2.7	0.8
423	LkHα 332/G1*	M1	1	3.566	0.9	14	0.6	0.45

Notes: (*) denotes binary stars that fall within the completeness region, i.e., have separations in the range 14 to 225 AU and magnitudes differences between 0.0 and 2.0 mag.
References for Column 4 (Spectral Type) and Column 7 (Stellar Luminosity). Also noted are the assumed distances to the star forming regions used in the references, which derive stellar luminosities. The stellar luminosities listed in Column 6 have been shifted, when necessary for the distances assumed in this work (d_{Tau} = 140 pc and d_{Oph} = 120 pc).
(1) Cohen & Kuhi (1979); d_{Tau} = 160 pc and d_{Oph} = 170 pc
(2) Bouvier & Appenzeller (1991); d_{Oph} = 170 pc
(3) Basri & Batalha (1990)
(4) Herbig & Robbin-Bell (1988)
(5) Montmerle et al. (1983)
(6) Herbst & Warner (1981)

(7) Hartigan et al. (1991); $d_{Tau} = 160\ pc$
(8) Beckwith et al. (1990); $d_{Tau} = 140\ pc$
(9) Herbig (1977)
(10) Walter et al. (1988)
(11) Herbig et al. (1986)
(12) Cabrit et al. (1990); $d_{Tau} = 160\ pc$
(13) Strom et al. (1989); $d_{Tau} = 160\ pc$
(14) Cohen et al. (1989); $d_{Tau} = 160\ pc$
(15) Ghez et al. (1991); $d_{Tau} = 140\ pc$
(16) Simon et al. (1992)
(17) Walter (1992)

Figure Captions

Figure 4.1: The distribution of the observed binary stars (circles) and the limits of the completeness region (the outlined area).

Figure 4.2: The binary star frequency as a function of projected linear separation for Tau - Aur (filled circles) and Oph - Sco (unfilled circles). There appears to be no statistically significant difference in the overall binary star frequency between these two star forming regions.

Figure 4.3: The binary star frequency as a function of projected linear separation for the WTTS (filled circles) and the CTTS (unfilled circles). The WTTS dominate the binary star distribution at shorter separations whereas the CTTS are more abundant at wider binary star separations.

Figure 4.4: HR diagram for the stars in the sample with known effective temperatures. Also plotted are the evolutionary tracks from Cohen & Kuhi (1979). observed sample. The filled circles are stars observed without companion stars. The unfilled points are those stars observed with companions.

Figure 4.5: (a) The distribution of spectral types for the complete sample. (b) The restricted binary star frequency as a function of spectral type.

Figure 4.6: The distribution of estimated masses for the stars in the observed sample.

Figure 4.7: The estimated mass as a function of effective temperature (or equivalently spectral type).

Figure 4.8: (a) The distribution of companion stars in the nearby sample of solar type main sequence stars as a function of orbital period, taken from Duquennoy & Mayor (1991) (b) The hatched histogram is the binary star frequency of the solar type main sequence stars as a function of average projected linear separation. Also shown is the binary star frequency of the T Tauri stars (the unhatched region).

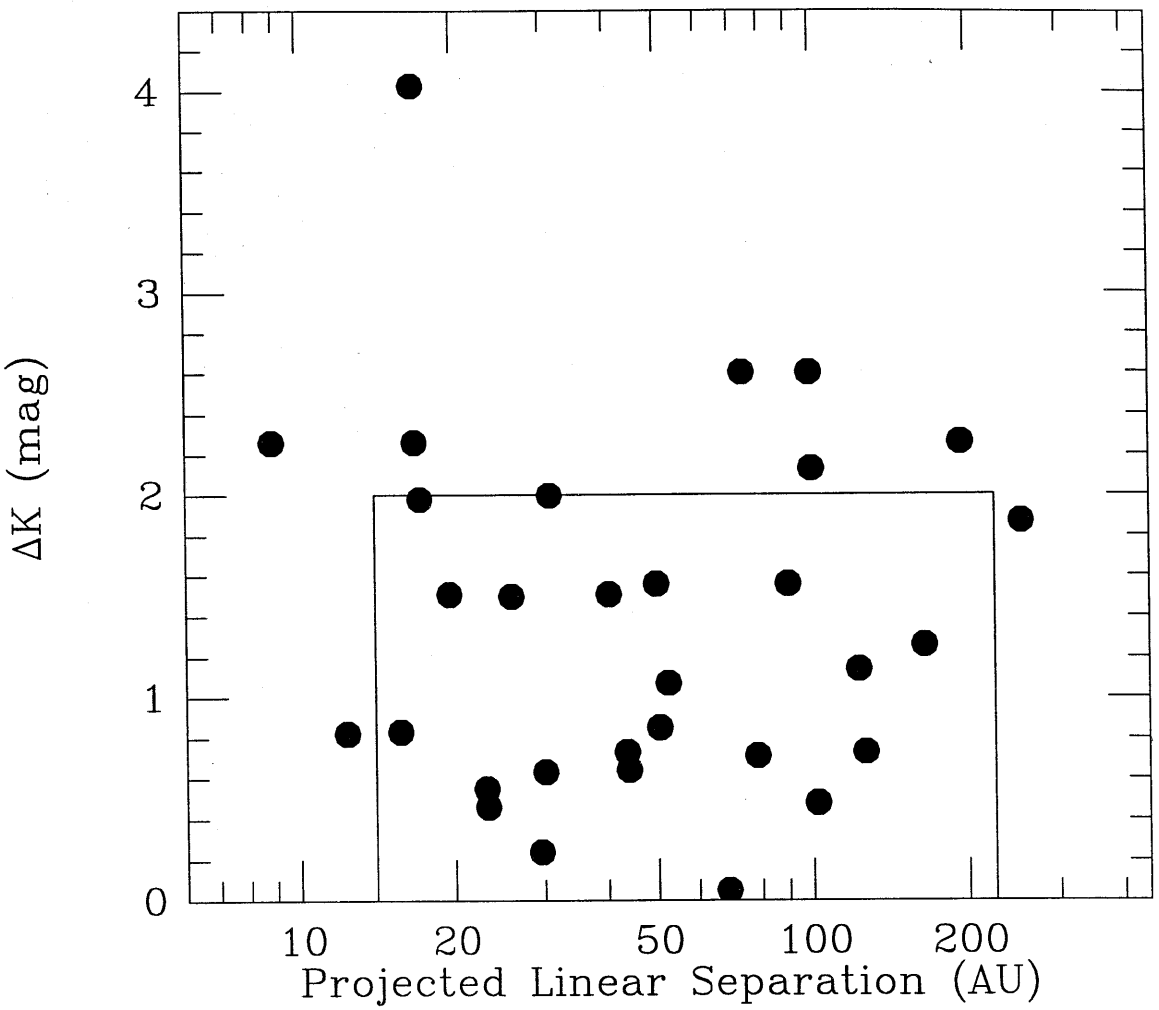

Figure 4.1

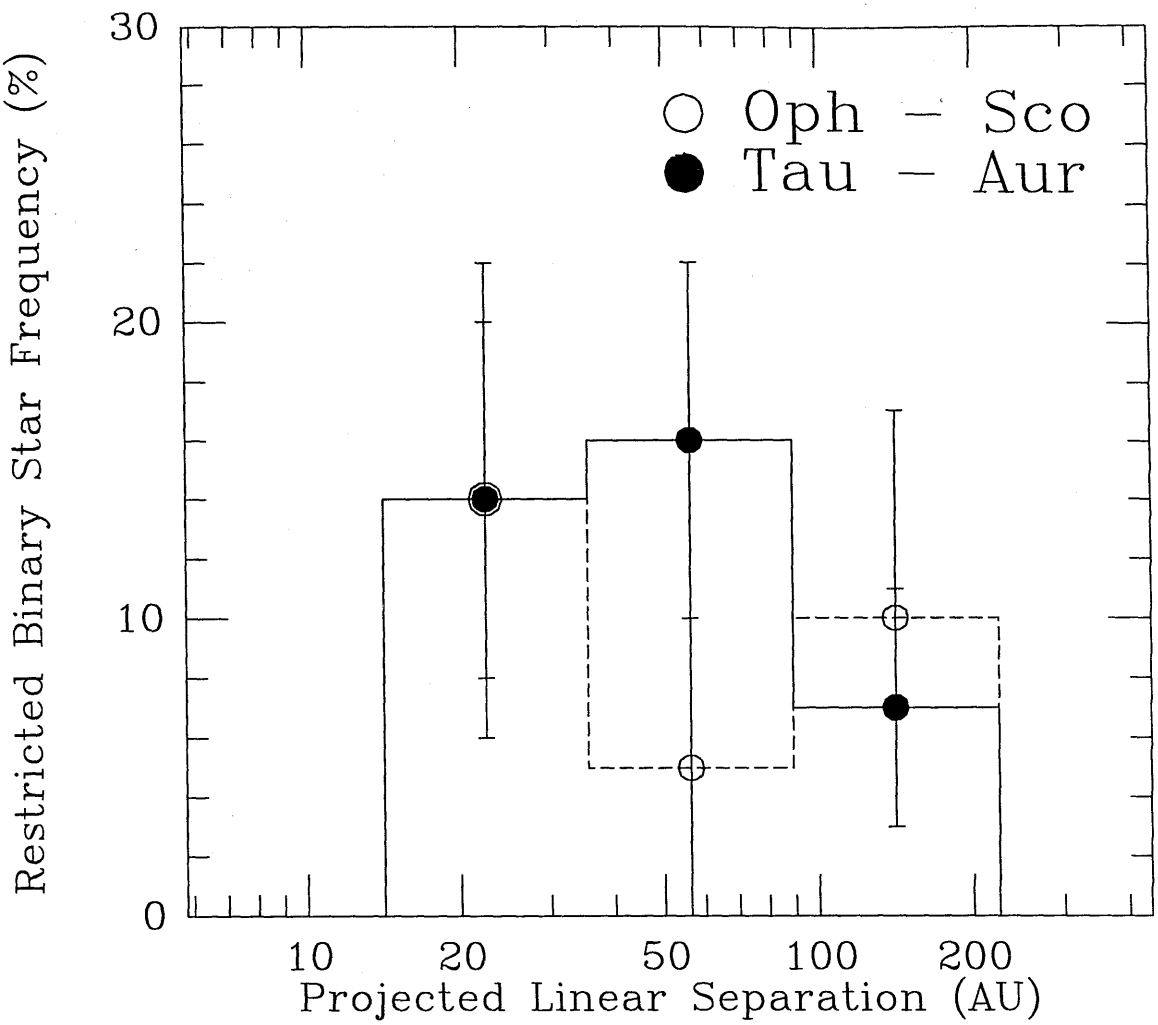
Restricted Binary Star Frequency (%)
30
20
10
0
Oph – Sco
Tau – Aur
10
20
50
100
200
Projected Linear Separation (AU)

Figure 4.2

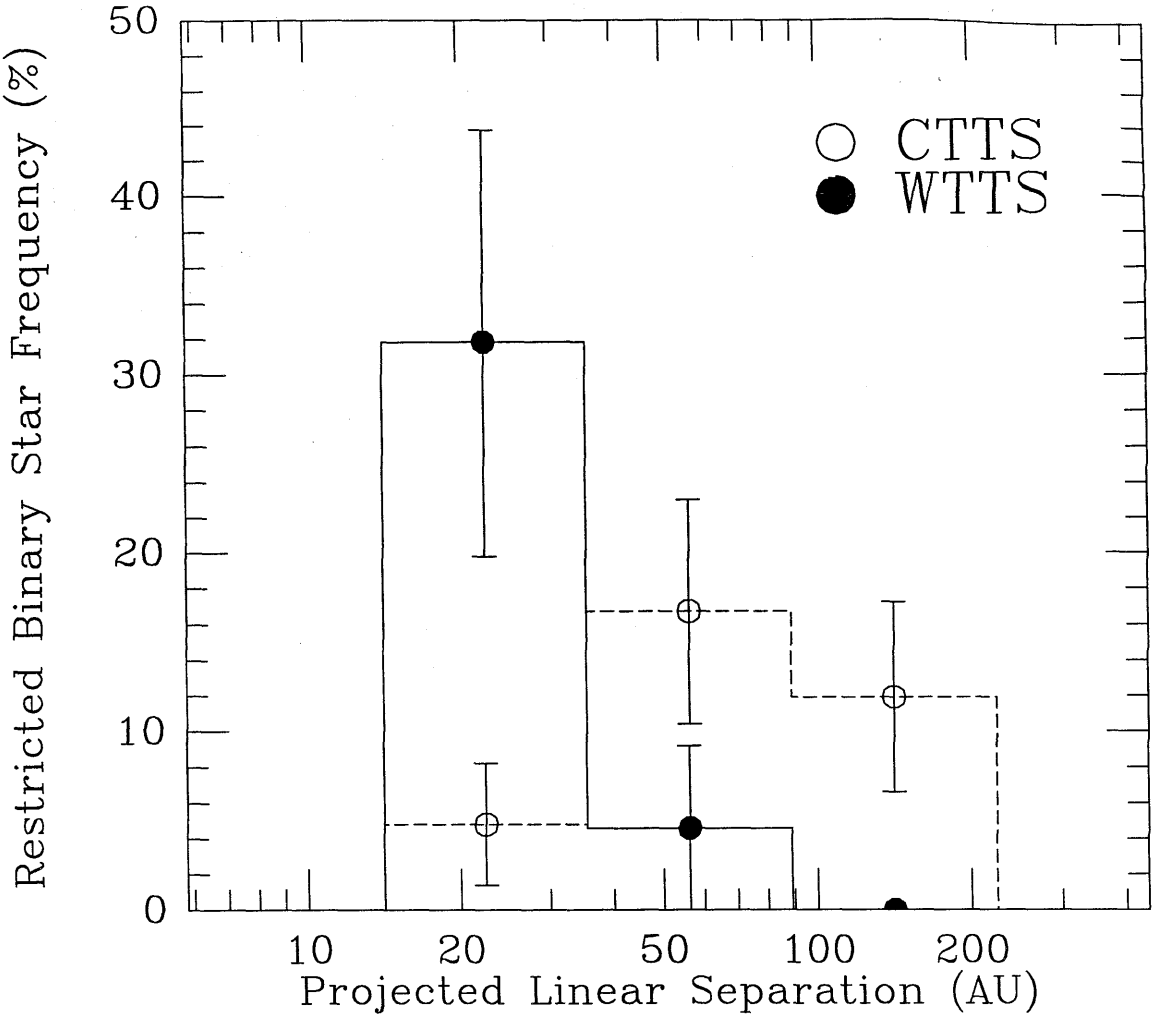
Restricted Binary Star Frequency (%)
50
40
30
20
10
0
CTTS
WTTS
10
20
50
100
200
Projected Linear Separation (AU)

Figure 4.3

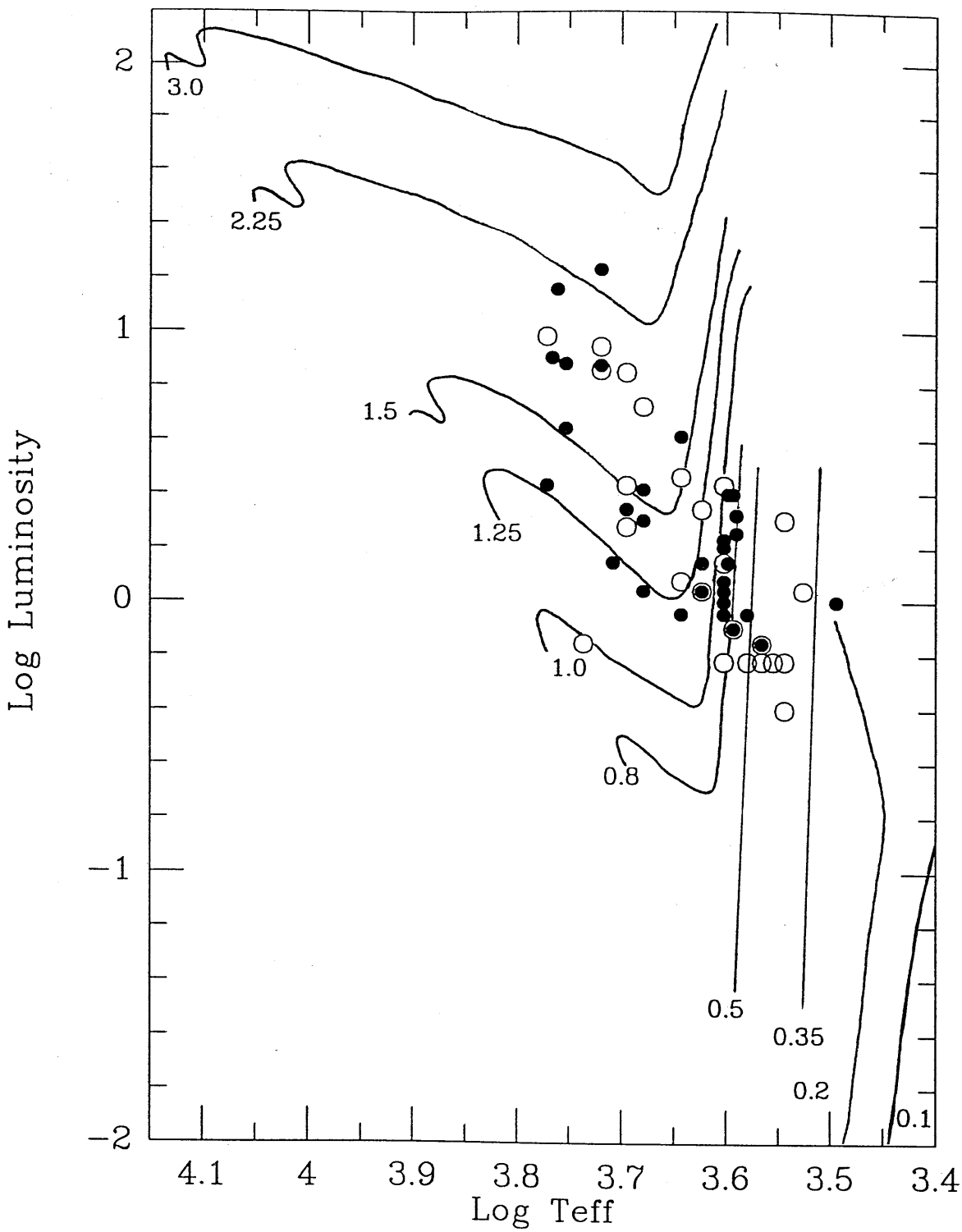
Log Luminosity
2
1
0
−1
−2
3.0
2.25
1.5
1.25
1.0
0.8
0.5
0.35
0.2
0.1
4.1
4
3.9
3.8
3.7
3.6
3.5
3.4
Log Teff

Figure 4.4

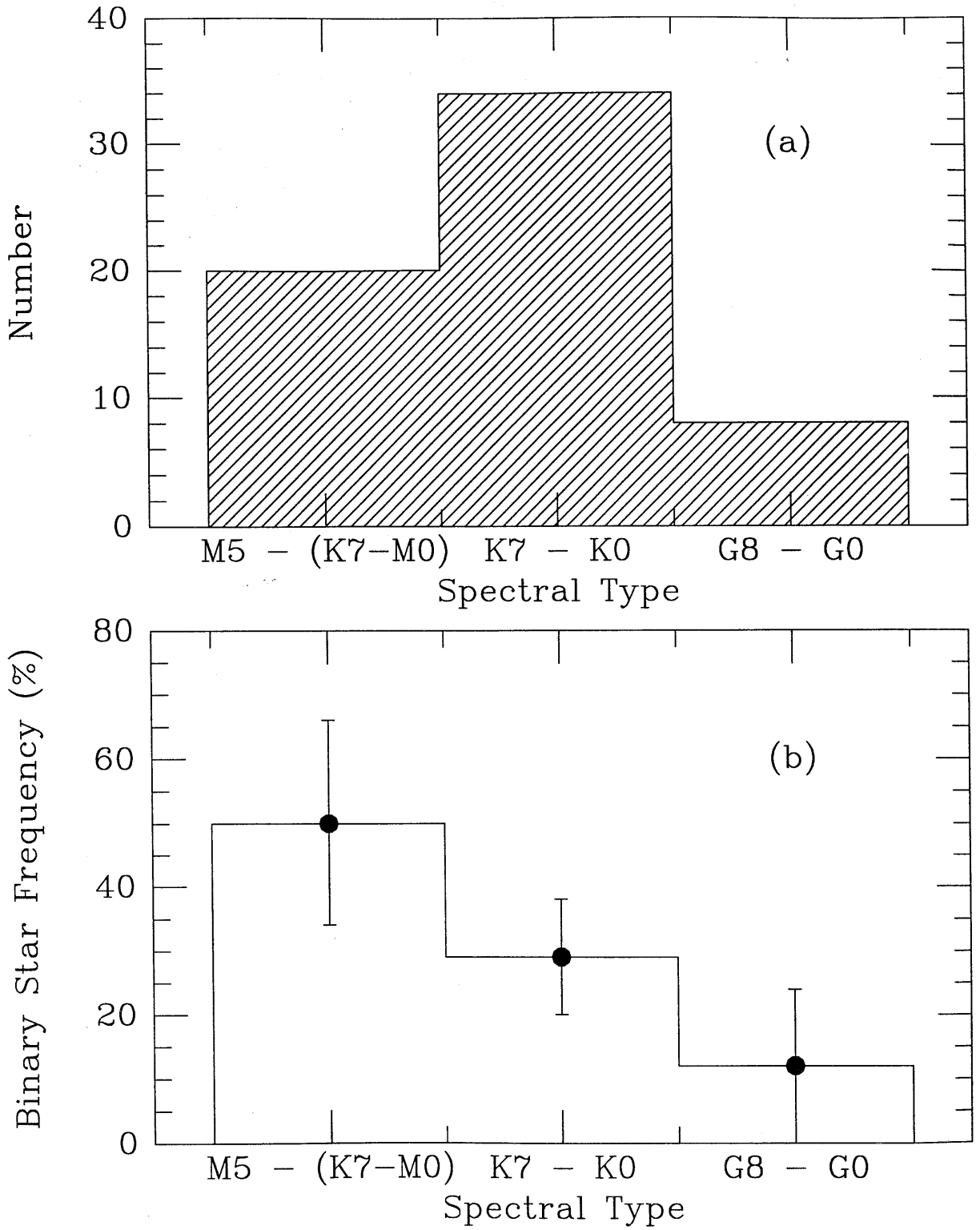
40
30
20
10
0
Number
(a)
M5 – (K7–M0)
K7 – K0
G8 – G0
Spectral Type
80
60
40
20
0
Binary Star Frequency (%)
(b)
M5 – (K7–M0)
K7 – K0
G8 – G0
Spectral Type

Figure 4.5

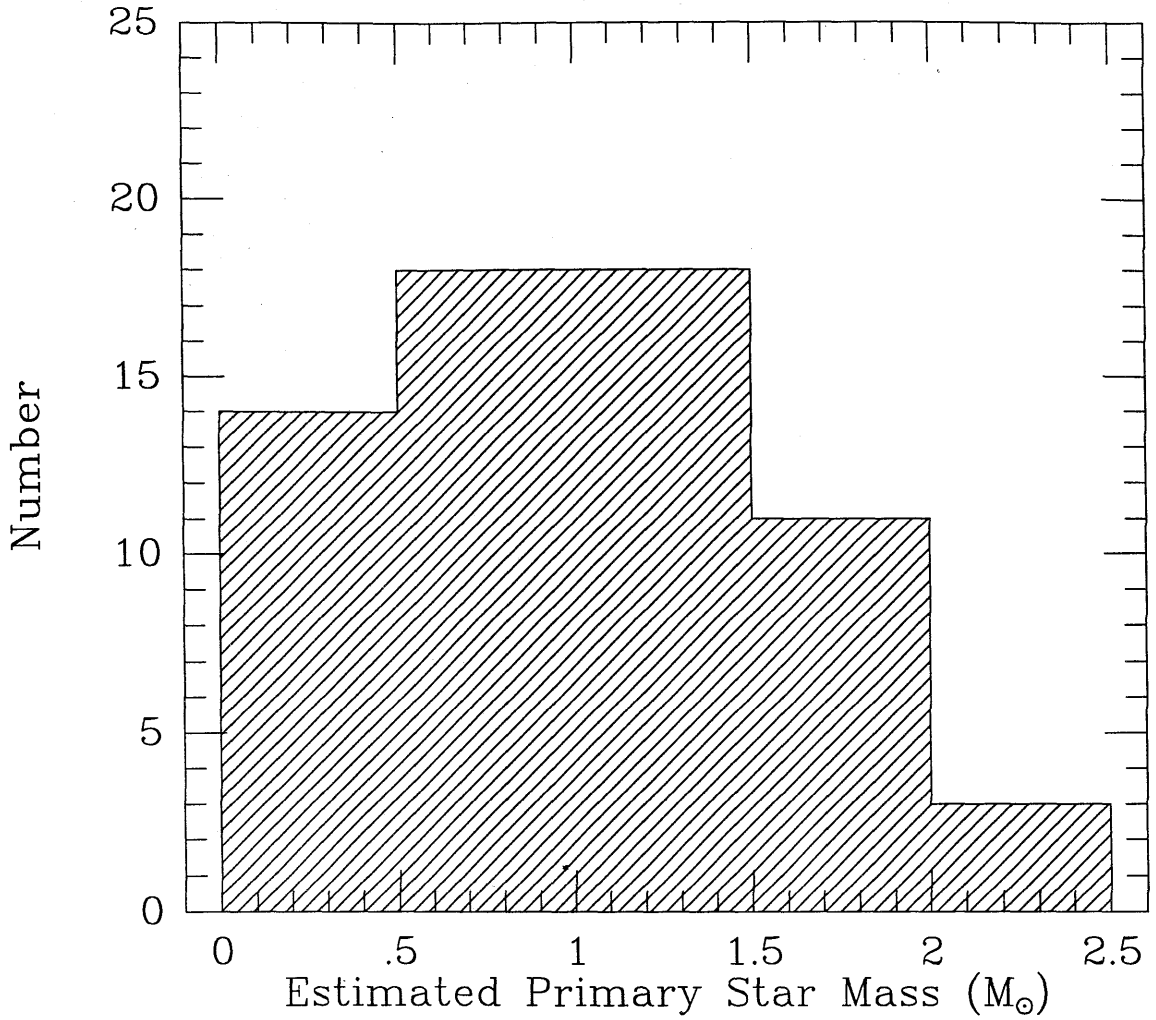
25
20
15
10
5
0
Number
0
.5
1
1.5
2
2.5
Estimated Primary Star Mass ($M_\odot$)

Figure 4.6

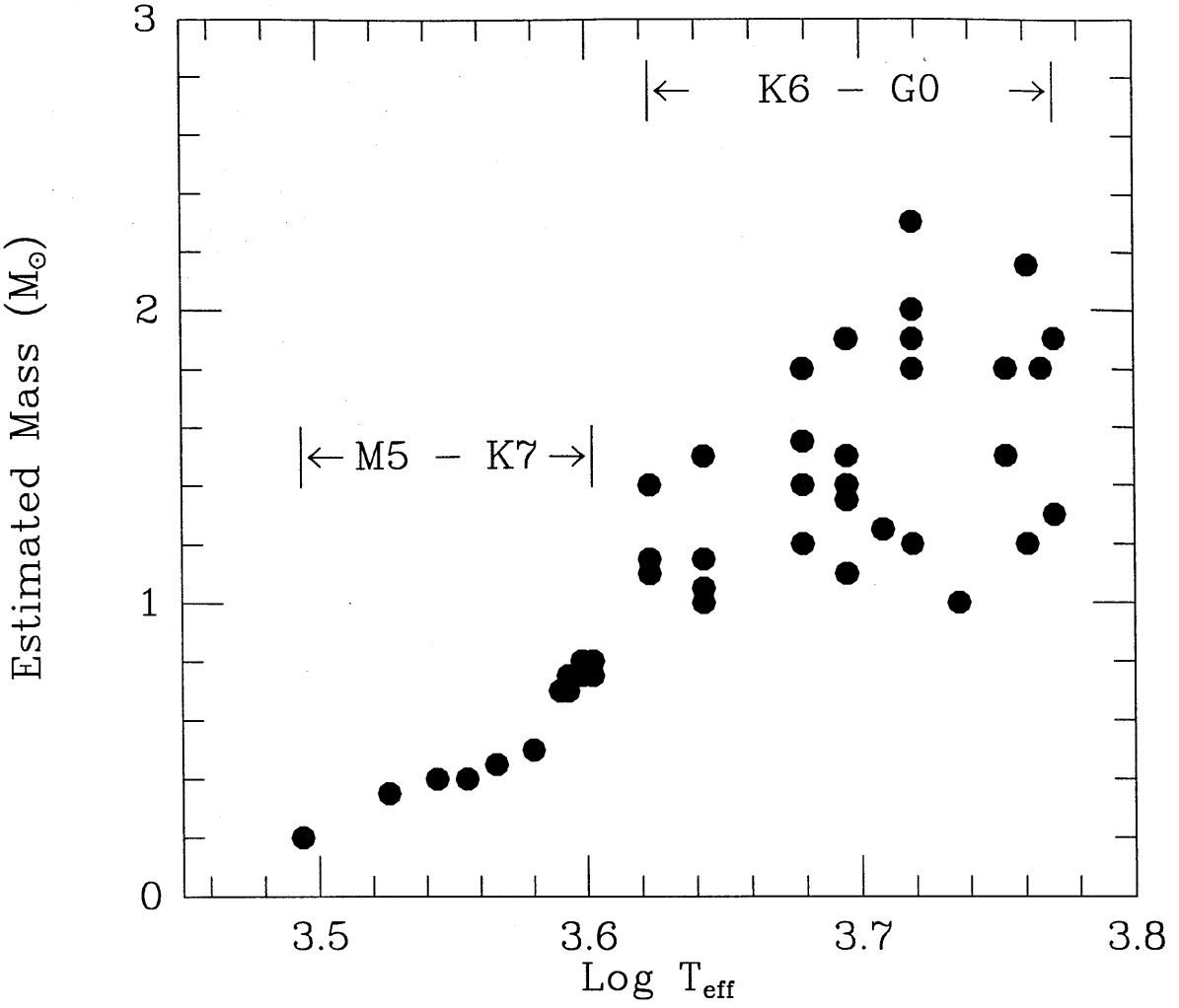

Figure 4.7

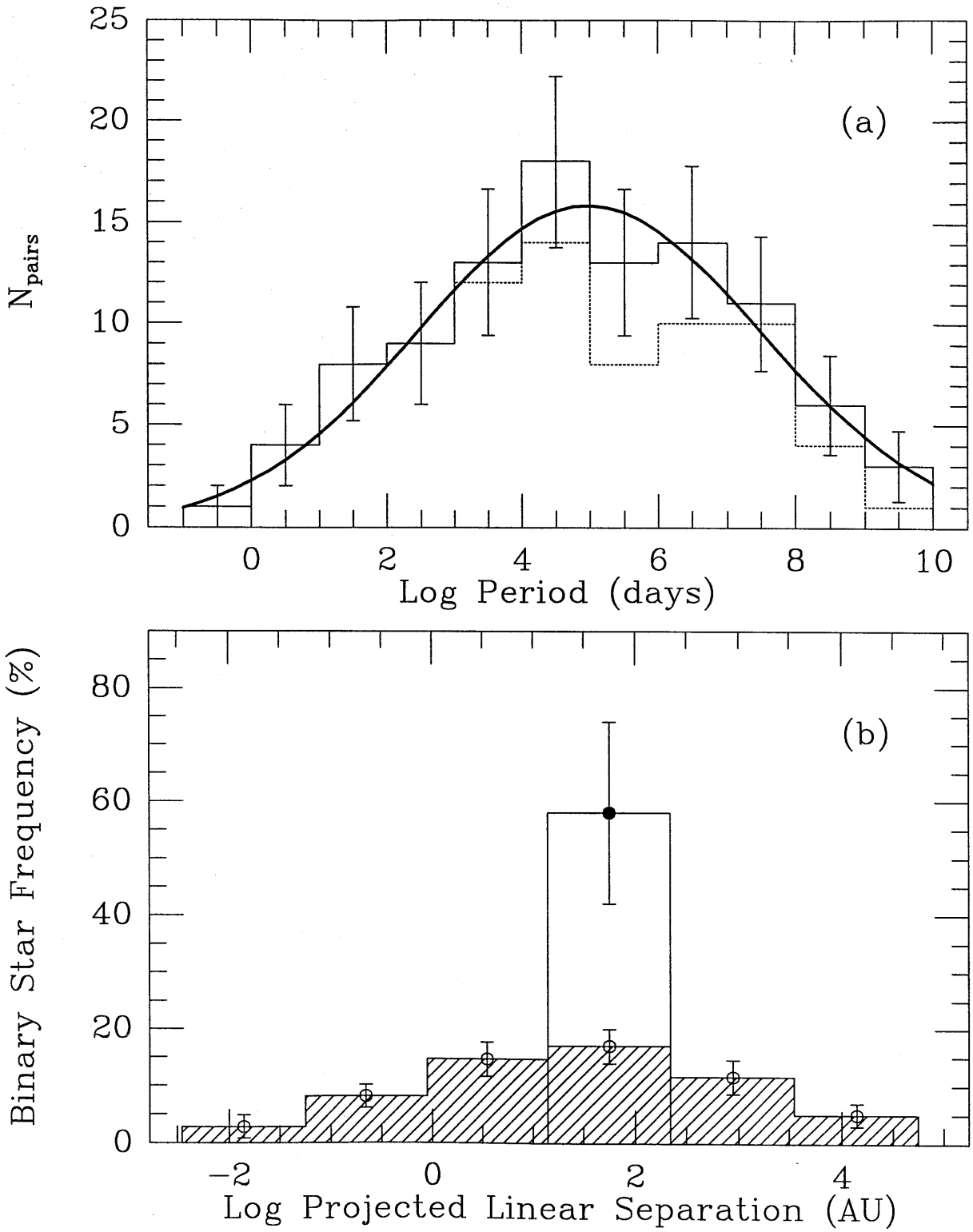
25
20
15
10
5
0
N_{pairs}
(a)
0
2
4
6
8
10
Log Period (days)
80
60
40
20
0
Binary Star Frequency (%)
(b)
−2
0
2
4
Log Projected Linear Separation (AU)

Figure 4.8

Appendix A

Projected Power Spectra for Binary Model Fits and Undetected Companion Limits

The plots found in this section are the projected power spectra described in Chapter Three for entire survey data set. For observations in which we detected a companion star, the power spectra projected along the separation axis of each binary system as described in §3.2.1 are shown in Figures A.1 - A.36. The binary star model fits are also shown in these plots; the fitted curves are solid over spatial frequencies for which the data was fit and dashed where the fit was extrapolated.

Figures A.37 - A.76 show the projected power spectra for the measurements for which no companion was detected, as described in §3.2.2. It is the minimum values found in these plots that set the upper limit for the flux density ratio of an undetected companion stars in each observation. Limits for additional companions were determined for the multiple star systems by projecting the power spectra with the fringe pattern due to the detected companion stars removed, as described in §3.2.2; these projected power spectra are shown in Figures A.77 - A.111.

Figure Captions

Figure A.1: The projected power spectrum of SR 20, along the axis of the binary system's separation vector, and the binary model fit.

Figure A.2: The projected power spectrum of ROXs 47C (1990 July 8), along the axis of the binary system's separation vector, and the binary model fit.

Figure A.3: The projected power spectrum of ROXs 47C (1991 May 3), along the axis of the binary system's separation vector, and the binary model fit.

Figure A.4: The projected power spectrum of 160946-1851, along the axis of the binary system's separation vector, and the binary model fit.

Figure A.5: The projected power spectrum of 162218-2420, along the axis of the binary system's separation vector, and the binary model fit.

Figure A.6: The projected power spectrum of 155913-2233, along the axis of the binary system's separation vector, and the binary model fit.

Figure A.7: The projected power spectrum of V853 Oph, along the axis of the binary system's separation vector, and the binary model fit.

Figure A.8: The projected power spectrum of SR 9 (1990 July 9), along the axis of the binary system's separation vector, and the binary model fit.

Figure A.9: The projected power spectrum of SR 9 (1990 August 5), along the axis of the binary system's separation vector, and the binary model fit.

Figure A.10: The projected power spectrum of Haro 1-4, along the axis of the binary system's separation vector, and the binary model fit.

Figure A.11: The projected power spectrum of 155203-2338, along the axis of the binary system's separation vector, and the binary model fit.

Figure A.12: The projected power spectrum of AS 205, along the axis of the binary system's separation vector, and the binary model fit.

Figure A.39: The 36 one-dimensional projected power spectra of SR 24 S, used to set limits on undetected companion stars.

Figure A.40: The 36 one-dimensional projected power spectra of Haro 1-16 (1990 August 6), used to set limits on undetected companion stars.

Figure A.41: The 36 one-dimensional projected power spectra of Haro 1-16 (1990 July 9), used to set limits on undetected companion stars.

Figure A.42: The 36 one-dimensional projected power spectra of 160815-1857, used to set limits on undetected companion stars.

Figure A.43: The 36 one-dimensional projected power spectra of SR 4 (1990 August 7), used to set limits on undetected companion stars.

Figure A.44: The 36 one-dimensional projected power spectra of SR 4 (1990 July 9), used to set limits on undetected companion stars.

Figure A.45: The 36 one-dimensional projected power spectra of DoAr 21, used to set limits on undetected companion stars.

Figure A.46: The 36 one-dimensional projected power spectra of ROXs 43A, used to set limits on undetected companion stars.

Figure A.47: The 36 one-dimensional projected power spectra of 160827-1813, used to set limits on undetected companion stars.

Figure A.48: The 36 one-dimensional projected power spectra of DoAr 24, used to set limits on undetected companion stars.

Figure A.49: The 36 one-dimensional projected power spectra of Haro 1-14, used to set limits on undetected companion stars.

Figure A.50: The 36 one-dimensional projected power spectra of 160905-1859, used to set limits on undetected companion stars.

Figure A.51: The 36 one-dimensional projected power spectra of 155828-2232, used to set limits on undetected companion stars.

Figure A.52: The 36 one-dimensional projected power spectra of DR Tau, used to set limits on undetected companion stars.

Figure A.53: The 36 one-dimensional projected power spectra of RY Tau (1990 Oct 2), used to set limits on undetected companion stars.

Figure A.54: The 36 one-dimensional projected power spectra of RY Tau (1990 Oct 4), used to set limits on undetected companion stars.

Figure A.55: The 36 one-dimensional projected power spectra of SU Aur, used to set limits on undetected companion stars.

Figure A.56: The 36 one-dimensional projected power spectra of CW Tau, used to set limits on undetected companion stars.

Figure A.57: The 36 one-dimensional projected power spectra of BP Tau, used to set limits on undetected companion stars.

Figure A.58: The 36 one-dimensional projected power spectra of Haro 6-13, used to set limits on undetected companion stars.

Figure A.59: The 36 one-dimensional projected power spectra of FZ Tau, used to set limits on undetected companion stars.

Figure A.60: The 36 one-dimensional projected power spectra of DO Tau, used to set limits on undetected companion stars.

Figure A.61: The 36 one-dimensional projected power spectra of UZ Tau E, used to set limits on undetected companion stars.

Figure A.62: The 36 one-dimensional projected power spectra of IQ Tau, used to set limits on undetected companion stars.

Figure A.63: The 36 one-dimensional projected power spectra of FN Tau, used to set limits on undetected companion stars.

Figure A.64: The 36 one-dimensional projected power spectra of HL Tau, used to set limits on undetected companion stars.

Figure A.65: The 36 one-dimensional projected power spectra of GI Tau, used to set limits on undetected companion stars.

Figure A.66: The 36 one-dimensional projected power spectra of 042417+1744, used to set limits on undetected companion stars.

Figure A.67: The 36 one-dimensional projected power spectra of DG Tau, used to set limits on undetected companion stars.

Figure A.68: The 36 one-dimensional projected power spectra of V819 Tau, used to set limits on undetected companion stars.

Figure A.69: The 36 one-dimensional projected power spectra of CY Tau, used to set limits on undetected companion stars.

Figure A.70: The 36 one-dimensional projected power spectra of HP Tau, used to set limits on undetected companion stars.

Figure A.71: The 36 one-dimensional projected power spectra of GK Tau, used to set limits on undetected companion stars.

Figure A.72: The 36 one-dimensional projected power spectra of CI Tau, used to set limits on undetected companion stars.

Figure A.73: The 36 one-dimensional projected power spectra of HDE 28372, used to set limits on undetected companion stars.

Figure A.74: The 36 one-dimensional projected power spectra of HP Tau/G2, used to set limits on undetected companion stars.

Figure A.75: The 36 one-dimensional projected power spectra of Hubble 4, used to set limits on undetected companion stars.

Figure A.76: The 36 one-dimensional projected power spectra of DE Tau, used to set limits on undetected companion stars.

Figure A.77: The 36 one-dimensional projected power spectra of SR 20 after the binary system fringe pattern was removed. These are used to set limits on

additional companion stars.

Figure A.78: The 36 one-dimensional projected power spectra of SR 9 (1990 August 5) after the binary system fringe pattern was removed. These are used to set limits on additional companion stars.

Figure A.79: The 36 one-dimensional projected power spectra of SR 9 (1990 July 9) after the binary system fringe pattern was removed. These are used to set limits on additional companion stars.

Figure A.80: The 36 one-dimensional projected power spectra of ROXs 42C (1991 May 3) after the binary system fringe pattern was removed. These are used to set limits on additional companion stars.

Figure A.81: The 36 one-dimensional projected power spectra of ROXs 42C (1990 July 8) after the binary system fringe pattern was removed. These are used to set limits on additional companion stars.

Figure A.82: The 36 one-dimensional projected power spectra of Haro 1-4 after the binary system fringe pattern was removed. These are used to set limits on additional companion stars.

Figure A.83: The 36 one-dimensional projected power spectra of 160946-1851 after the binary system fringe pattern was removed. These are used to set limits on additional companion stars.

Figure A.84: The 36 one-dimensional projected power spectra of 162218-2420 after the binary system fringe pattern was removed. These are used to set limits on additional companion stars.

Figure A.85: The 36 one-dimensional projected power spectra of DoAr 24 E after the binary system fringe pattern was removed. These are used to set limits on additional companion stars.

Figure A.86: The 36 one-dimensional projected power spectra of 155203-2338 after the binary system fringe pattern was removed. These are used to set limits on additional companion stars.

Figure A.87: The 36 one-dimensional projected power spectra of AS 205 after the binary system fringe pattern was removed. These are used to set limits on additional companion stars.

Figure A.88: The 36 one-dimensional projected power spectra of V853 Oph after the binary system fringe pattern was removed. These are used to set limits on additional companion stars.

Figure A.89: The 36 one-dimensional projected power spectra of 155913-2233 after the binary system fringe pattern was removed. These are used to set limits on additional companion stars.

Figure A.90: The 36 one-dimensional projected power spectra of T Tau after the binary system fringe pattern was removed. These are used to set limits on additional companion stars.

Figure A.91: The 36 one-dimensional projected power spectra of DD Tau (1990 Oct 4) after the binary system fringe pattern was removed. These are used to set limits on additional companion stars.

Figure A.92: The 36 one-dimensional projected power spectra of DD Tau (1990 Oct 2) after the binary system fringe pattern was removed. These are used to set limits on additional companion stars.

Figure A.93: The 36 one-dimensional projected power spectra of RW Aur after the binary system fringe pattern was removed. These are used to set limits on additional companion stars.

Figure A.94: The 36 one-dimensional projected power spectra of UY Aur after the binary system fringe pattern was removed. These are used to set limits on

additional companion stars.

Figure A.95: The 36 one-dimensional projected power spectra of V807 Tau after the binary system fringe pattern was removed. These are used to set limits on additional companion stars.

Figure A.96: The 36 one-dimensional projected power spectra of FO Tau after the binary system fringe pattern was removed. These are used to set limits on additional companion stars.

Figure A.97: The 36 one-dimensional projected power spectra of UZ tau W after the binary system fringe pattern was removed. These are used to set limits on additional companion stars.

Figure A.98: The 36 one-dimensional projected power spectra of V928 Tau after the binary system fringe pattern was removed. These are used to set limits on additional companion stars.

Figure A.99: The 36 one-dimensional projected power spectra of DF Tau after the binary system fringe pattern was removed. These are used to set limits on additional companion stars.

Figure A.100: The 36 one-dimensional projected power spectra of DI Tau after the binary system fringe pattern was removed. These are used to set limits on additional companion stars.

Figure A.101: The 36 one-dimensional projected power spectra of LkHα 332/G2 (1990 Oct 4) after the binary system fringe pattern was removed. These are used to set limits on additional companion stars.

Figure A.102: The 36 one-dimensional projected power spectra of LkHα 332/G2 (1990 Oct 2) after the binary system fringe pattern was removed. These are used to set limits on additional companion stars.

Figure A.103: The 36 one-dimensional projected power spectra of XZ Tau after the binary system fringe pattern was removed. These are used to set limits on additional companion stars.

Figure A.104: The 36 one-dimensional projected power spectra of IS Tau after the binary system fringe pattern was removed. These are used to set limits on additional companion stars.

Figure A.105: The 36 one-dimensional projected power spectra of GG Tau after the binary system fringe pattern was removed. These are used to set limits on additional companion stars.

Figure A.106: The 36 one-dimensional projected power spectra of FX Tau after the binary system fringe pattern was removed. These are used to set limits on additional companion stars.

Figure A.107: The 36 one-dimensional projected power spectra of V410 Tau after the binary system fringe pattern was removed. These are used to set limits on additional companion stars.

Figure A.108: The 36 one-dimensional projected power spectra of FV Tau after the binary system fringe pattern was removed. These are used to set limits on additional companion stars.

Figure A.109: The 36 one-dimensional projected power spectra of V773 Tau after the binary system fringe pattern was removed. These are used to set limits on additional companion stars.

Figure A.110: The 36 one-dimensional projected power spectra of LkCa 3 after the binary system fringe pattern was removed. These are used to set limits on additional companion stars.

Figure A.111: The 36 one-dimensional projected power spectra of GH Tau after the binary system fringe pattern was removed. These are used to set limits on

additional companion stars.

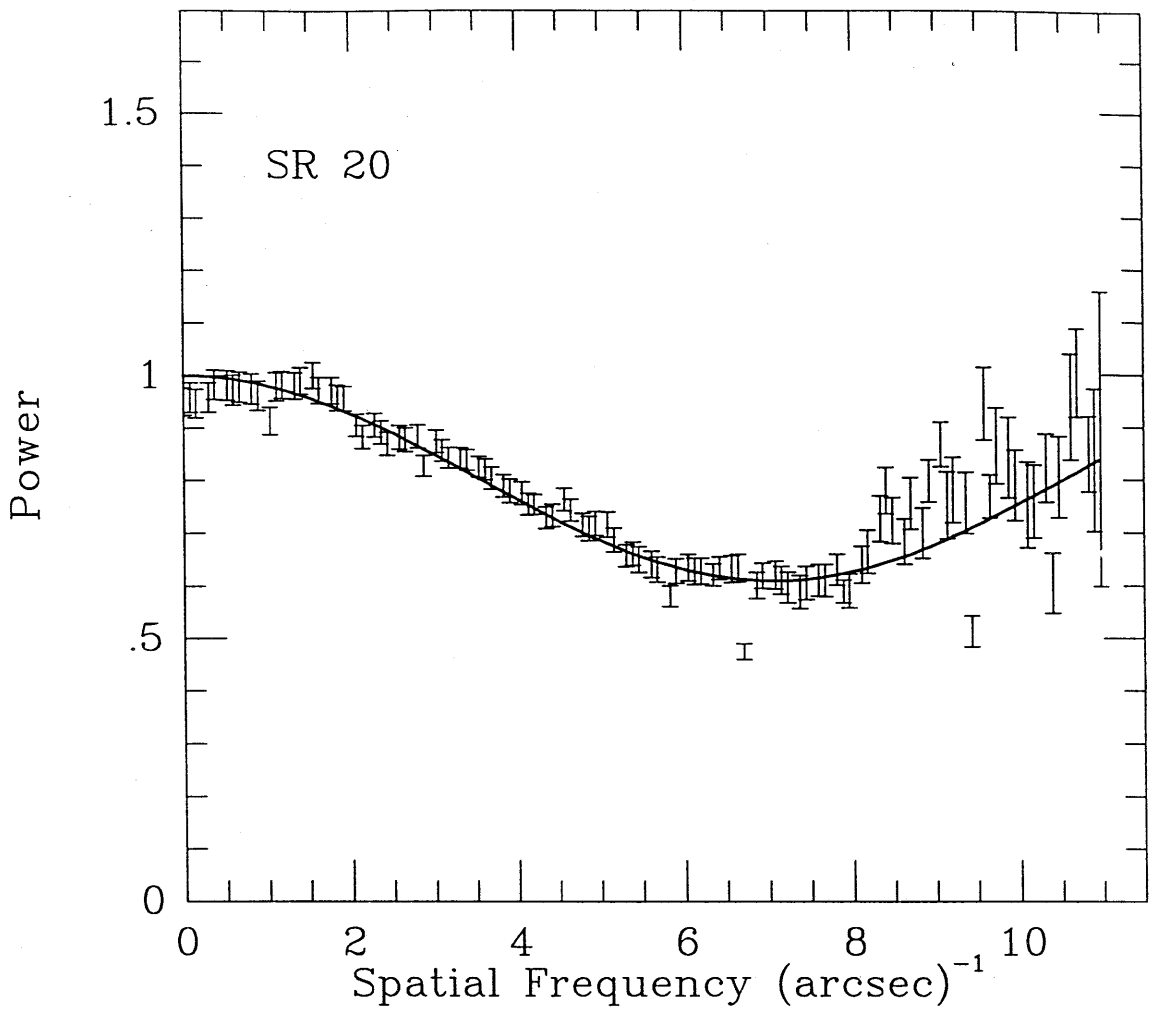

Figure A.1

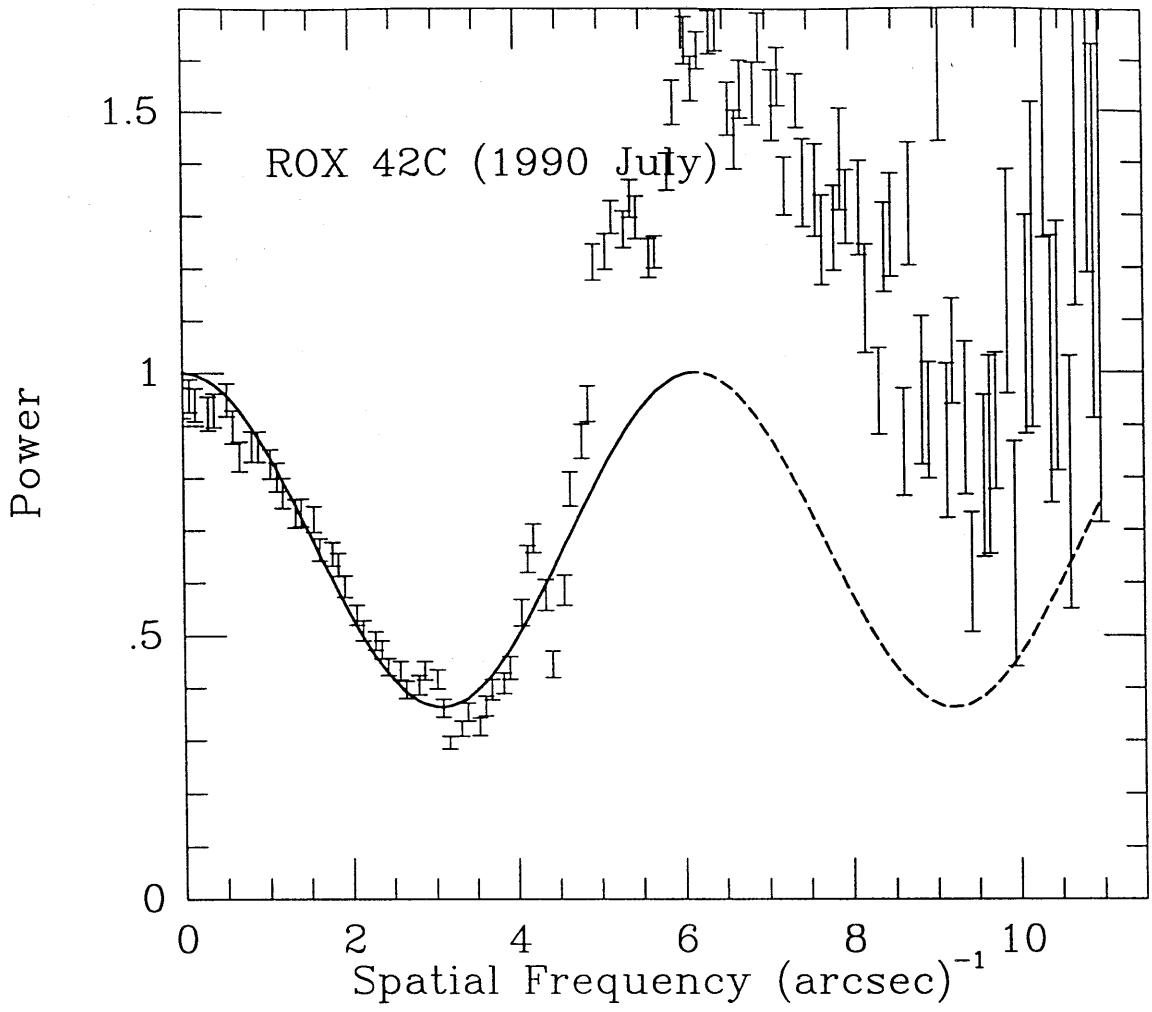
ROX 42C (1990 July)
Power
1.5
1
.5
0
0
2
4
6
8
10
Spatial Frequency (arcsec)$^{-1}$

Figure A.2

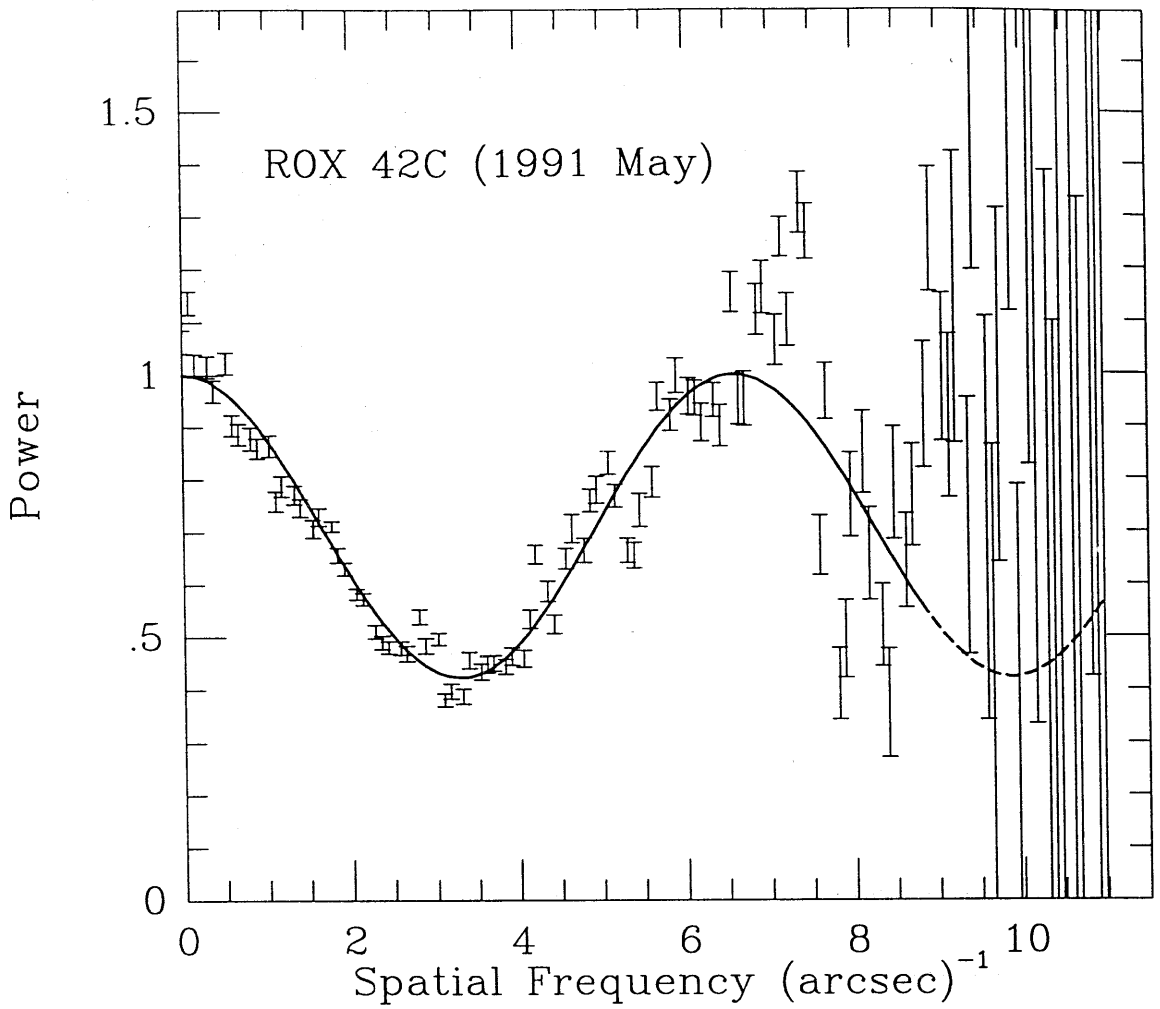
ROX 42C (1991 May)
Power
1.5
1
.5
0
0
2
4
6
8
10
Spatial Frequency (arcsec)$^{-1}$

Figure A.3

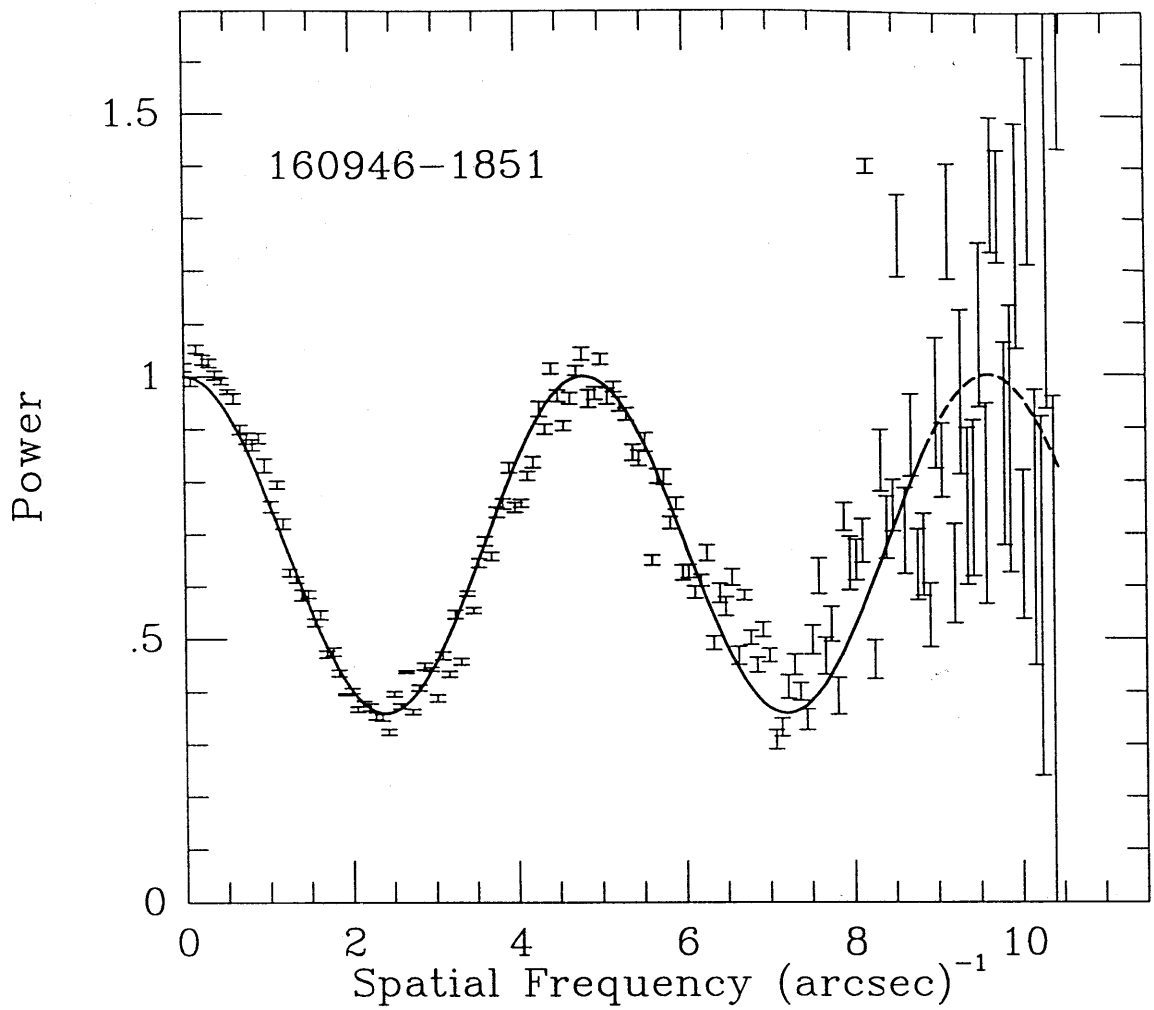
160946−1851
Power
1.5
1
.5
0
0
2
4
6
8
10
Spatial Frequency (arcsec)$^{-1}$

Figure A.4

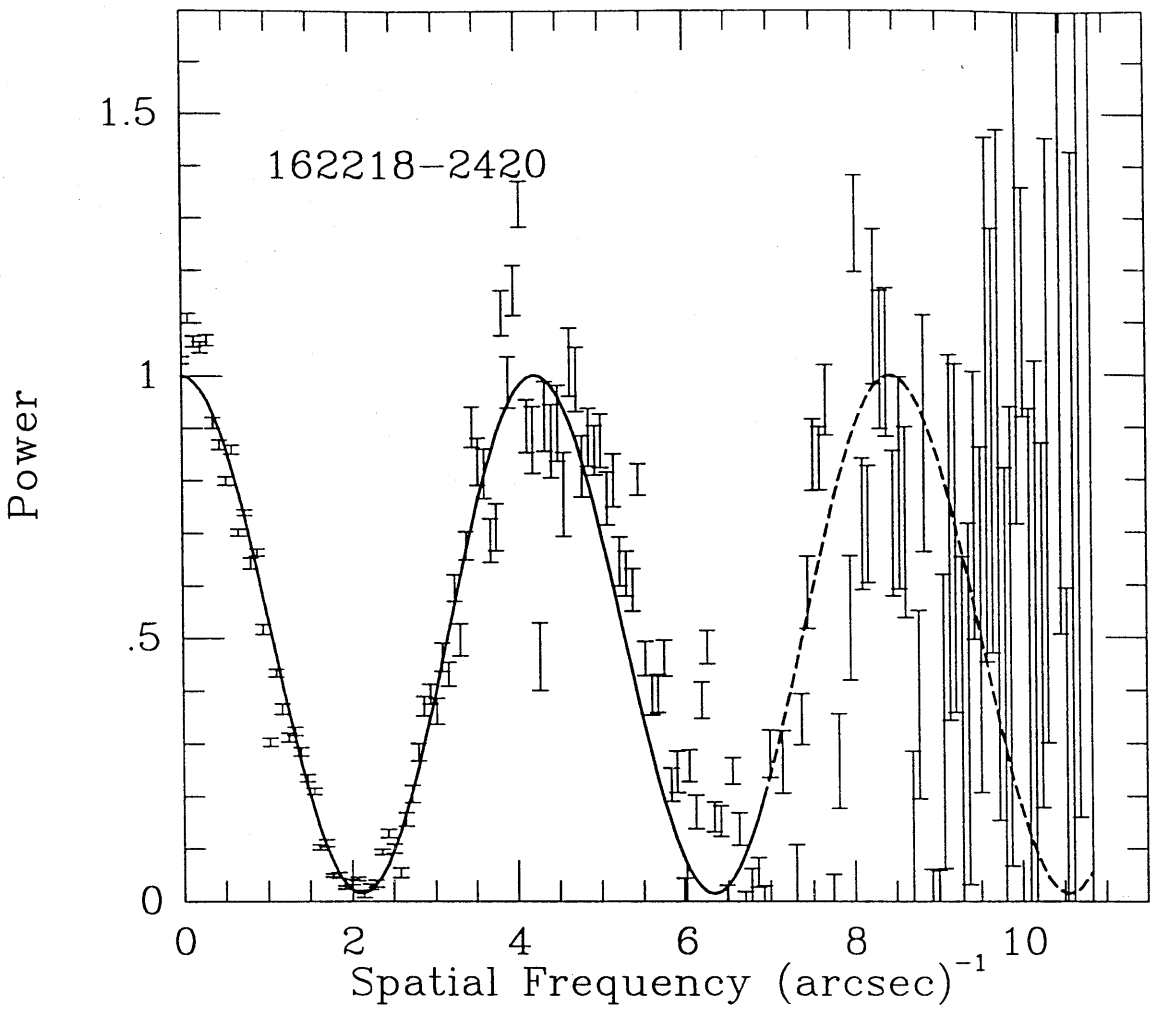
162218−2420
Power
1.5
1
.5
0
0
2
4
6
8
10
Spatial Frequency (arcsec)$^{-1}$

Figure A.5

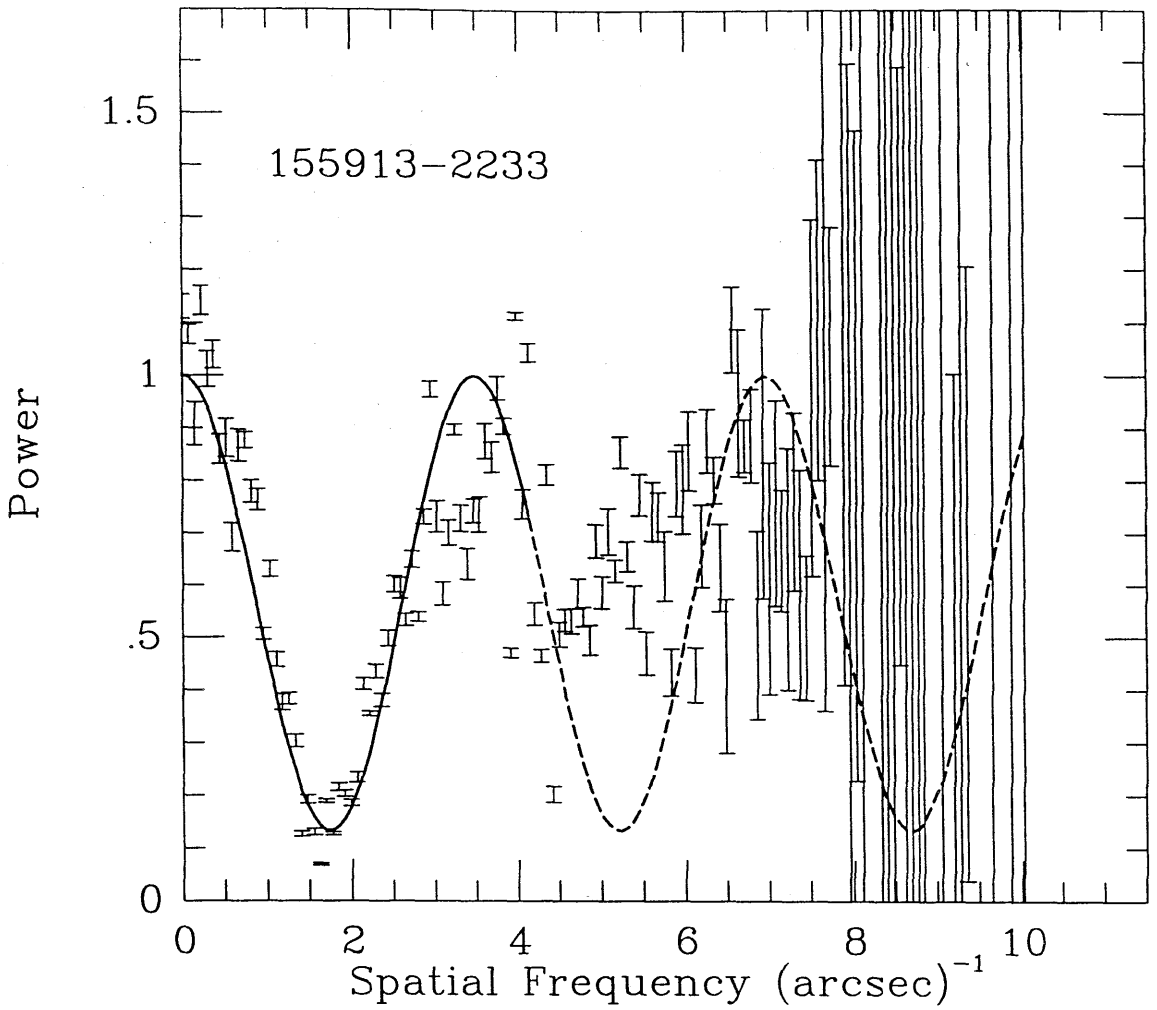
155913−2233
Power
1.5
1
.5
0
0
2
4
6
8
10
Spatial Frequency (arcsec)$^{-1}$

Figure A.6

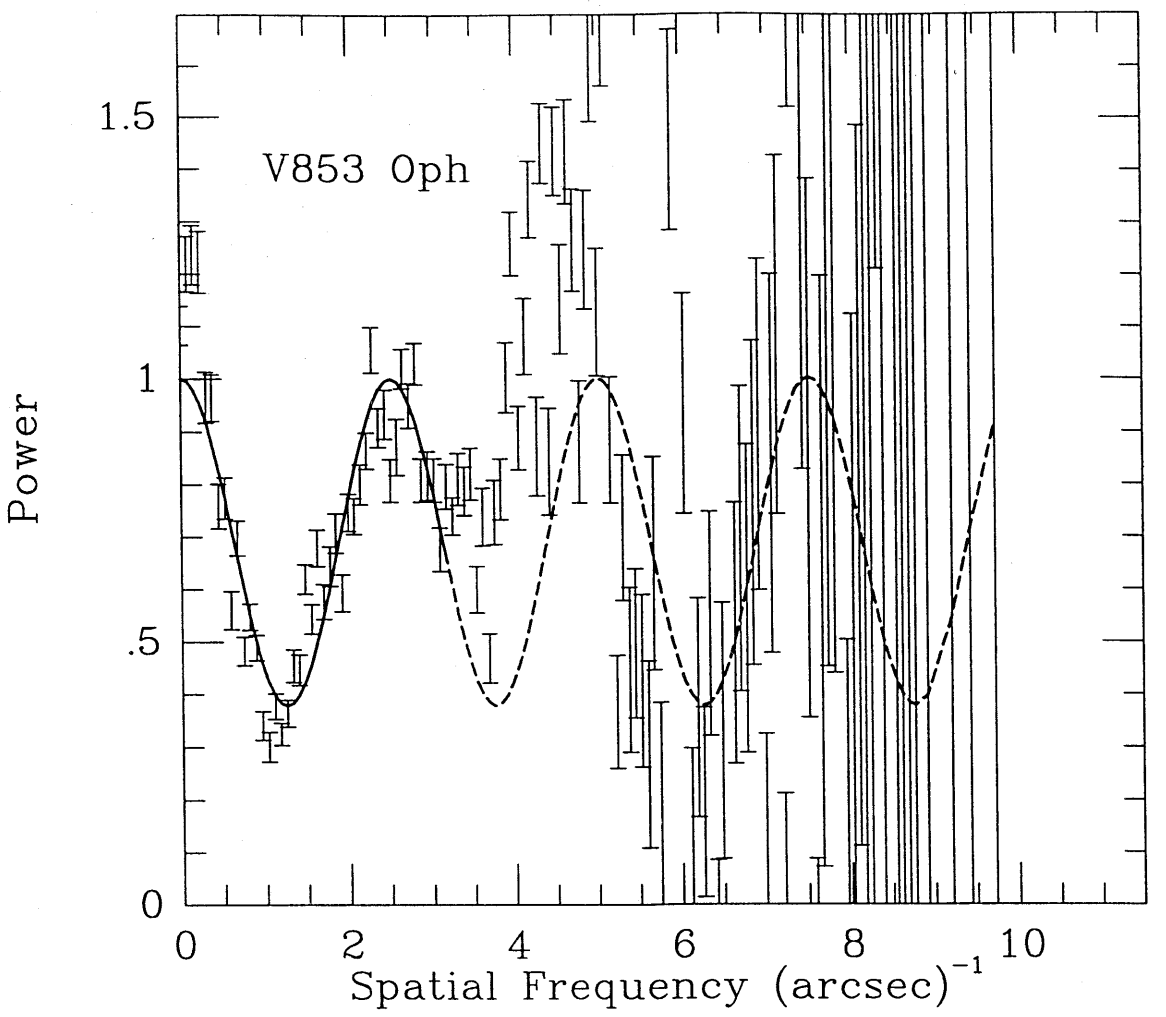

Figure A.7

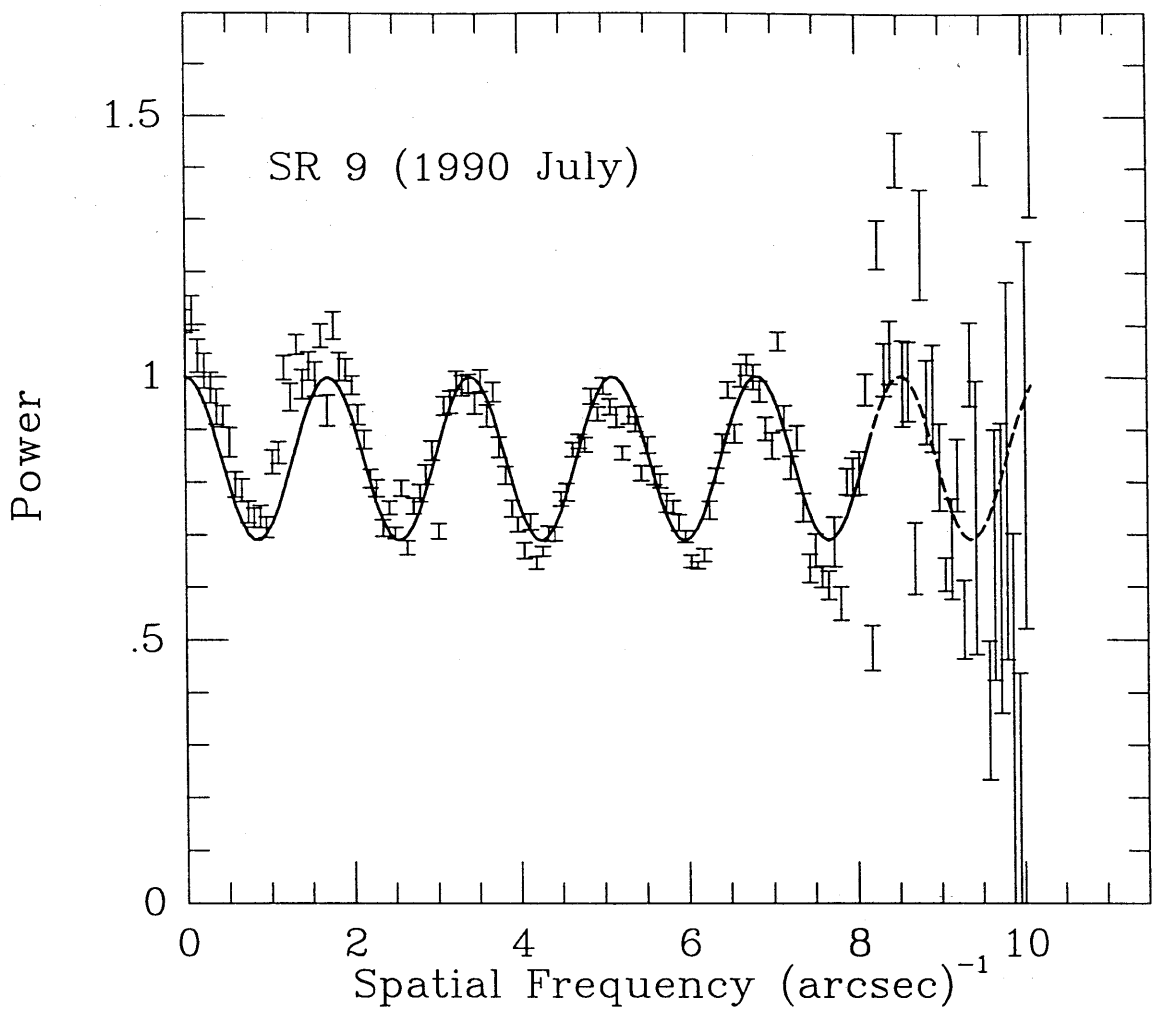
SR 9 (1990 July)
Power
1.5
1
.5
0
0
2
4
6
8
10
Spatial Frequency (arcsec)$^{-1}$

Figure A.8

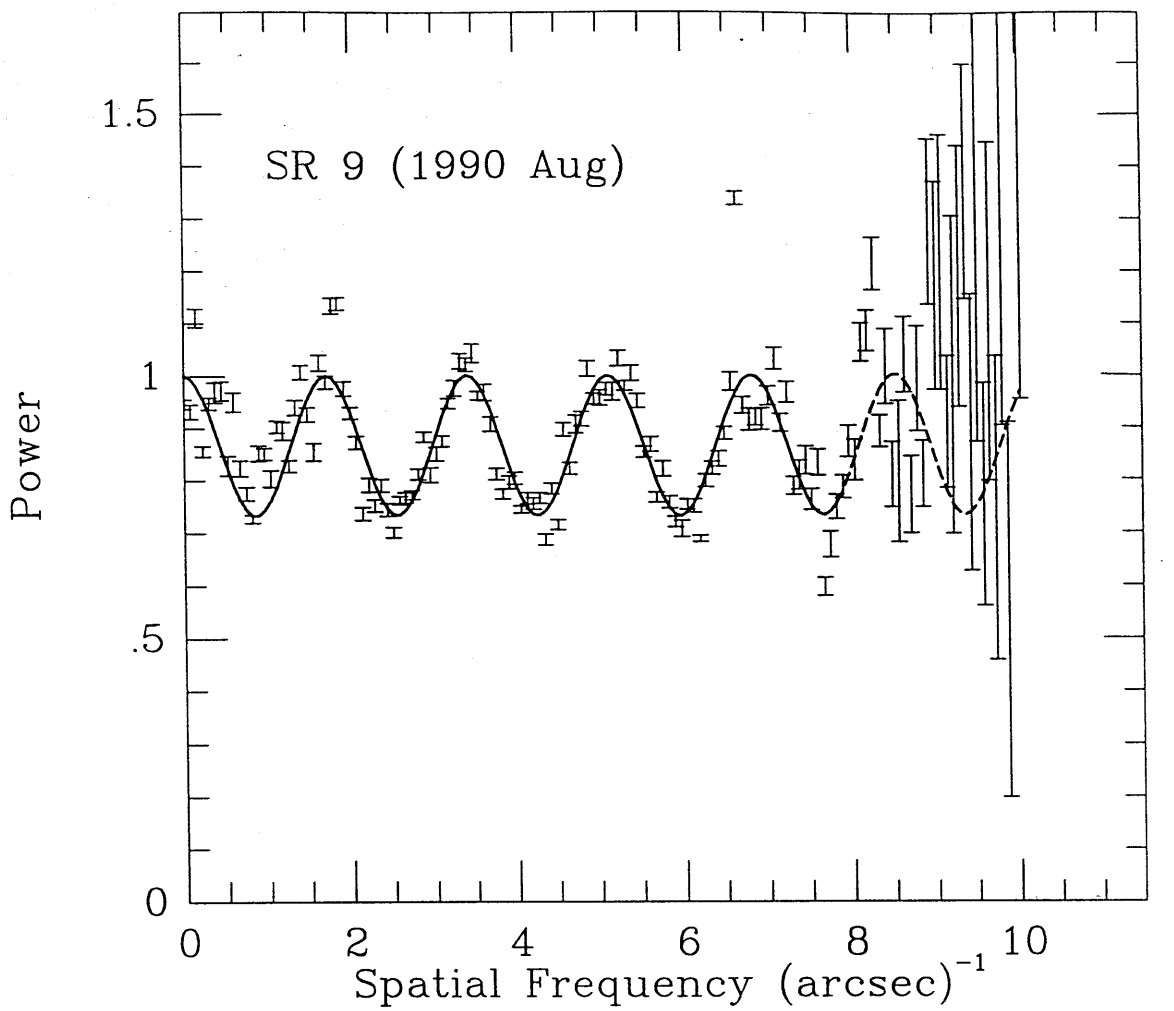
SR 9 (1990 Aug)
Power
1.5
1
.5
0
0
2
4
6
8
10
Spatial Frequency (arcsec)$^{-1}$

Figure A.9

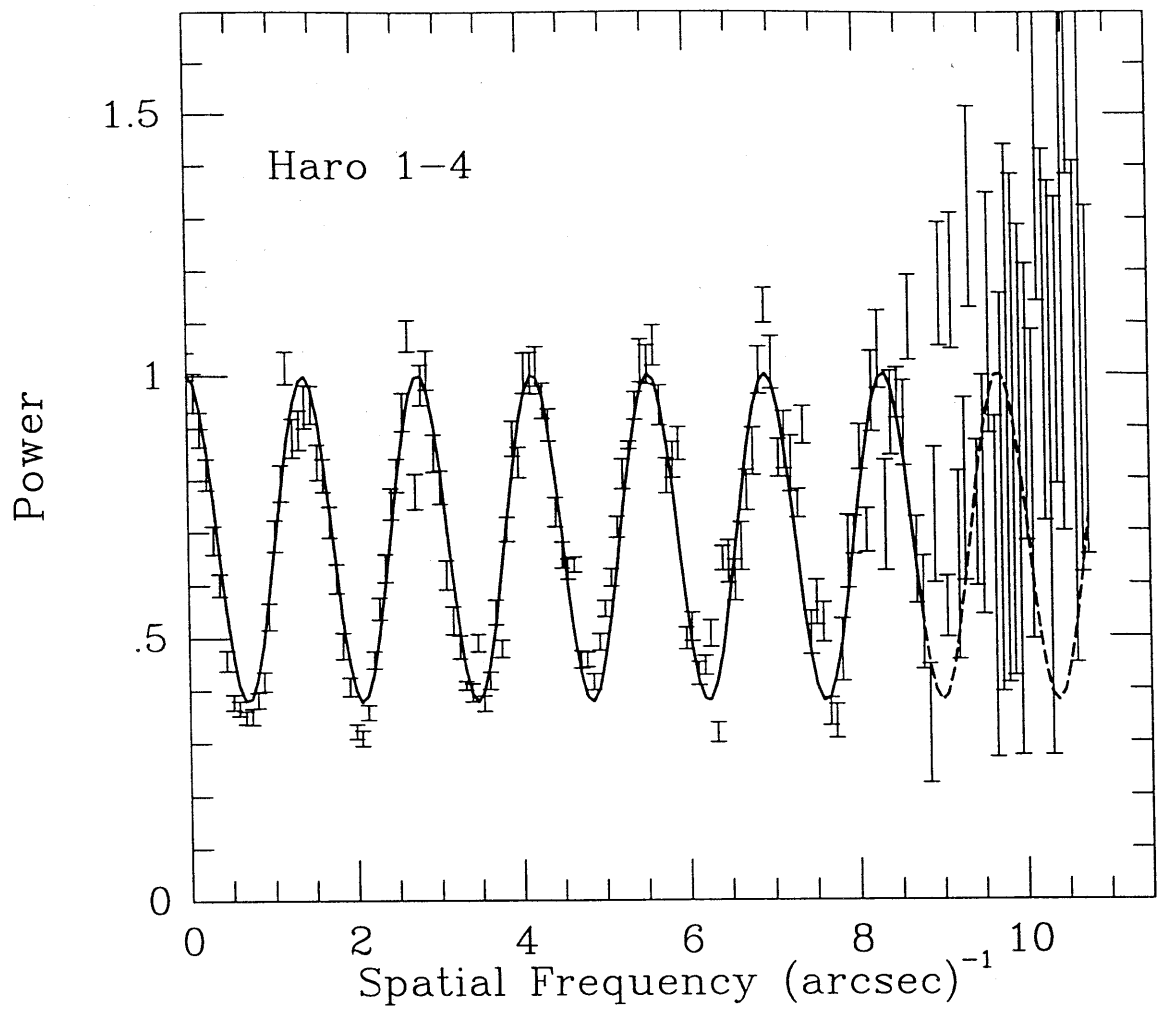

Figure A.10

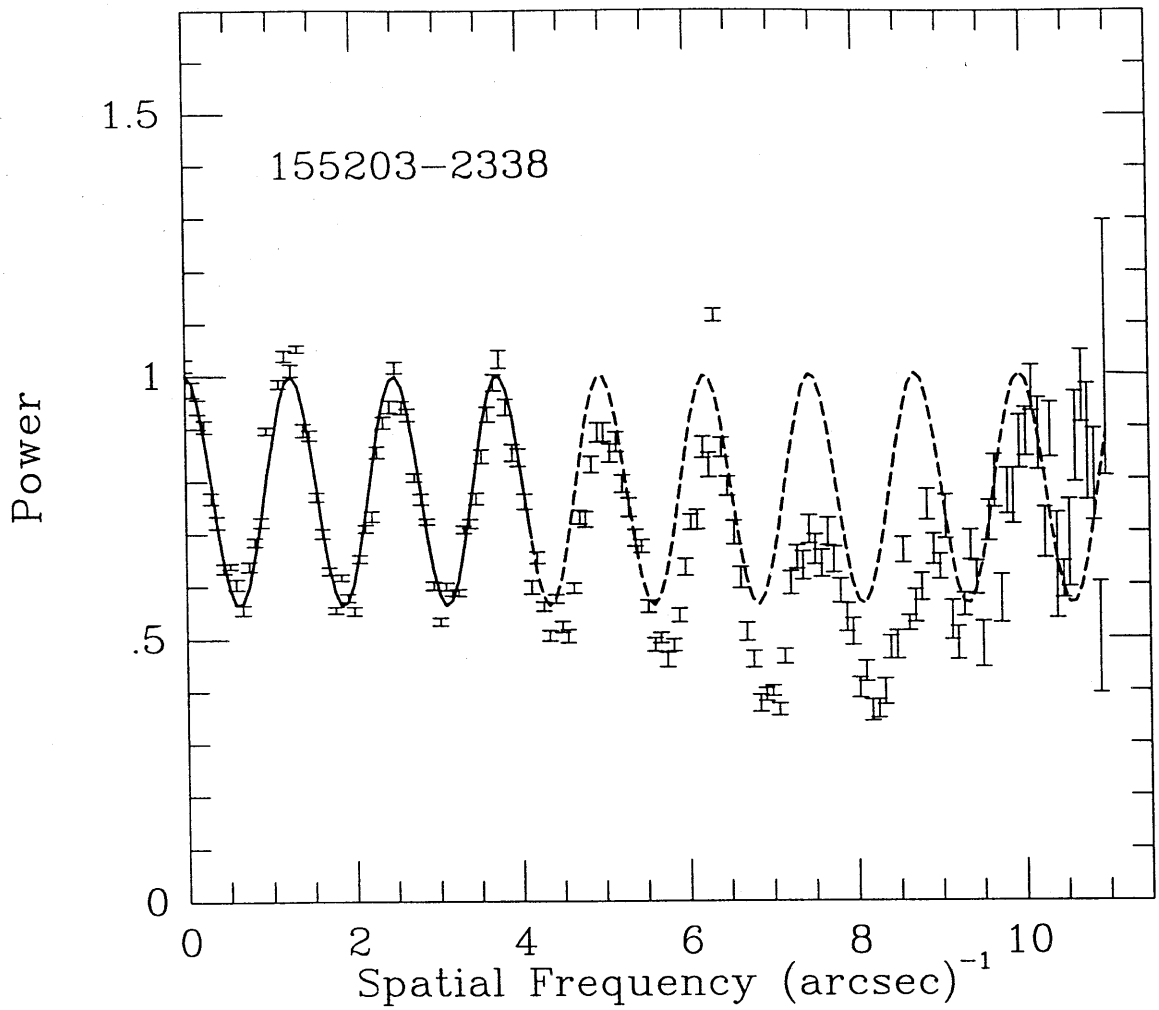
155203−2338
Power
1.5
1
.5
0
0
2
4
6
8
10
Spatial Frequency (arcsec)$^{-1}$

Figure A.11

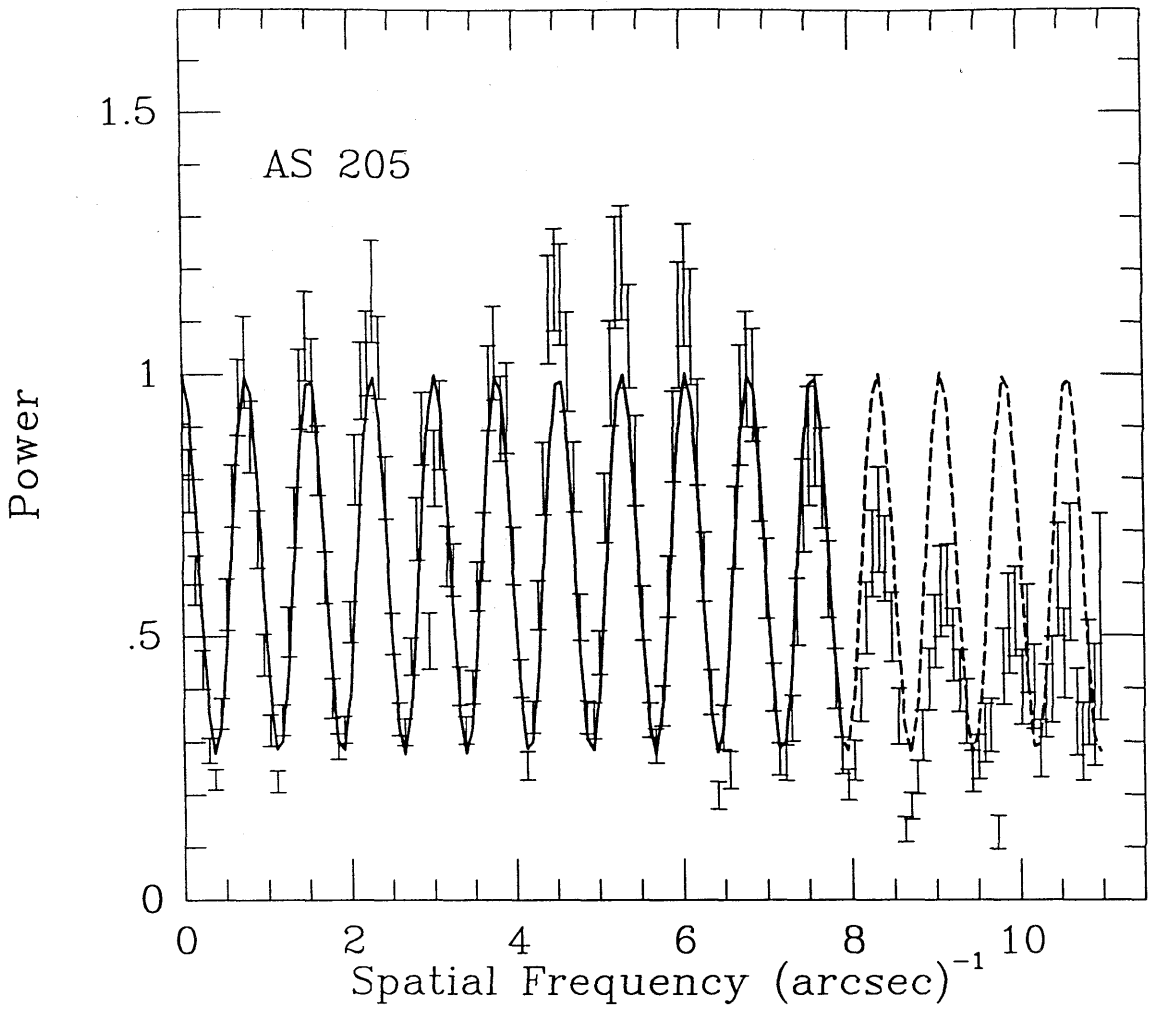

Figure A.12

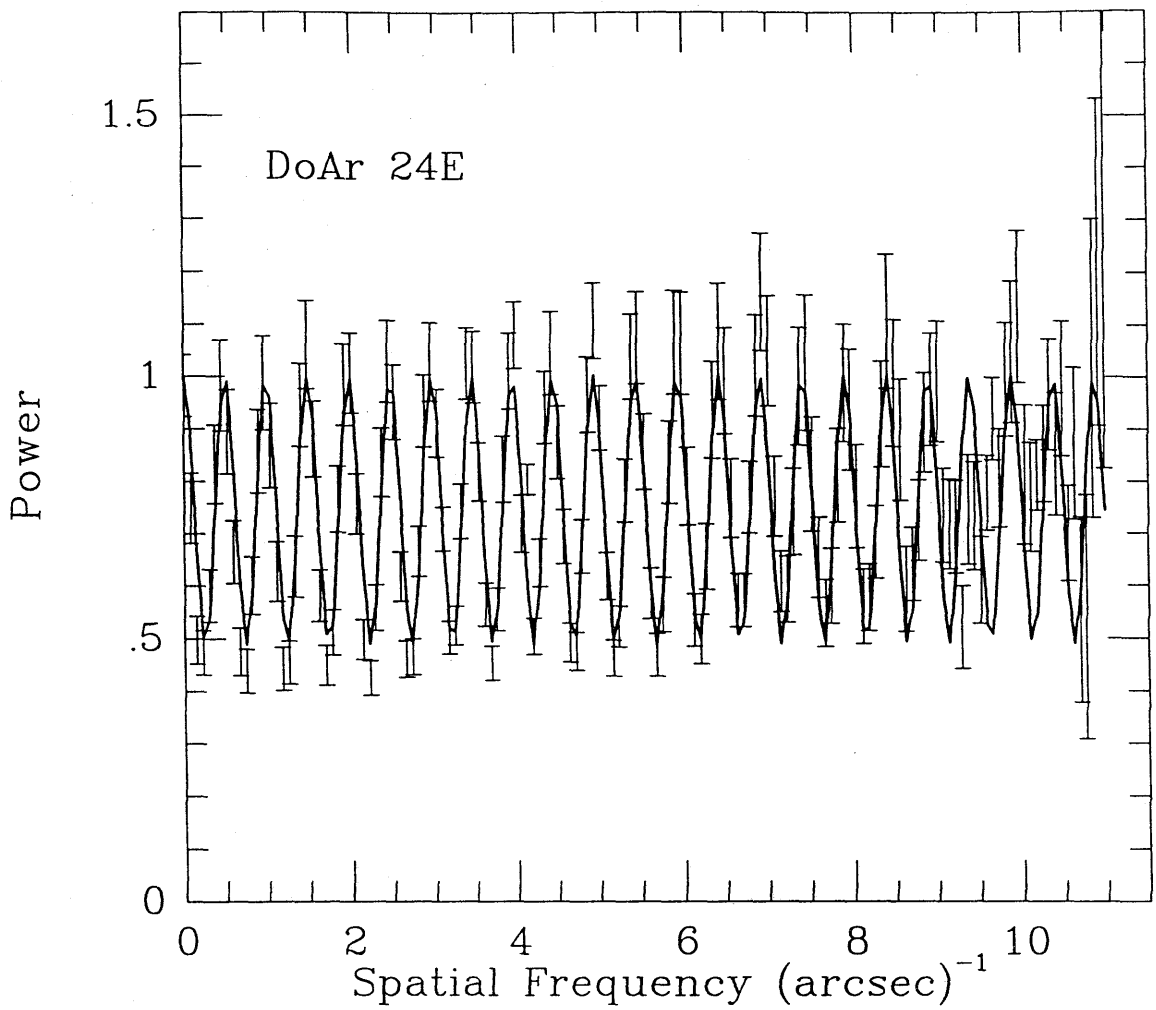

Figure A.13

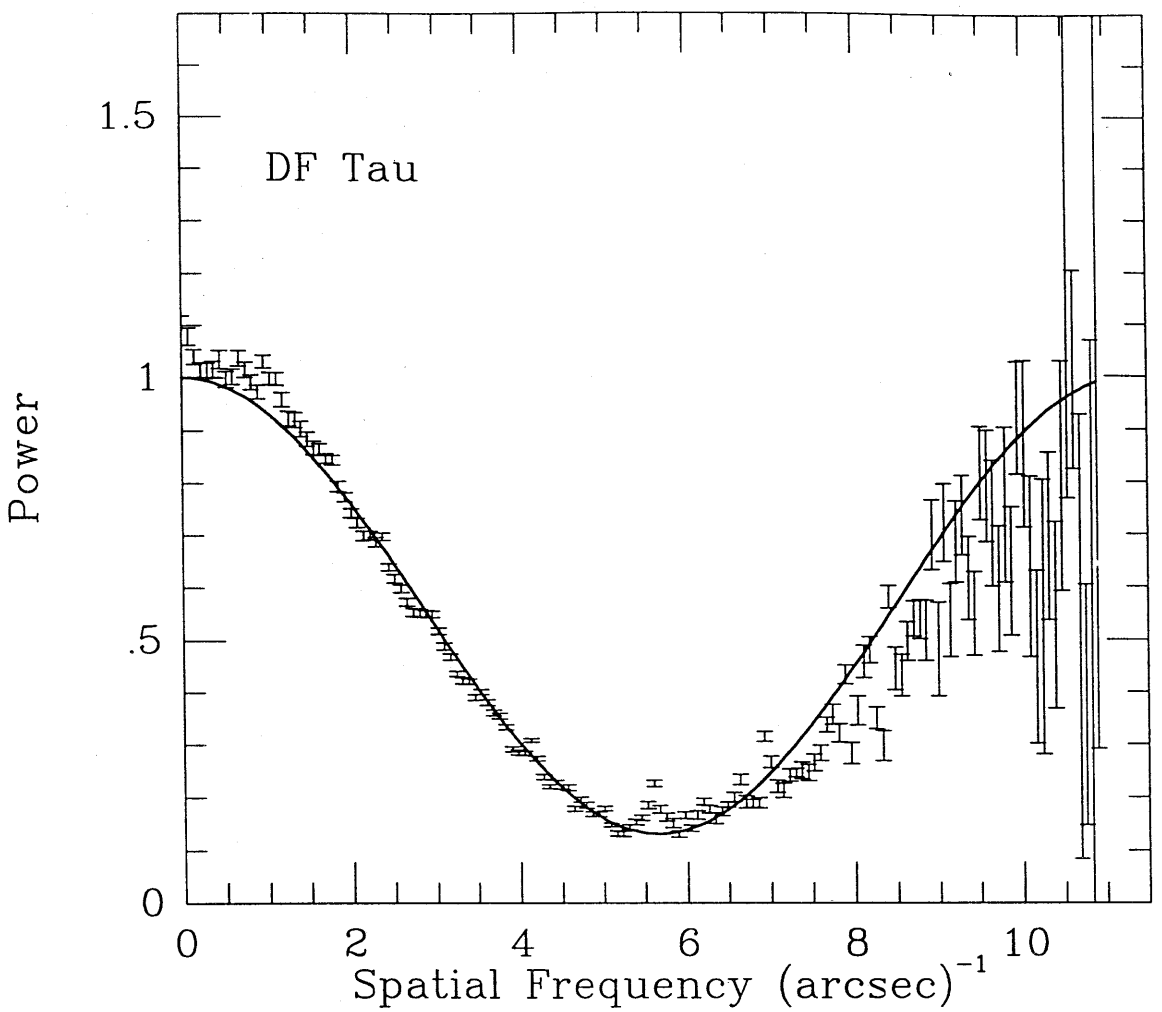

Figure A.14

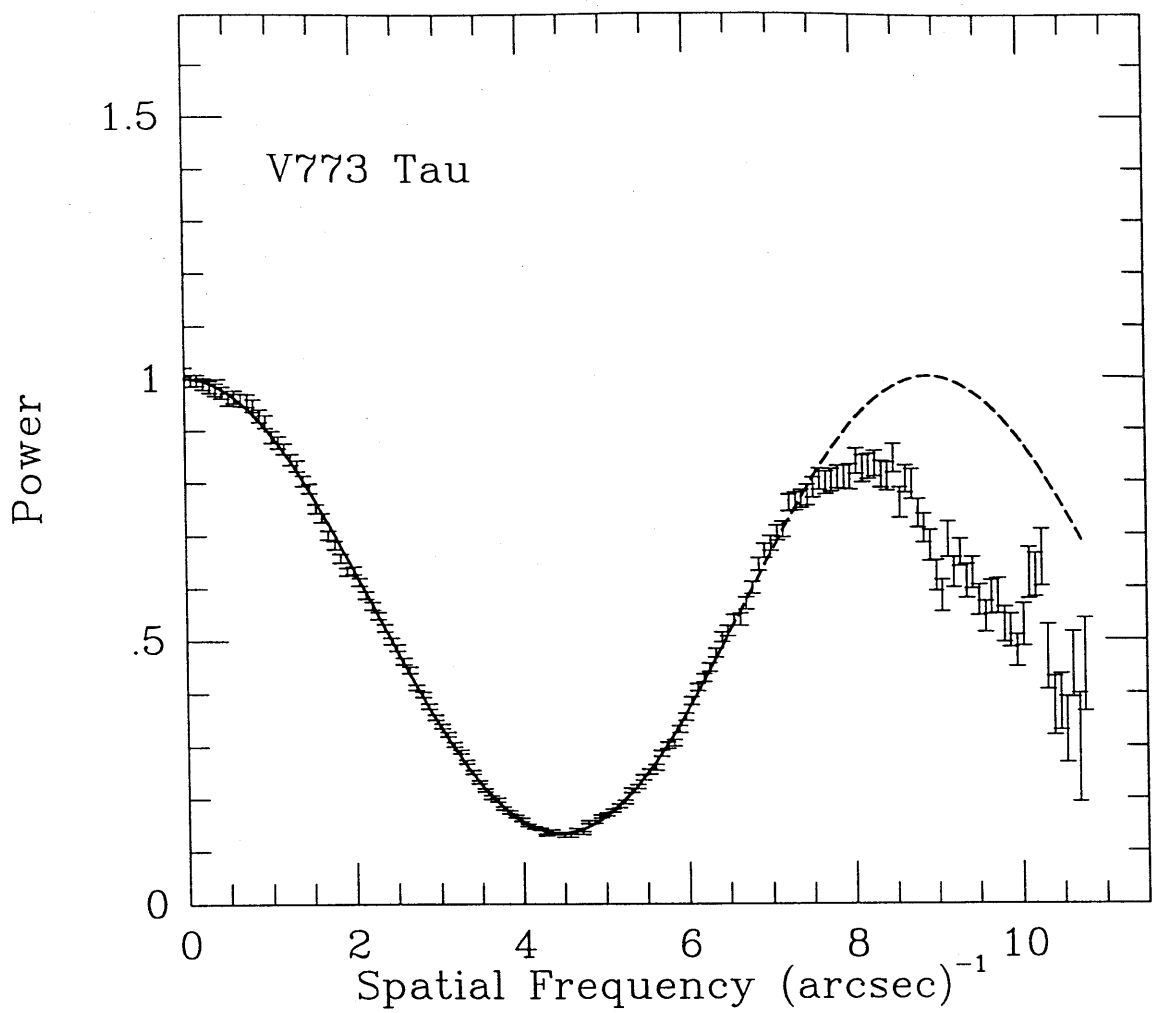

Figure A.15

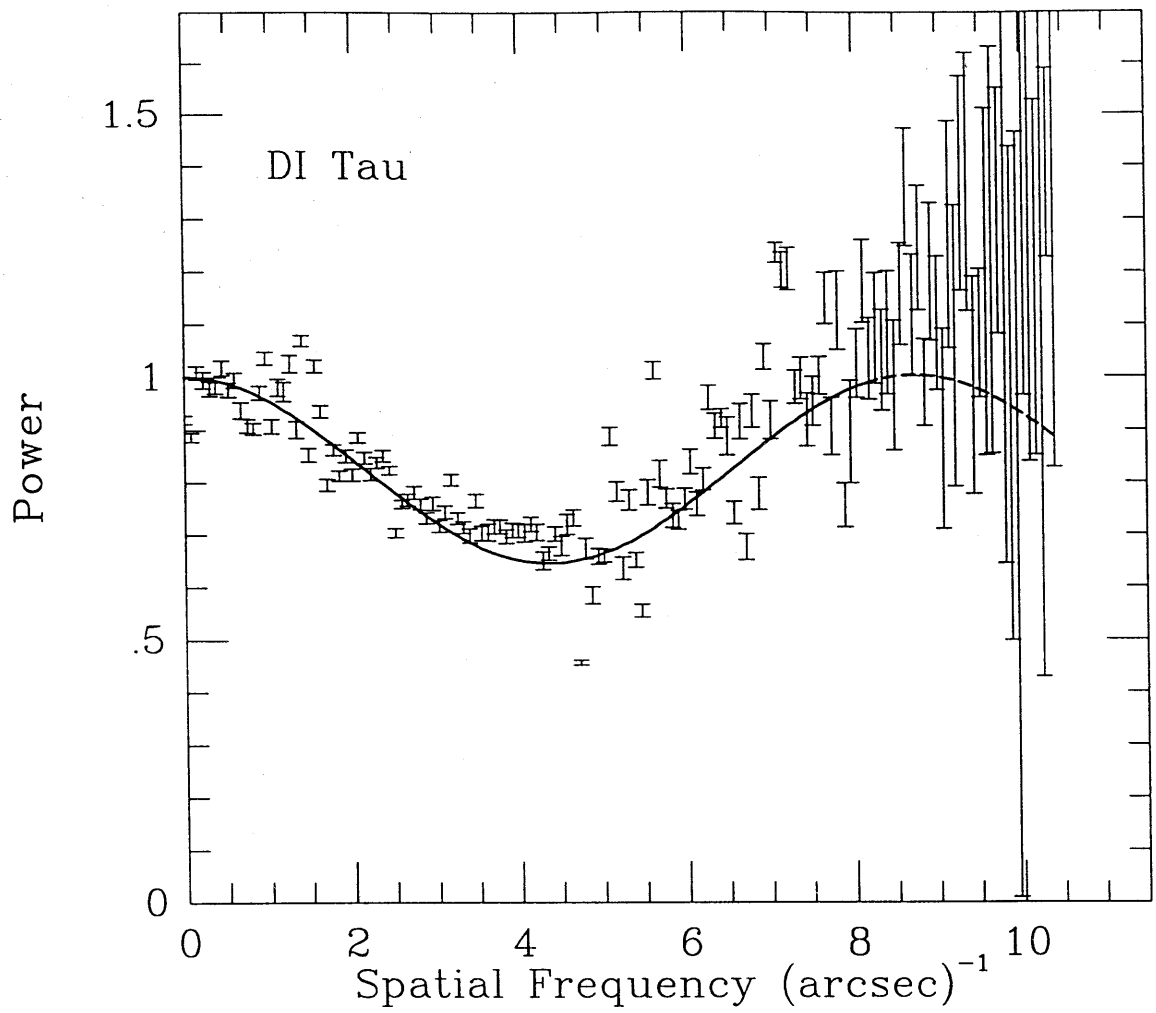

Figure A.16

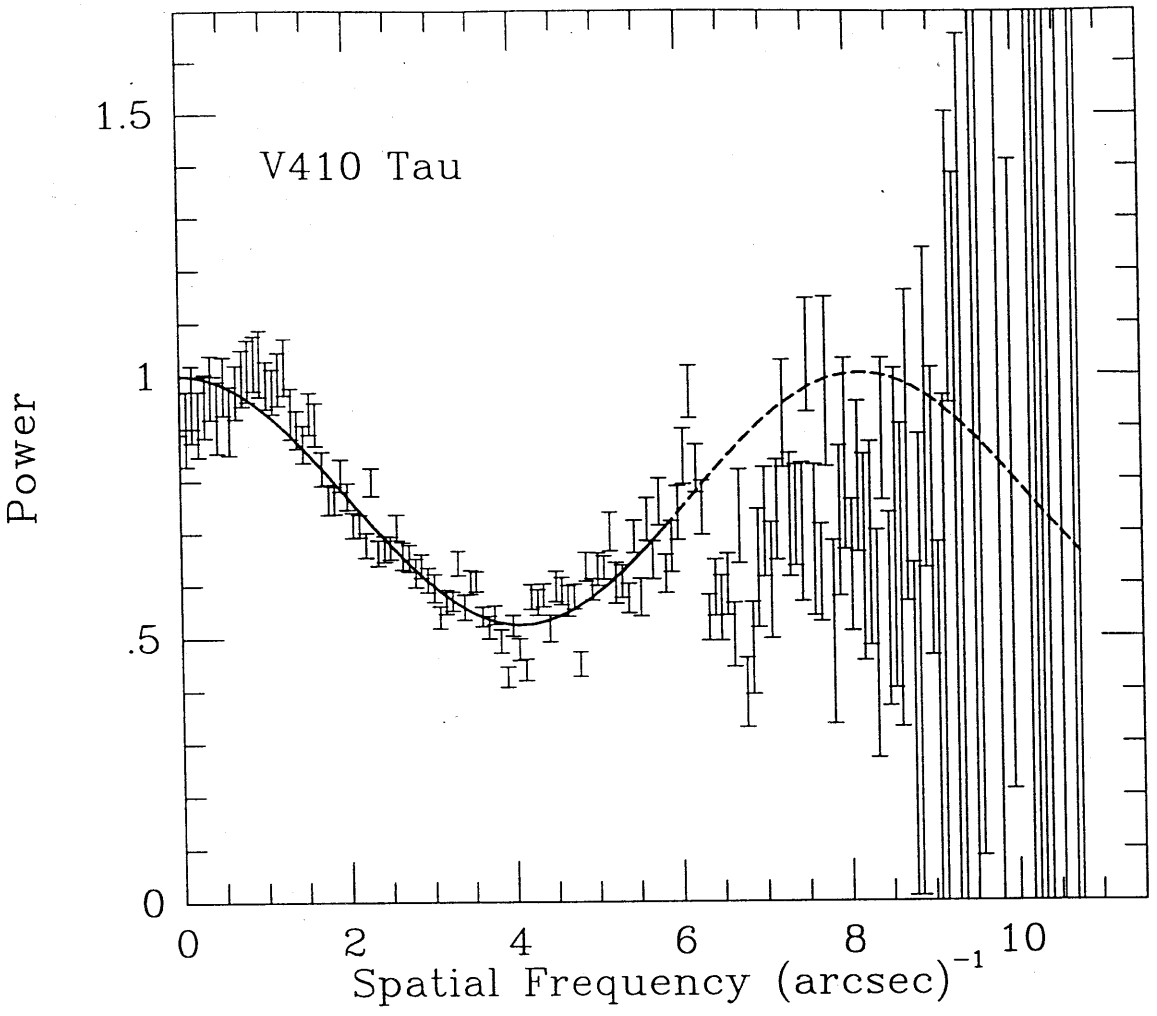

Figure A.17

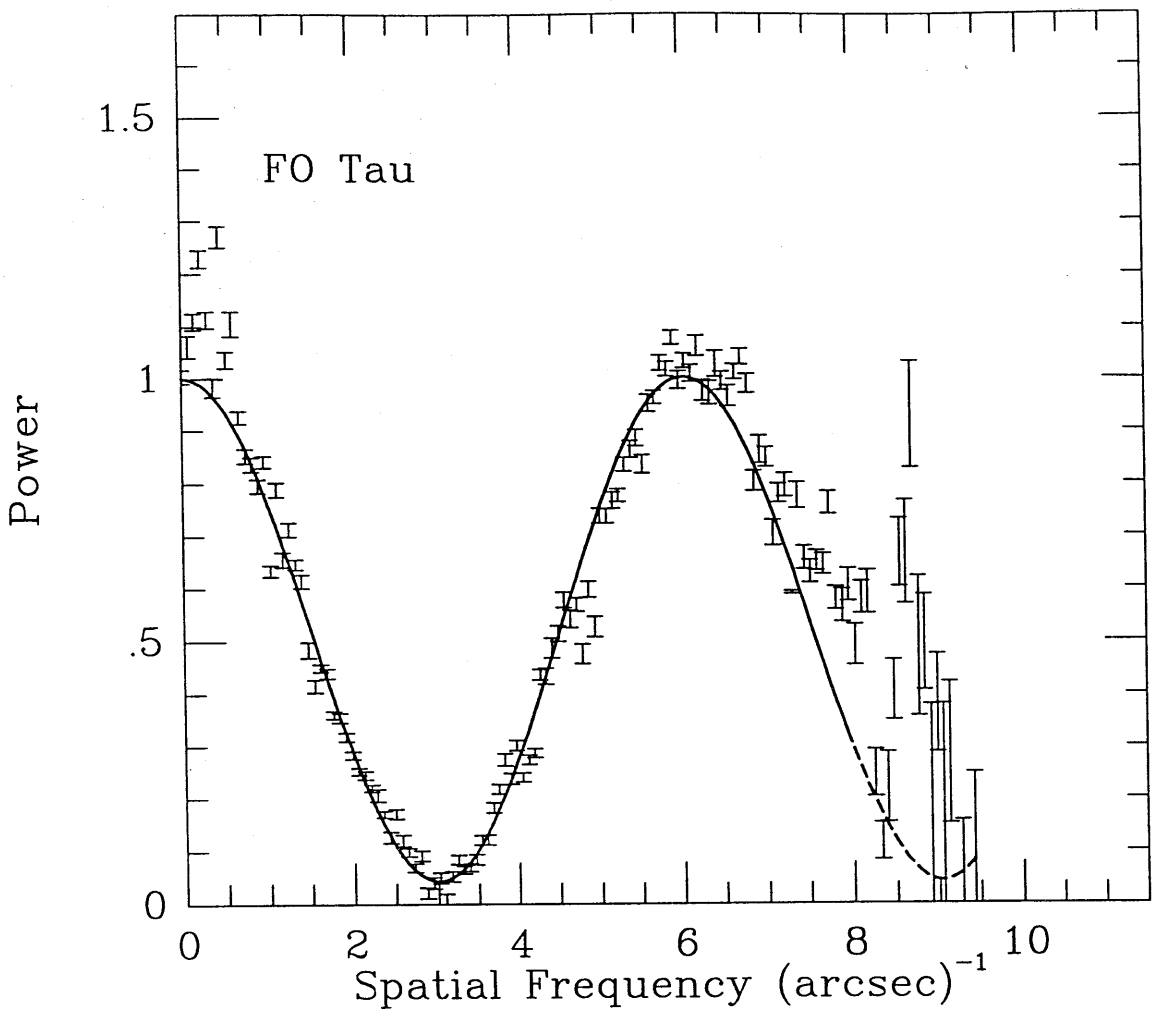

Figure A.18

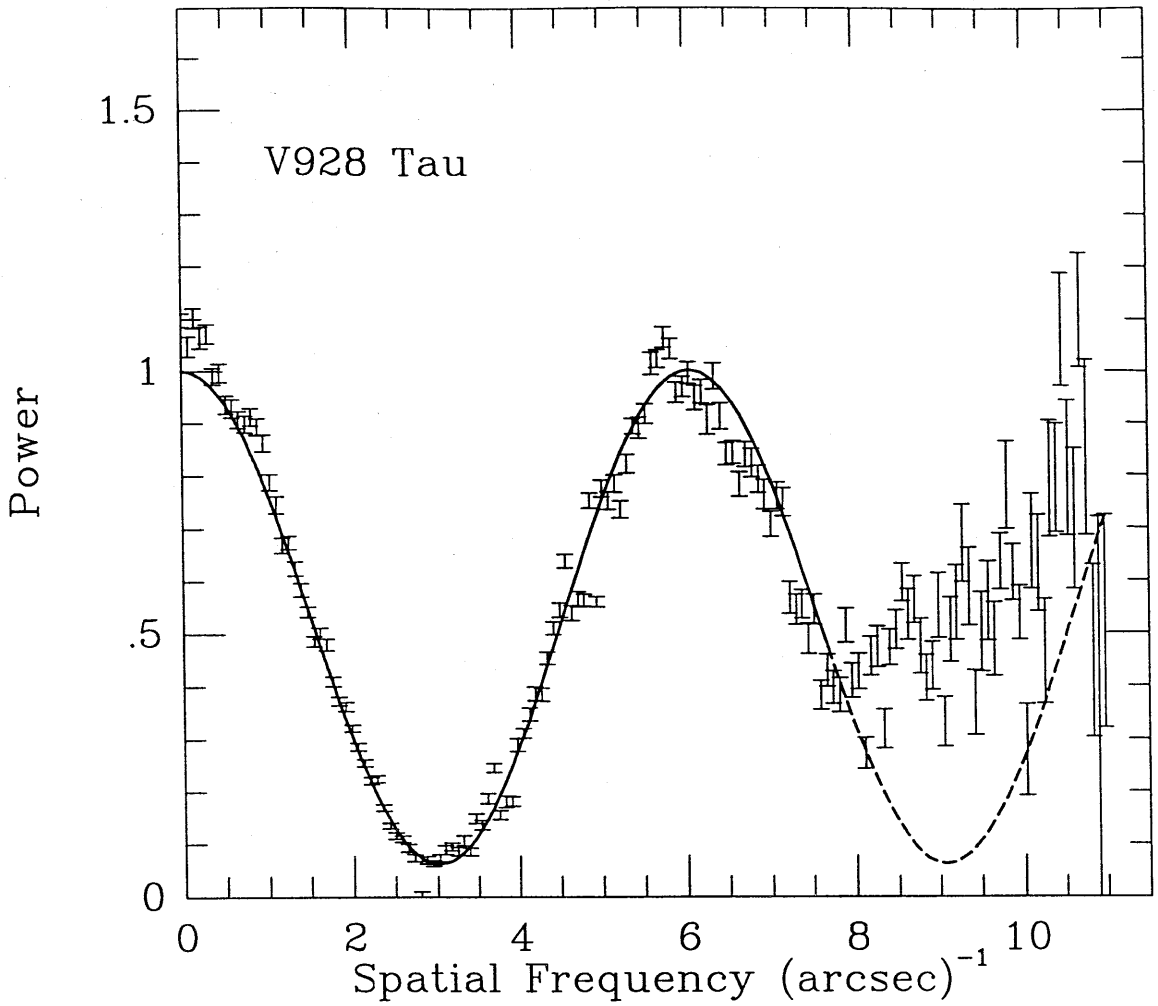

Figure A.19

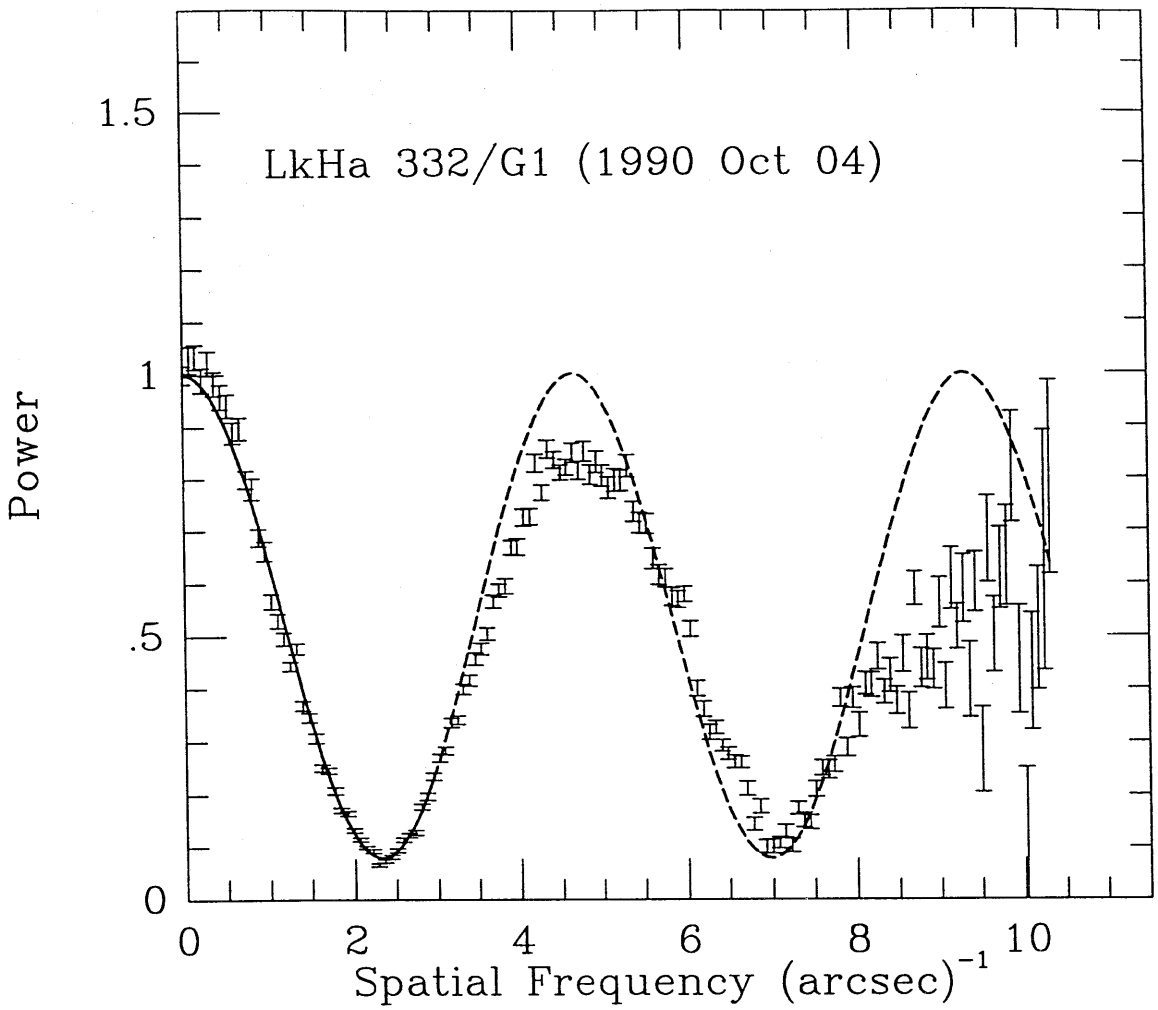
LkHa 332/G1 (1990 Oct 04)
Power
1.5
1
.5
0
0
2
4
6
8
10
Spatial Frequency (arcsec)$^{-1}$

Figure A.20

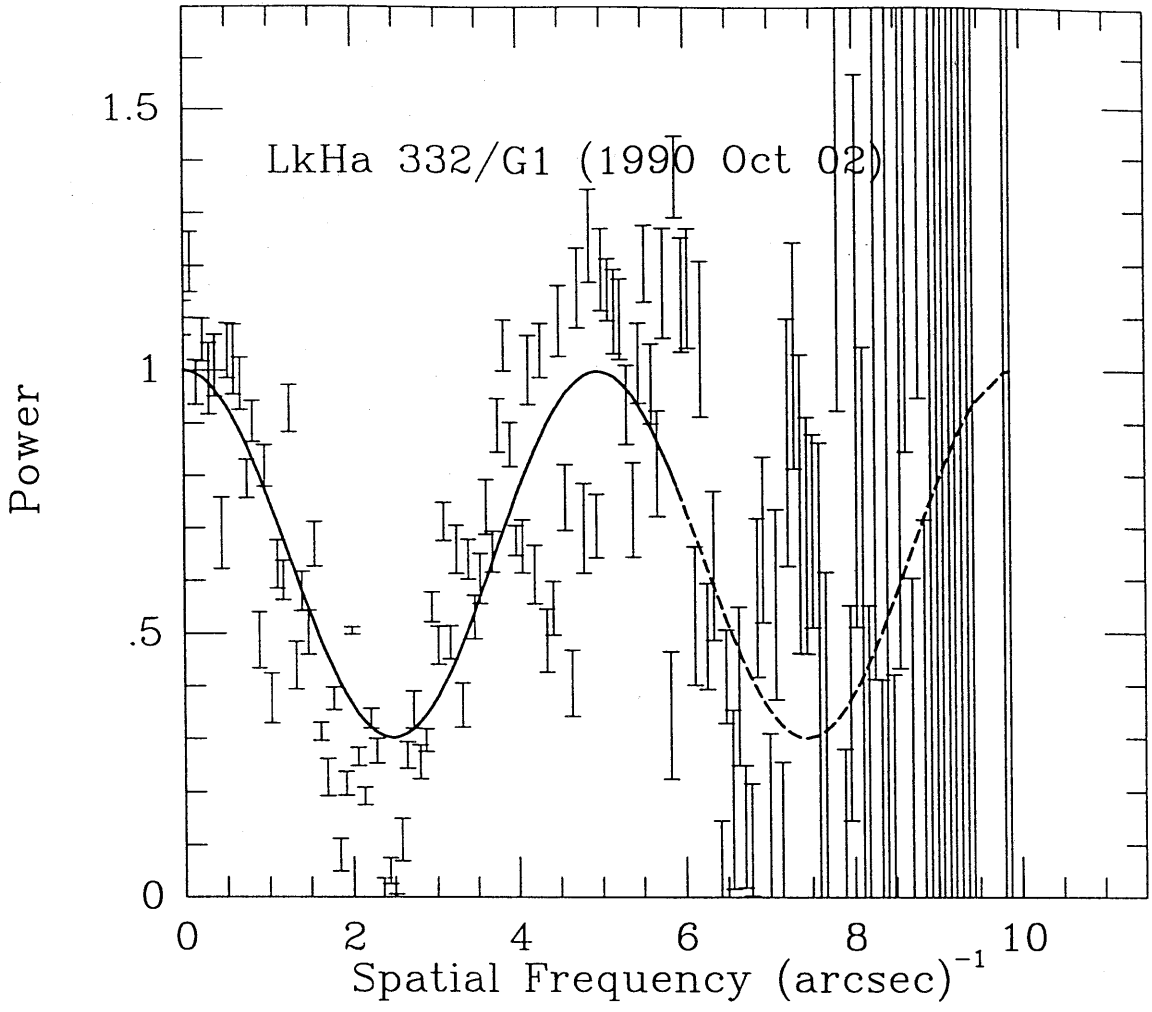
LkHa 332/G1 (1990 Oct 02)
Power
1.5
1
.5
0
0
2
4
6
8
10
Spatial Frequency (arcsec)$^{-1}$

Figure A.21

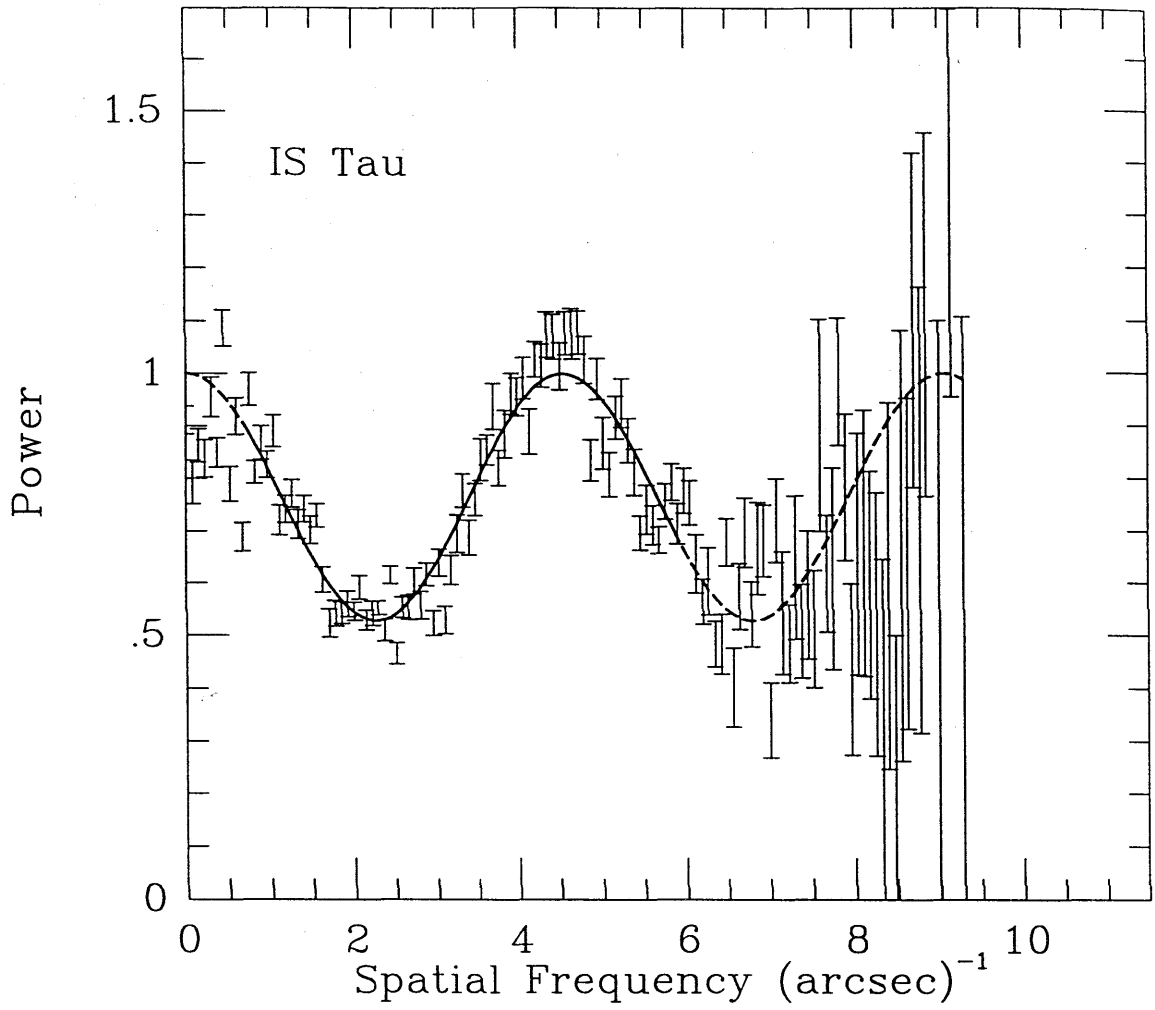

Figure A.22

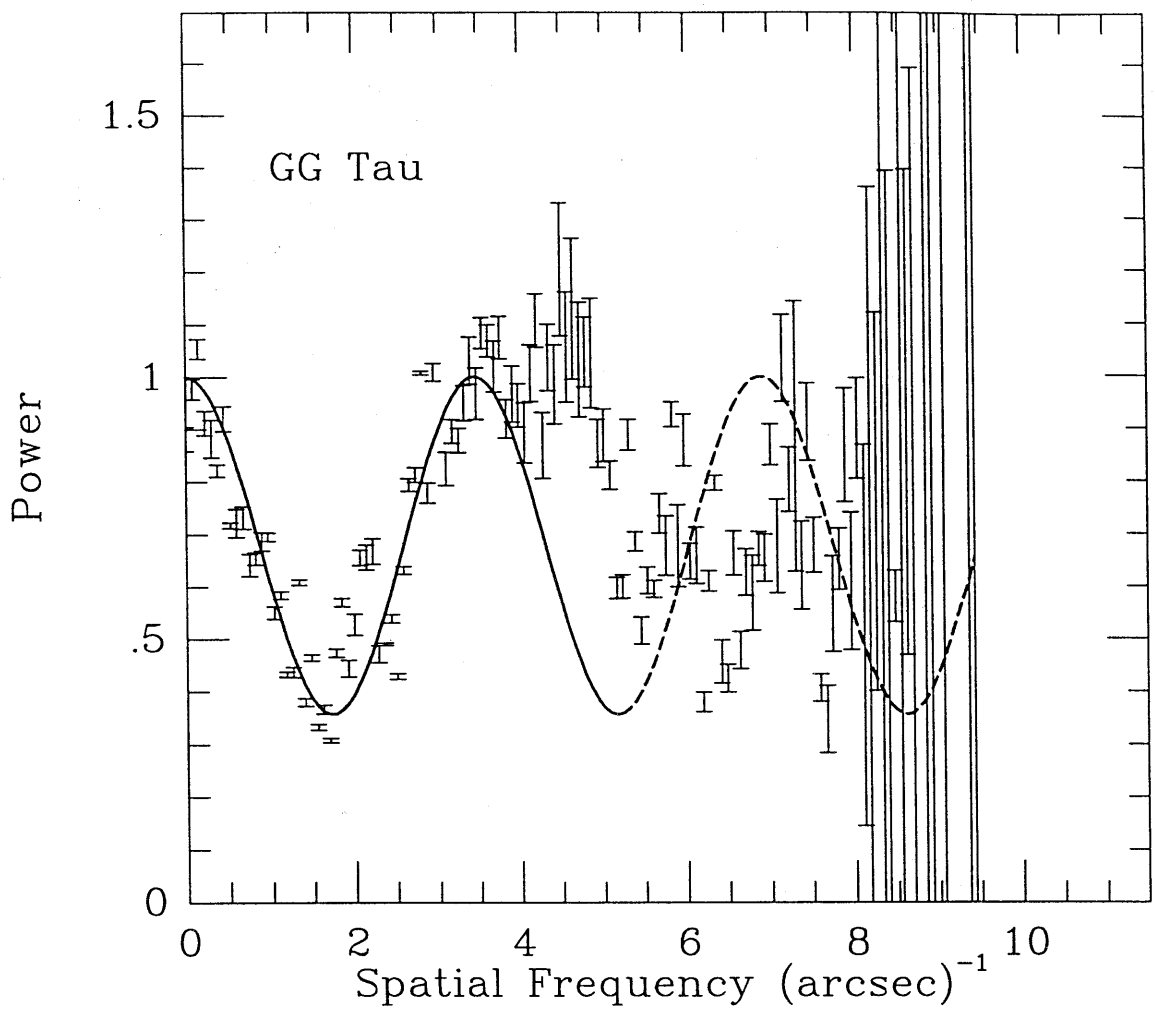

Figure A.23

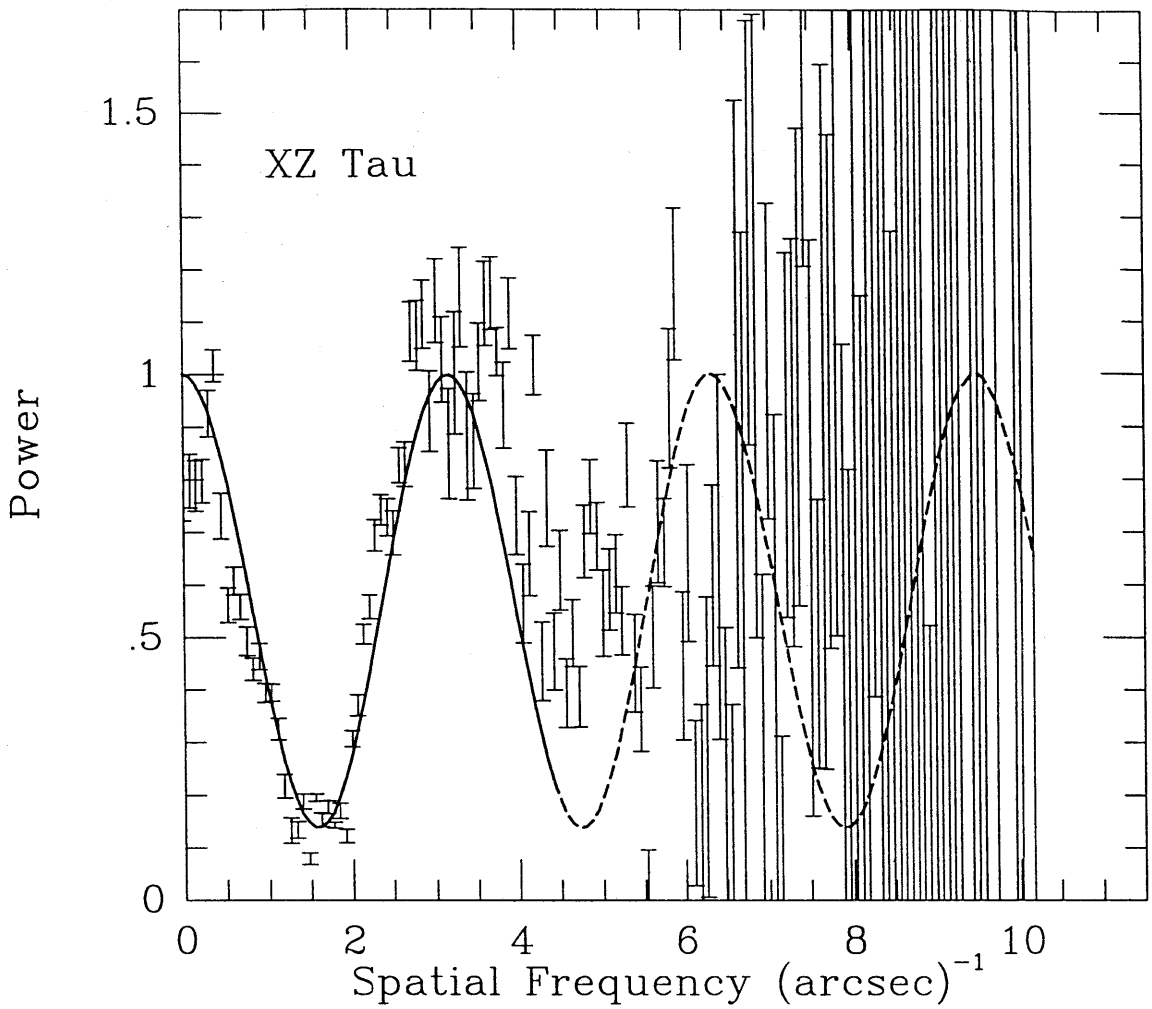

Figure A.24

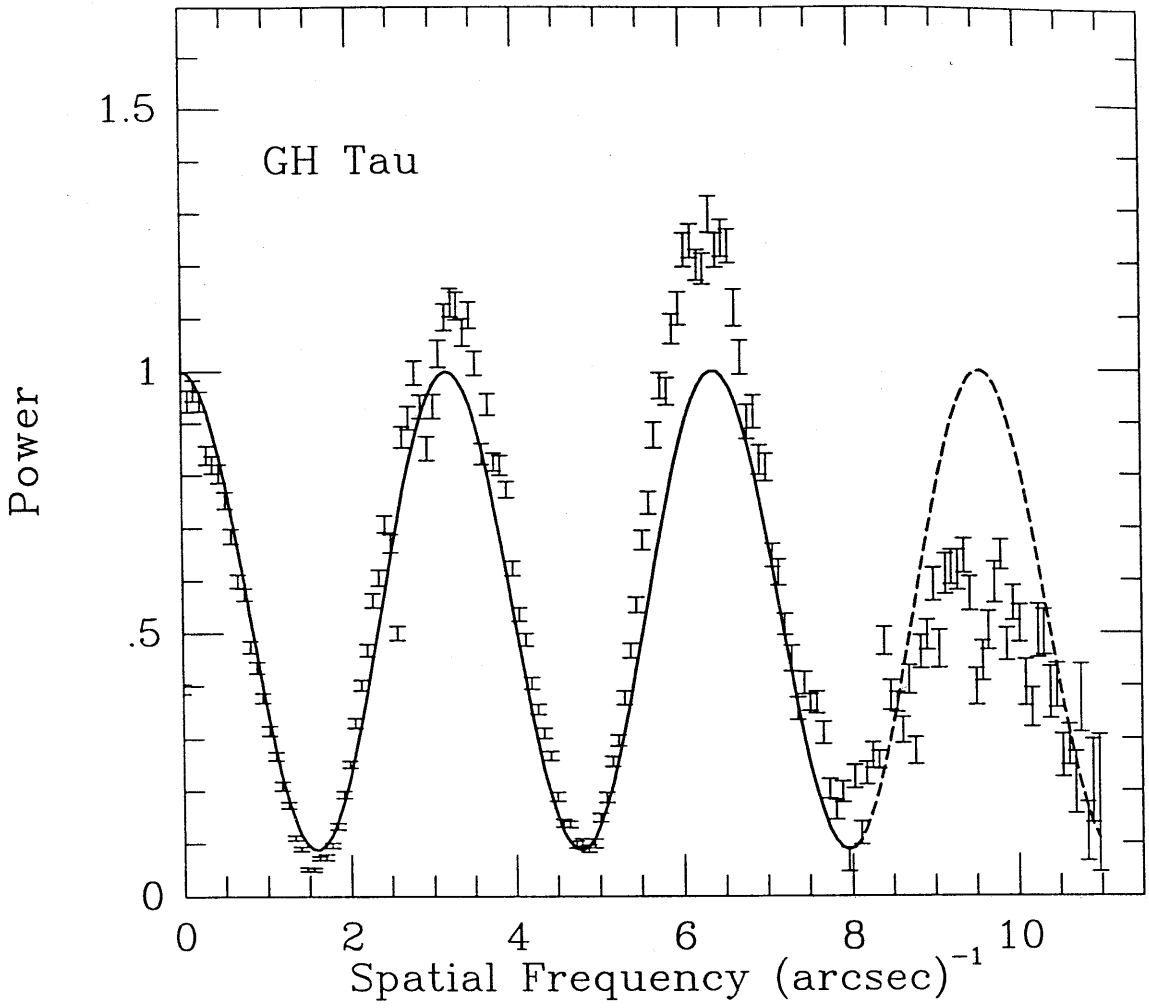

Figure A.25

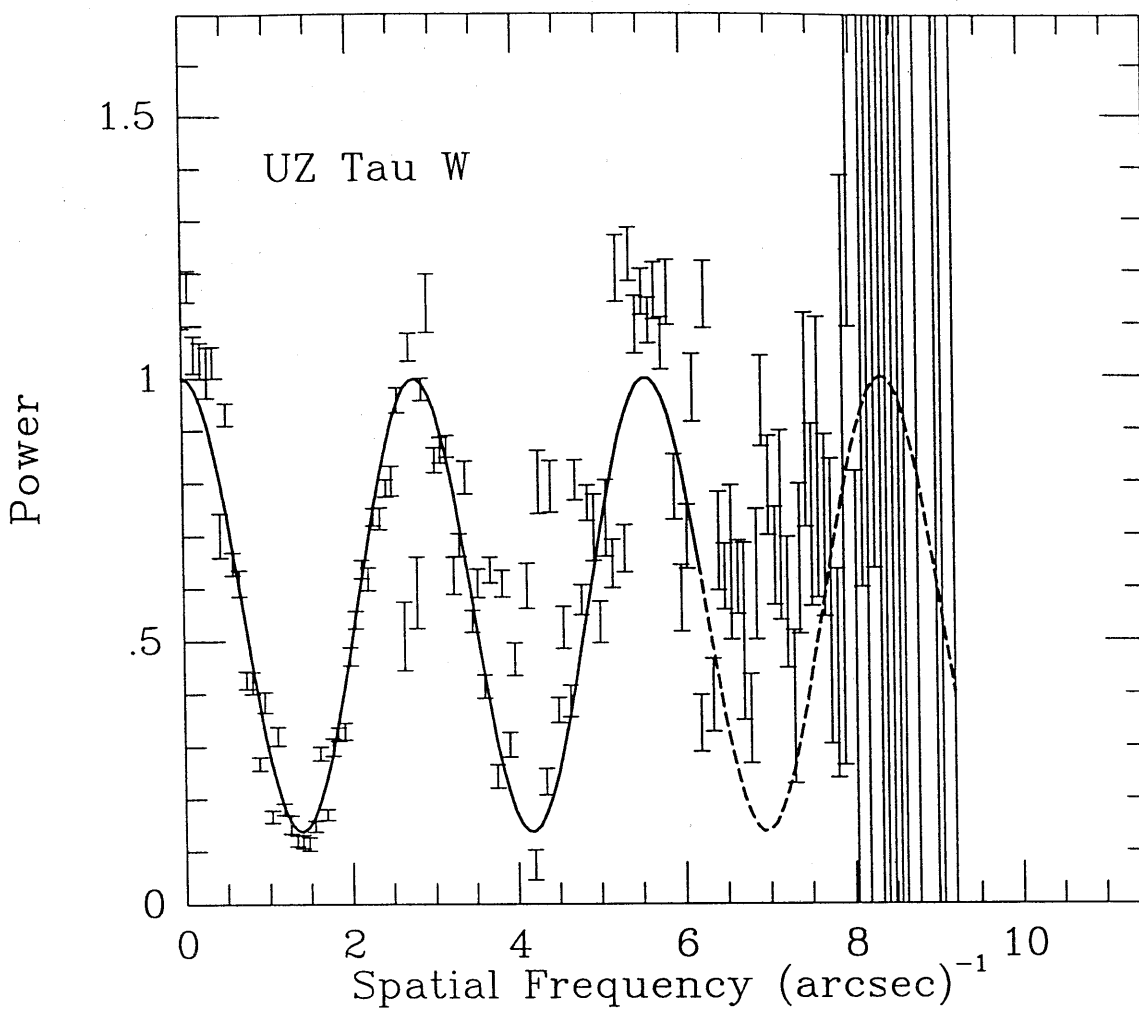

Figure A.26

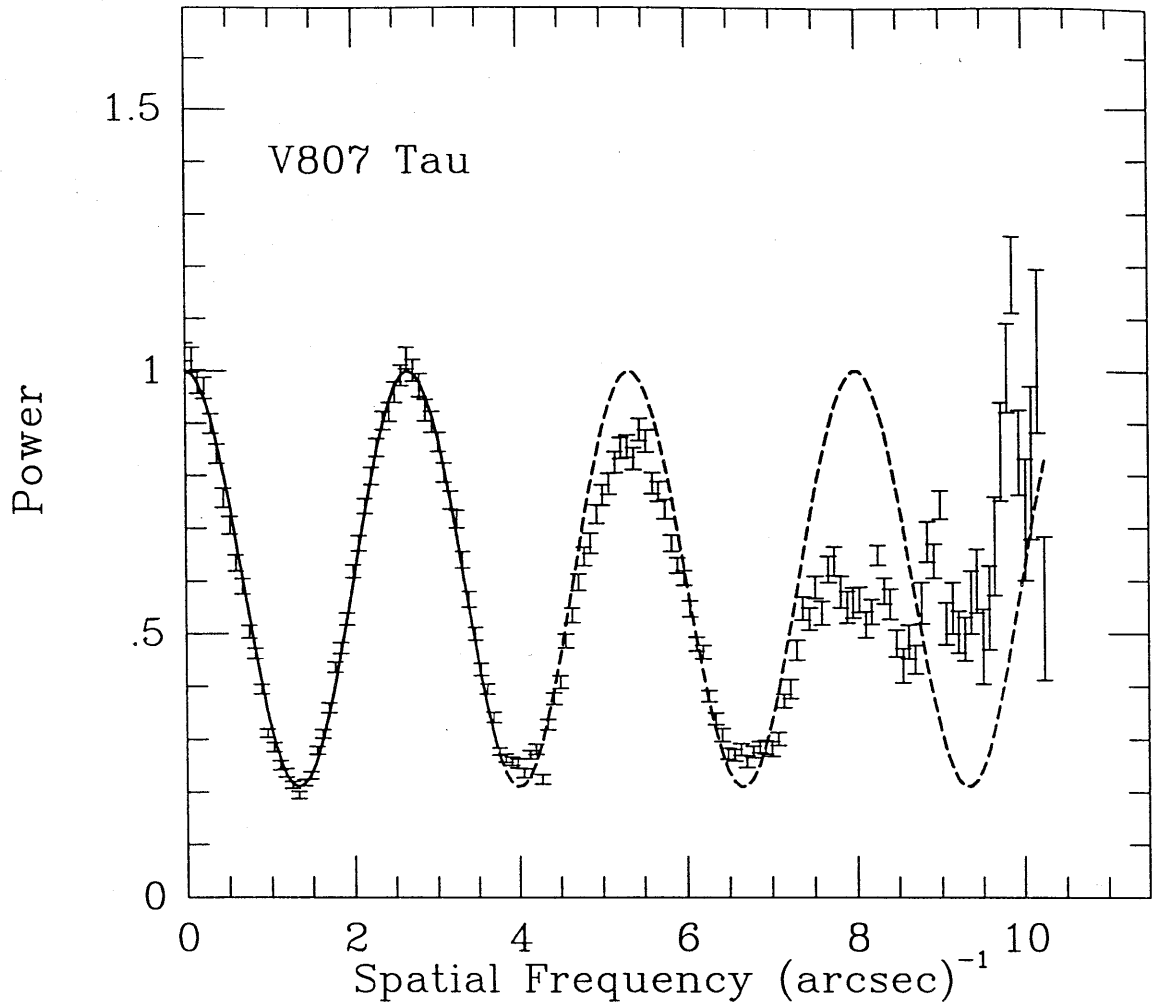

Figure A.27

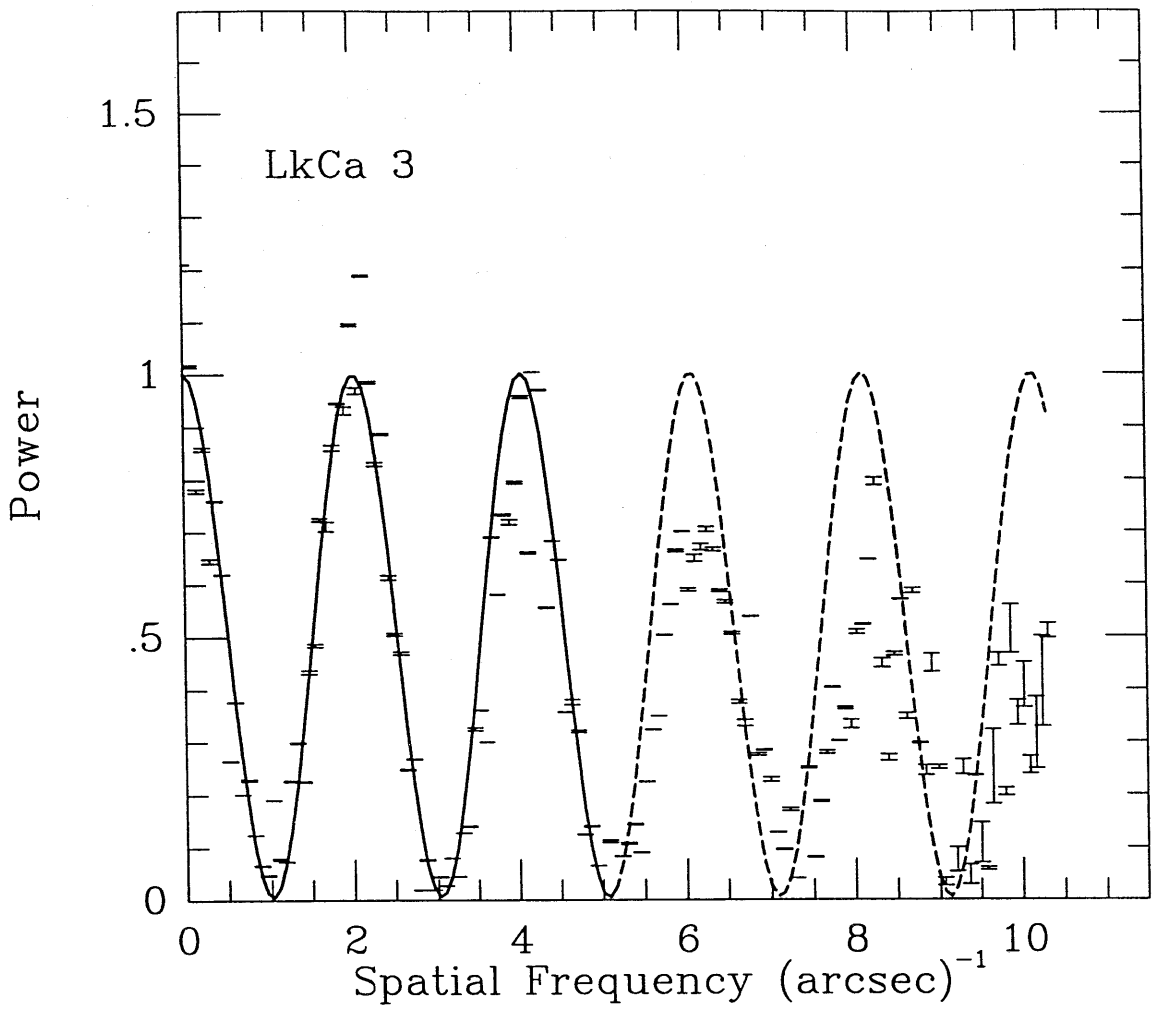

Figure A.28

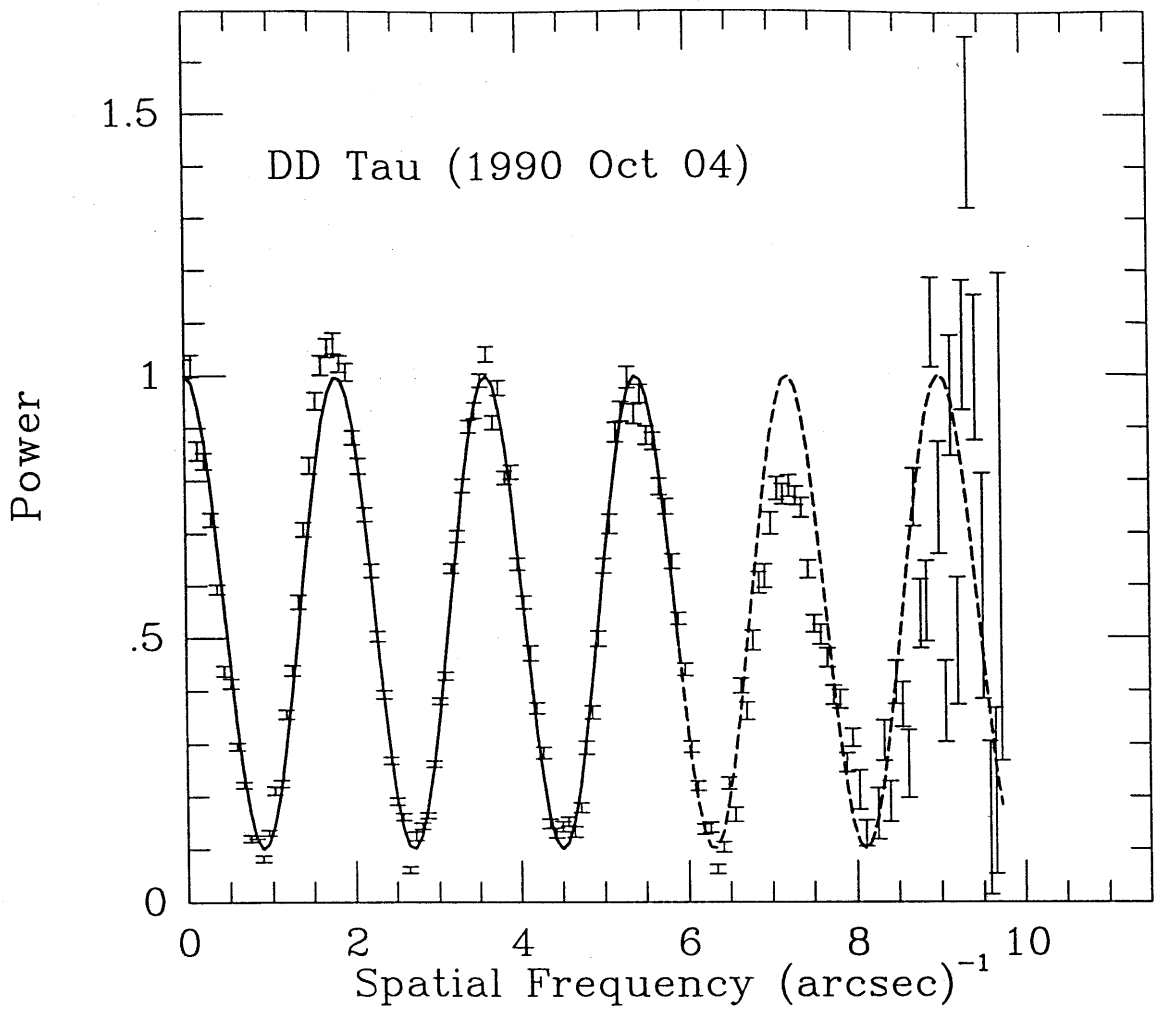
DD Tau (1990 Oct 04)
Power
1.5
1
.5
0
0
2
4
6
8
10
Spatial Frequency (arcsec)$^{-1}$

Figure A.29

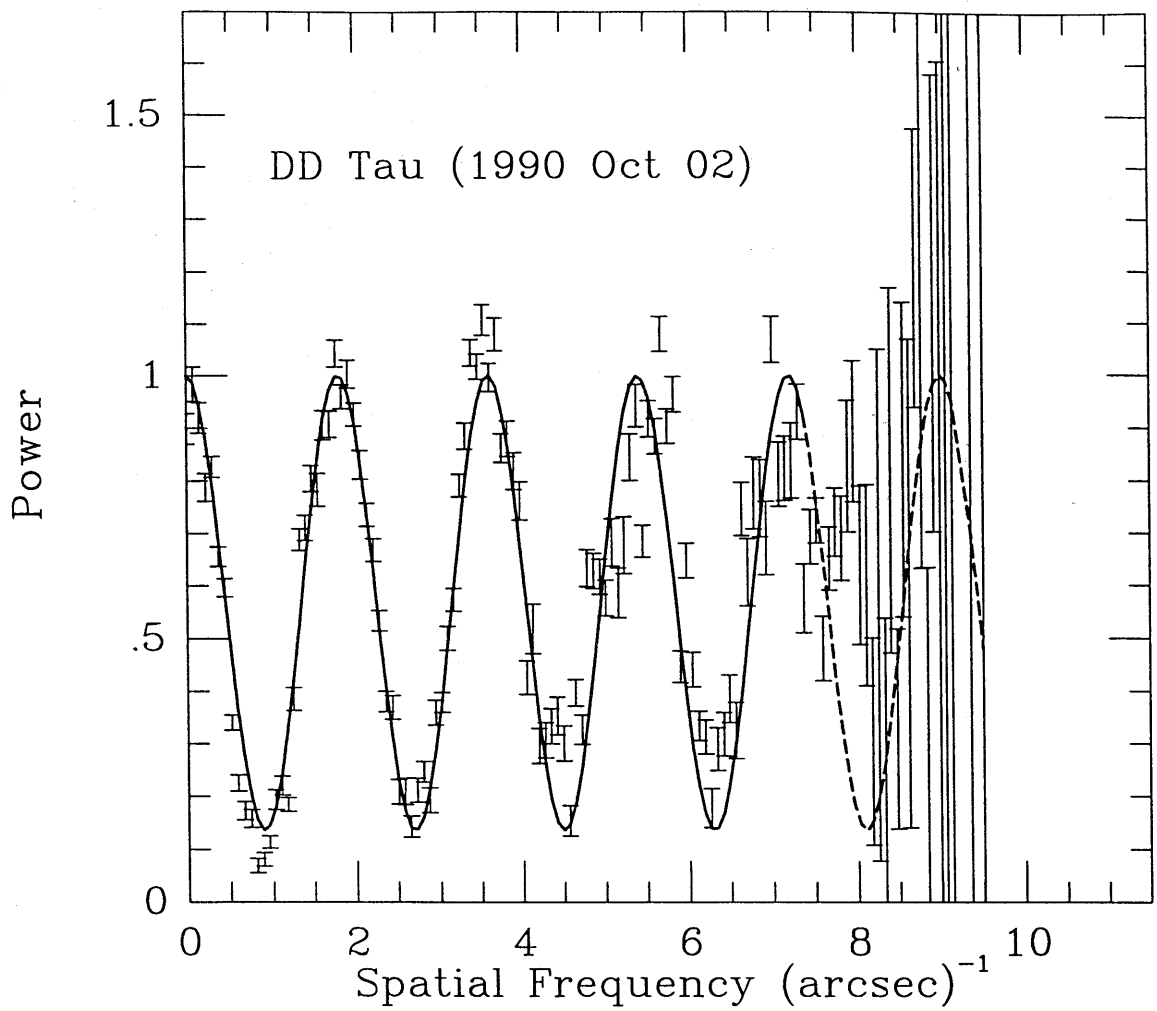
DD Tau (1990 Oct 02)
Power
1.5
1
.5
0
0
2
4
6
8
10
Spatial Frequency (arcsec)$^{-1}$

Figure A.30

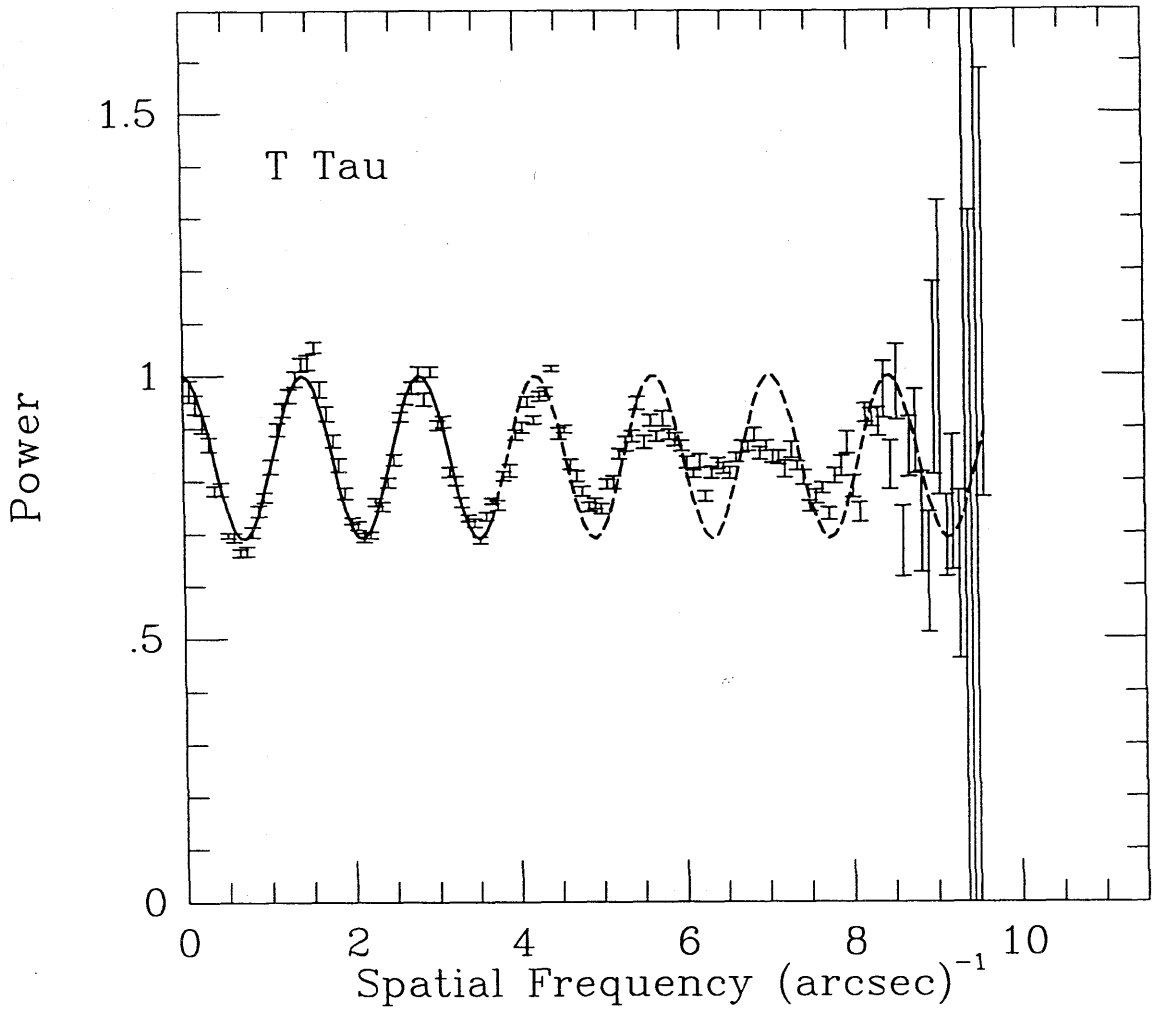

Figure A.31

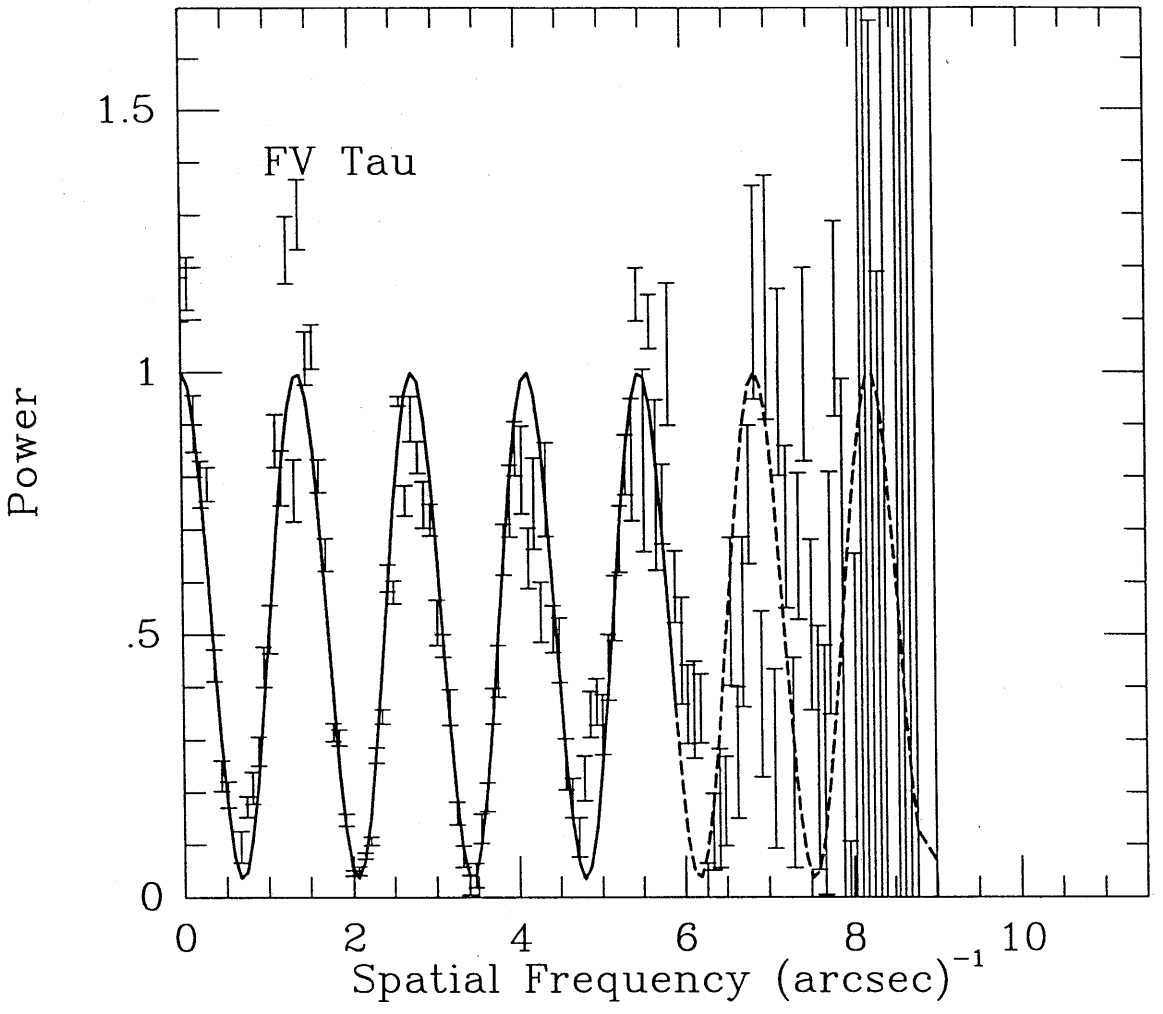

Figure A.32

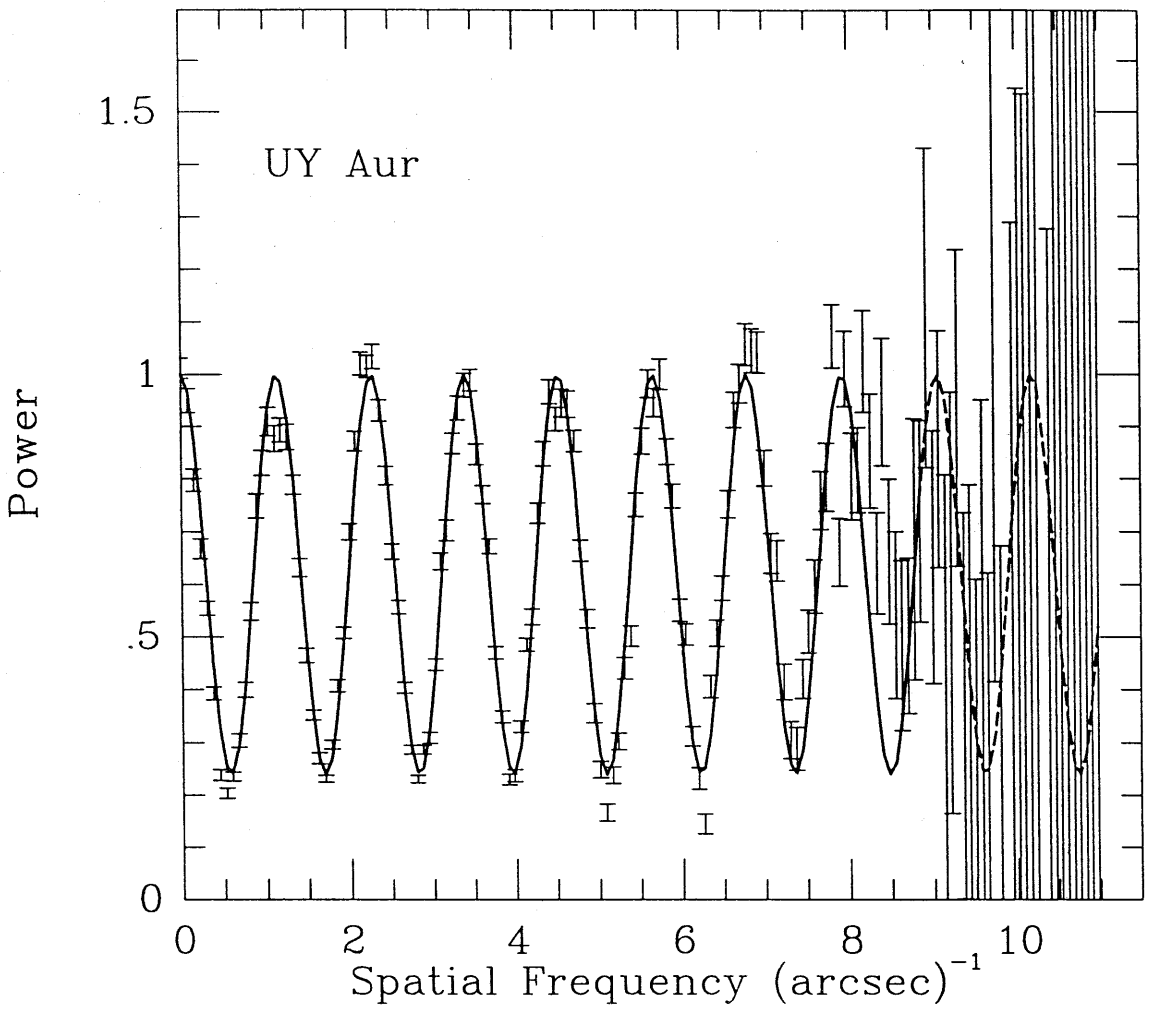

Figure A.33

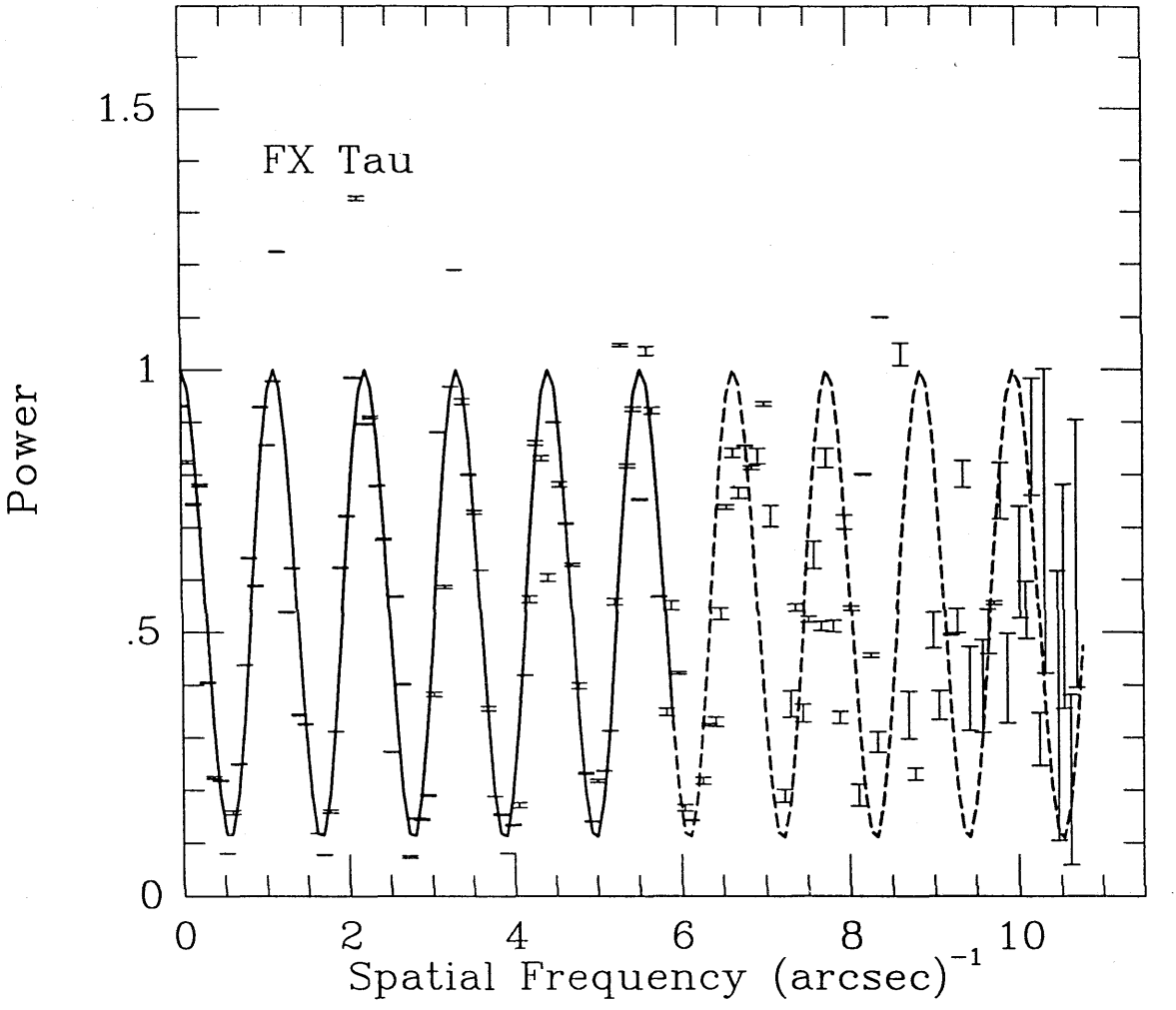

Figure A.34

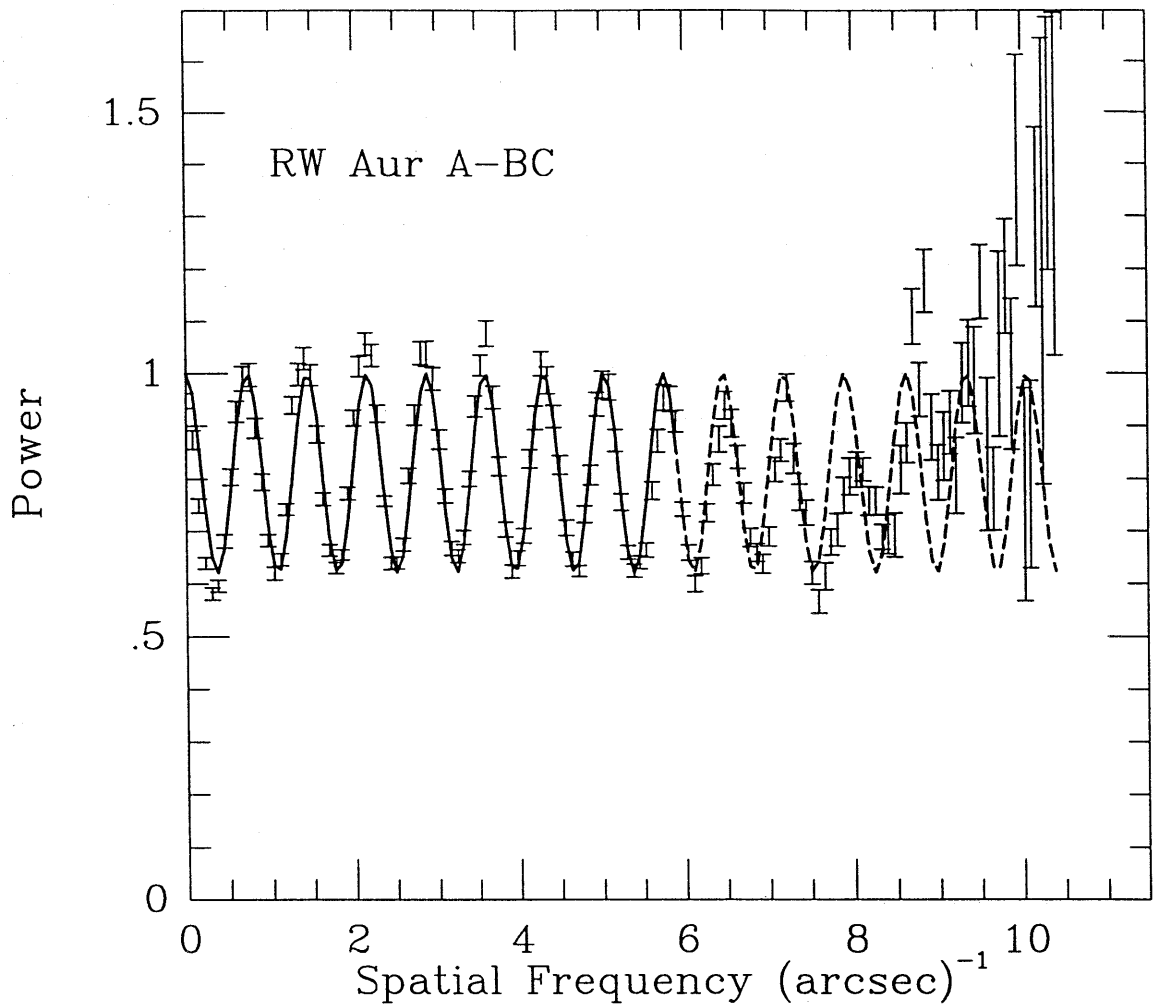

Figure A.35

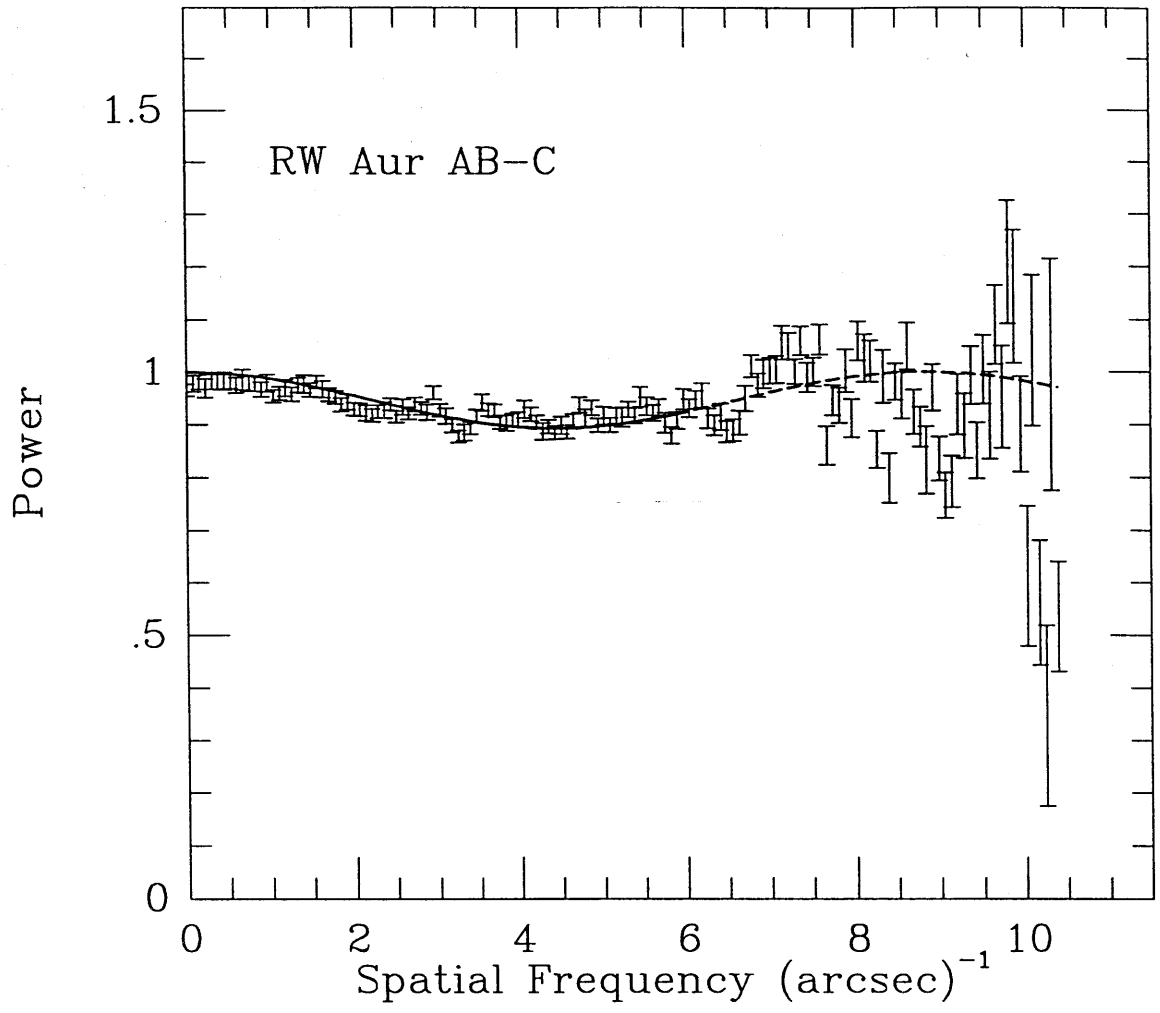

Figure A.36

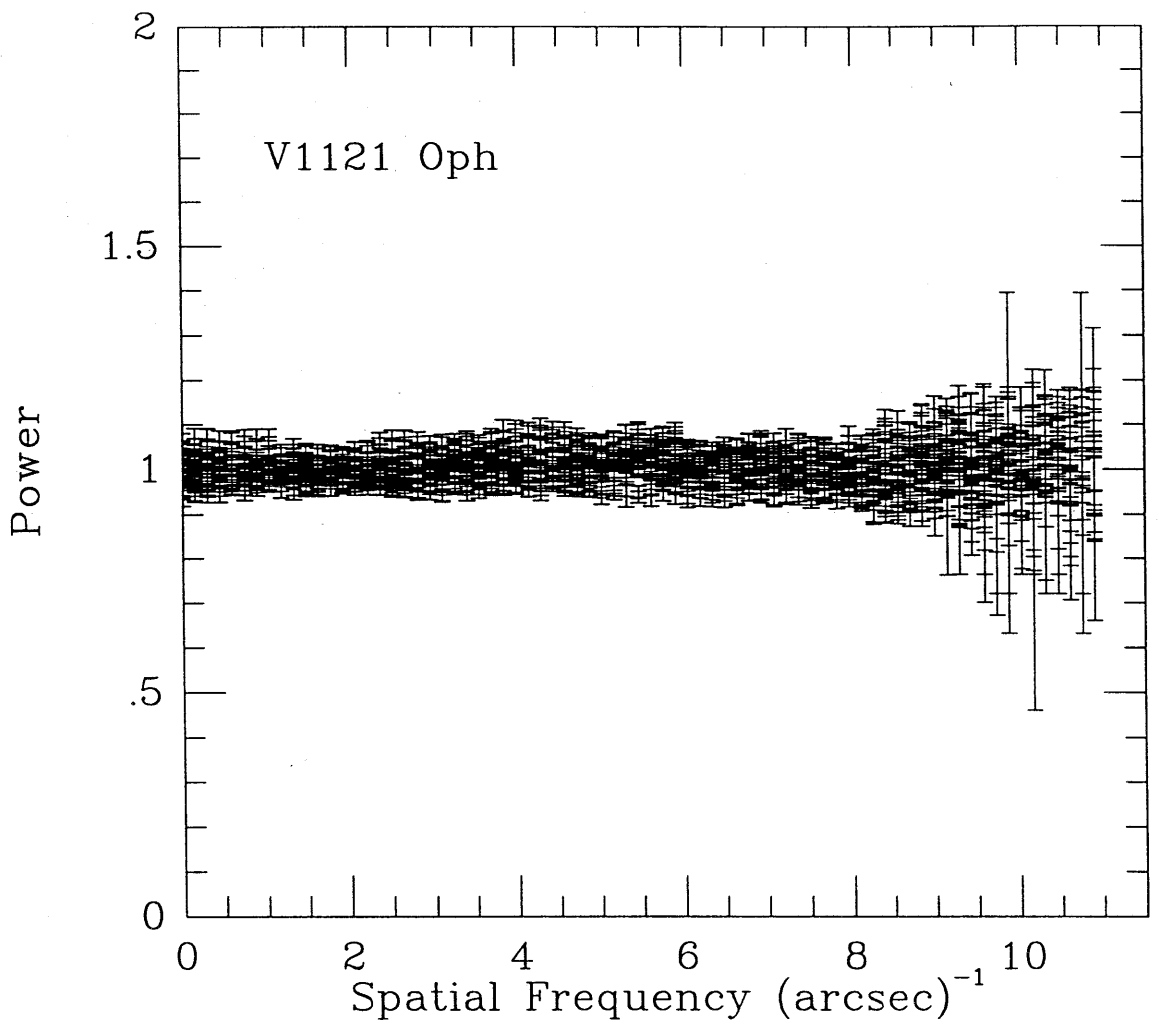

Figure A.37

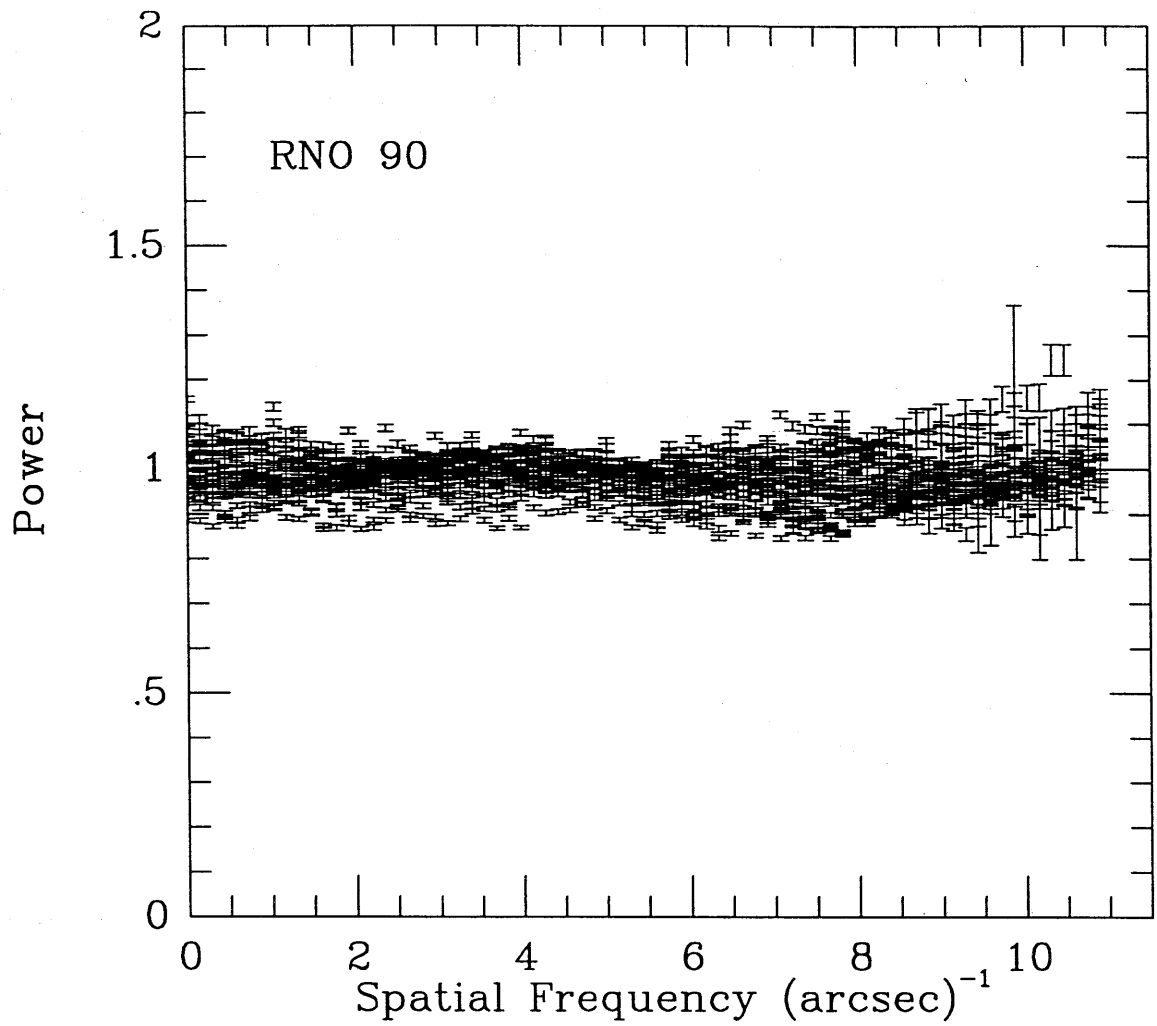

Figure A.38

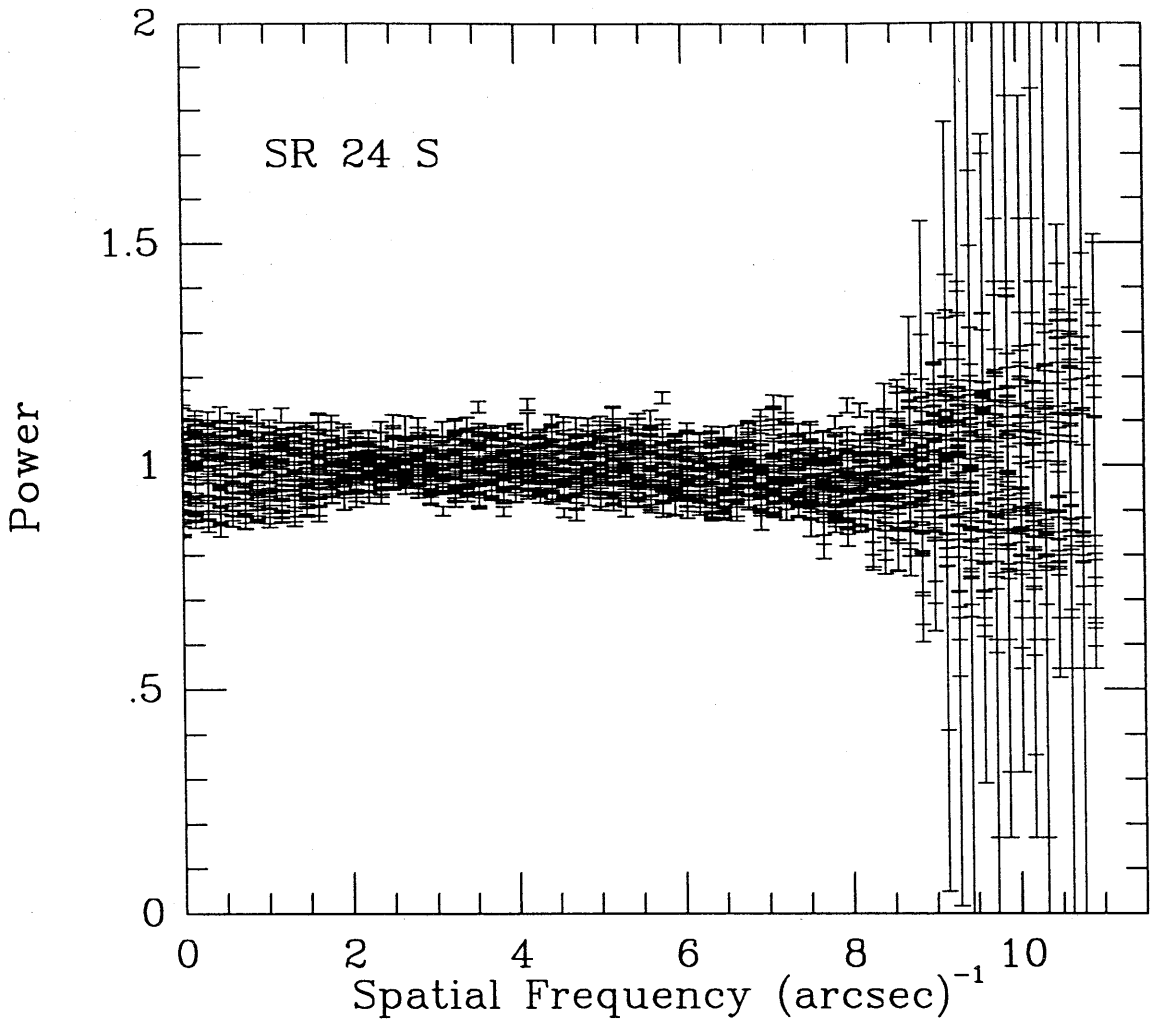

Figure A.39

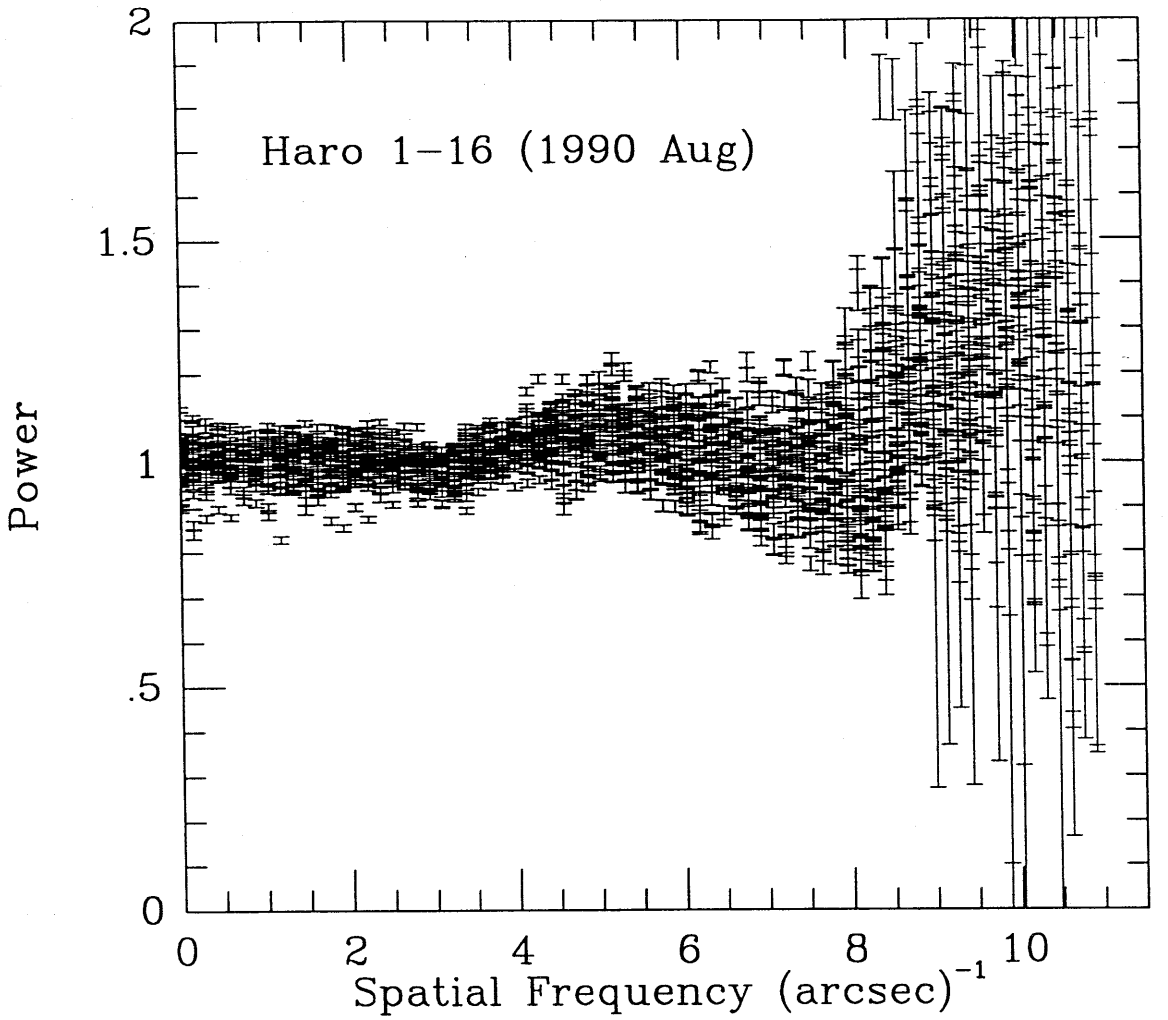
Haro 1−16 (1990 Aug)
Power
2
1.5
1
.5
0
0
2
4
6
8
10
Spatial Frequency (arcsec)$^{-1}$

Figure A.40

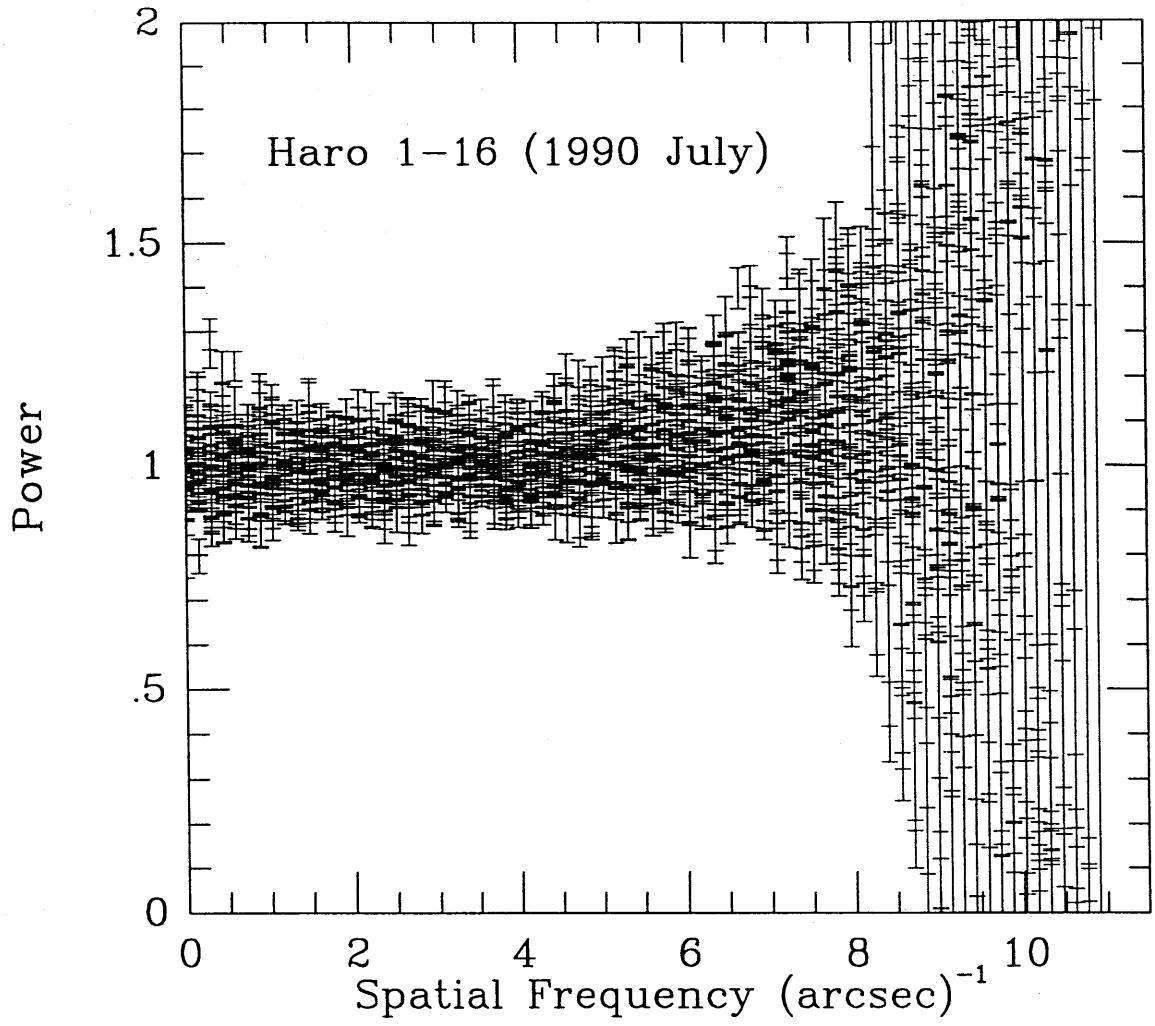
Haro 1−16 (1990 July)
Power
2
1.5
1
.5
0
0
2
4
6
8
10
Spatial Frequency (arcsec)$^{-1}$

Figure A.41

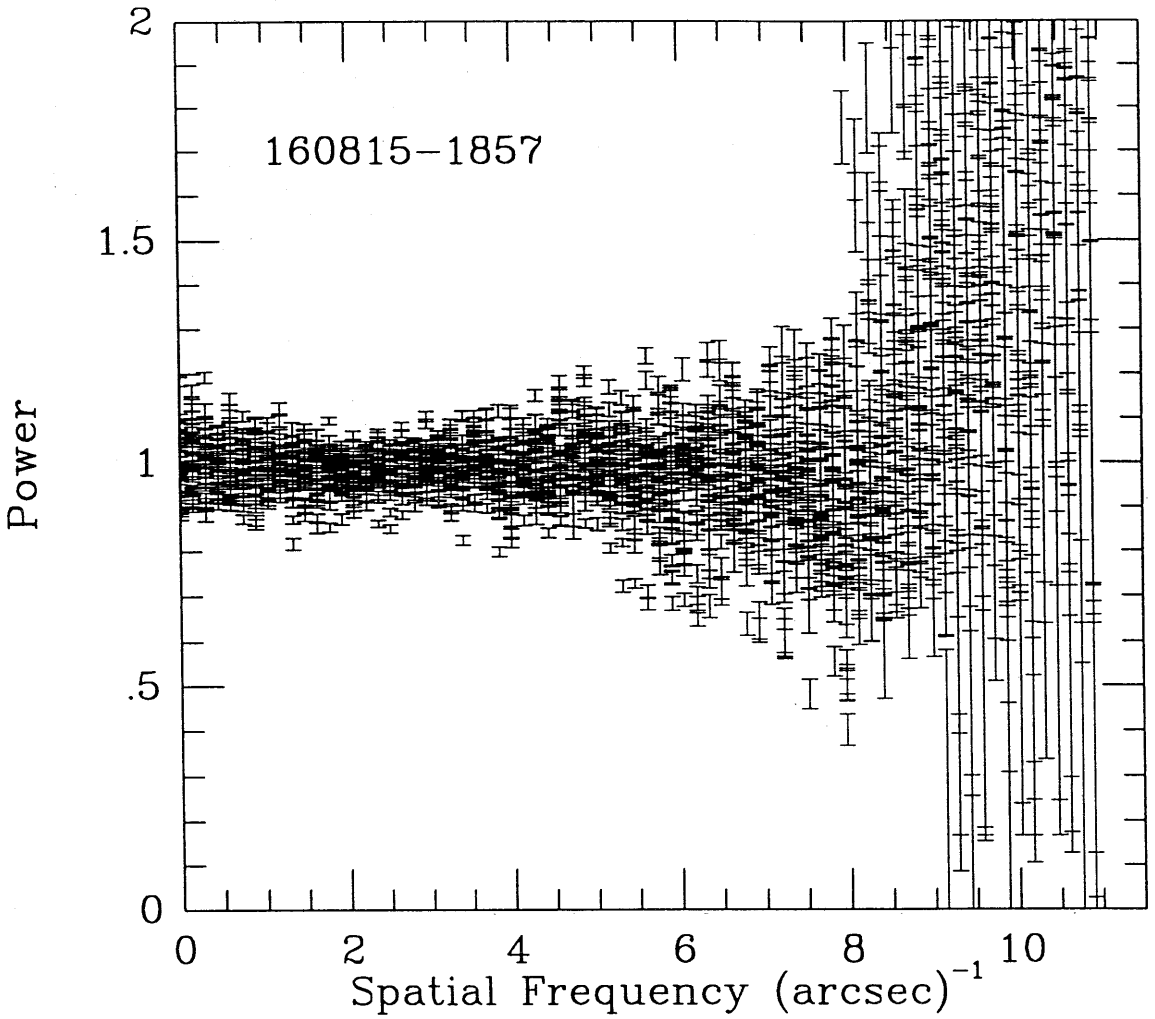
160815−1857
Power
Spatial Frequency (arcsec)$^{-1}$
0
.5
1
1.5
2
0
2
4
6
8
10

Figure A.42

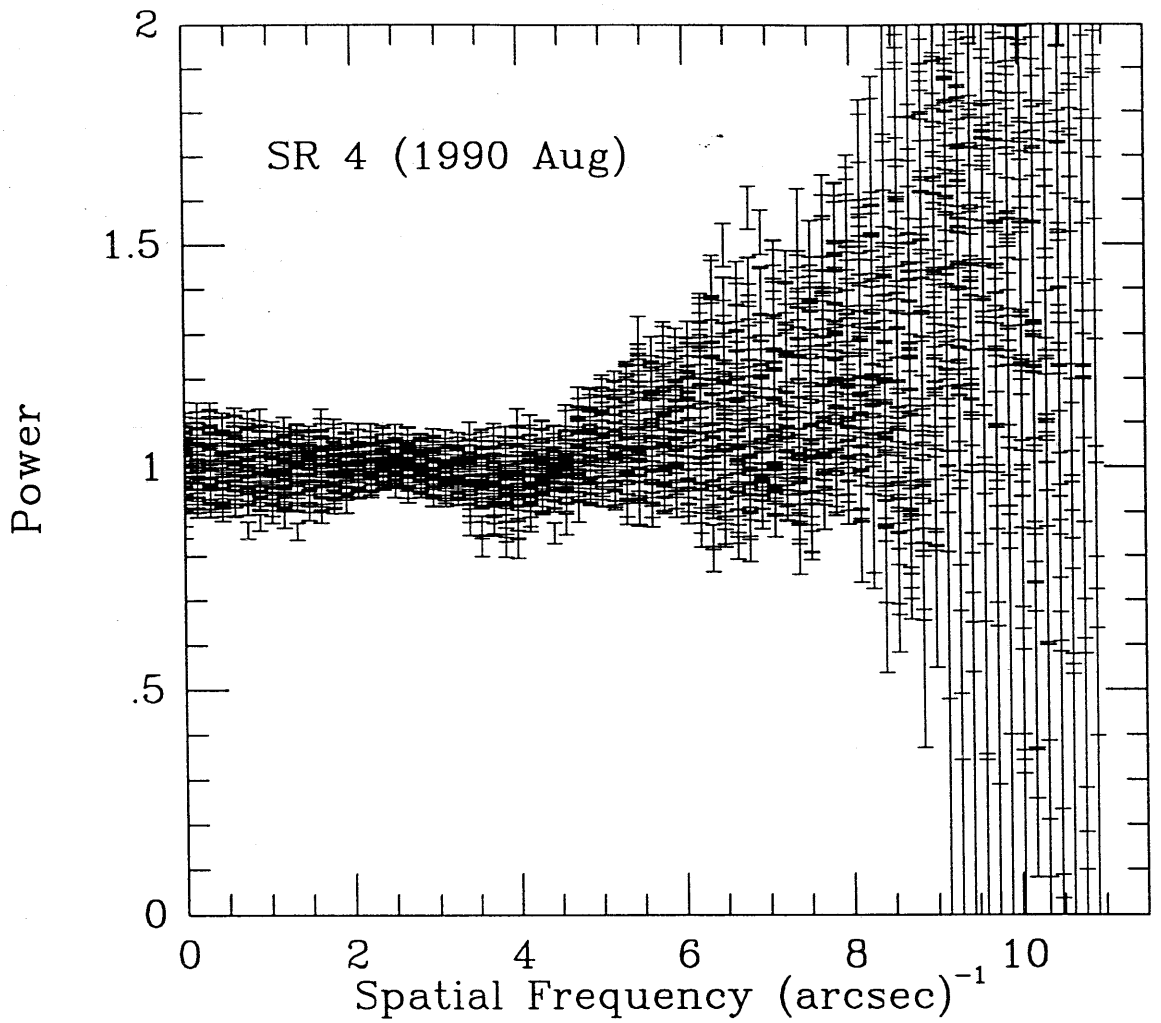
SR 4 (1990 Aug)
Power
2
1.5
1
.5
0
0
2
4
6
8
10
Spatial Frequency (arcsec)$^{-1}$

Figure A.43

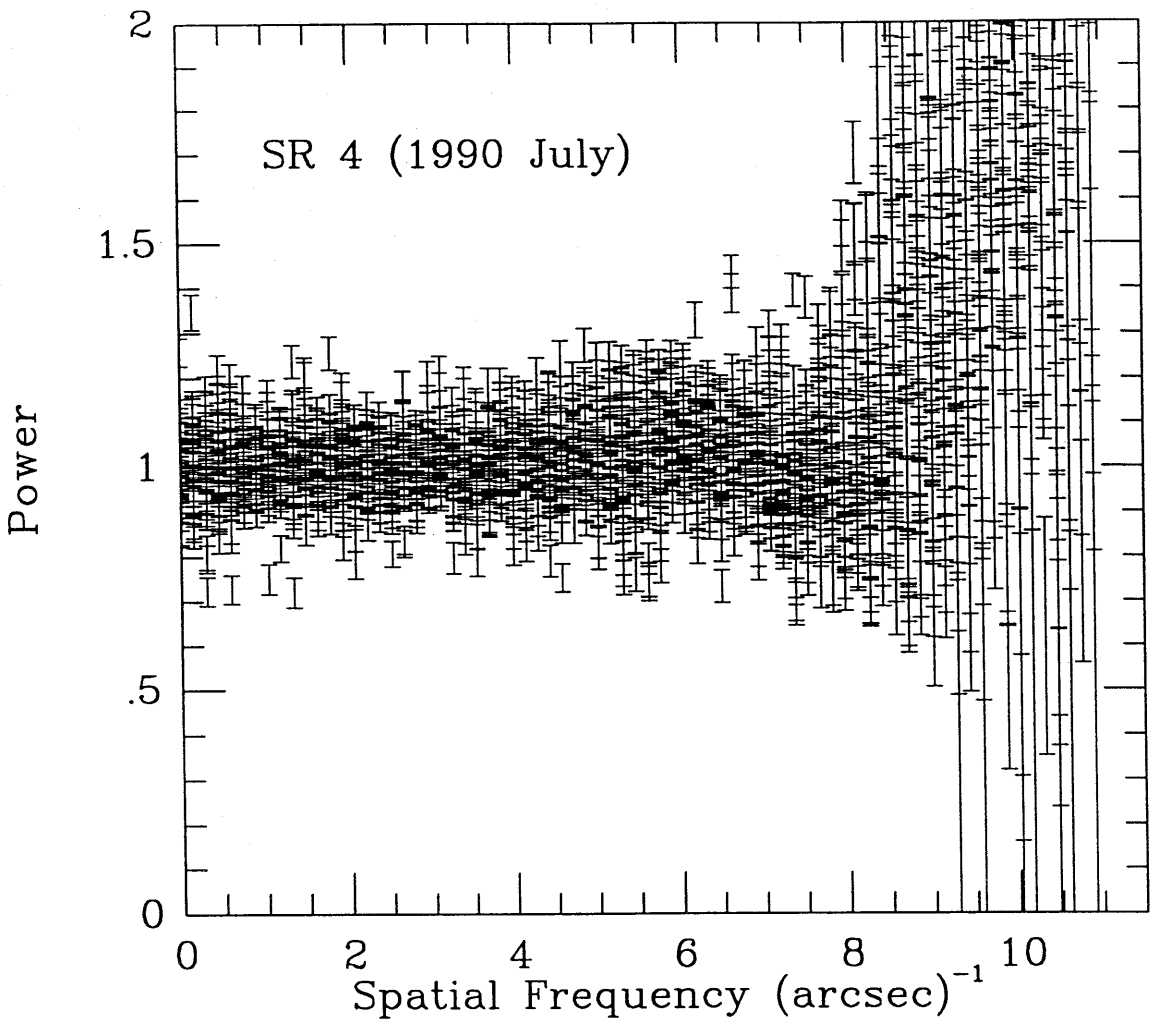
SR 4 (1990 July)
Power
2
1.5
1
.5
0
0
2
4
6
8
10
Spatial Frequency (arcsec)$^{-1}$

Figure A.44

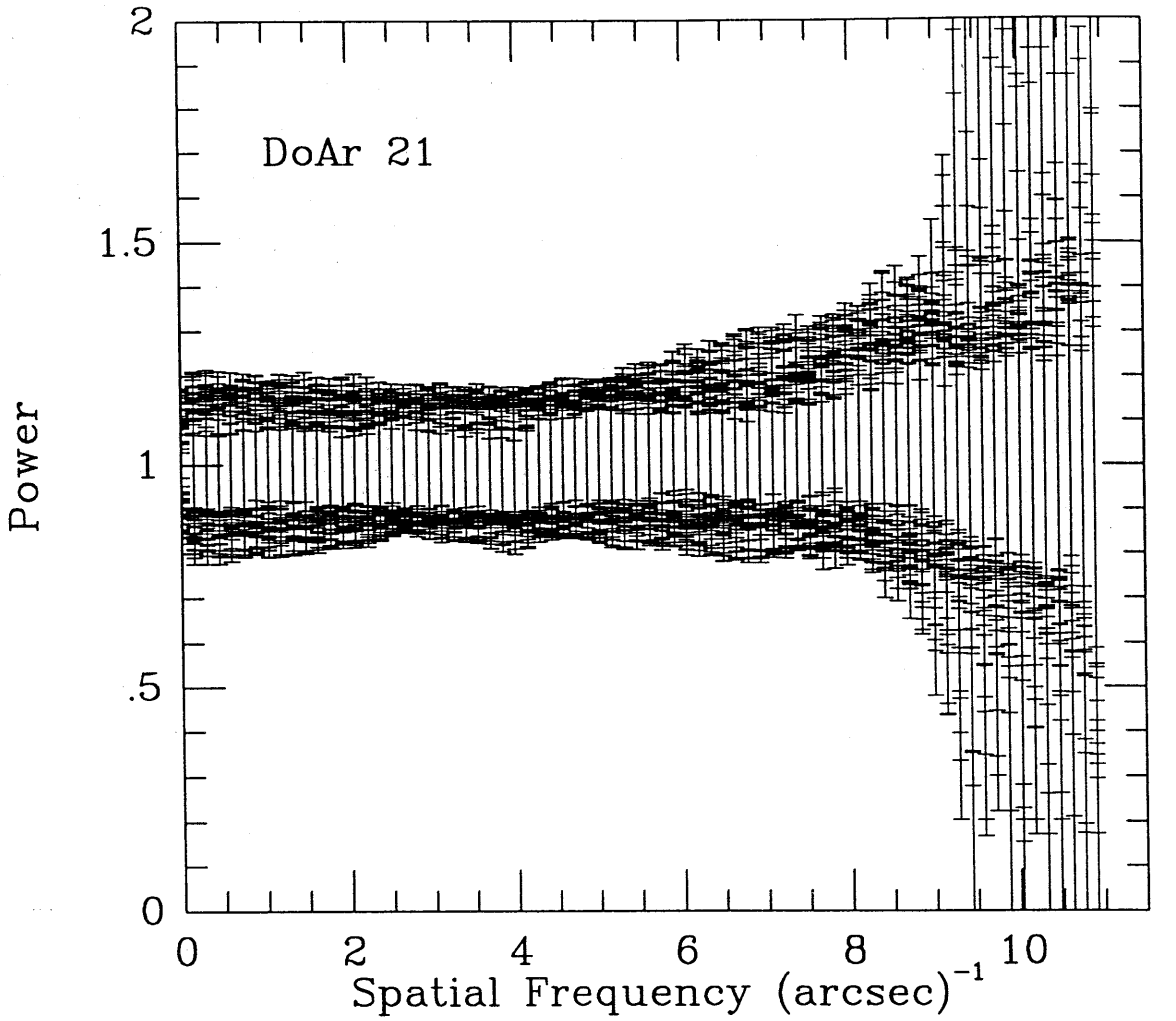

Figure A.45

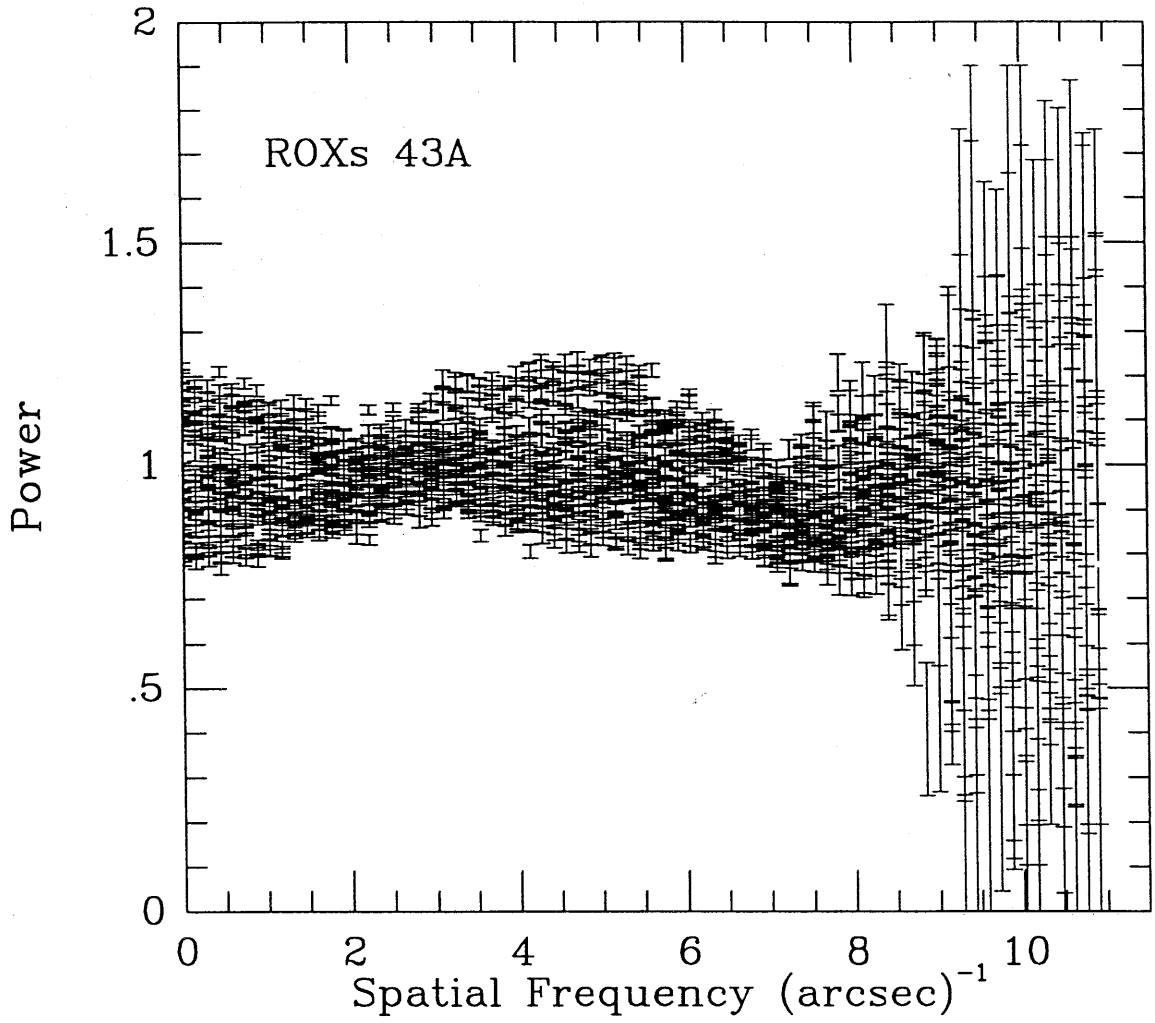

Figure A.46

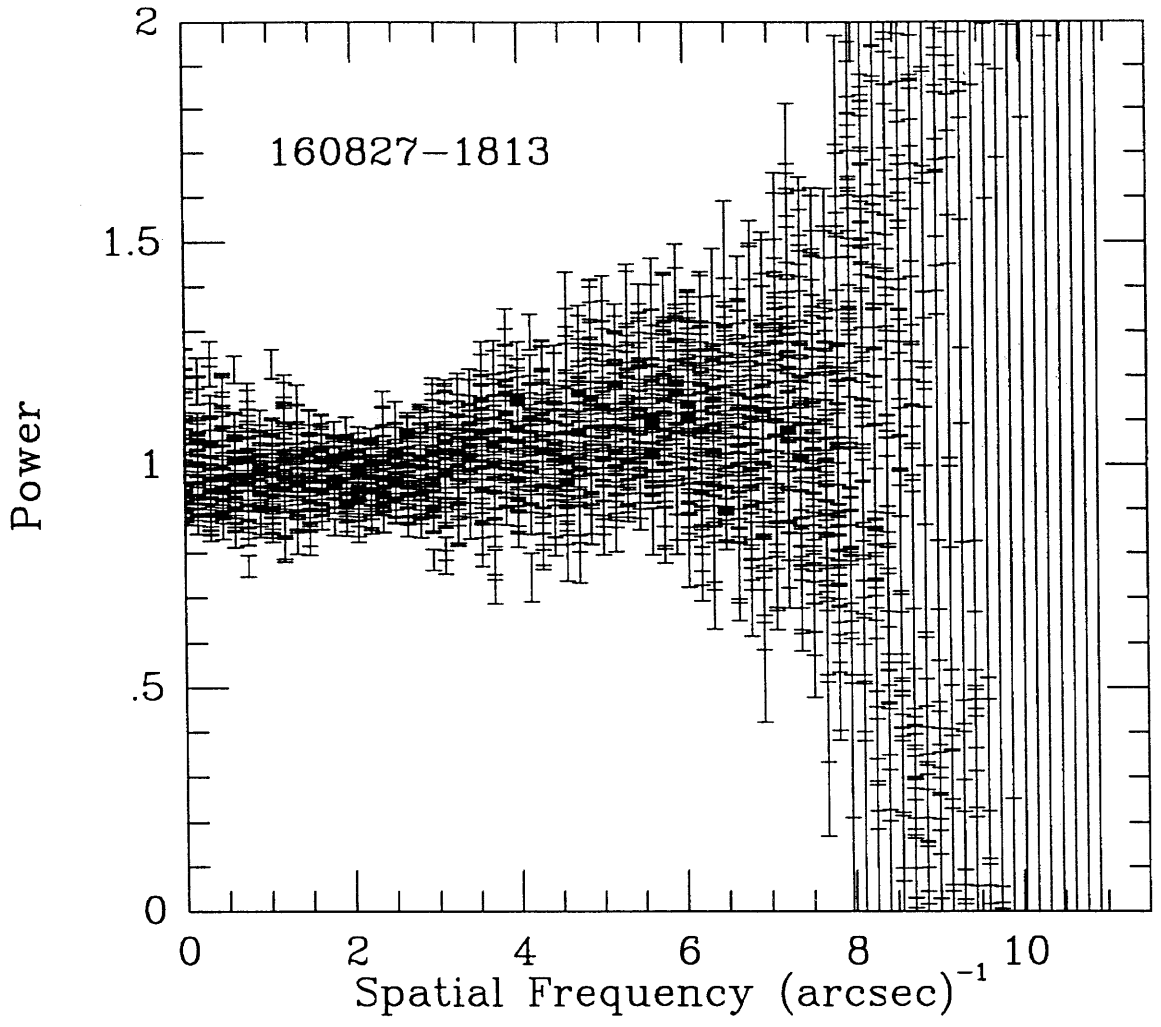
160827−1813
Power
Spatial Frequency (arcsec)$^{-1}$
0
.5
1
1.5
2
0
2
4
6
8
10

Figure A.47

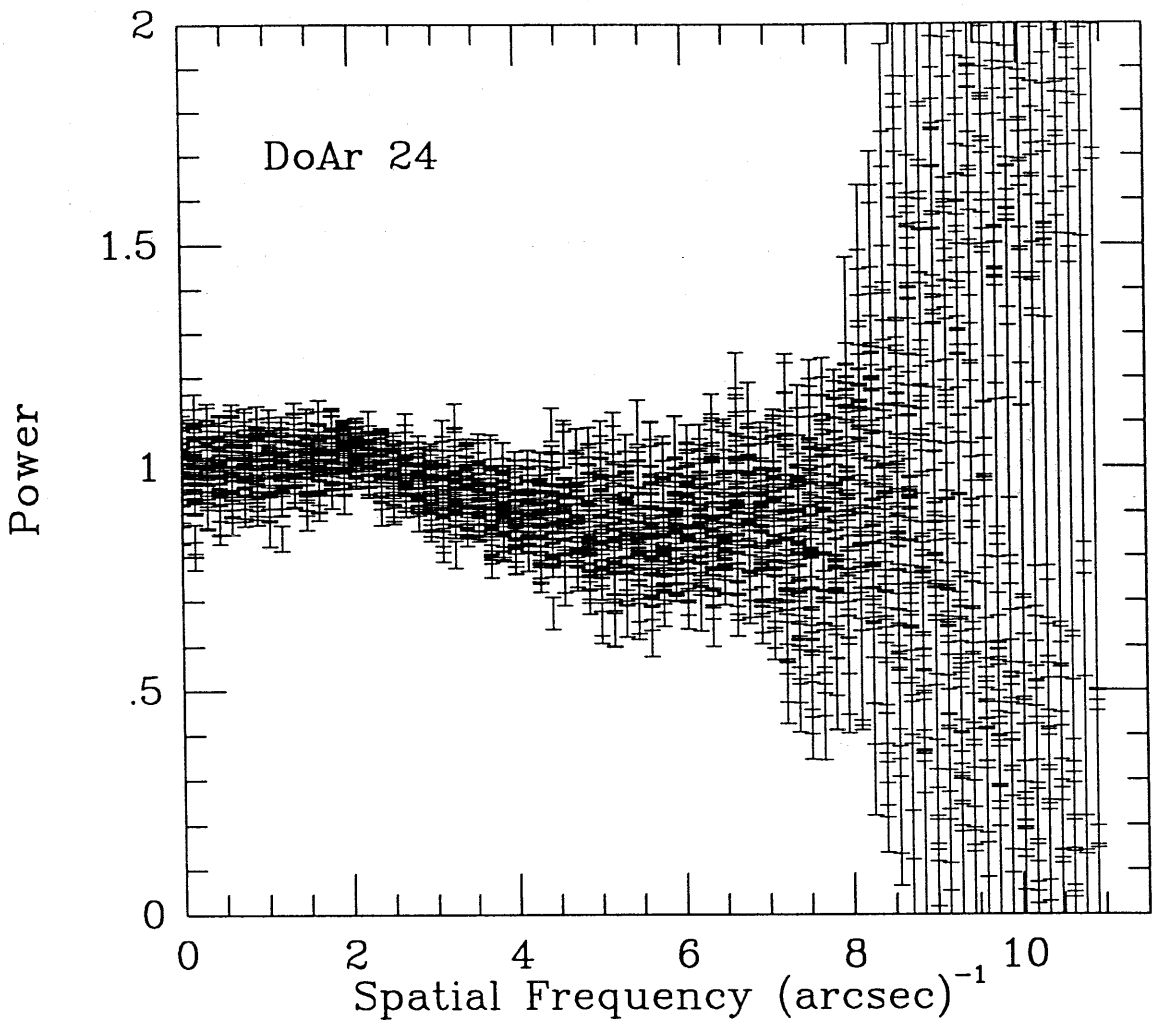

Figure A.48

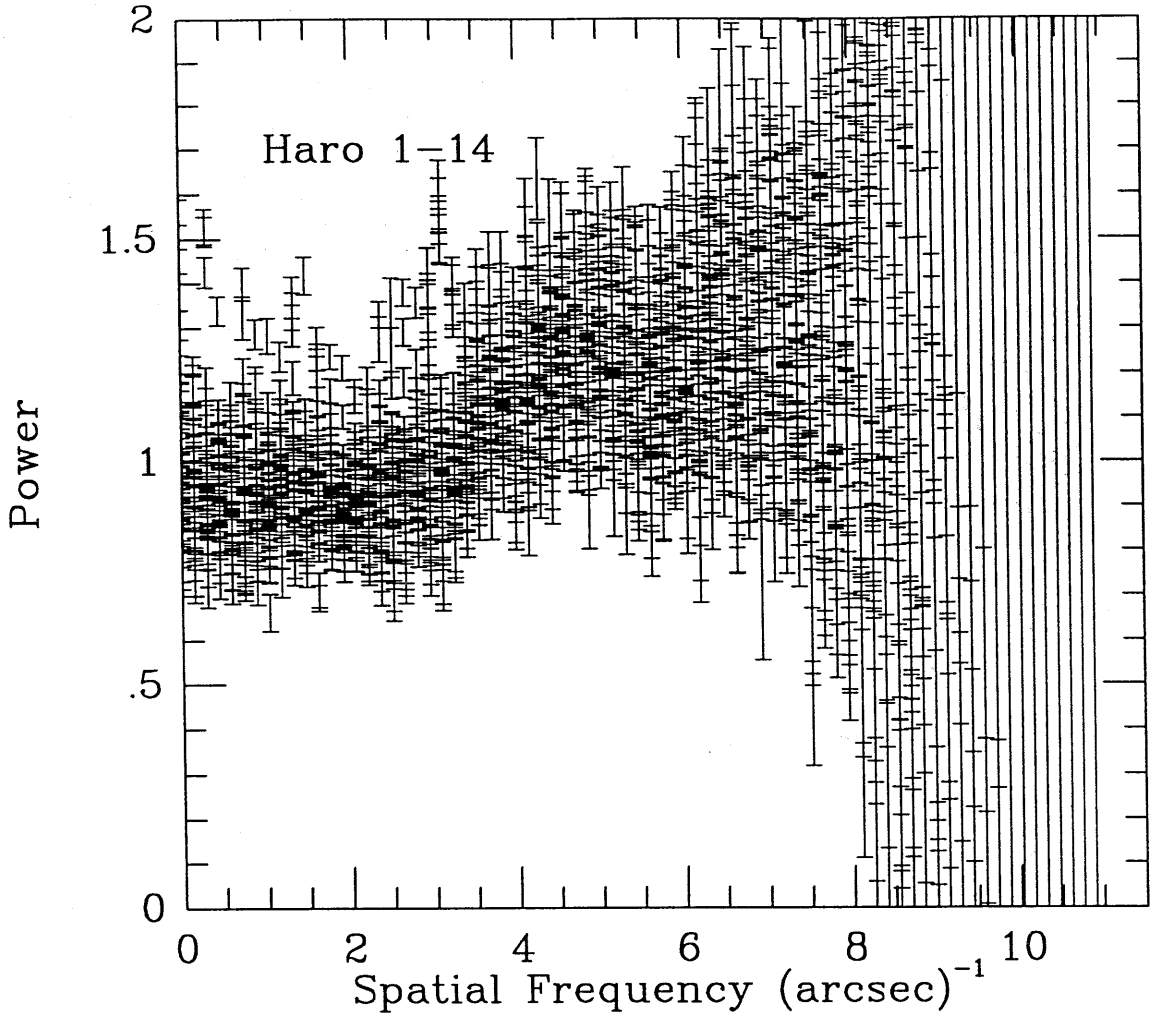

Figure A.49

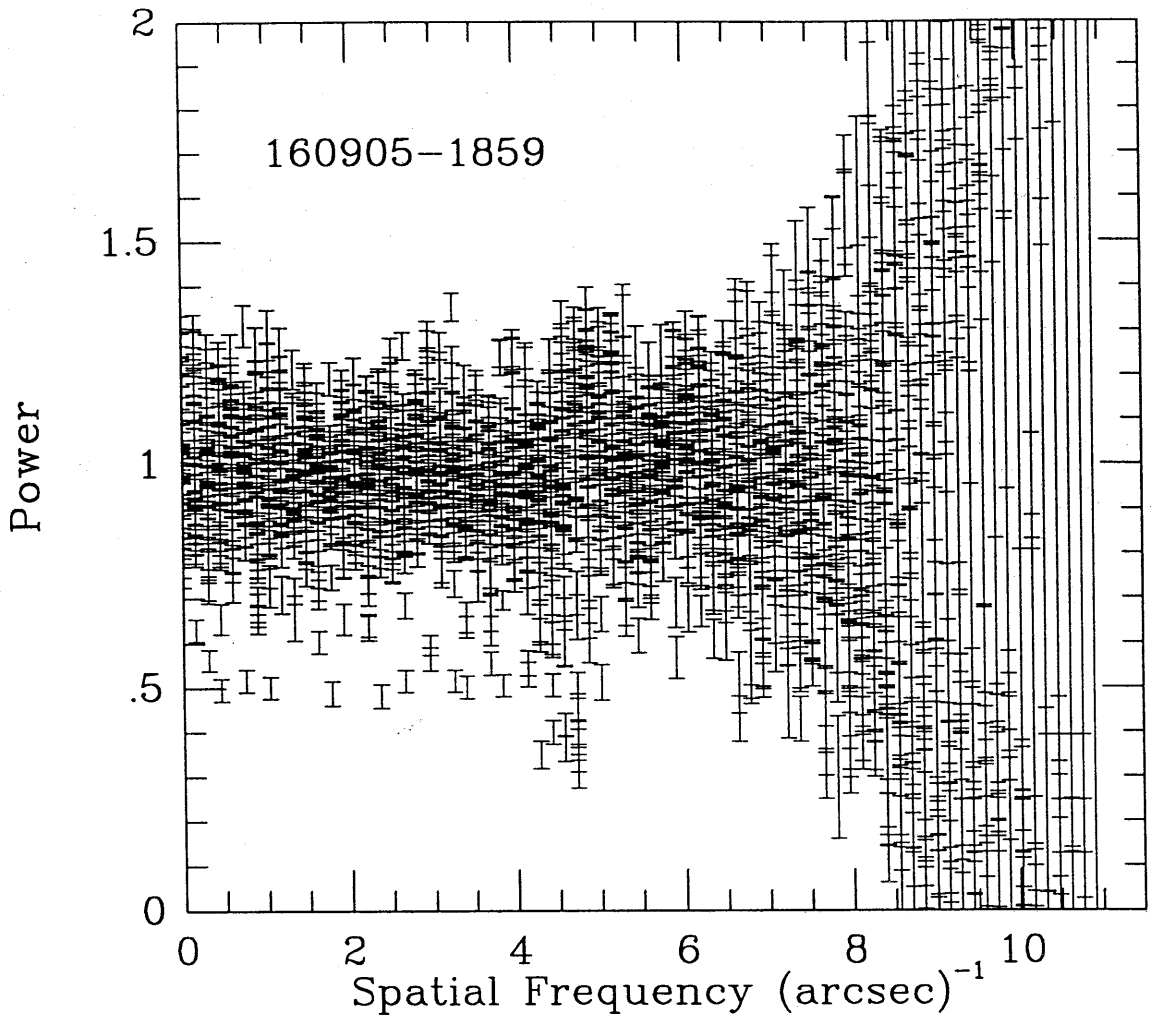
160905−1859
Power
Spatial Frequency (arcsec)$^{-1}$
0
.5
1
1.5
2
0
2
4
6
8
10

Figure A.50

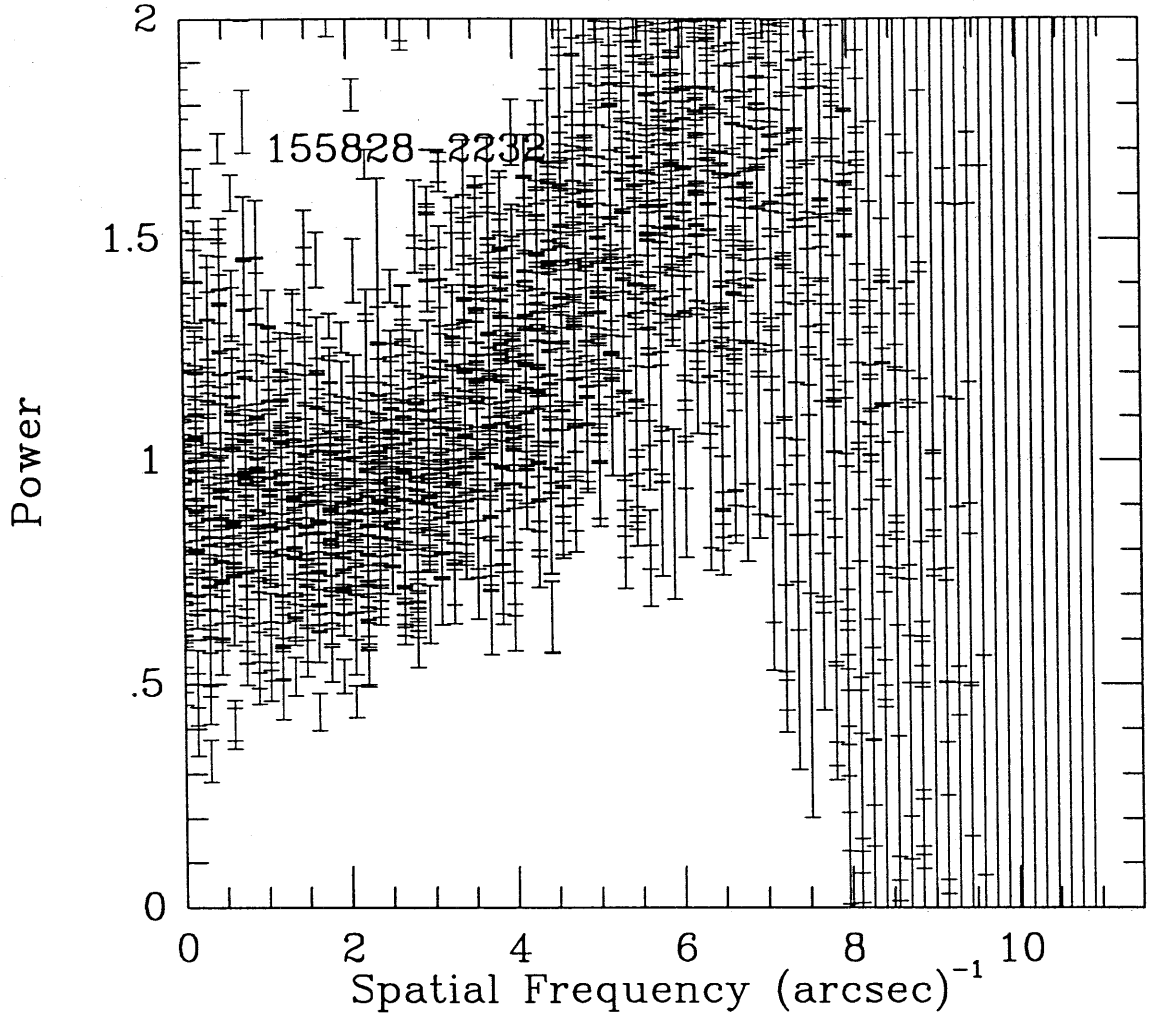
155828-2232
Power
Spatial Frequency (arcsec)$^{-1}$
0
.5
1
1.5
2
0
2
4
6
8
10

Figure A.51

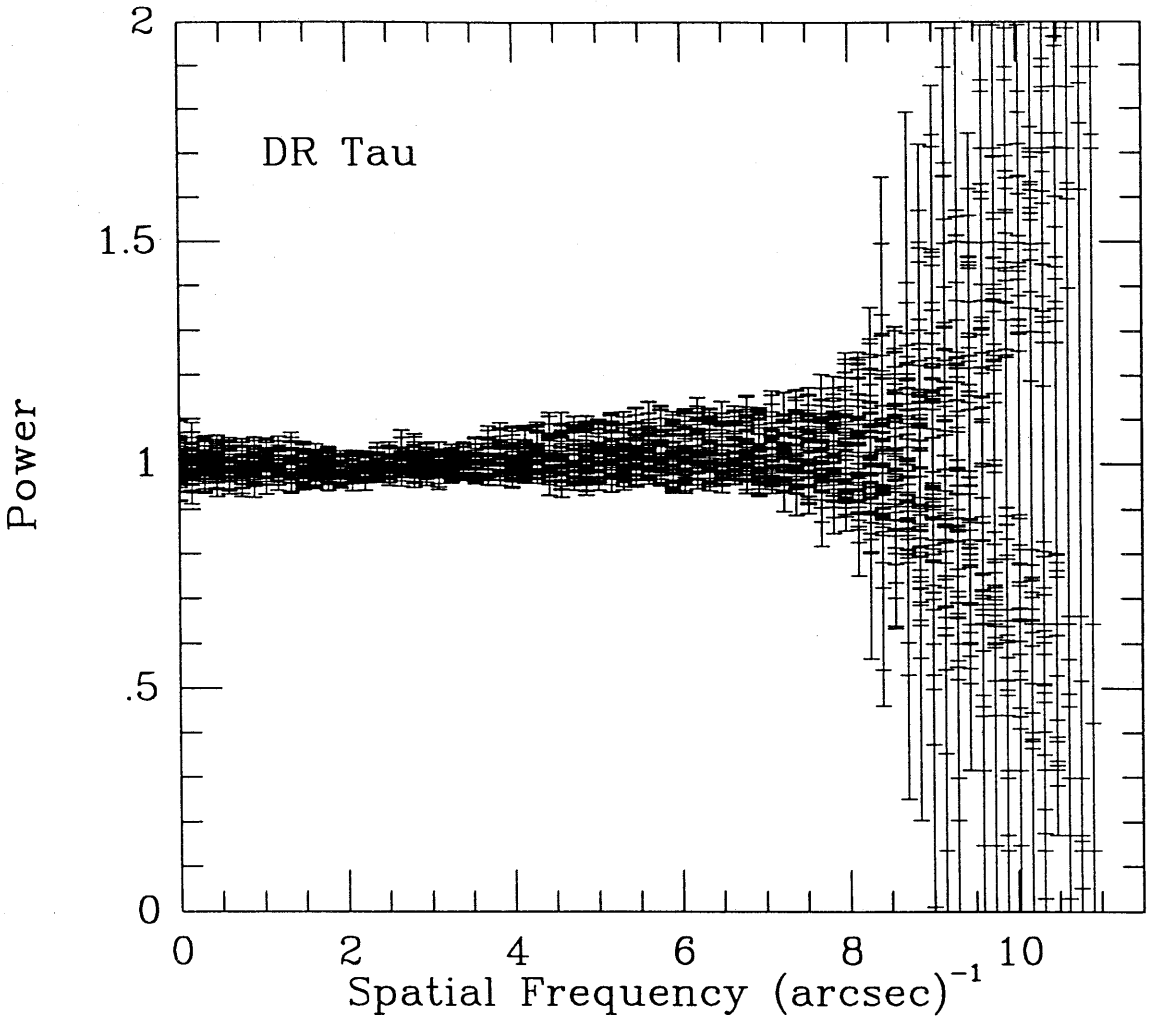

Figure A.52

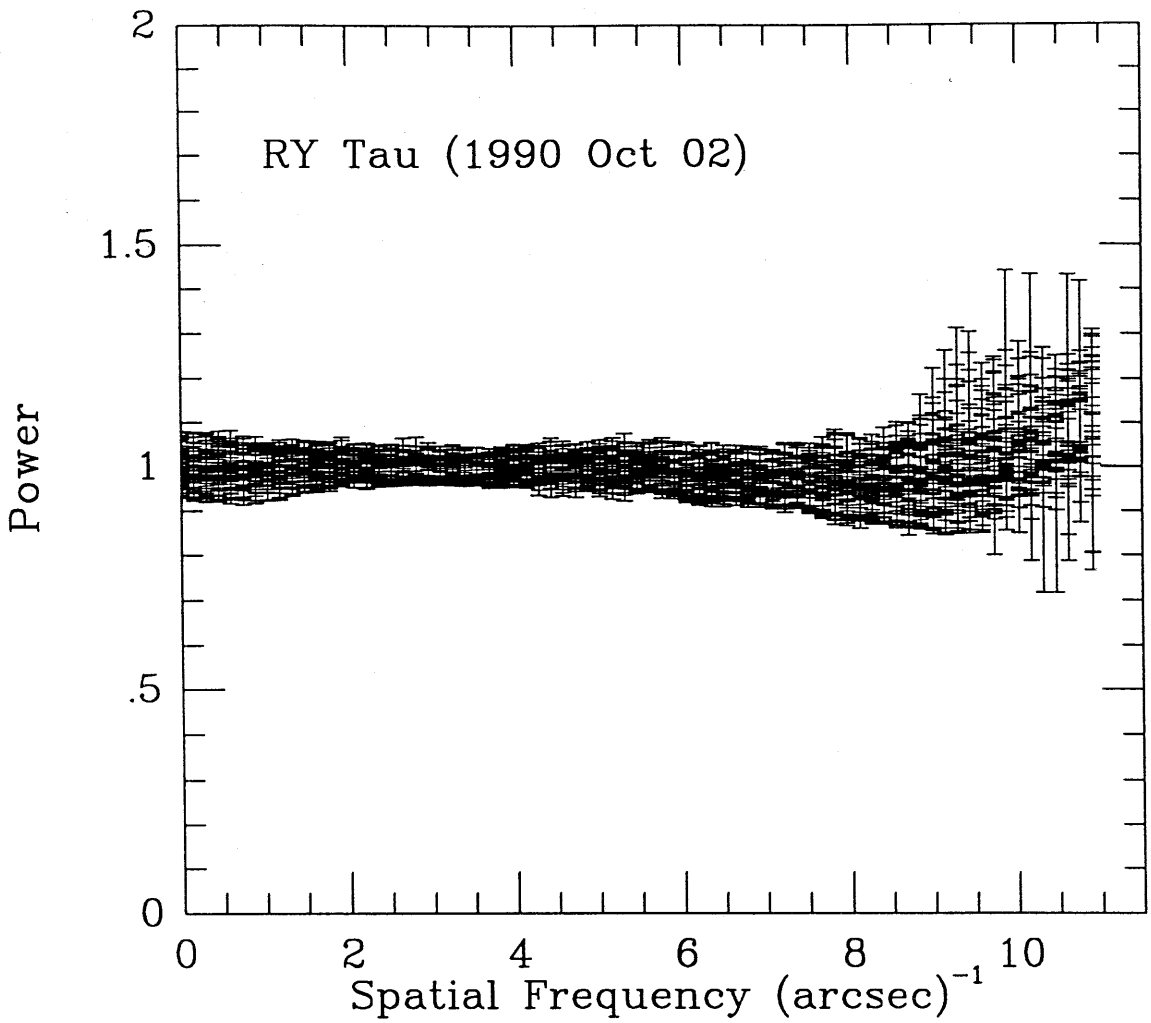
RY Tau (1990 Oct 02)
Power
Spatial Frequency (arcsec)$^{-1}$
0
.5
1
1.5
2
0
2
4
6
8
10

Figure A.53

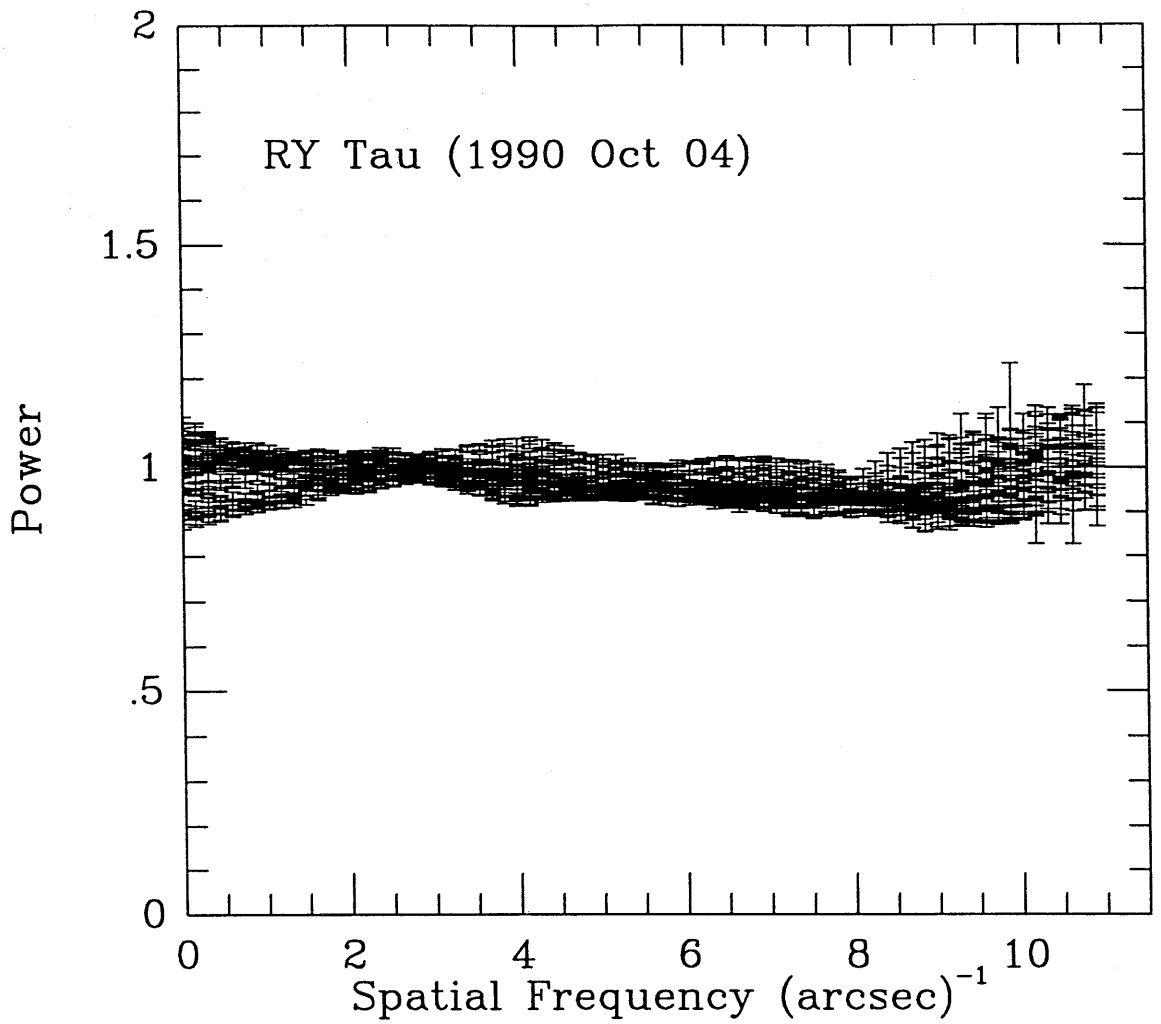
RY Tau (1990 Oct 04)
Power
2
1.5
1
.5
0
0
2
4
6
8
10
Spatial Frequency (arcsec)$^{-1}$

Figure A.54

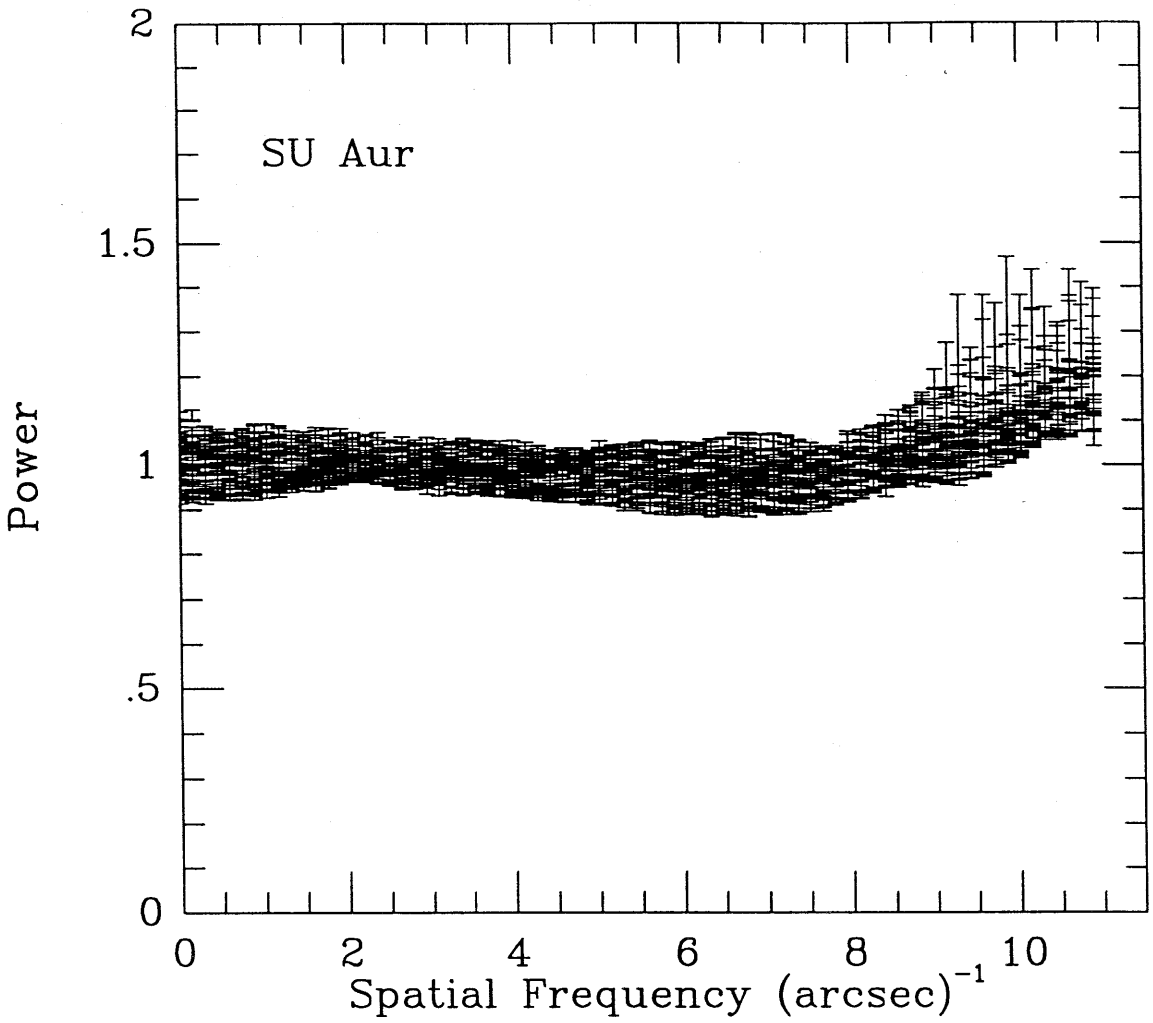

Figure A.55

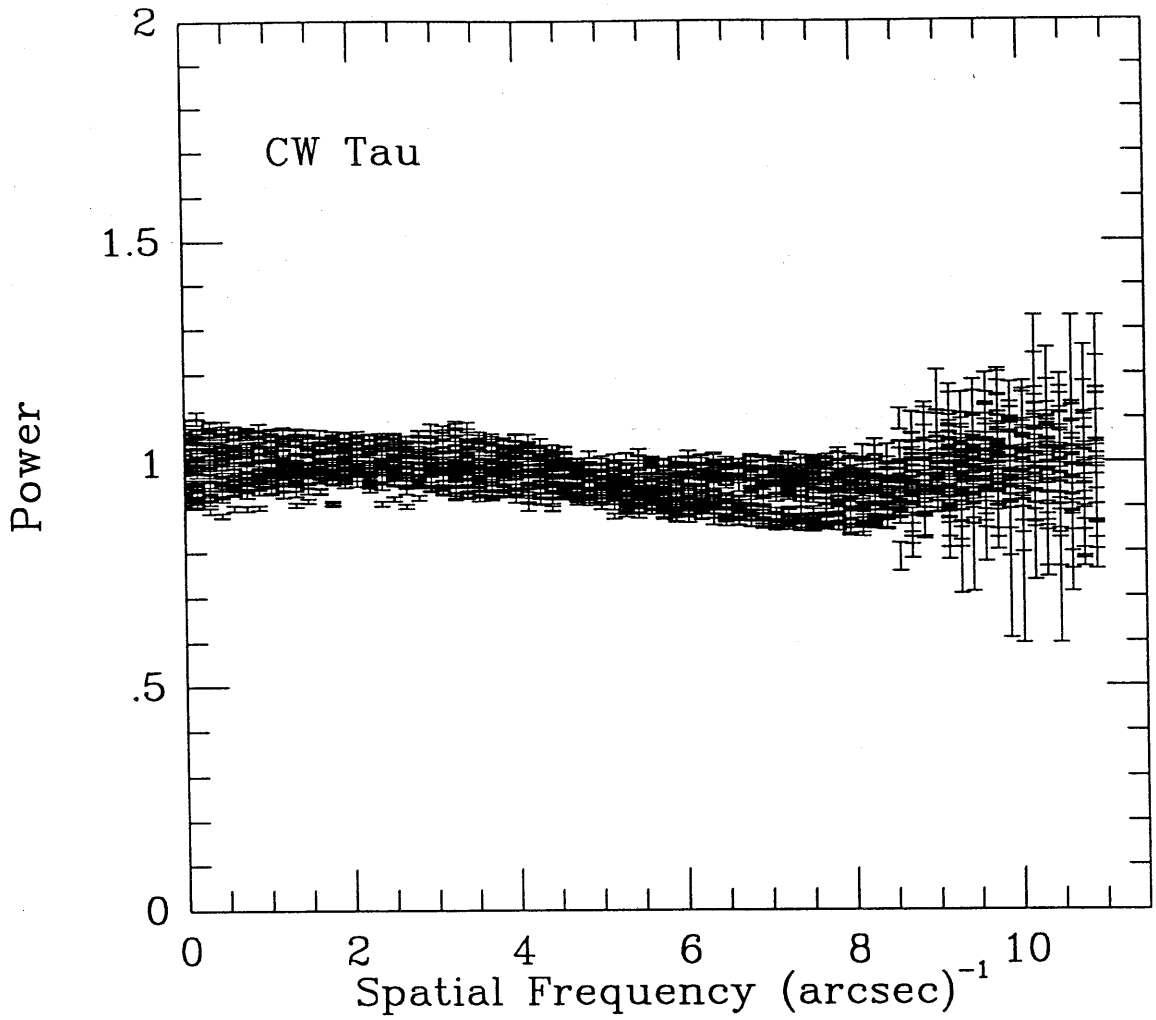

Figure A.56

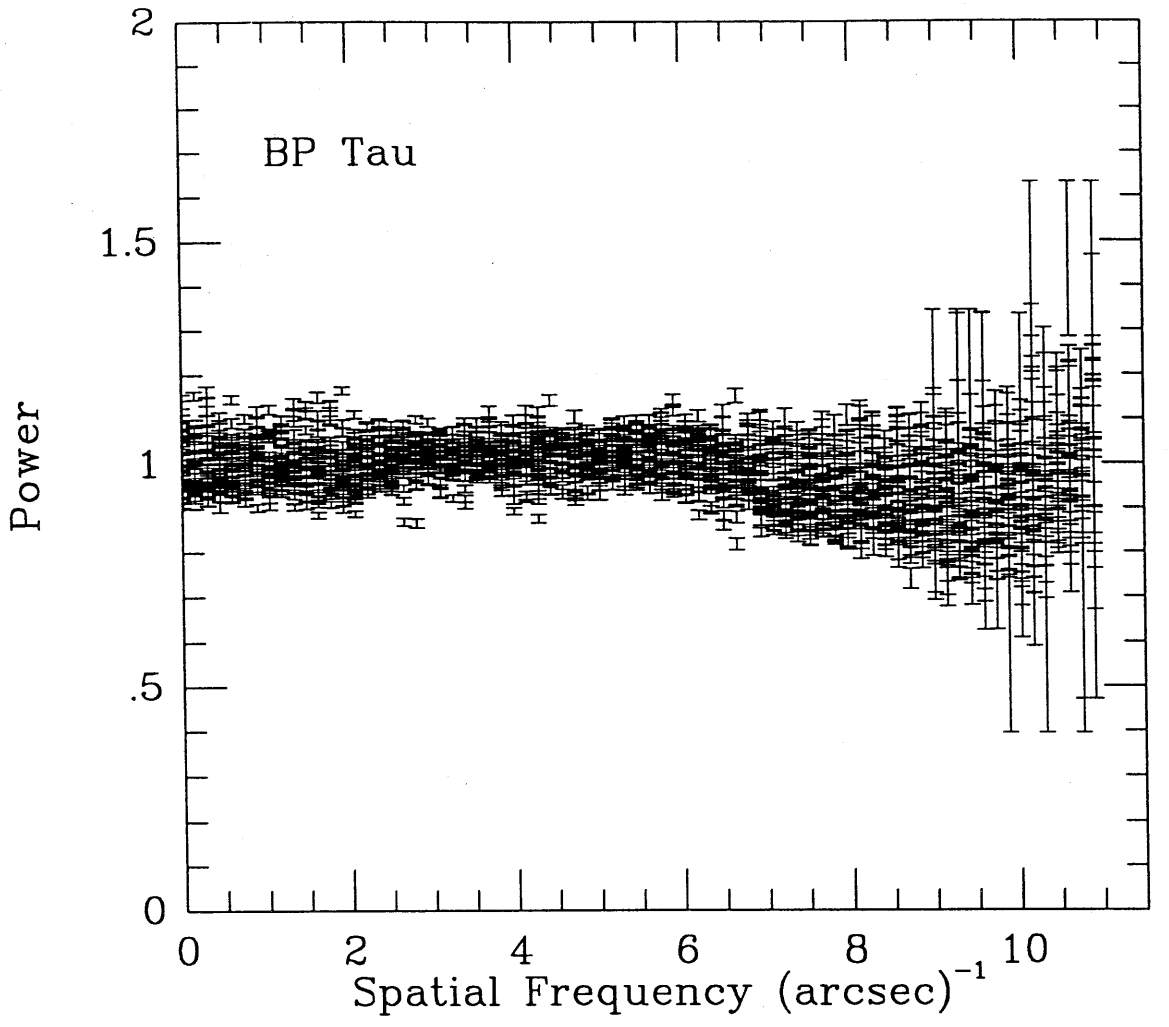

Figure A.57

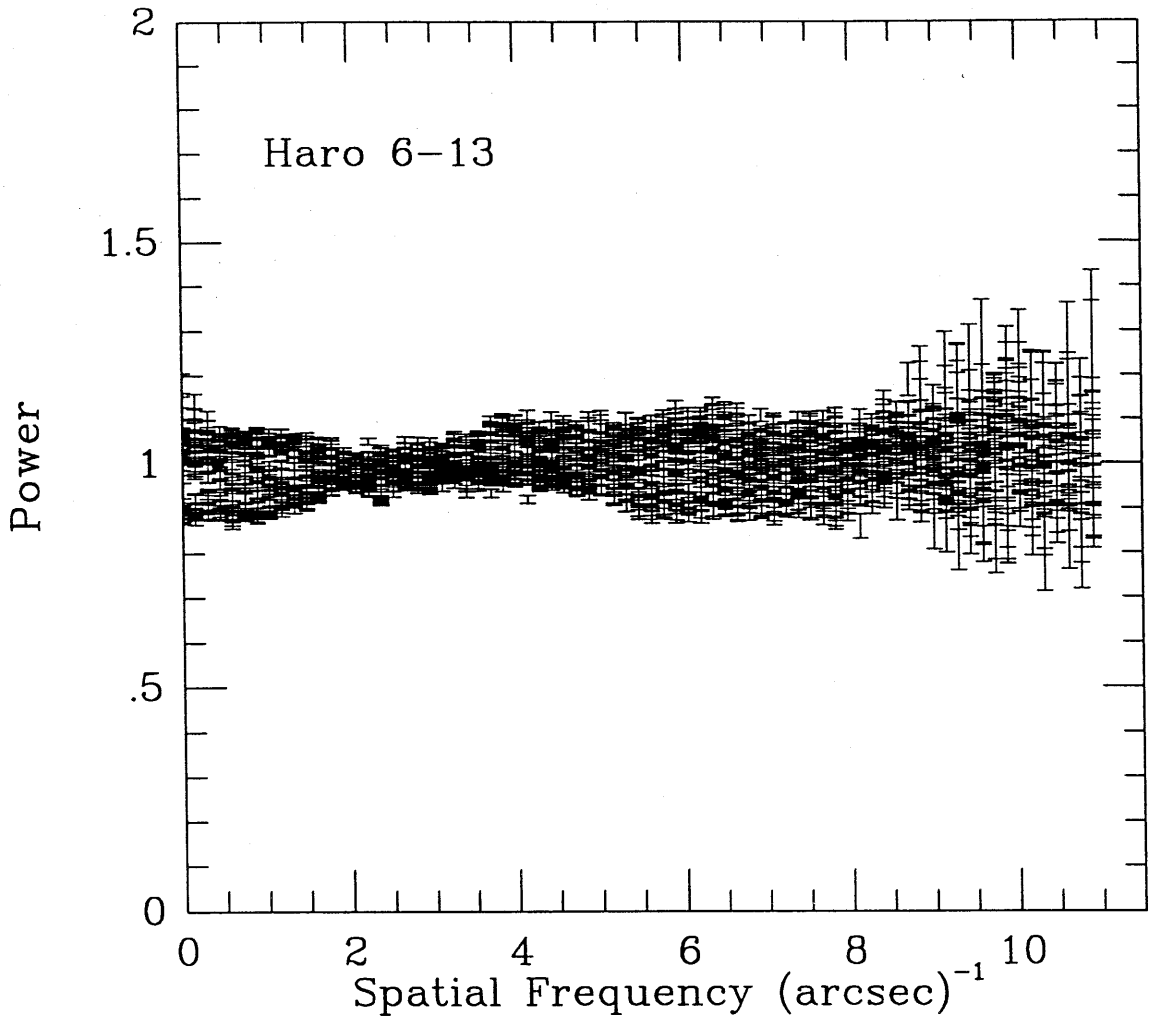

Figure A.58

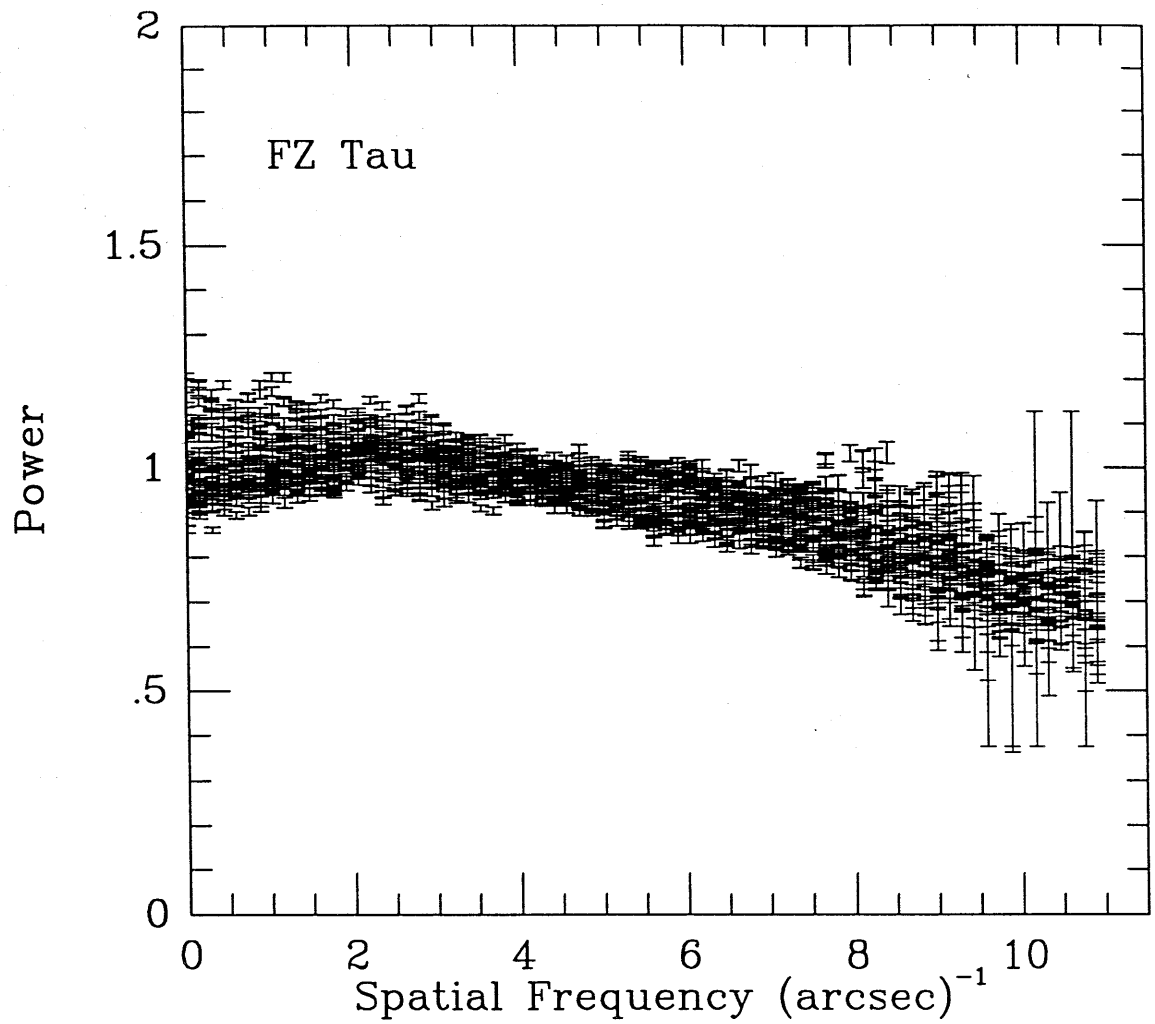

Figure A.59

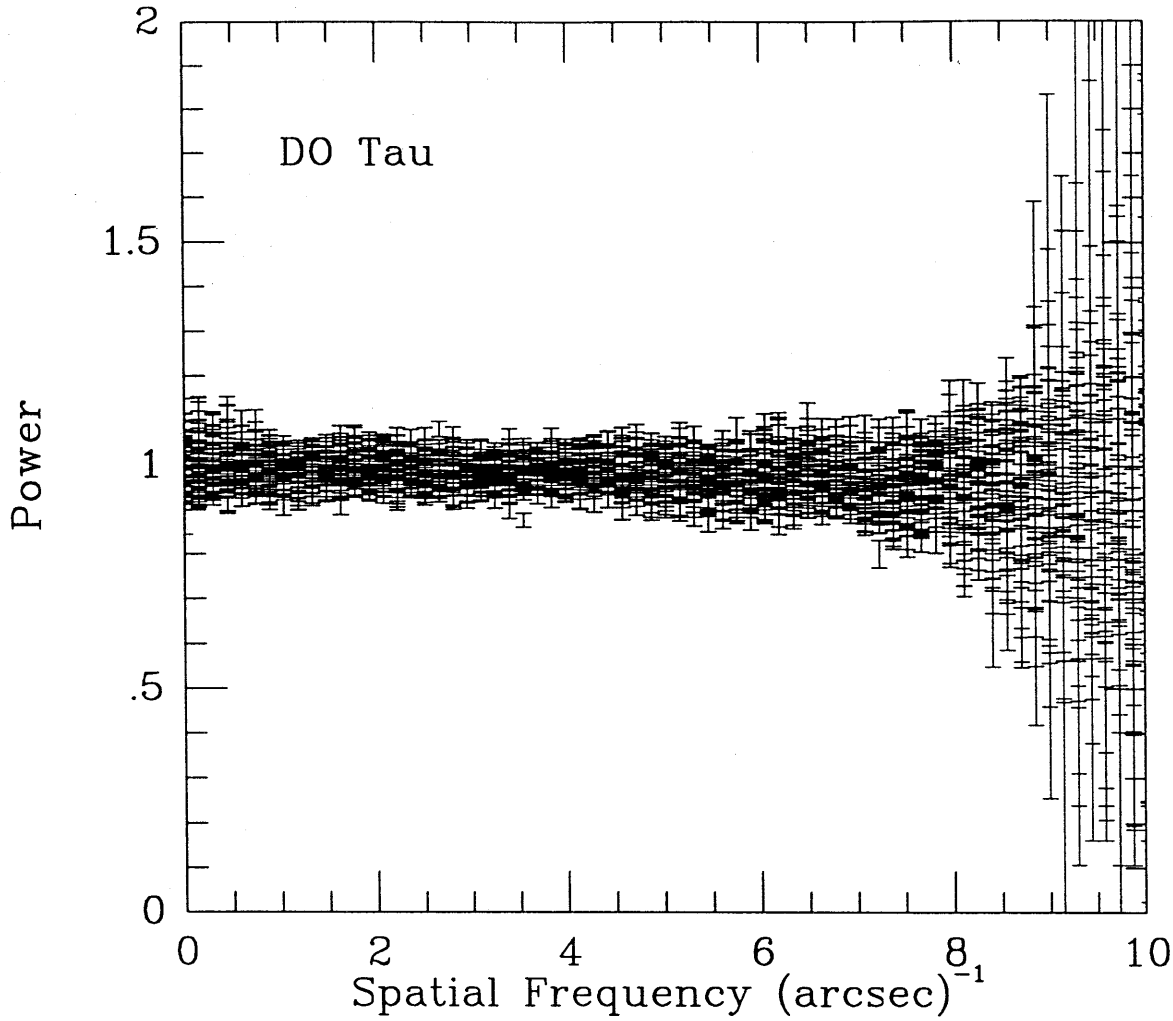

Figure A.60

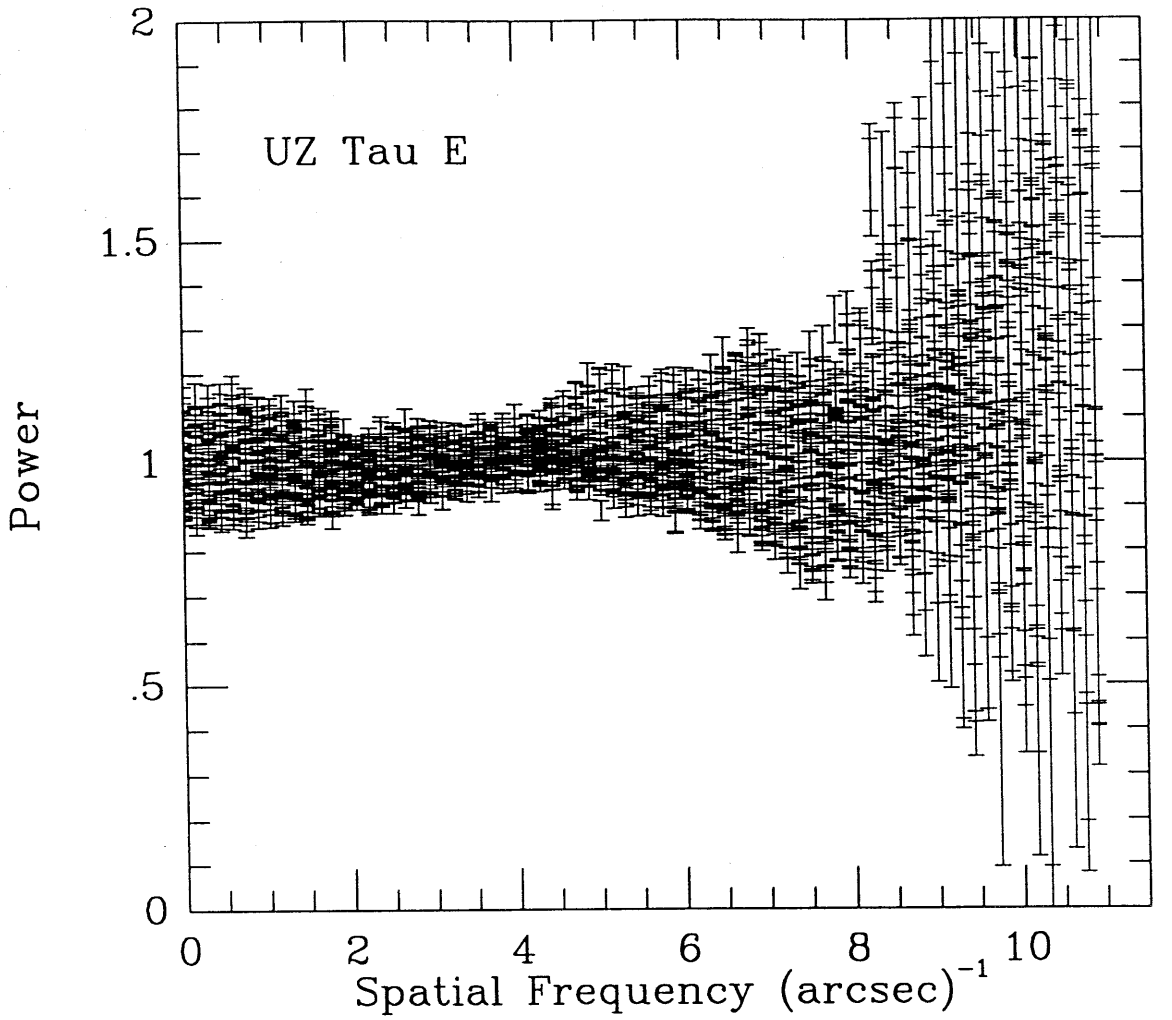

Figure A.61

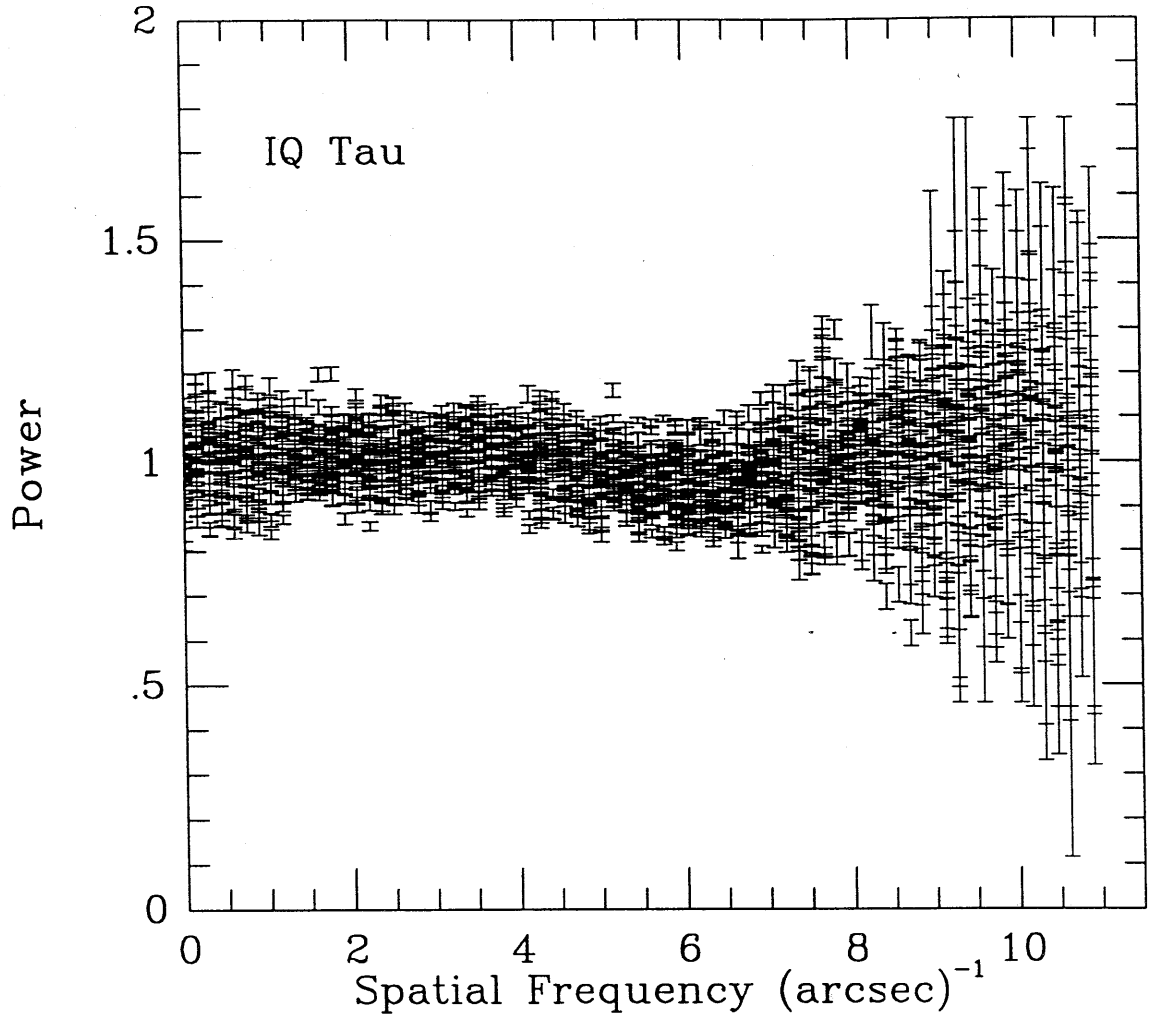

Figure A.62

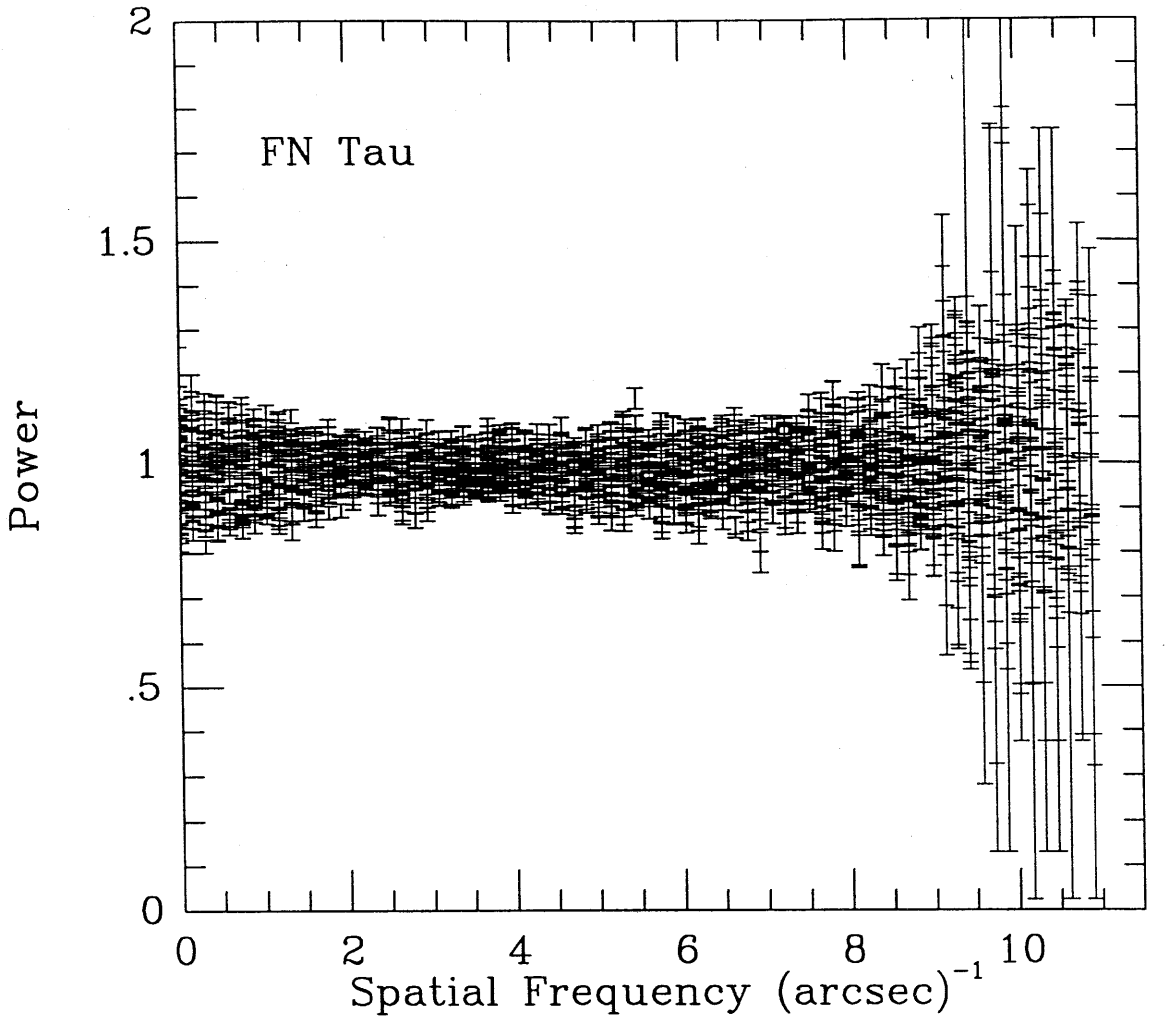

Figure A.63

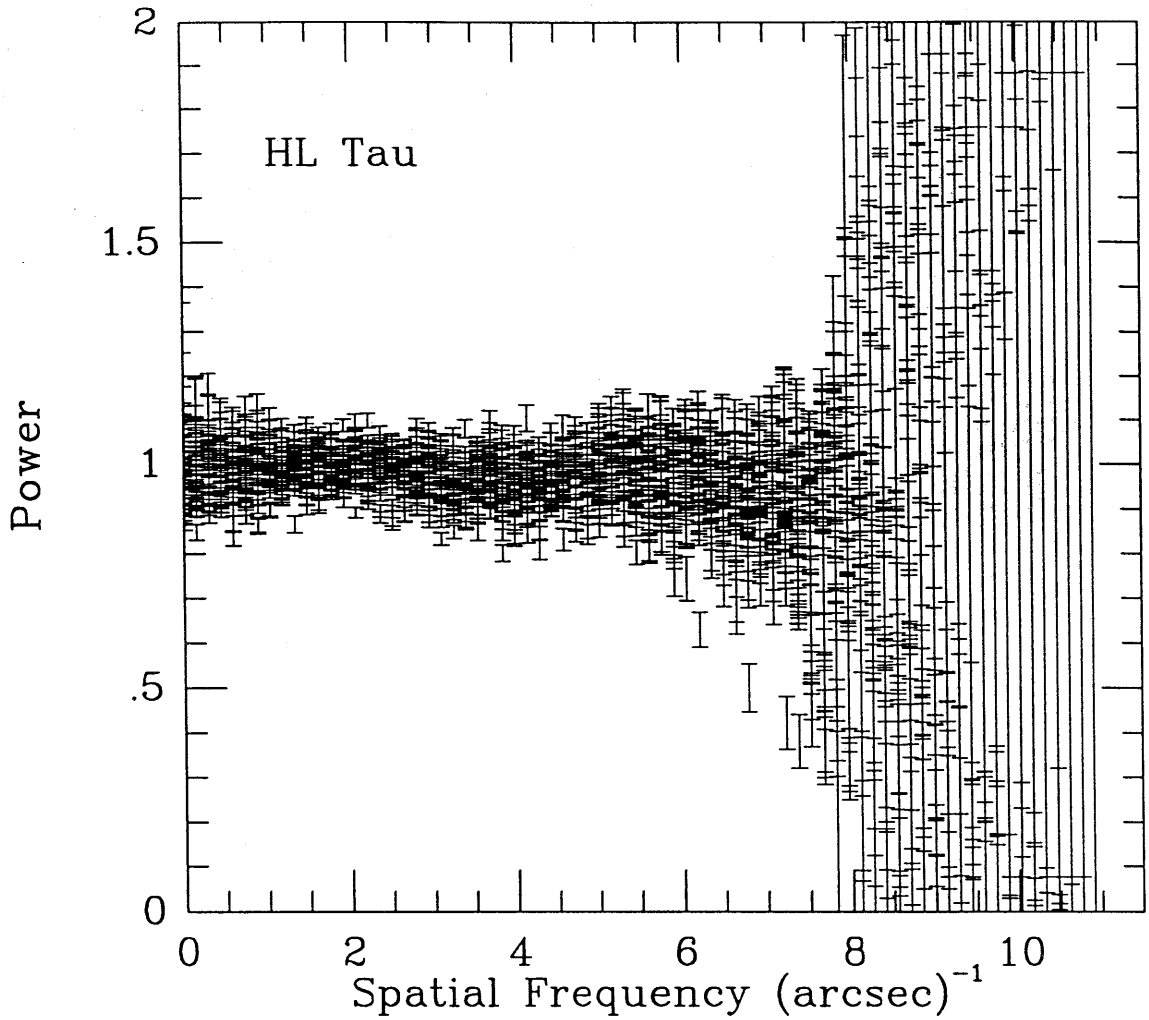

Figure A.64

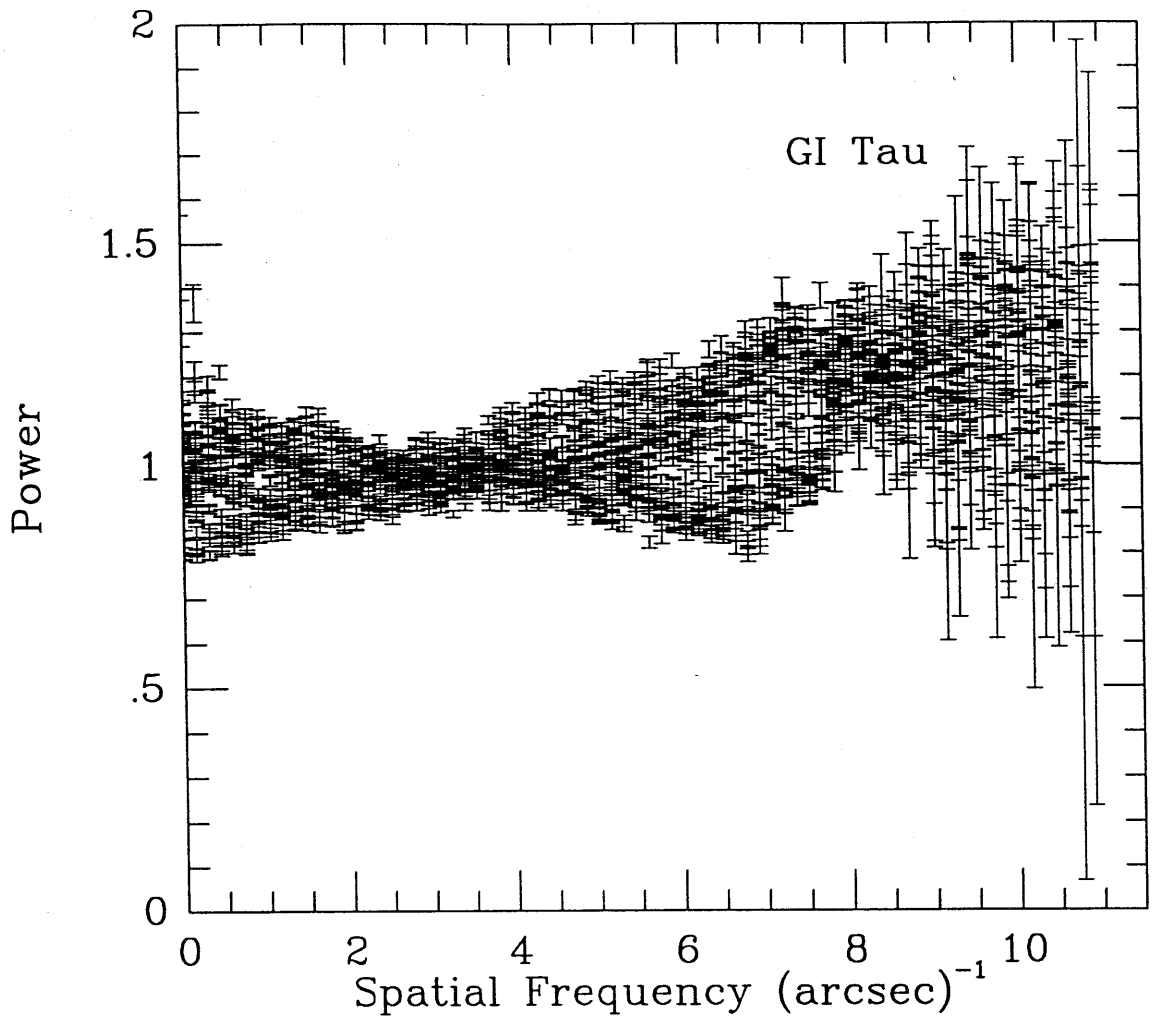

Figure A.65

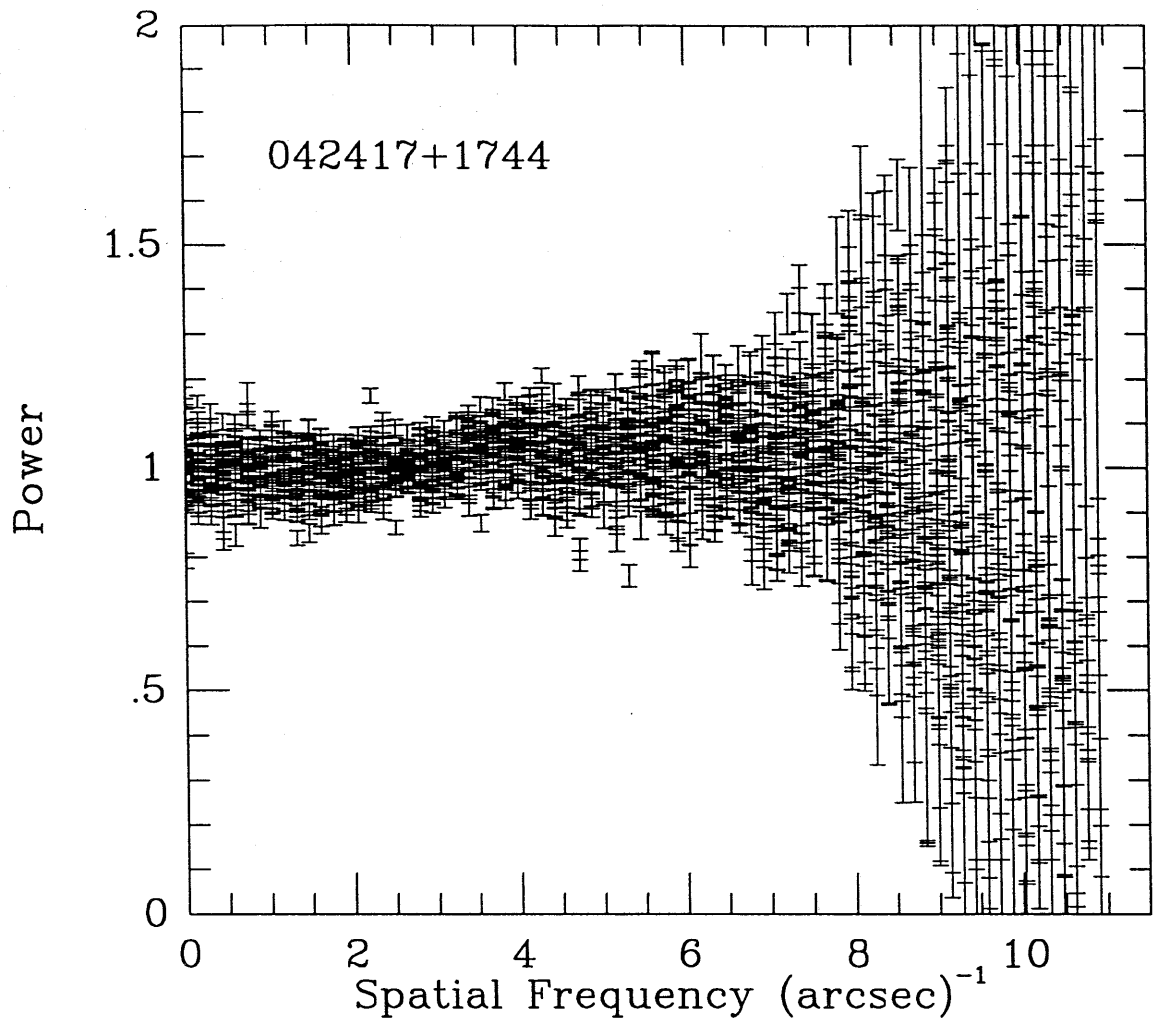
042417+1744
Power
Spatial Frequency (arcsec)$^{-1}$
0
.5
1
1.5
2
0
2
4
6
8
10

Figure A.66

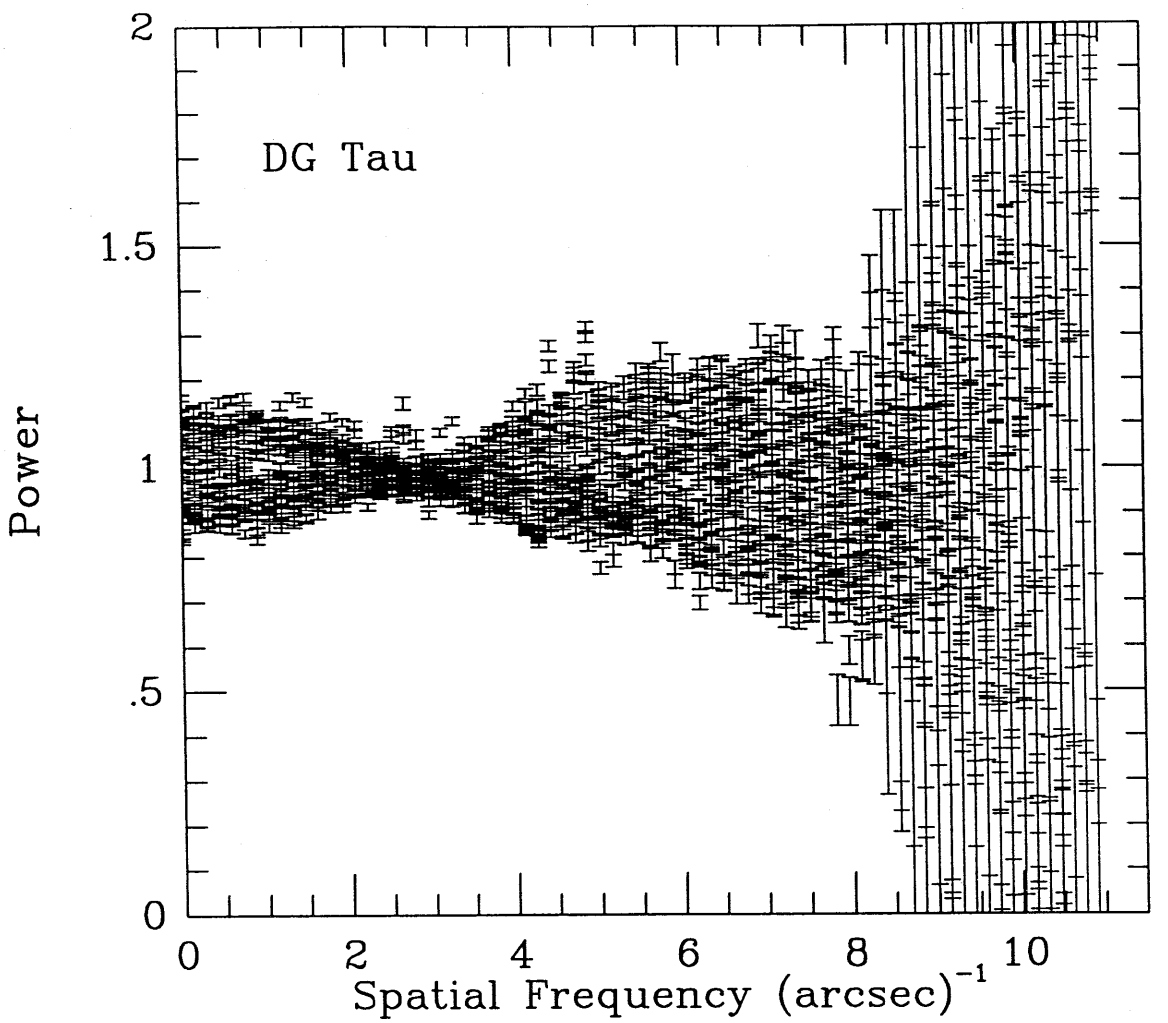

Figure A.67

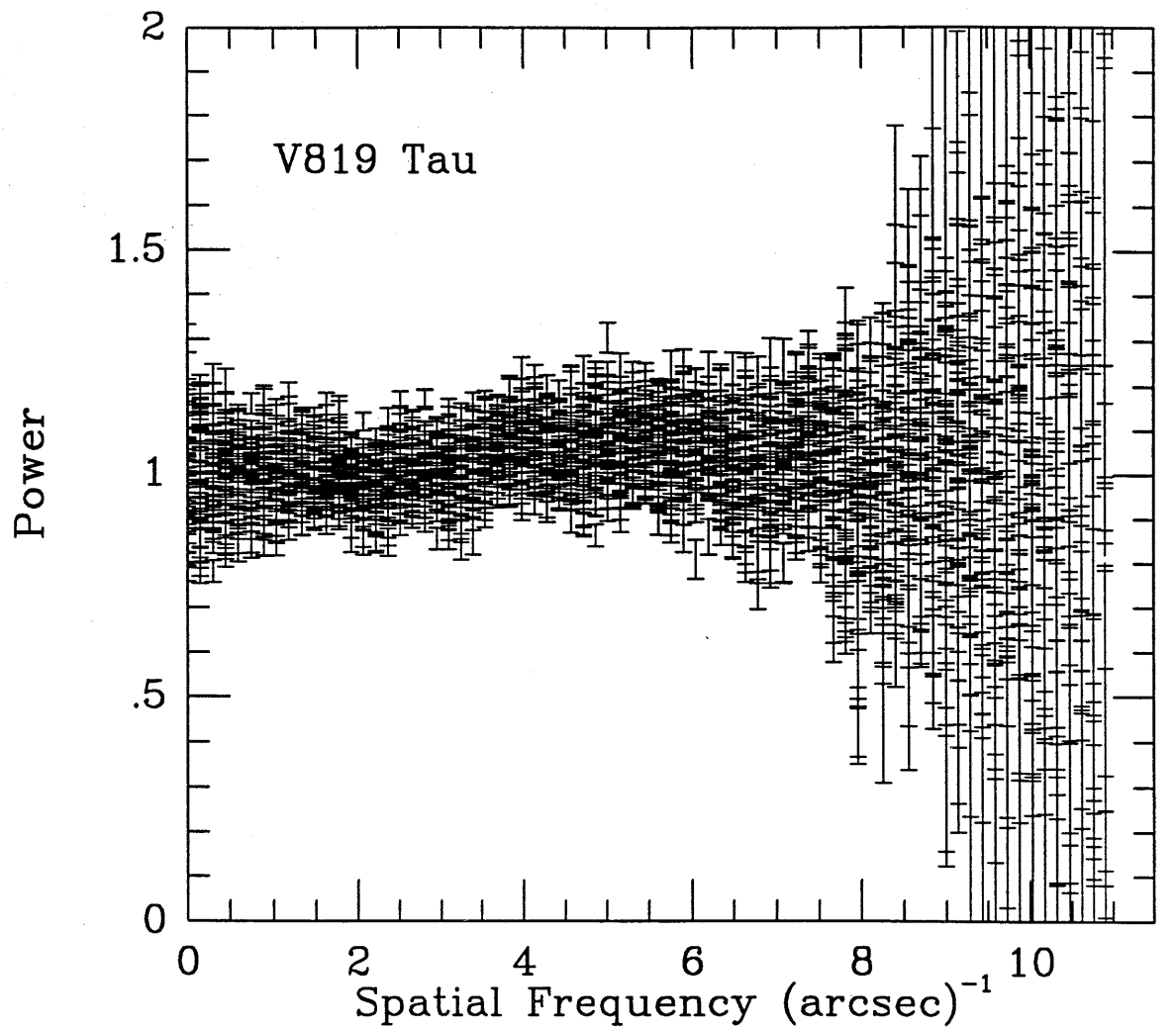

Figure A.68

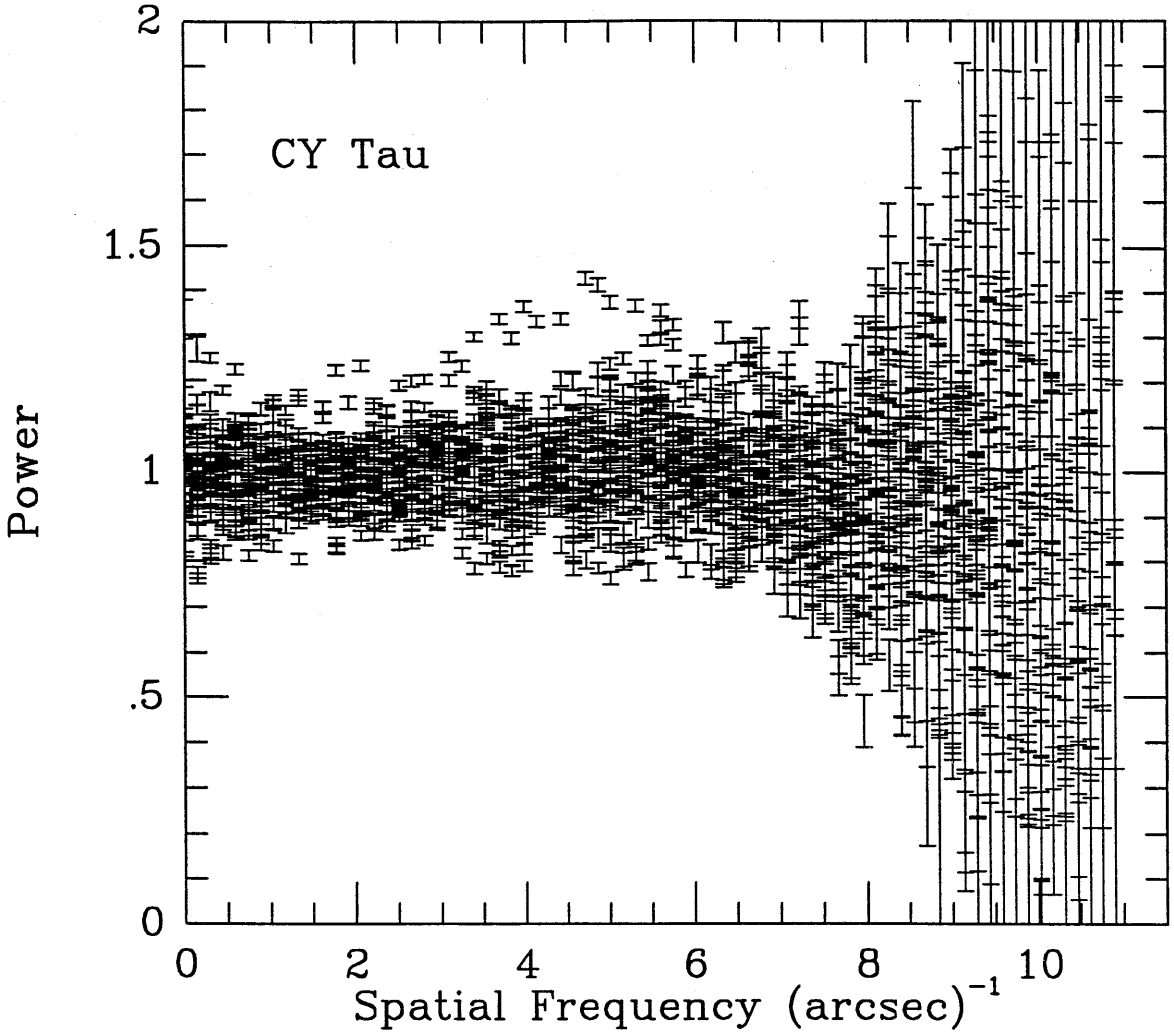

Figure A.69

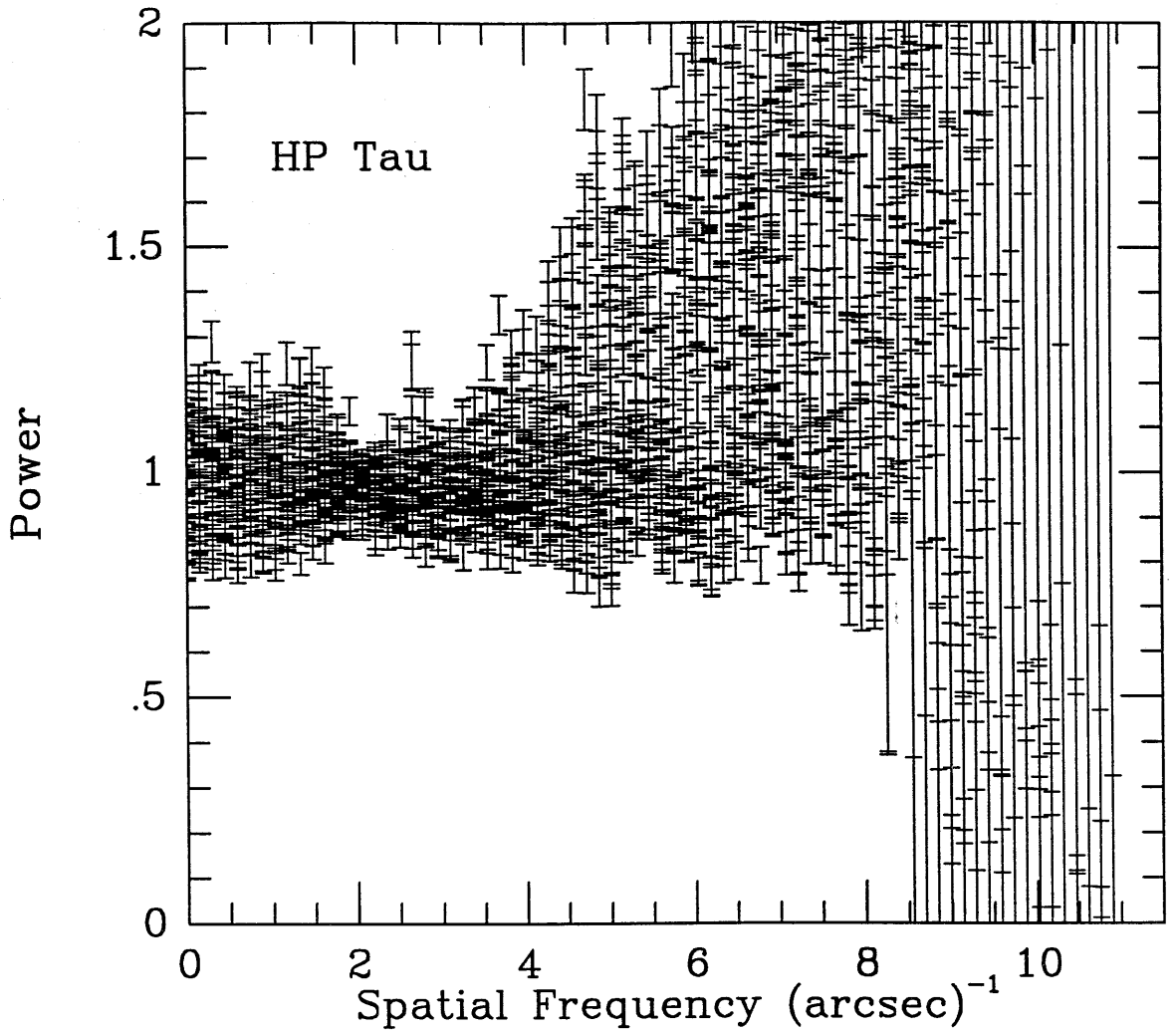

Figure A.70

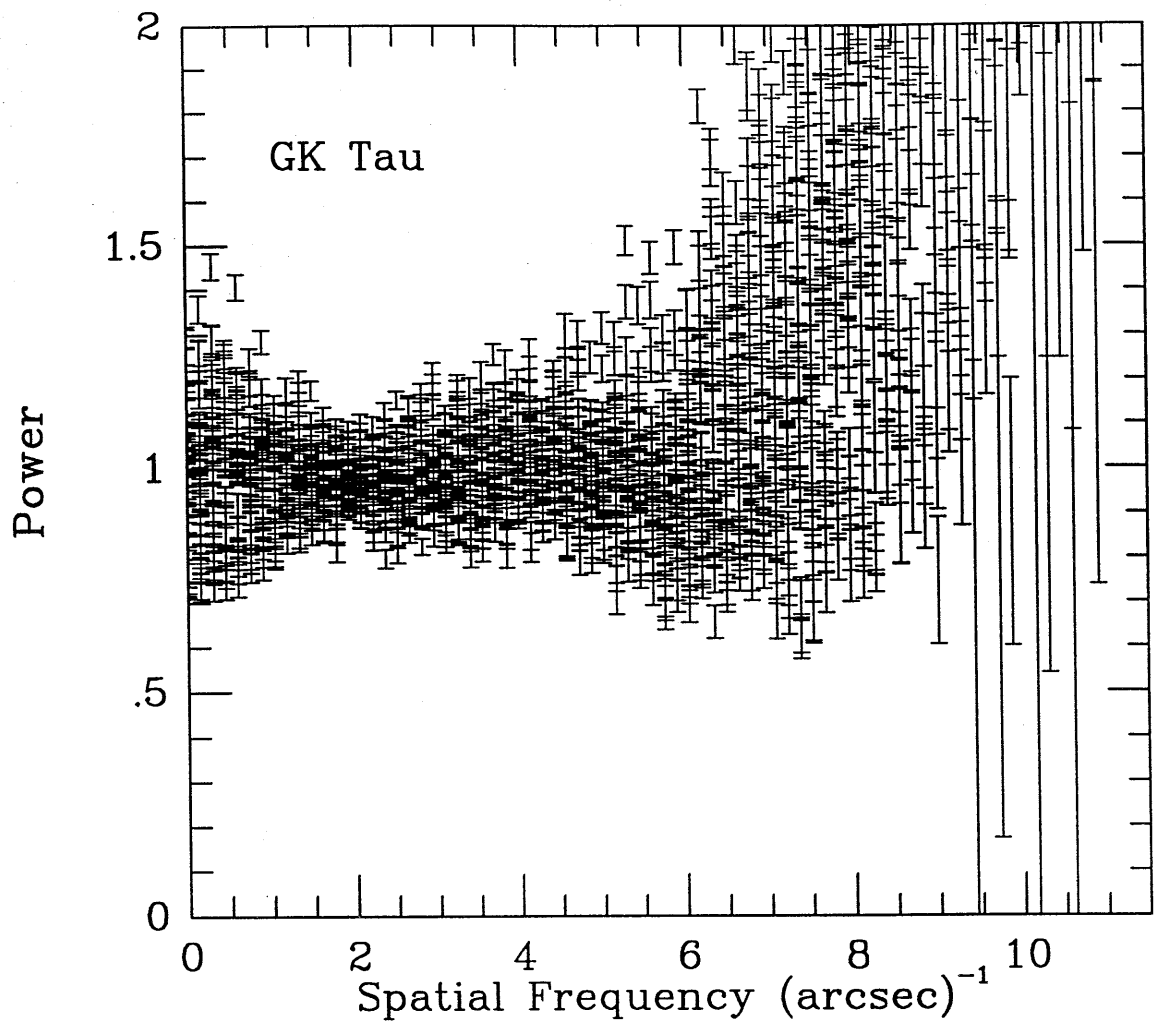

Figure A.71

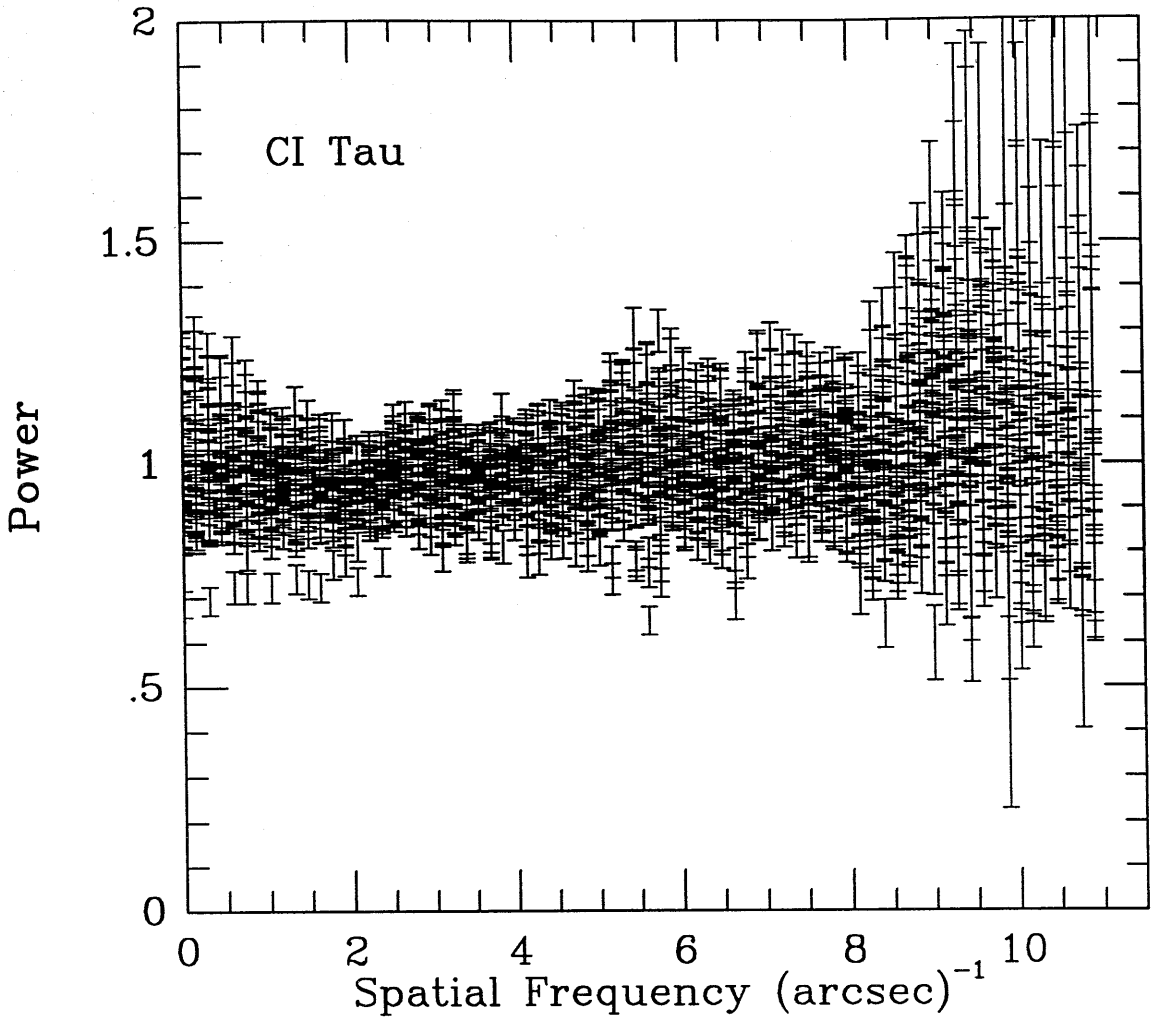

Figure A.72

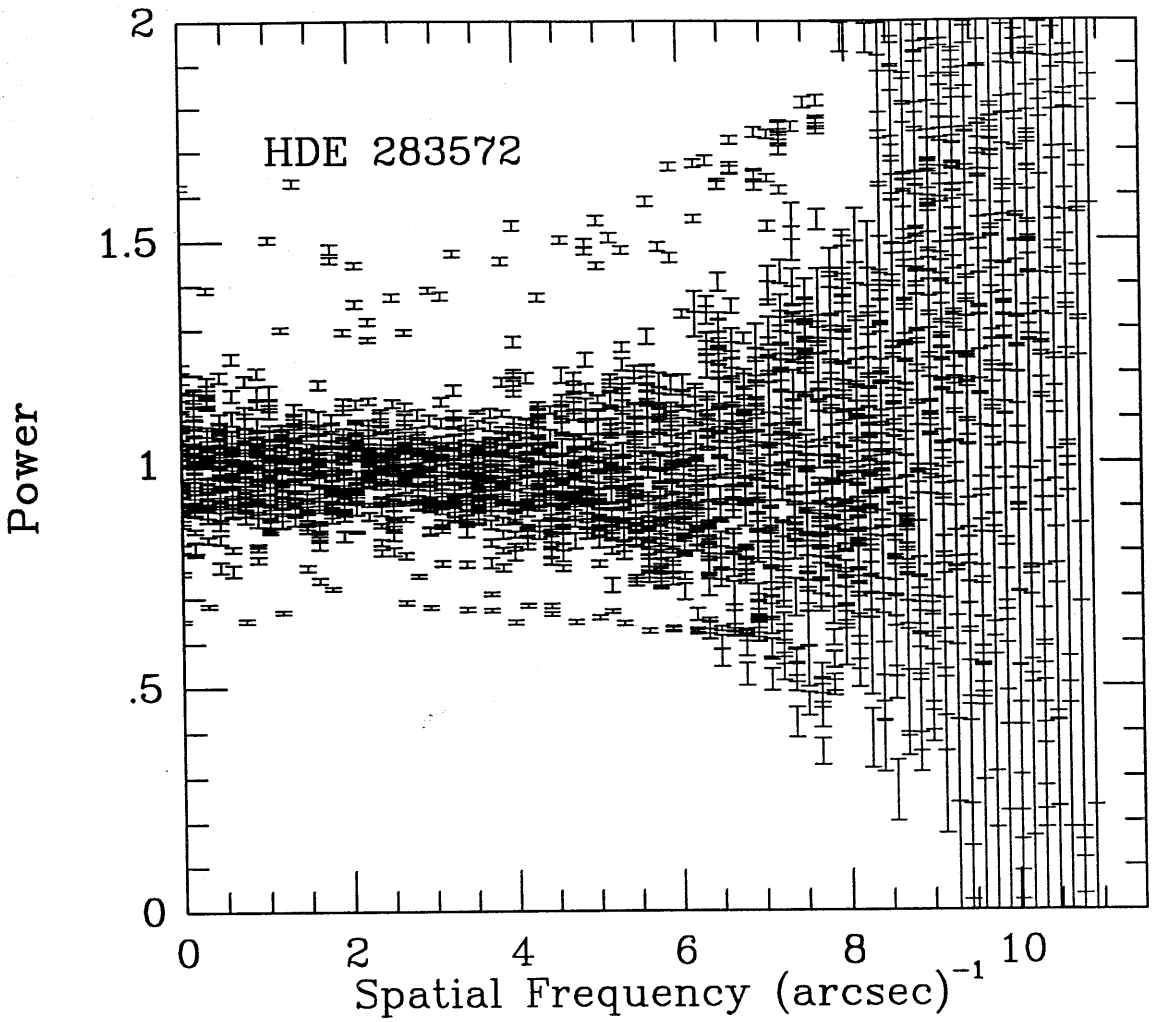
HDE 283572
Power
2
1.5
1
.5
0
0
2
4
6
8
10
Spatial Frequency (arcsec)$^{-1}$

Figure A.73

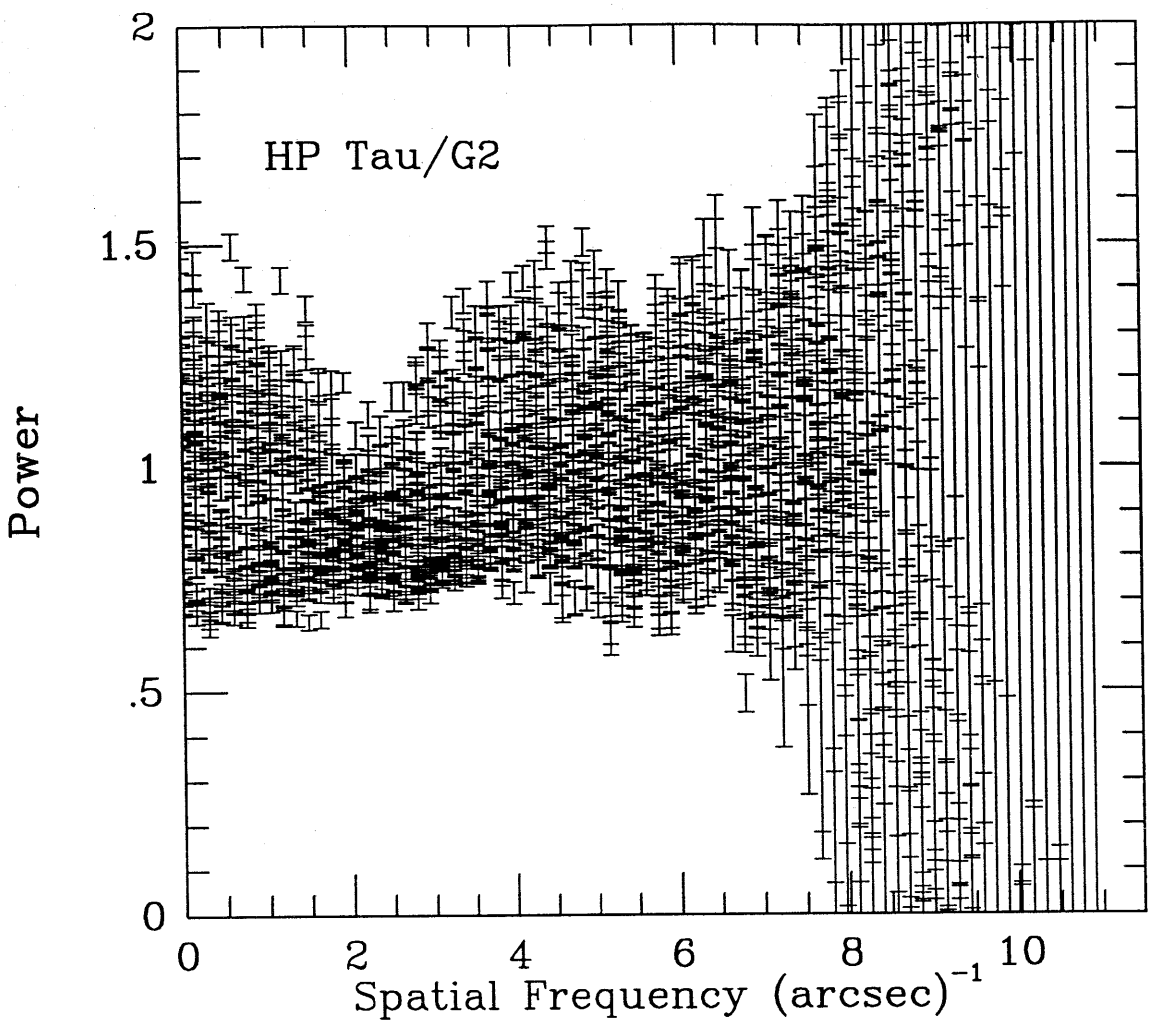

Figure A.74

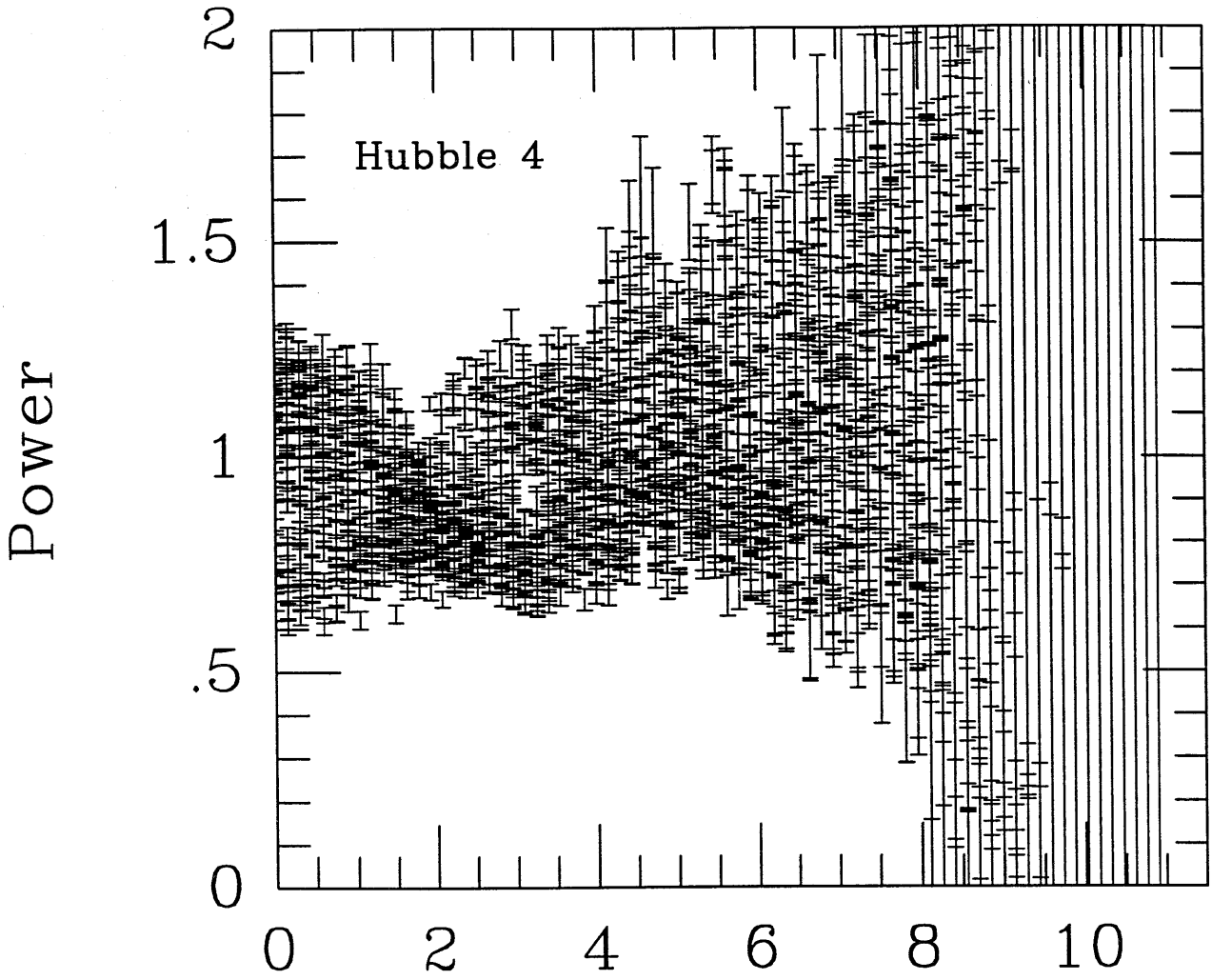

Figure A.75

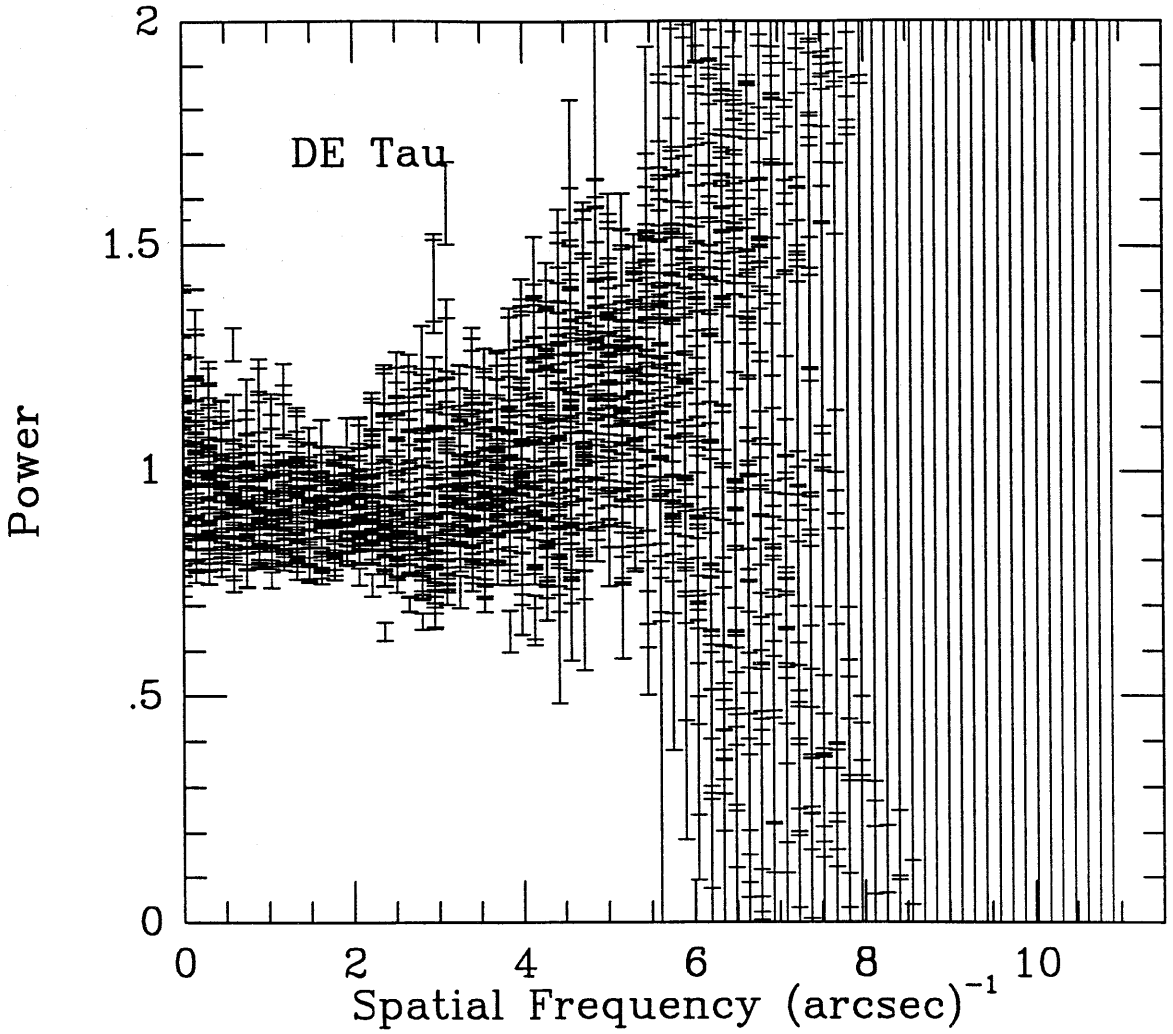

Figure A.76

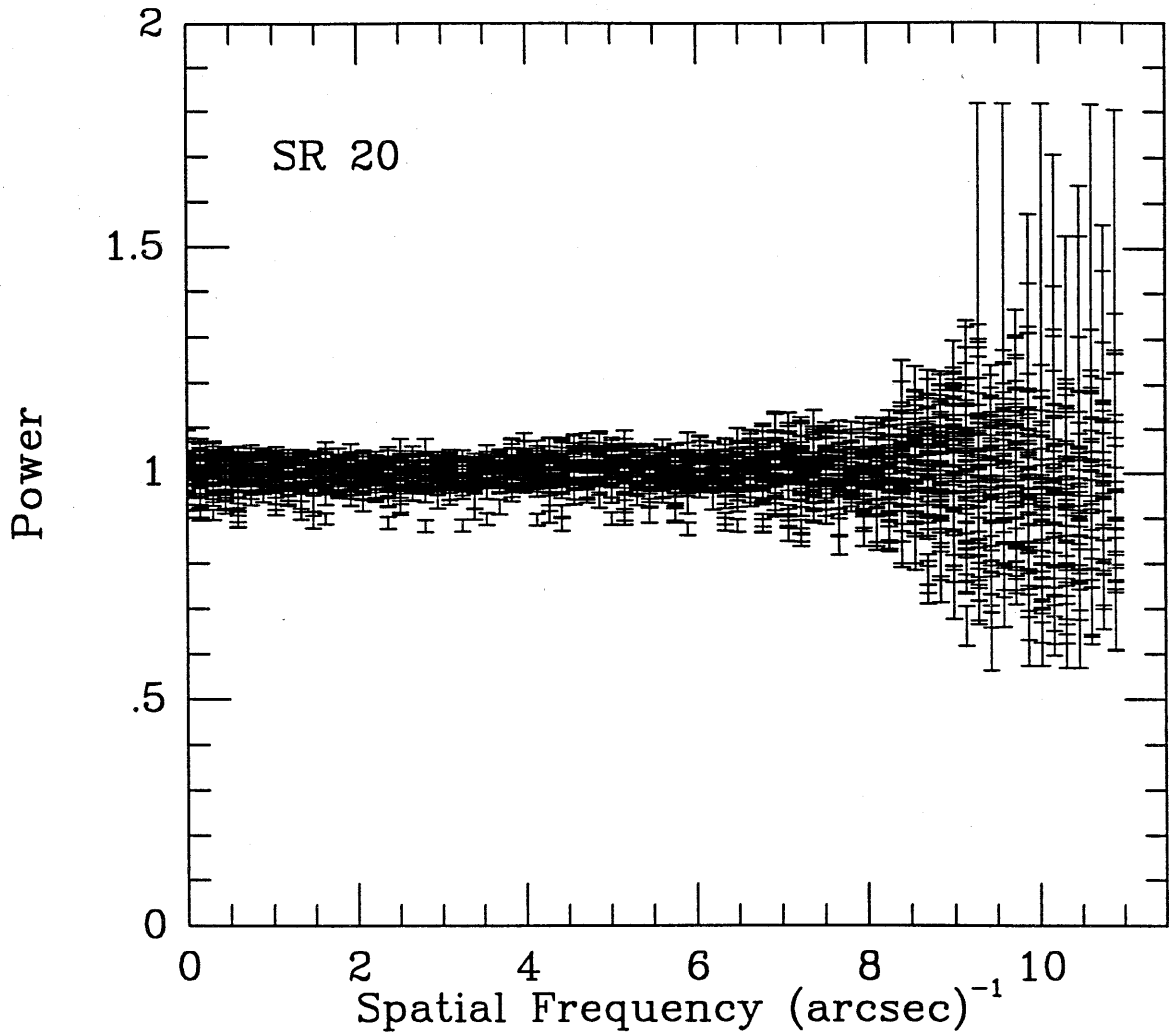

Figure A.77

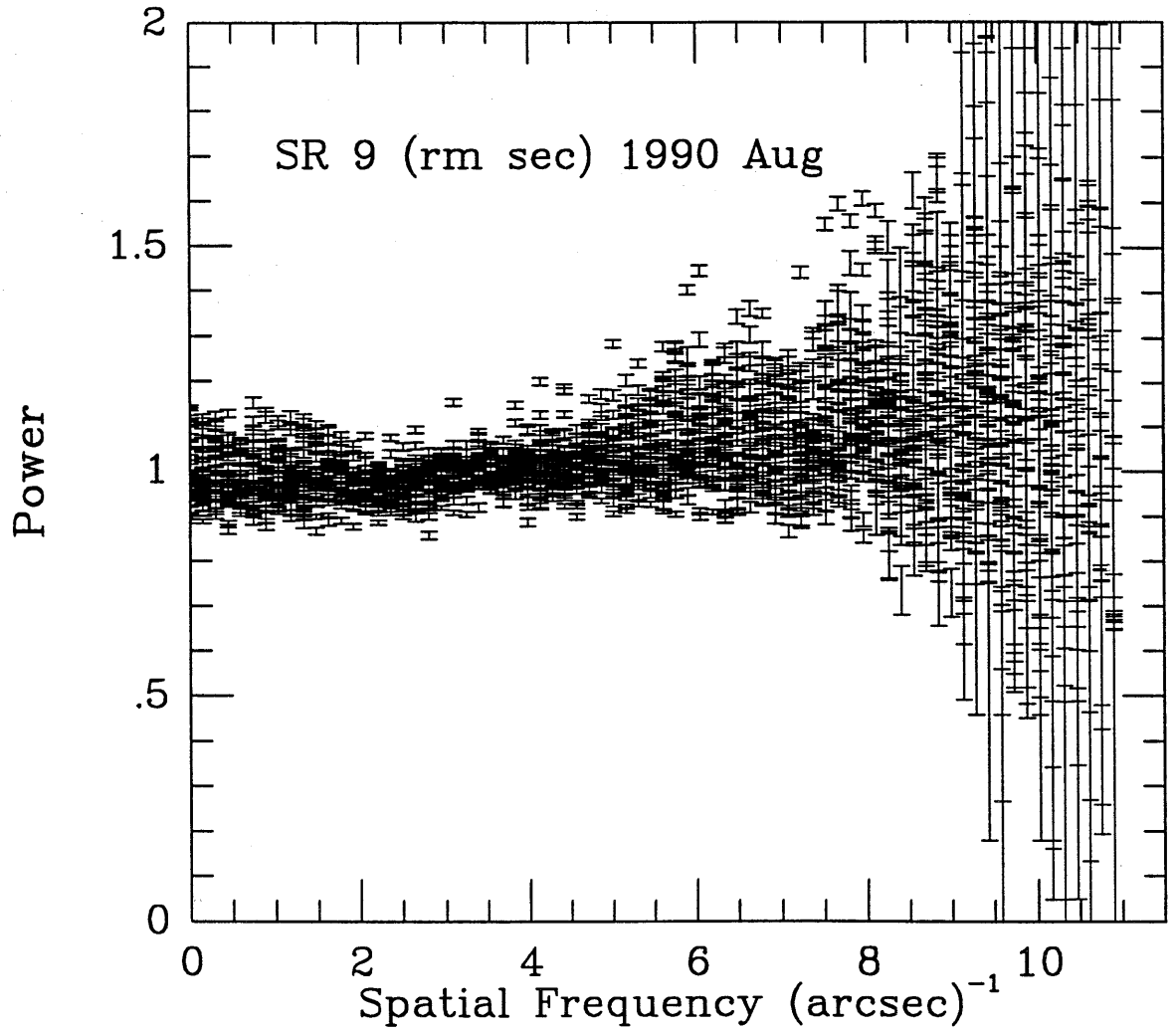
SR 9 (rm sec) 1990 Aug
Power
2
1.5
1
.5
0
0
2
4
6
8
10
Spatial Frequency (arcsec)$^{-1}$

Figure A.78

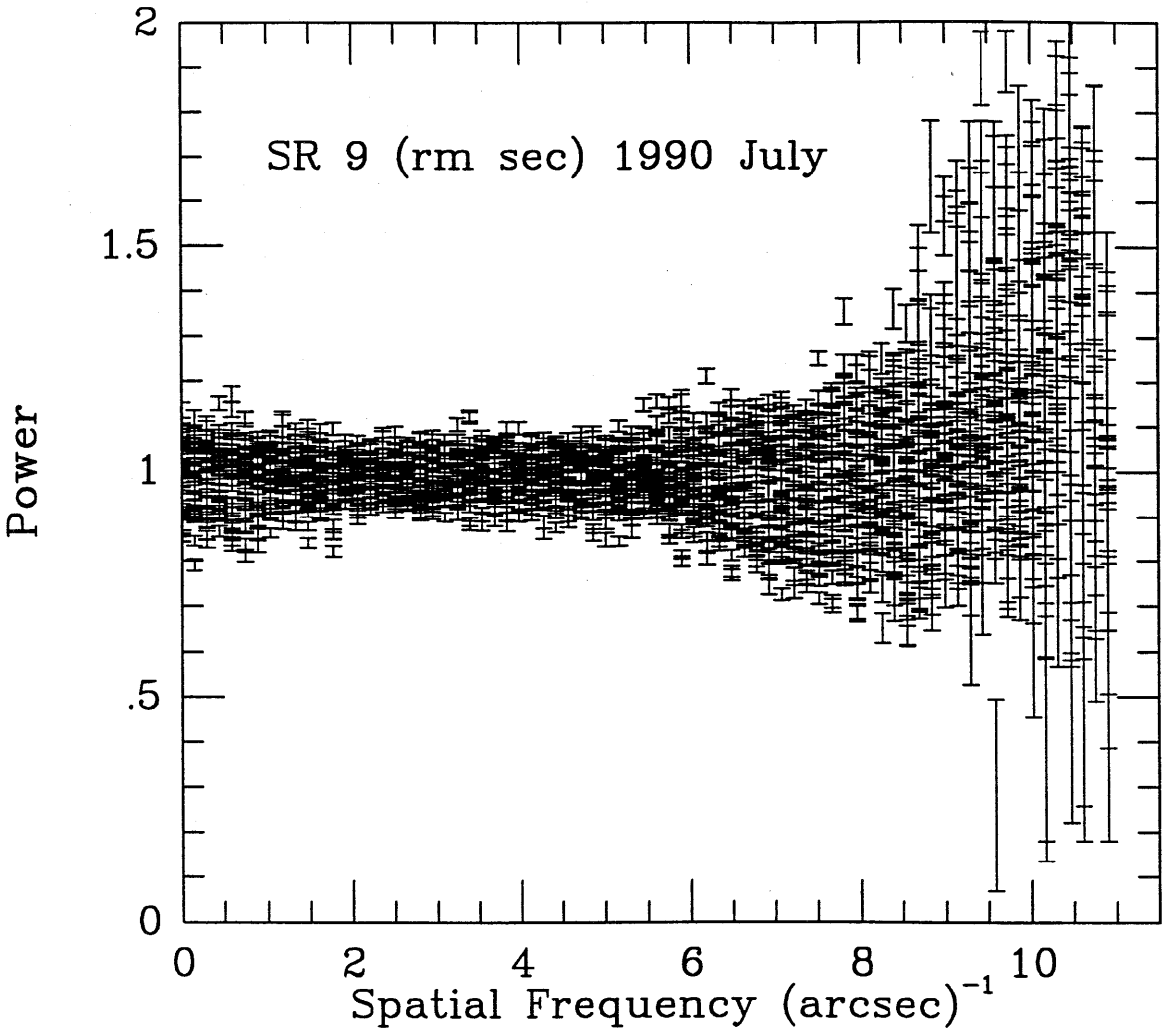
SR 9 (rm sec) 1990 July
Power
Spatial Frequency (arcsec)$^{-1}$
0
.5
1
1.5
2
0
2
4
6
8
10

Figure A.79

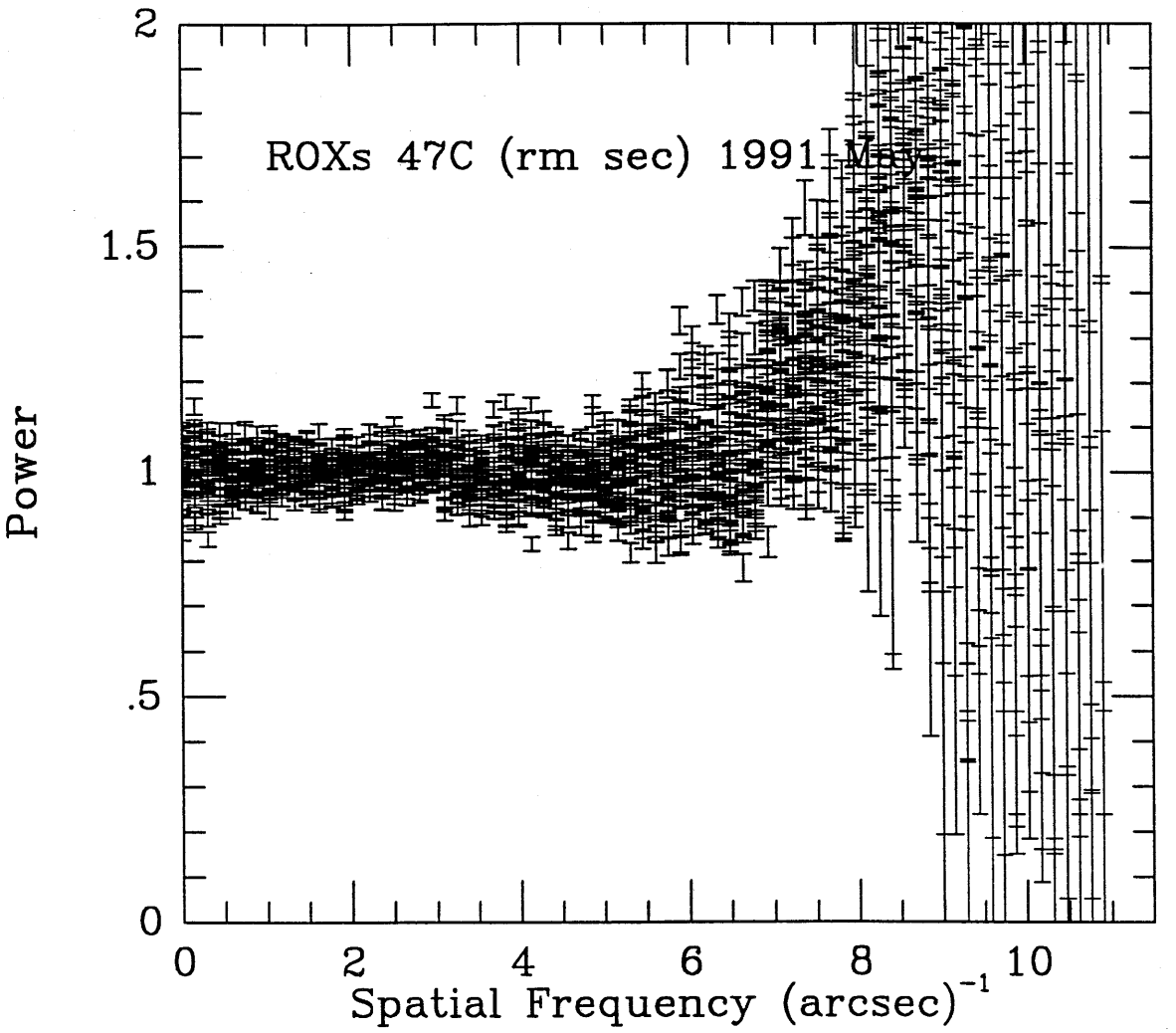
ROXs 47C (rm sec) 1991 May
Power
2
1.5
1
.5
0
0
2
4
6
8
10
Spatial Frequency (arcsec)$^{-1}$

Figure A.80

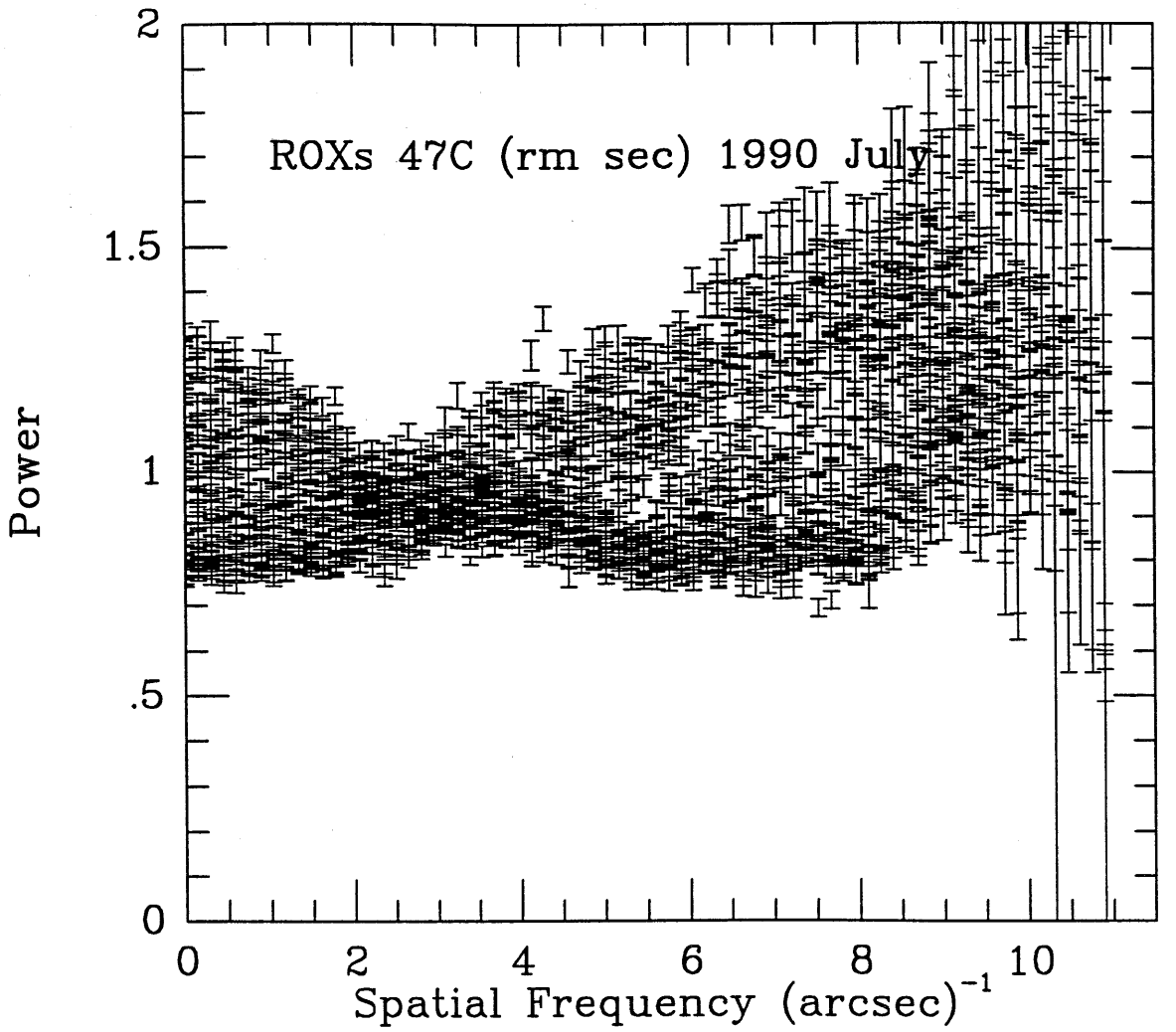
ROXs 47C (rm sec) 1990 July
Power
2
1.5
1
.5
0
0
2
4
6
8
10
Spatial Frequency (arcsec)$^{-1}$

Figure A.81

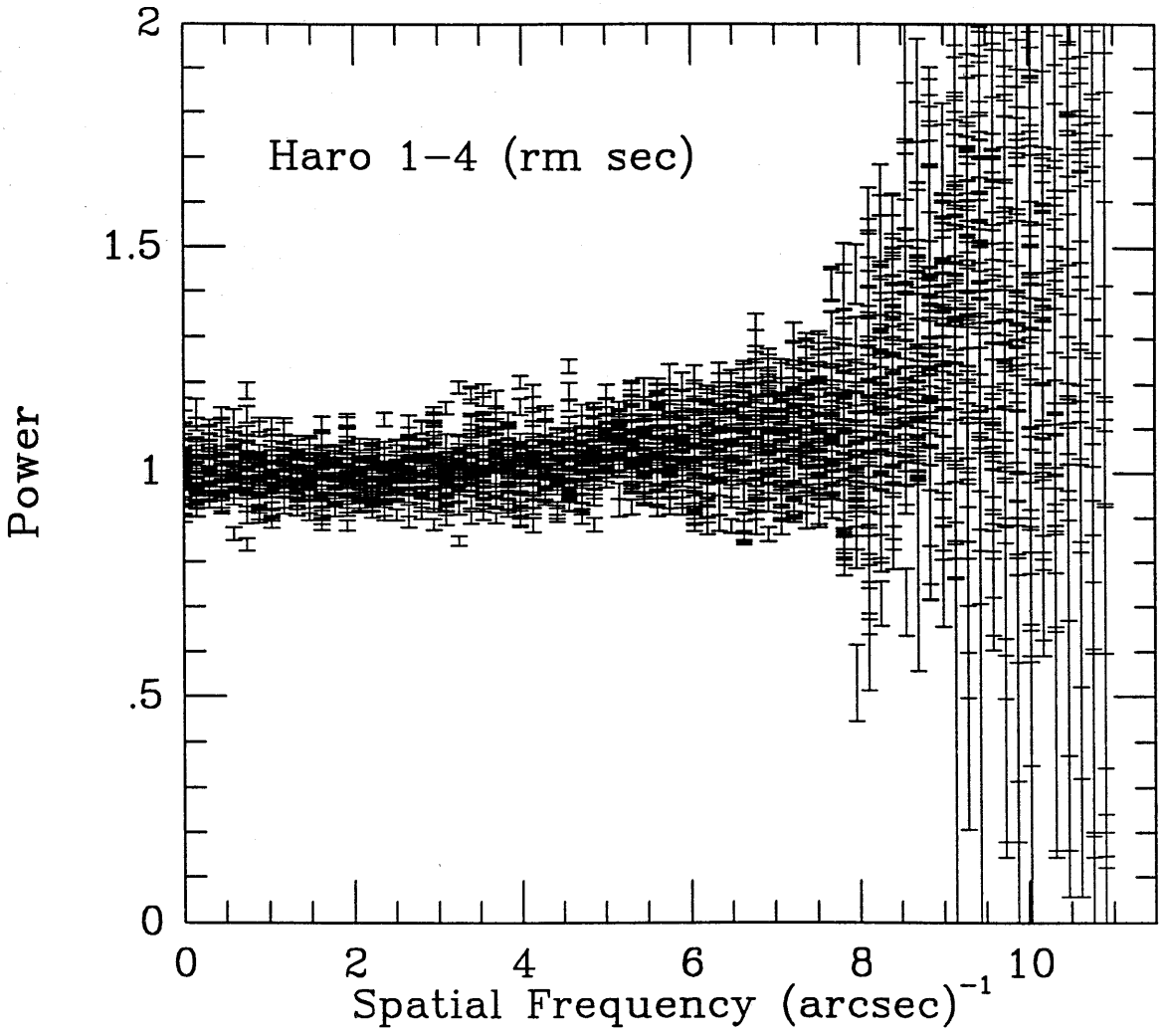
Haro 1−4 (rm sec)
Power
2
1.5
1
.5
0
0
2
4
6
8
10
Spatial Frequency (arcsec)$^{-1}$

Figure A.82

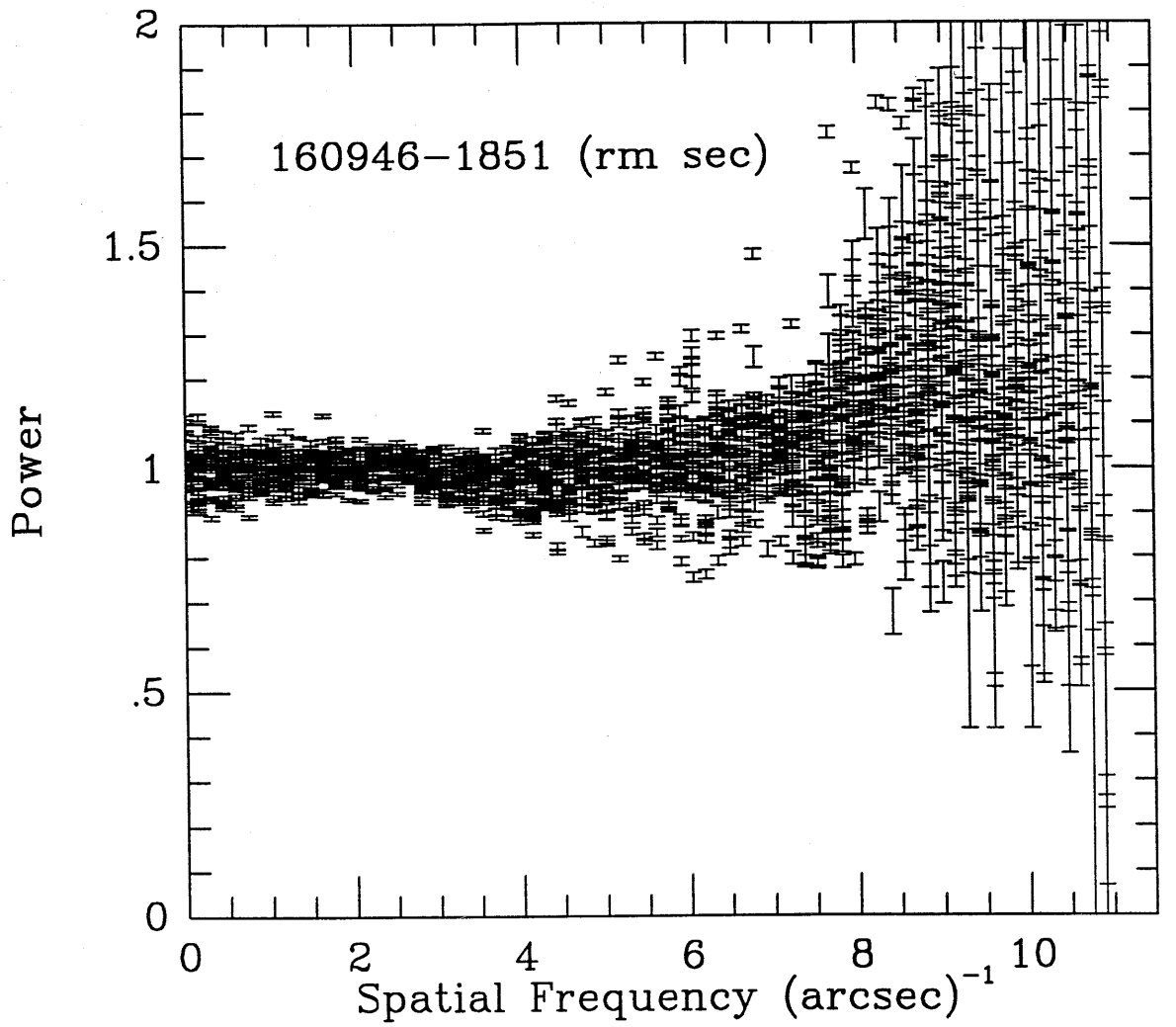
160946−1851 (rm sec)
Power
2
1.5
1
.5
0
0
2
4
6
8
10
Spatial Frequency (arcsec)$^{-1}$

Figure A.83

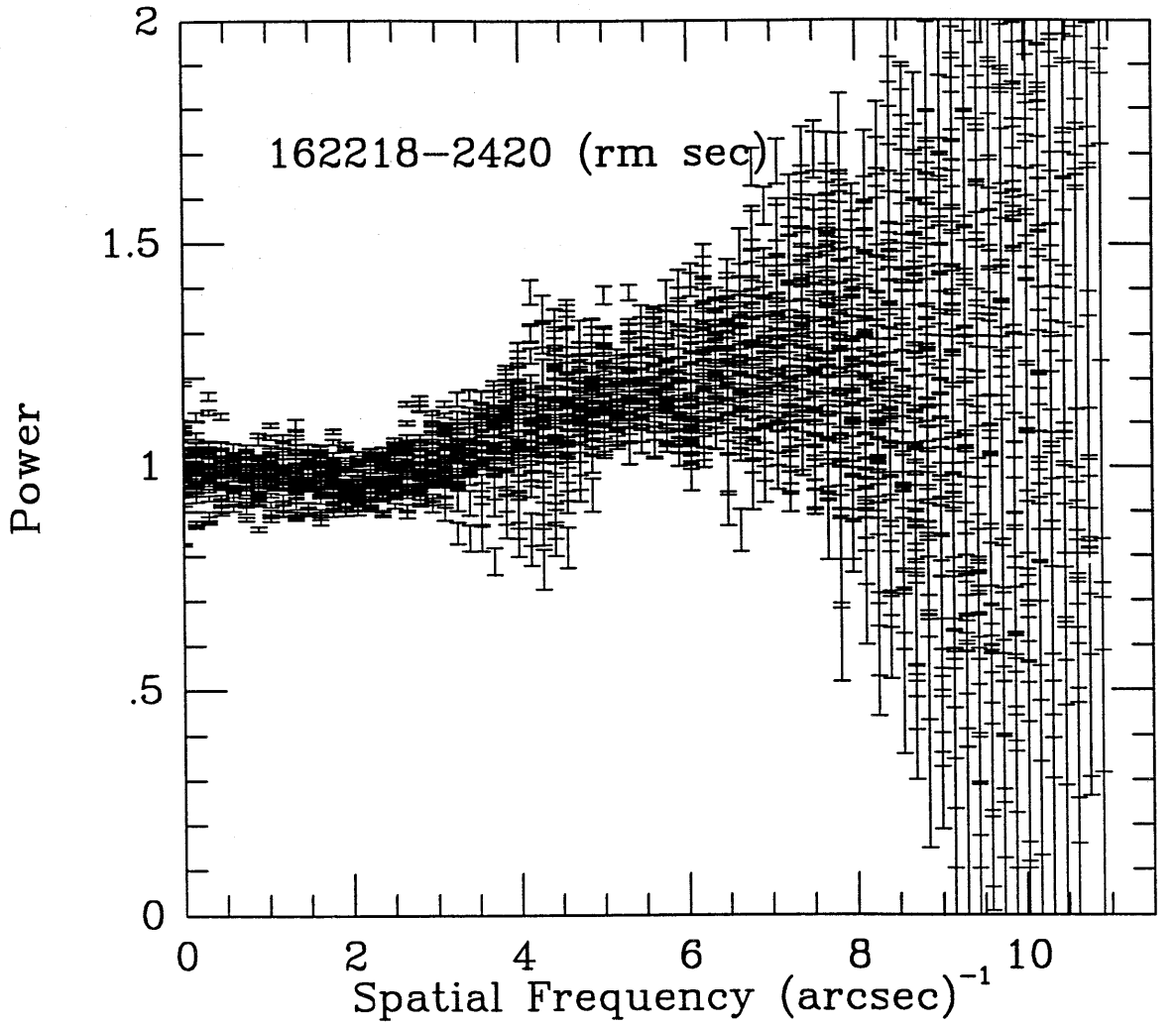
162218−2420 (rm sec)
Power
2
1.5
1
.5
0
0
2
4
6
8
10
Spatial Frequency (arcsec)$^{-1}$

Figure A.84

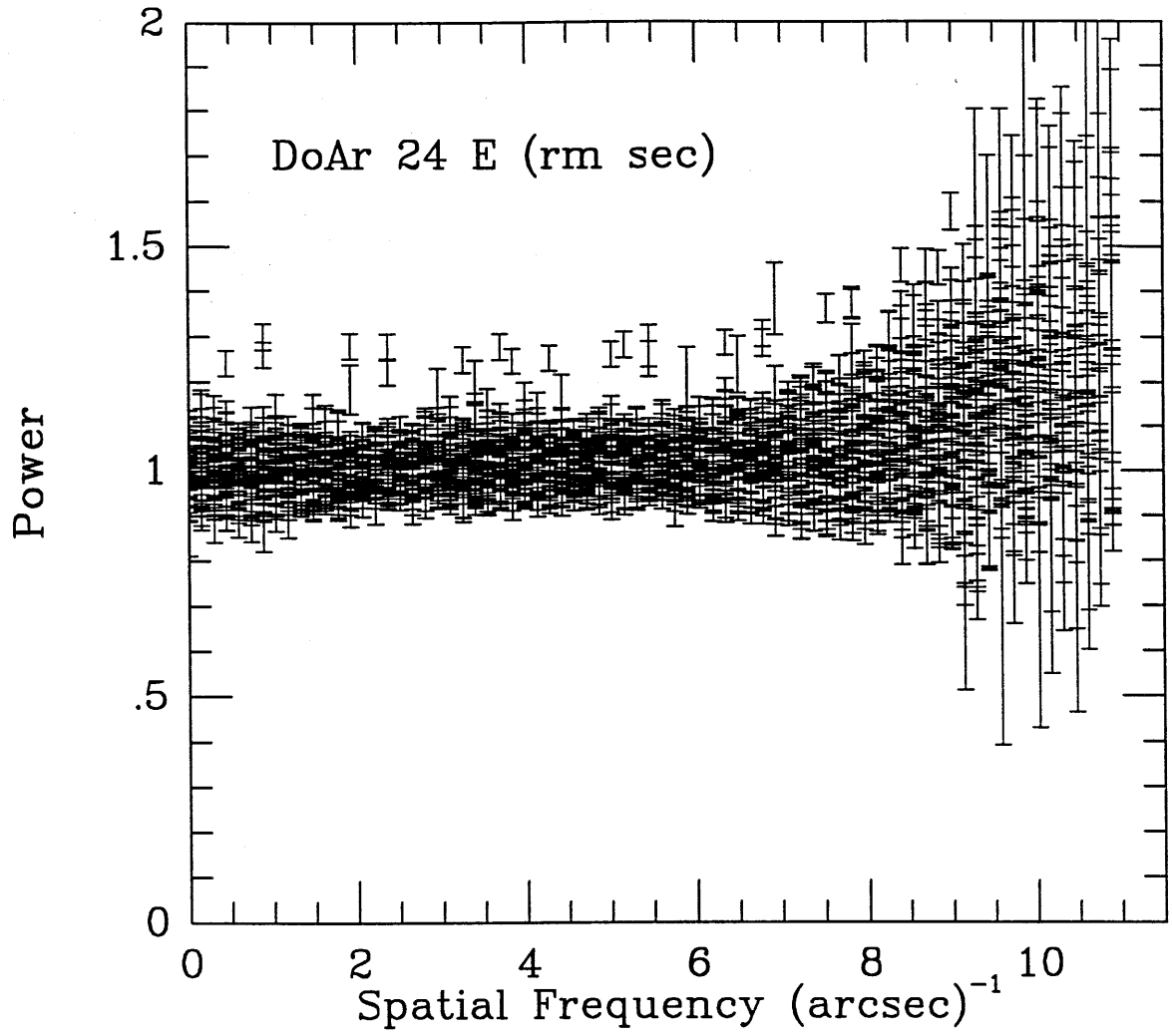
DoAr 24 E (rm sec)
Power
2
1.5
1
.5
0
0
2
4
6
8
10
Spatial Frequency (arcsec)$^{-1}$

Figure A.85

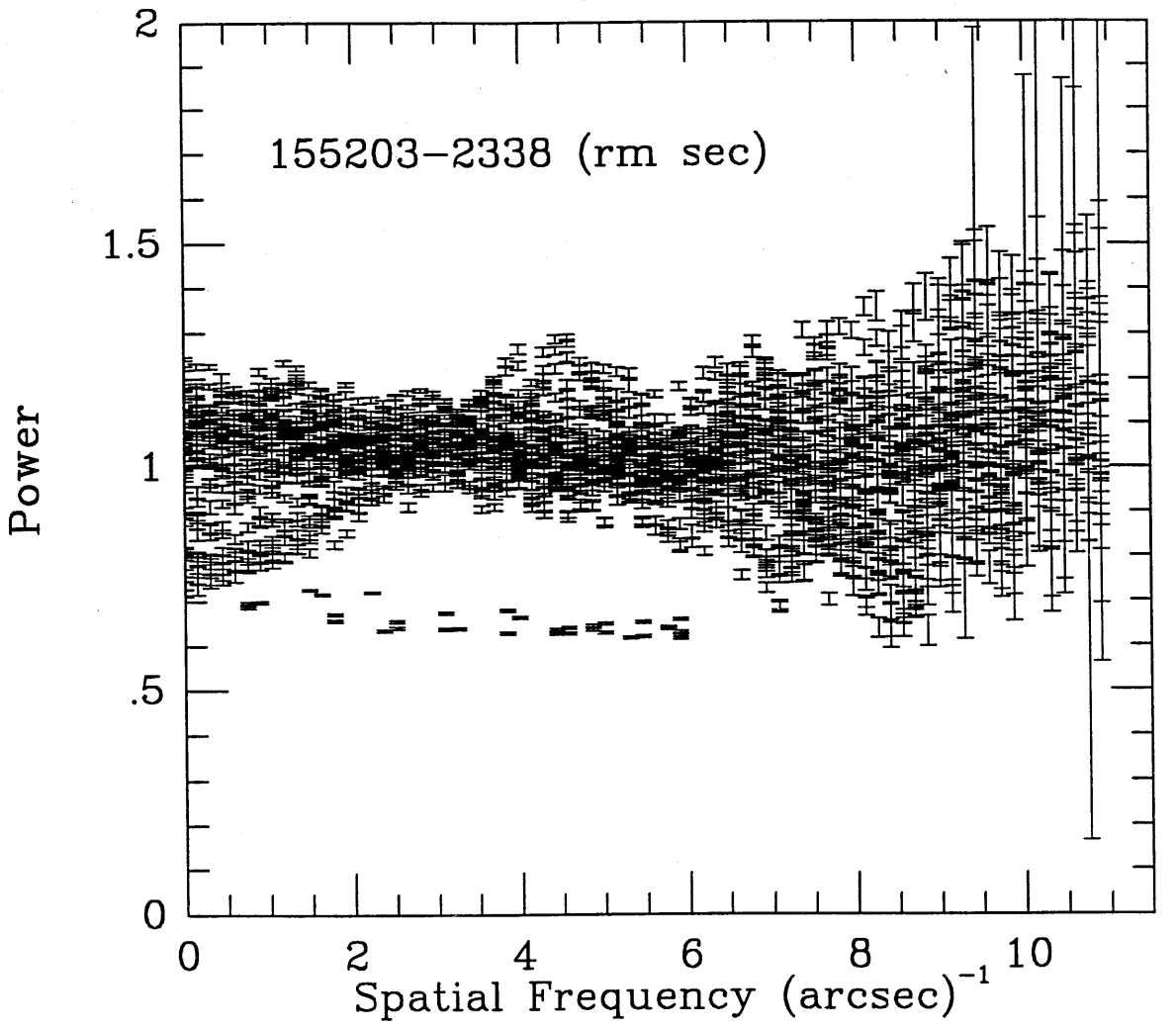
155203−2338 (rm sec)
Power
2
1.5
1
.5
0
0
2
4
6
8
10
Spatial Frequency (arcsec)$^{-1}$

Figure A.86

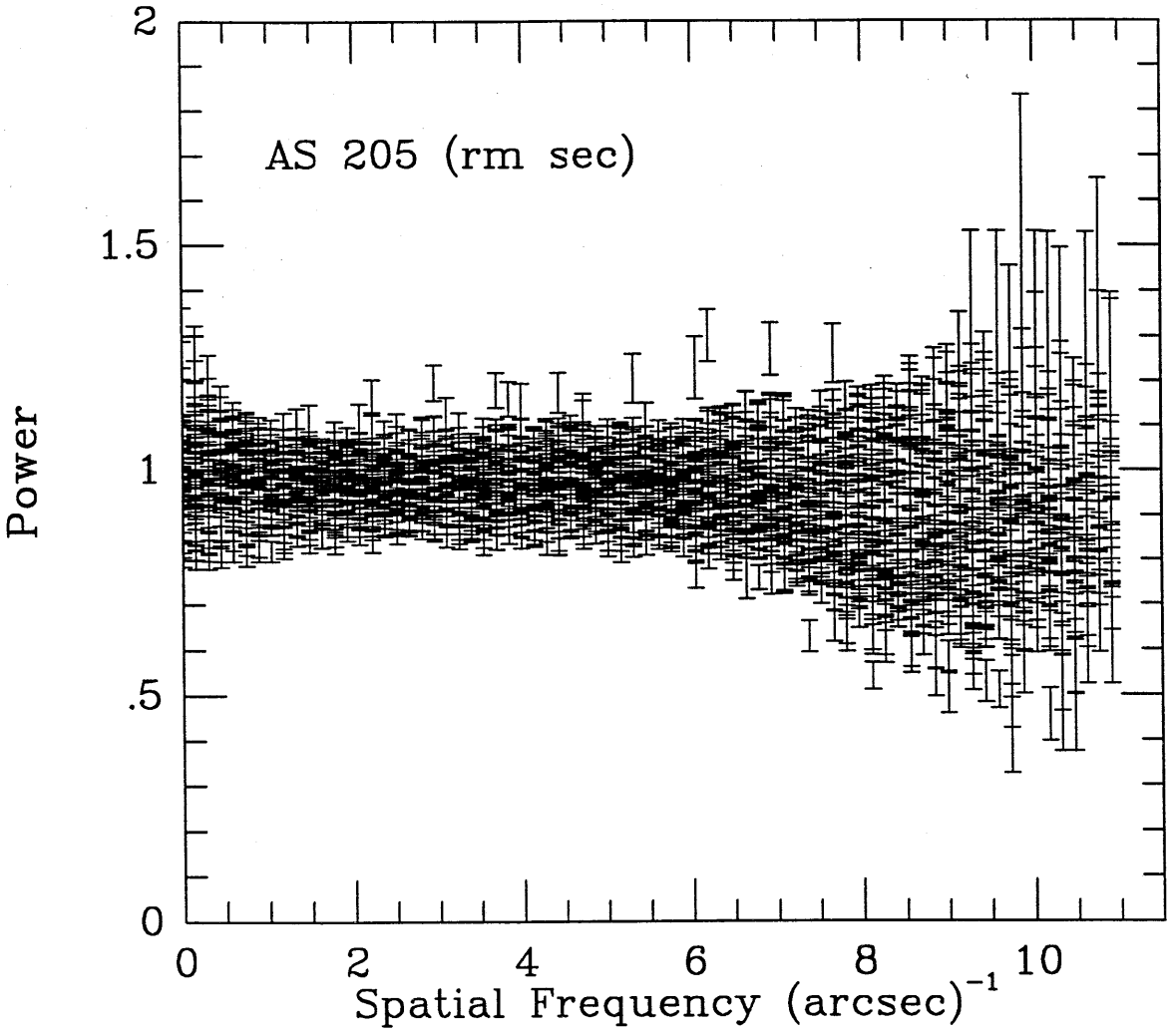
AS 205 (rm sec)
Power
2
1.5
1
.5
0
0
2
4
6
8
10
Spatial Frequency (arcsec)$^{-1}$

Figure A.87

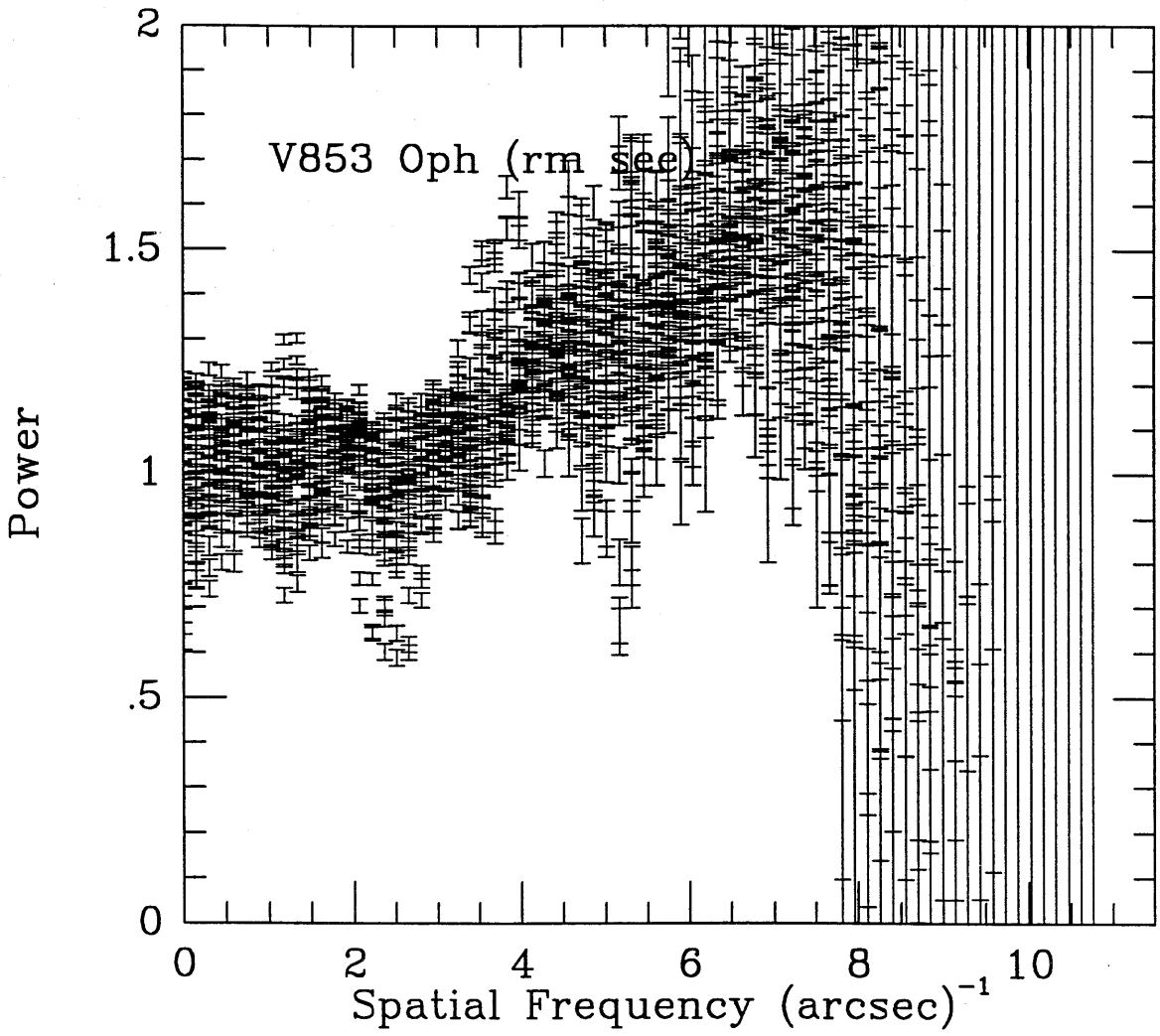
V853 Oph (rm see)
Power
Spatial Frequency (arcsec)$^{-1}$
0
.5
1
1.5
2
0
2
4
6
8
10

Figure A.88

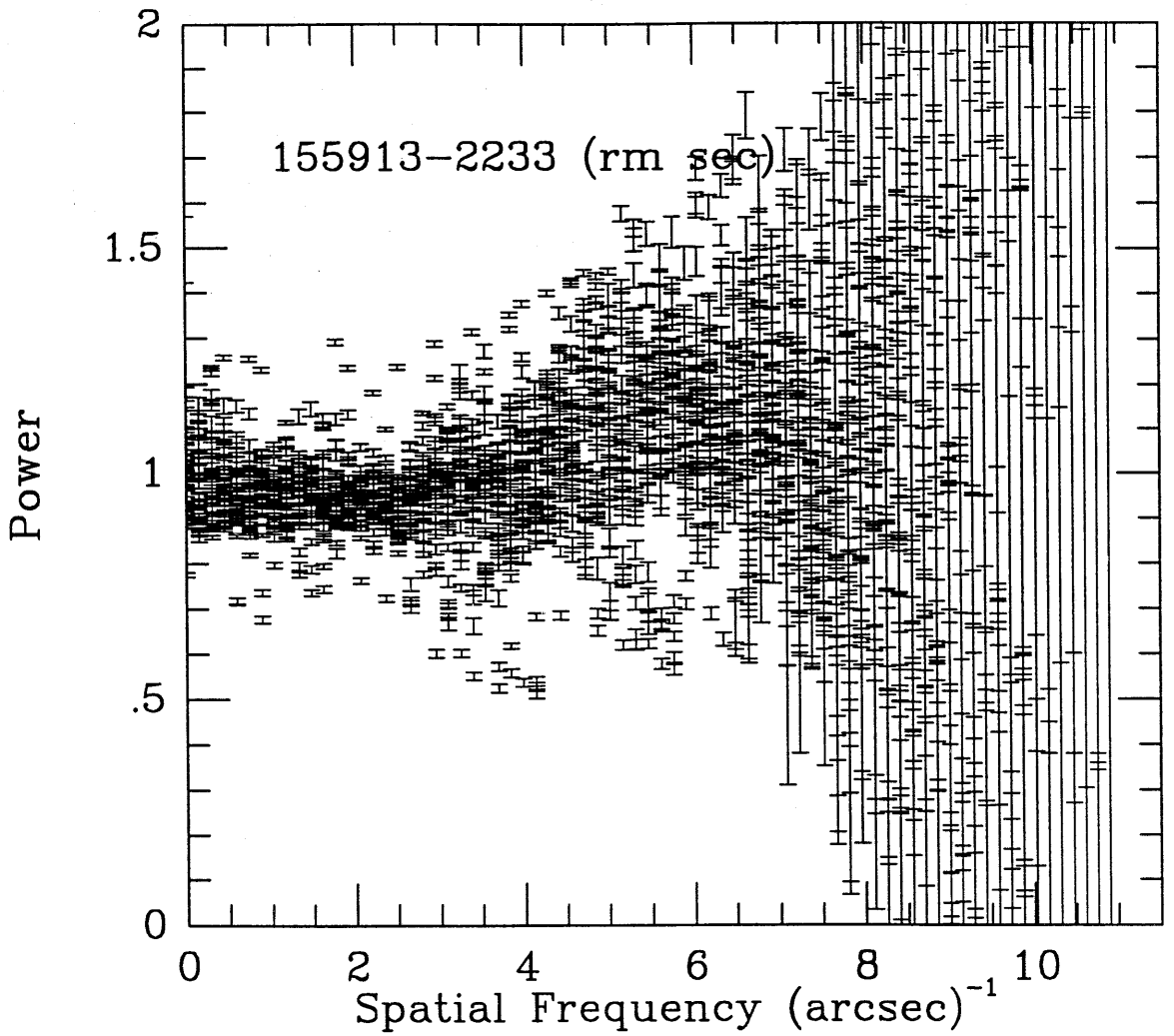
155913-2233 (rm sec)
Power
Spatial Frequency (arcsec)$^{-1}$
0
.5
1
1.5
2
0
2
4
6
8
10

Figure A.89

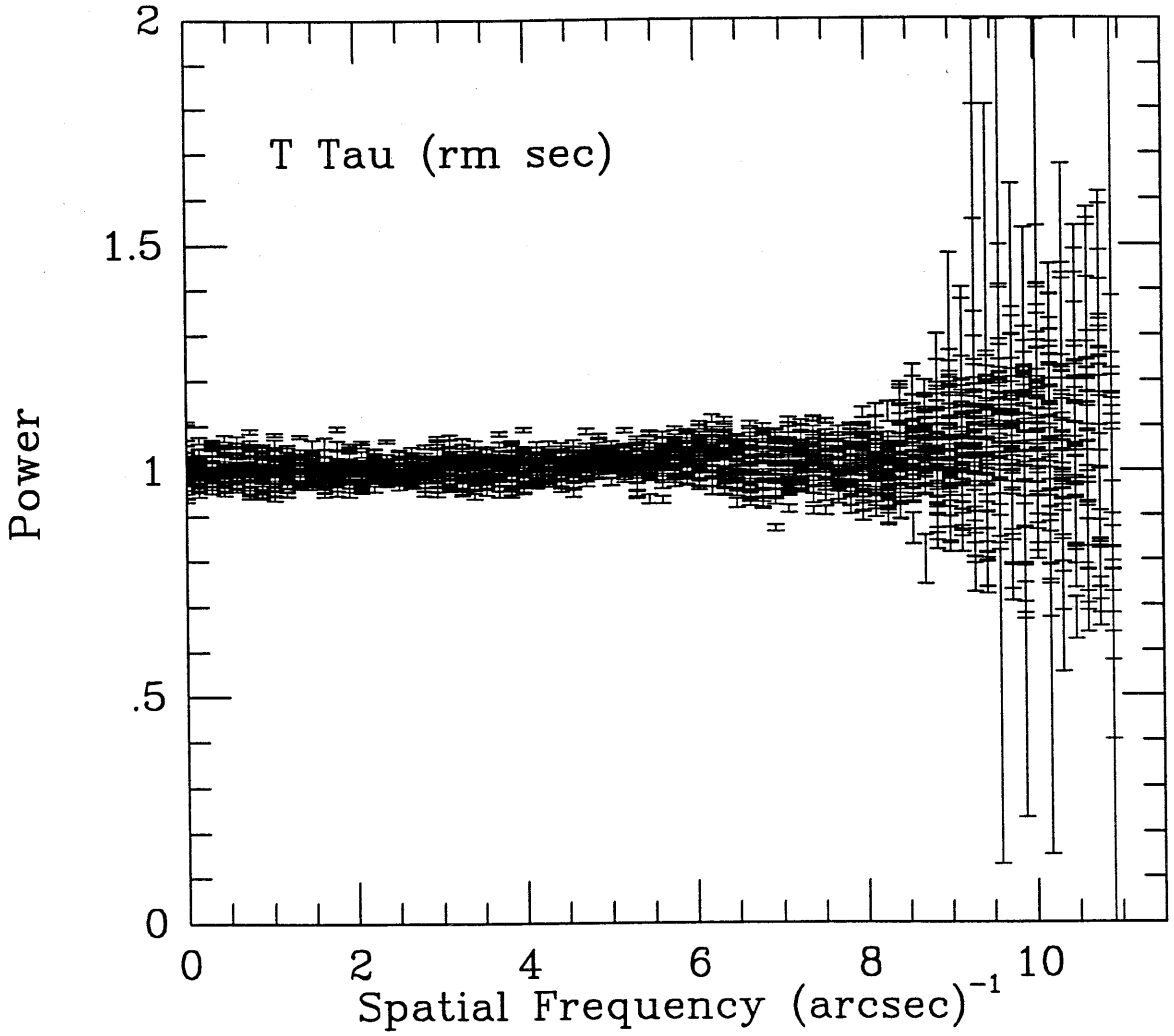
T Tau (rm sec)
Power
2
1.5
1
.5
0
0
2
4
6
8
10
Spatial Frequency (arcsec)$^{-1}$

Figure A.90

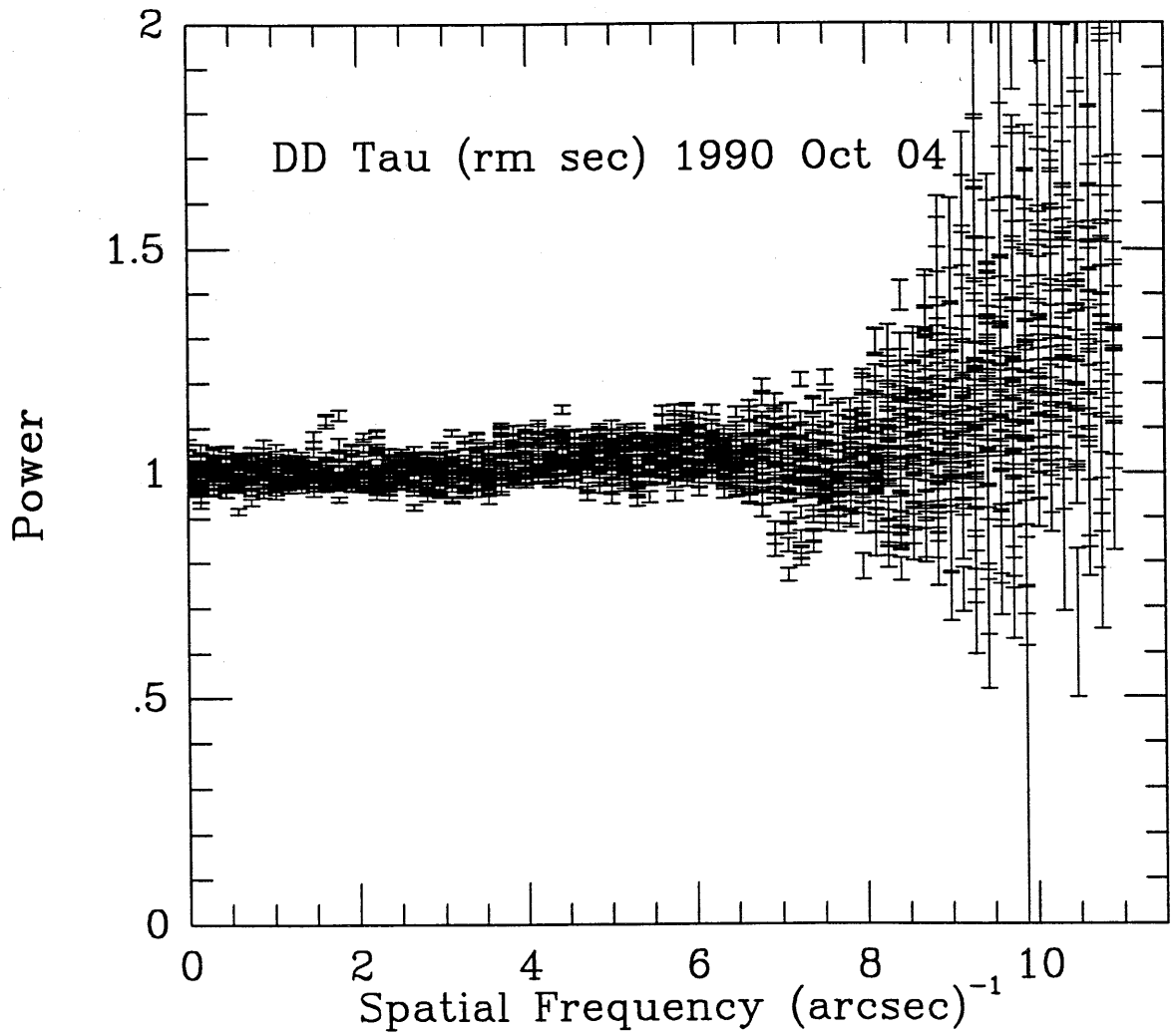
DD Tau (rm sec) 1990 Oct 04
Power
2
1.5
1
.5
0
0
2
4
6
8
10
Spatial Frequency (arcsec)$^{-1}$

Figure A.91

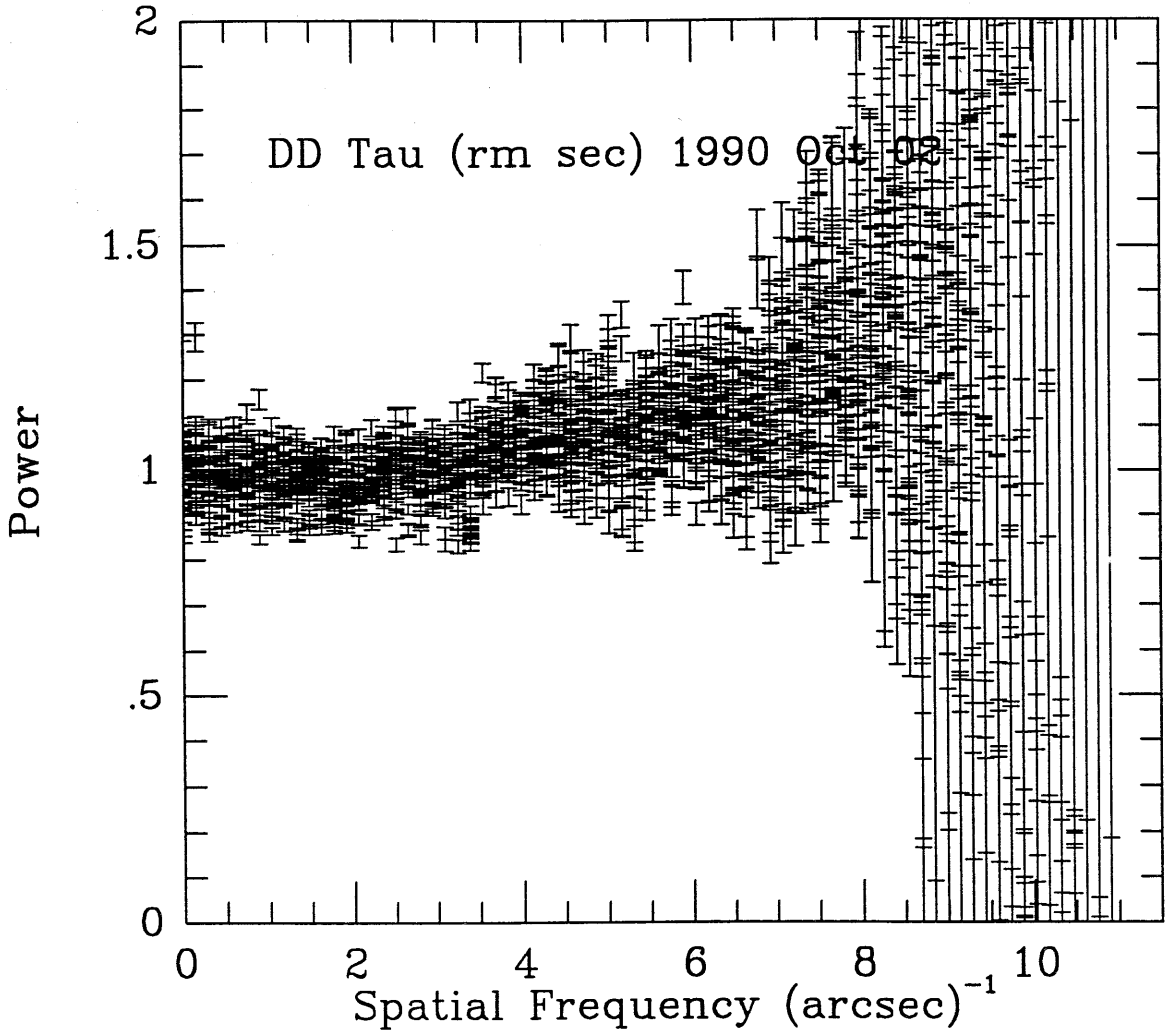
DD Tau (rm sec) 1990 Oct 02
Power
Spatial Frequency (arcsec)$^{-1}$
0
.5
1
1.5
2
0
2
4
6
8
10

Figure A.92

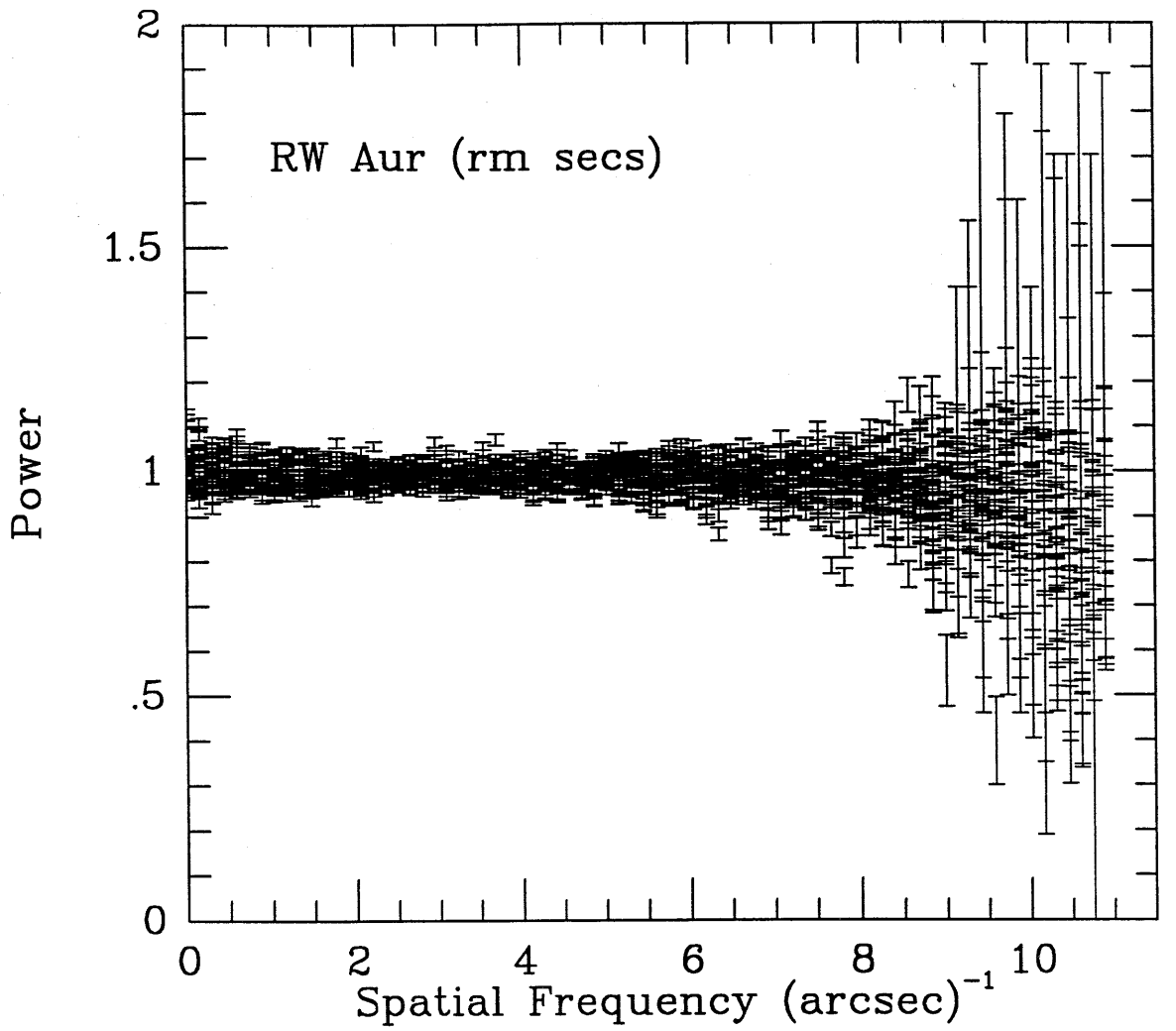
RW Aur (rm secs)
Power
2
1.5
1
.5
0
0
2
4
6
8
10
Spatial Frequency (arcsec)$^{-1}$

Figure A.93

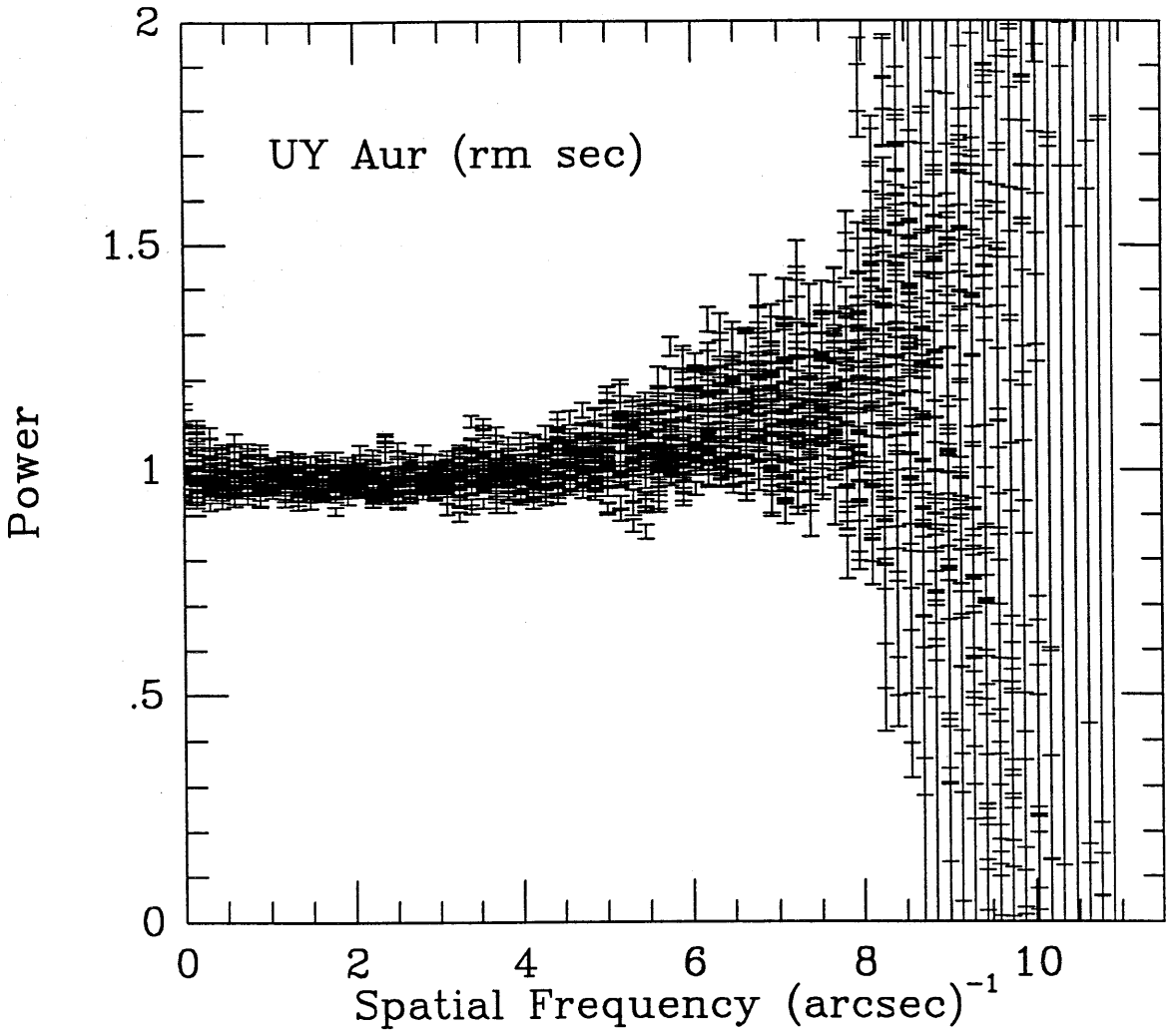
UY Aur (rm sec)
Power
2
1.5
1
.5
0
0
2
4
6
8
10
Spatial Frequency (arcsec)$^{-1}$

Figure A.94

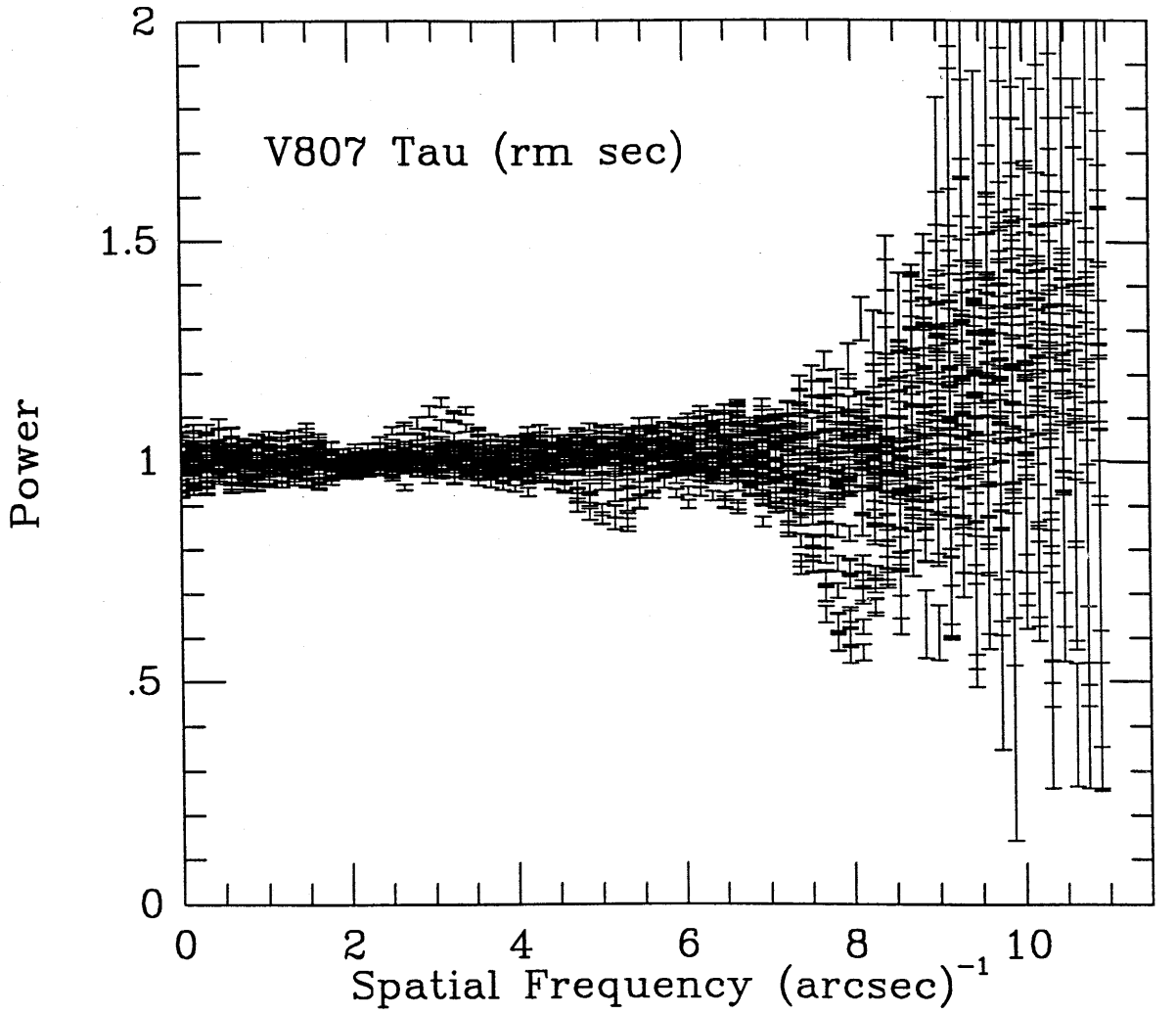
V807 Tau (rm sec)
Power
2
1.5
1
.5
0
0
2
4
6
8
10
Spatial Frequency (arcsec)$^{-1}$

Figure A.95

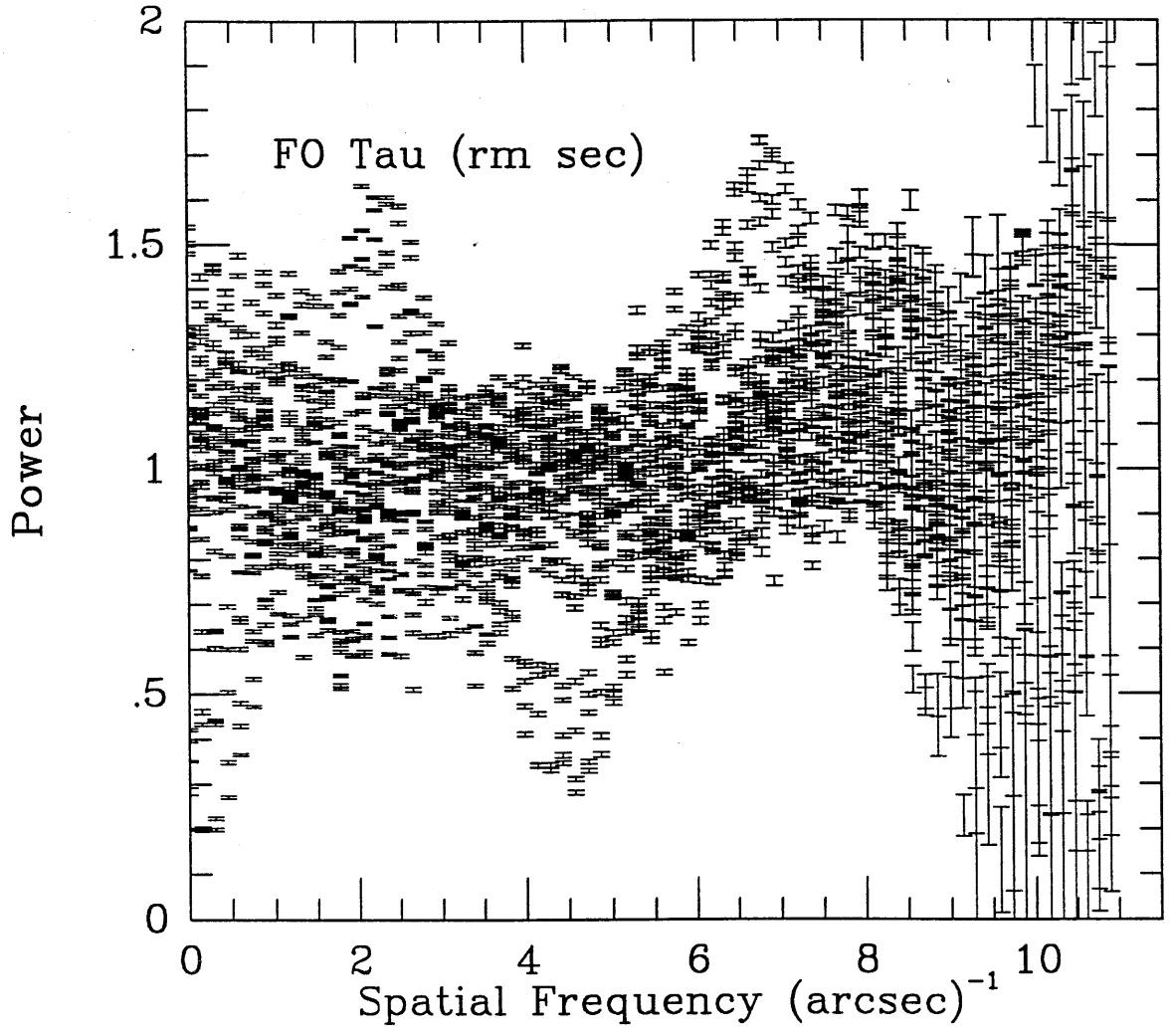
F0 Tau (rm sec)
Power
2
1.5
1
.5
0
0
2
4
6
8
10
Spatial Frequency (arcsec)$^{-1}$

Figure A.96

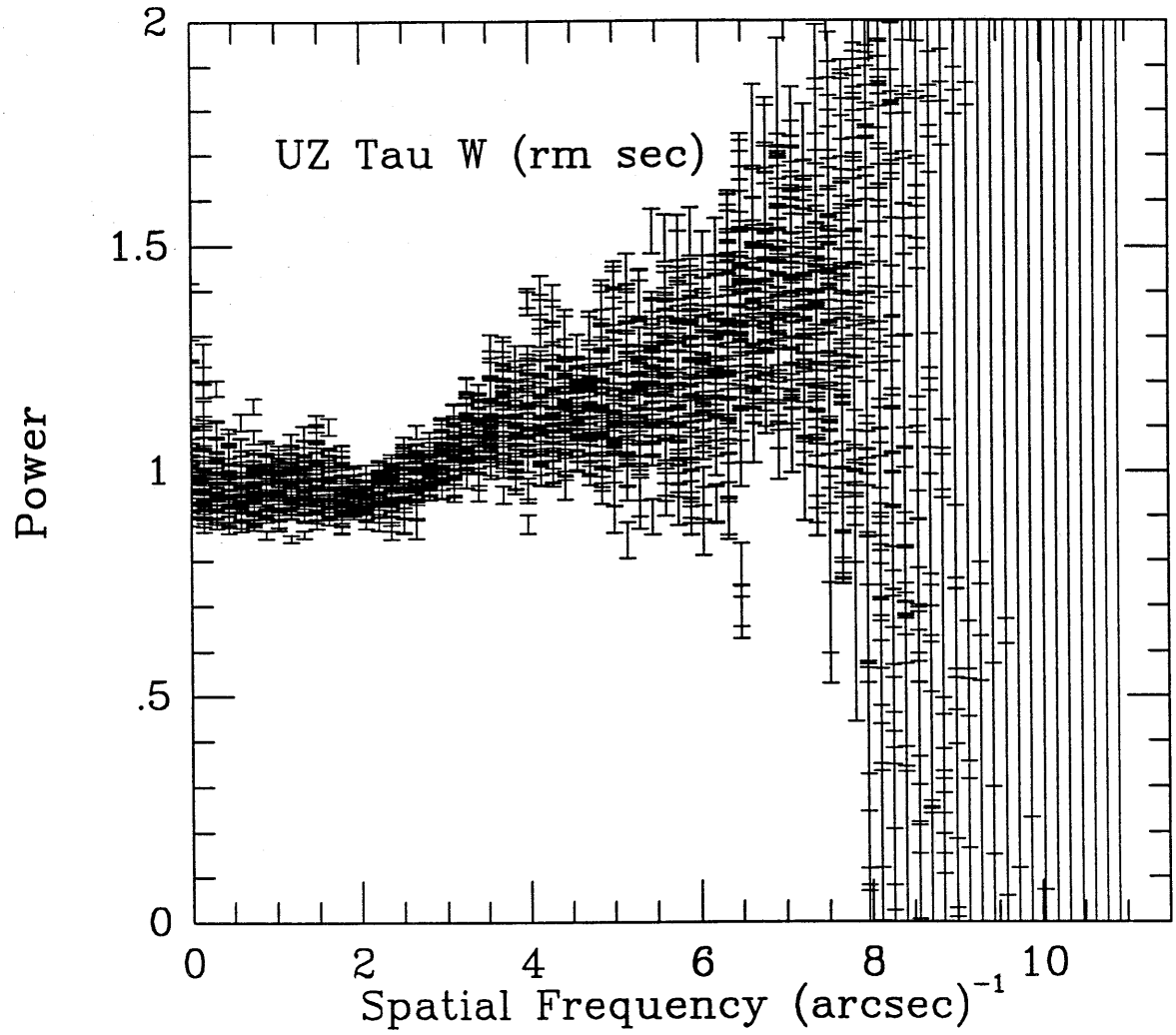
UZ Tau W (rm sec)
Power
2
1.5
1
.5
0
0
2
4
6
8
10
Spatial Frequency (arcsec)$^{-1}$

Figure A.97

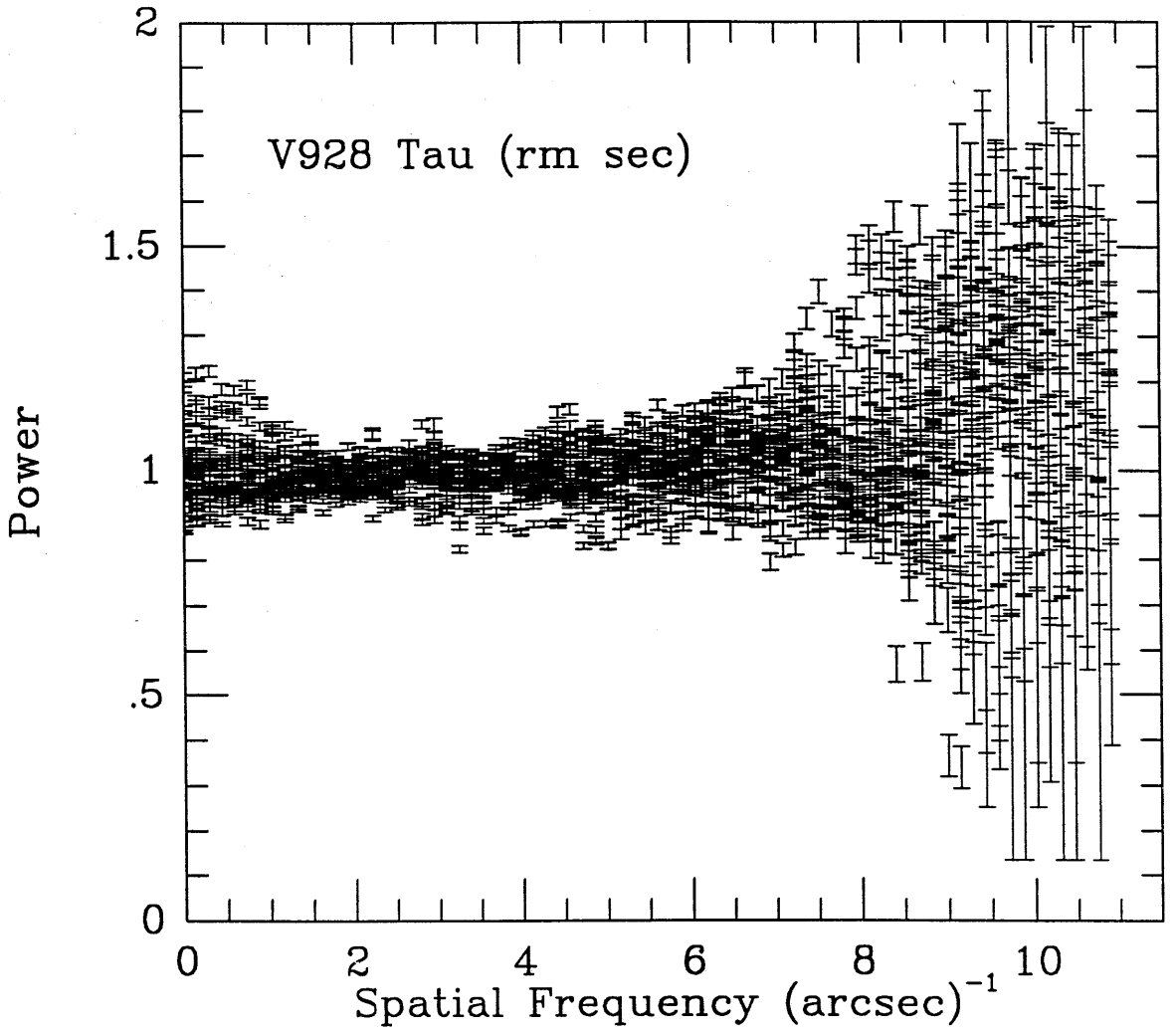
V928 Tau (rm sec)
Power
2
1.5
1
.5
0
0
2
4
6
8
10
Spatial Frequency (arcsec)$^{-1}$

Figure A.98

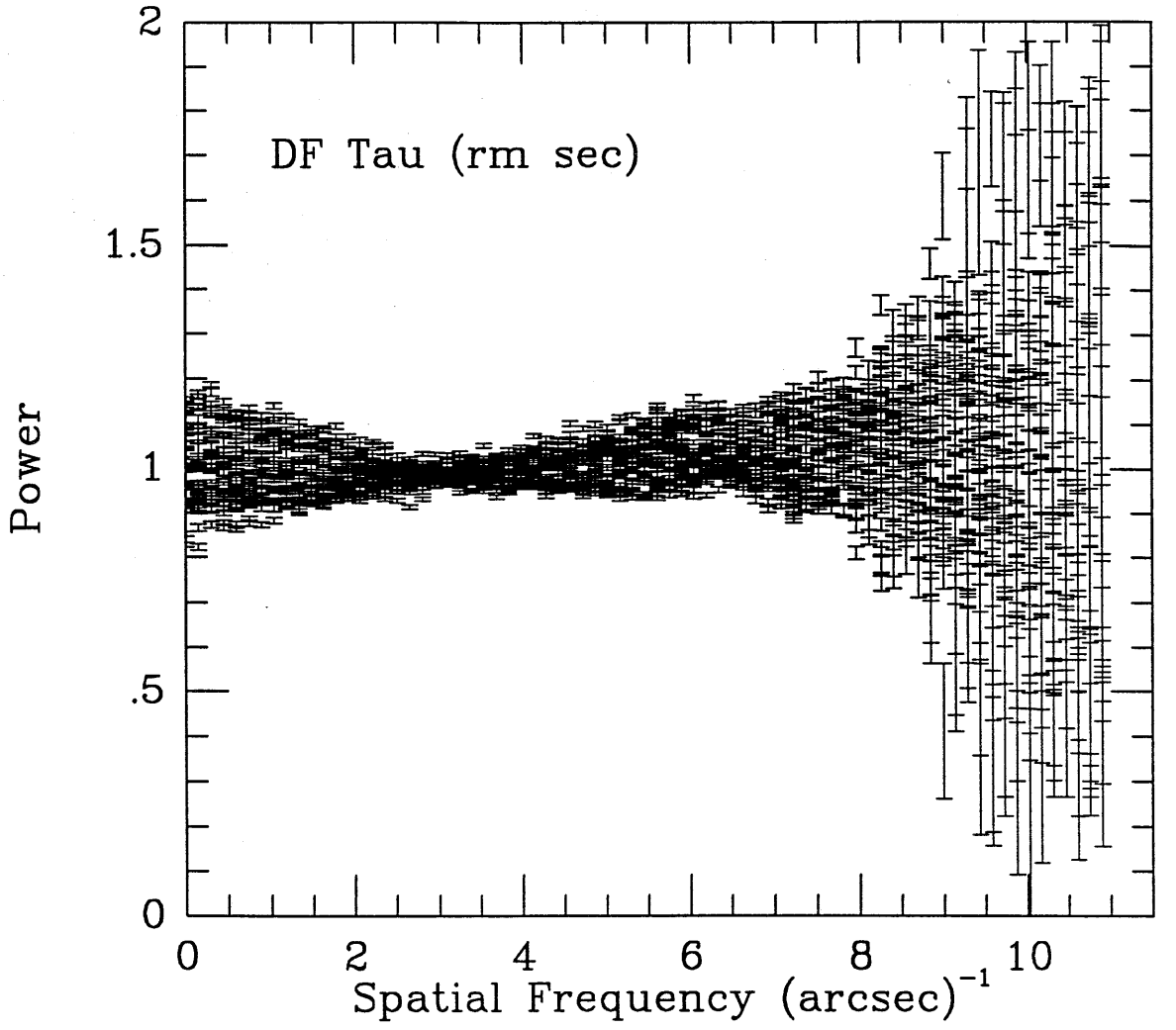
DF Tau (rm sec)
Power
2
1.5
1
.5
0
0
2
4
6
8
10
Spatial Frequency (arcsec)$^{-1}$

Figure A.99

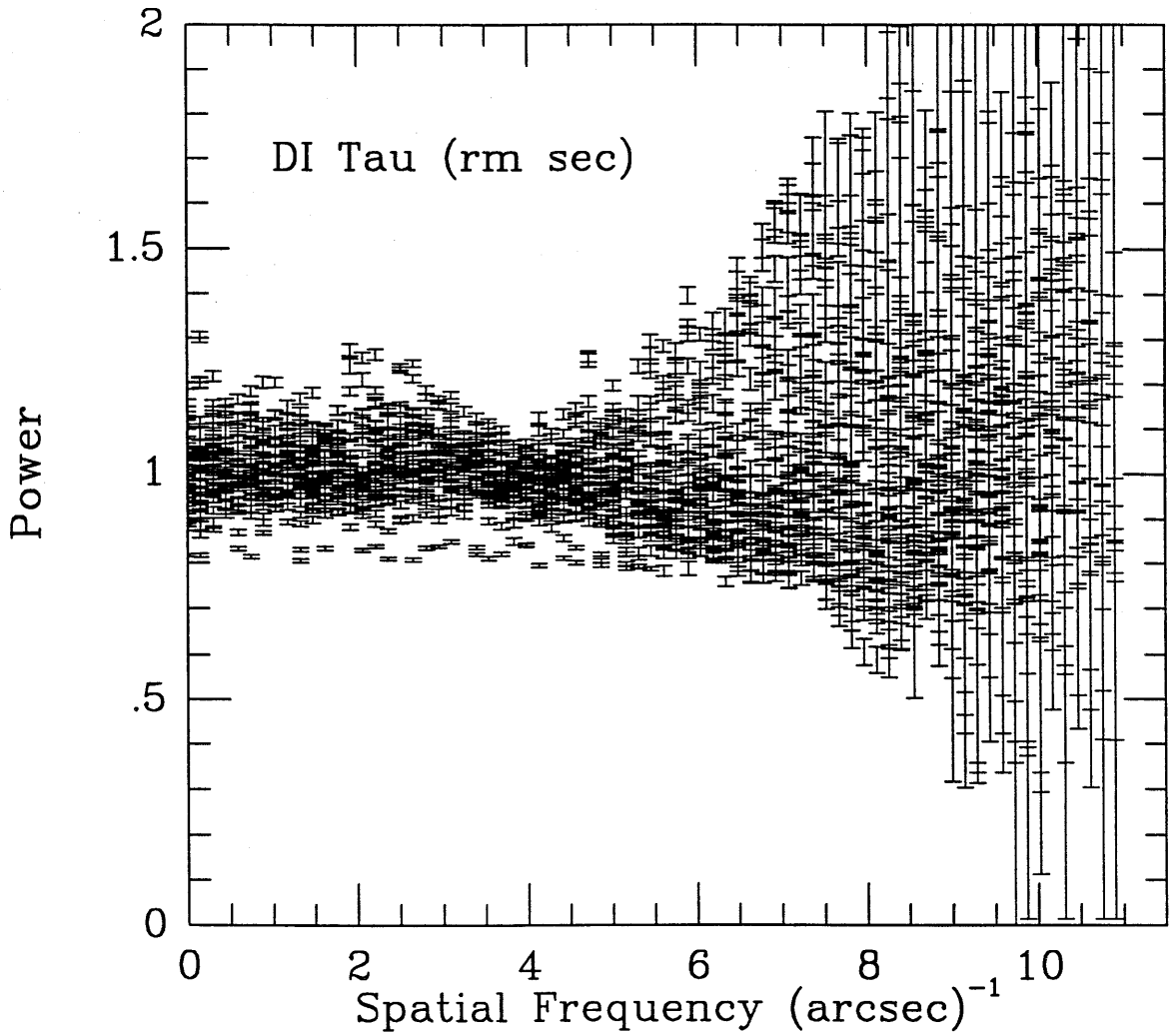
DI Tau (rm sec)
Power
2
1.5
1
.5
0
0
2
4
6
8
10
Spatial Frequency (arcsec)$^{-1}$

Figure A.100

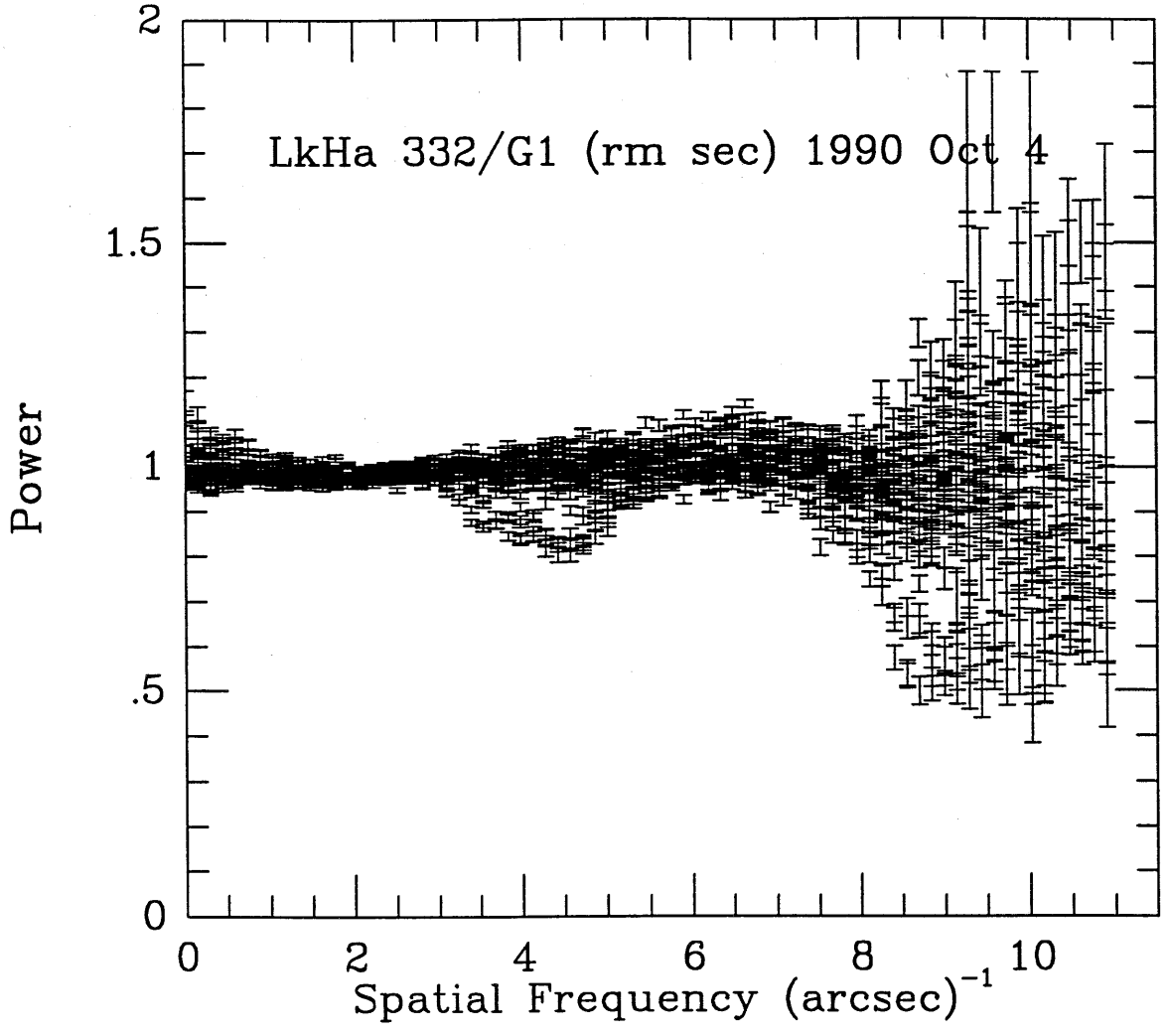
LkHa 332/G1 (rm sec) 1990 Oct 4
Power
2
1.5
1
.5
0
0
2
4
6
8
10
Spatial Frequency (arcsec)$^{-1}$

Figure A.101

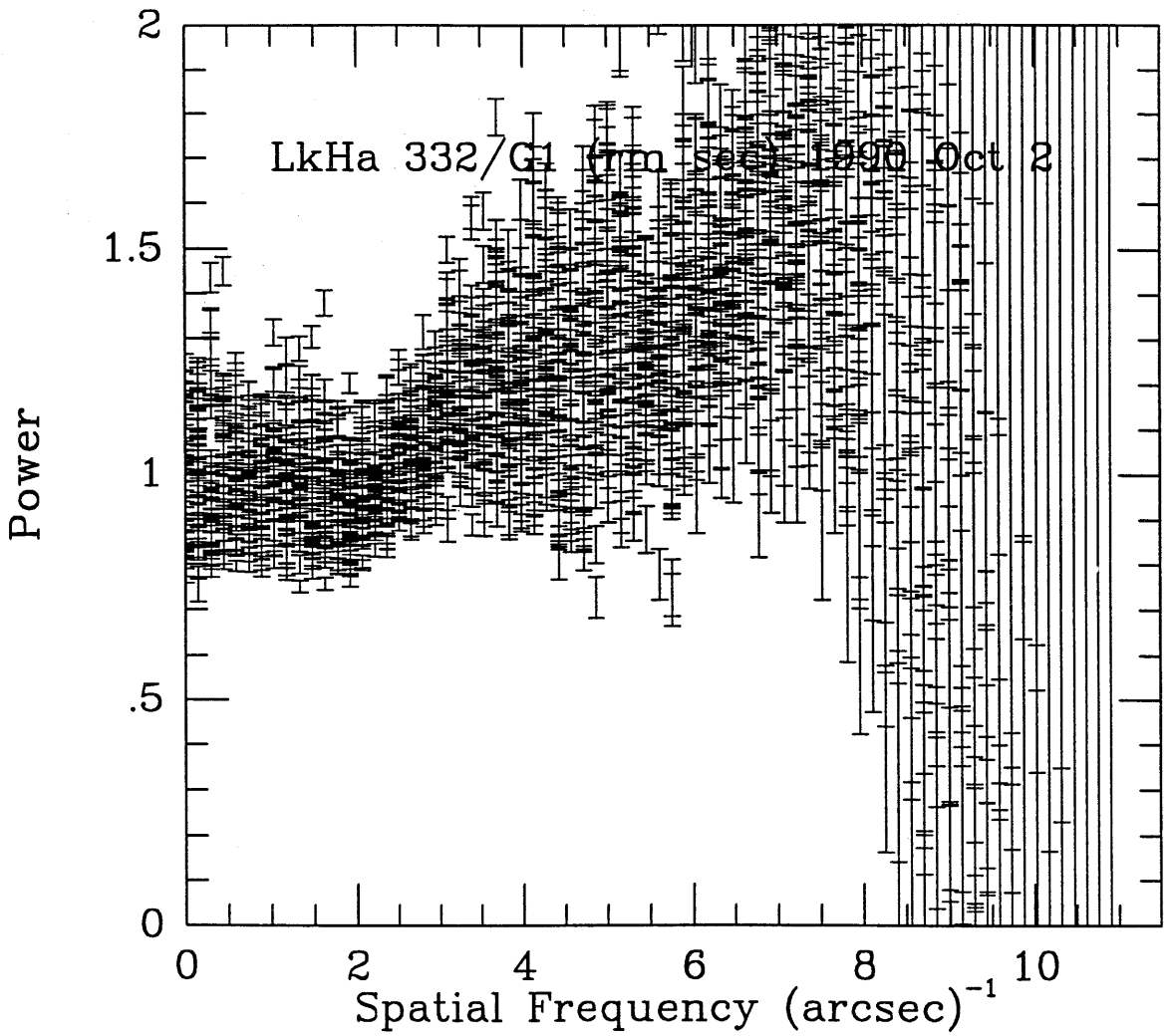
LkHa 332/G1 from sec. 1990 Oct 2
Power
Spatial Frequency (arcsec)$^{-1}$
0
.5
1
1.5
2
0
2
4
6
8
10

Figure A.102

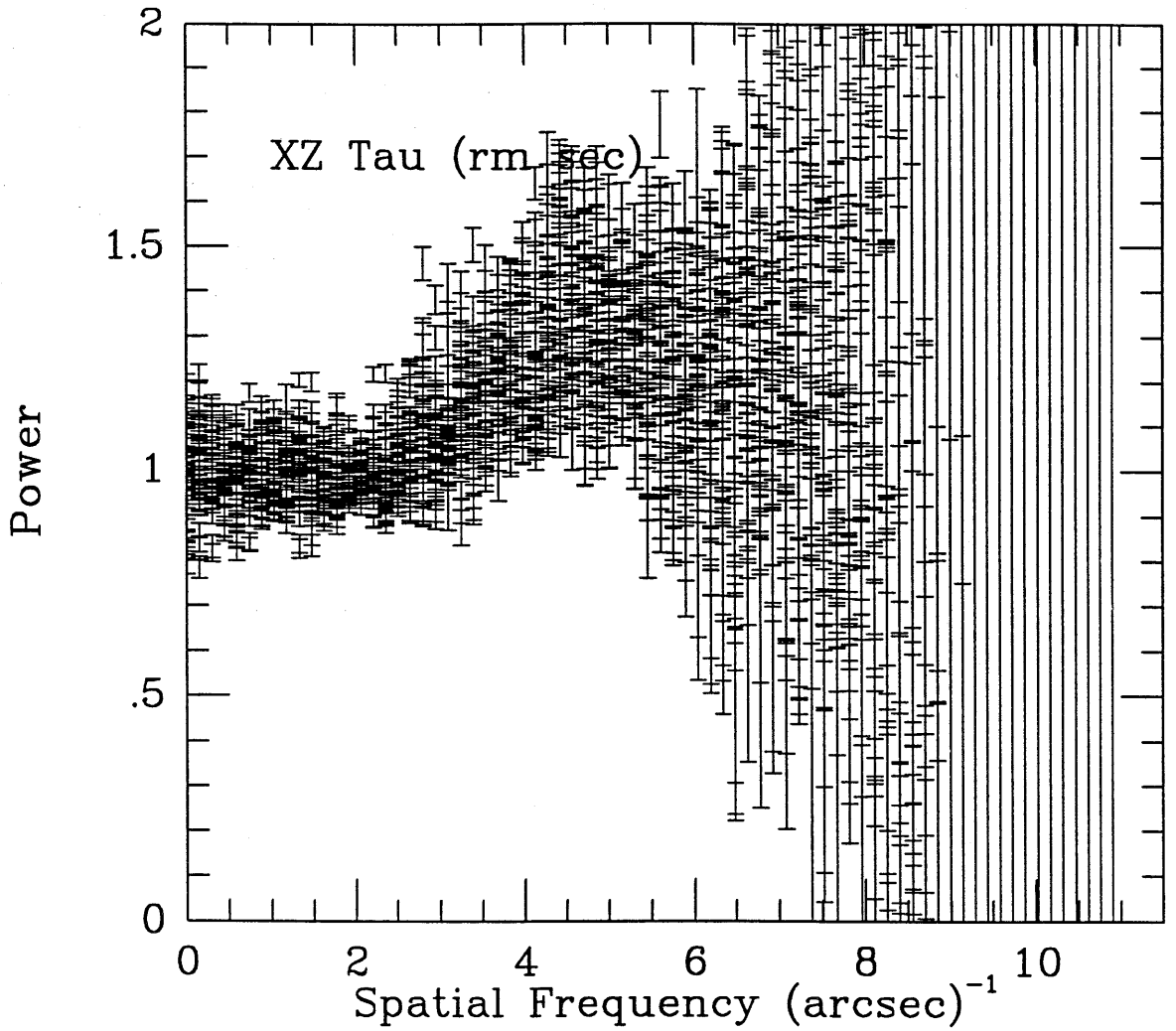
XZ Tau (rm sec)
Power
Spatial Frequency (arcsec)$^{-1}$
0
.5
1
1.5
2
0
2
4
6
8
10

Figure A.103

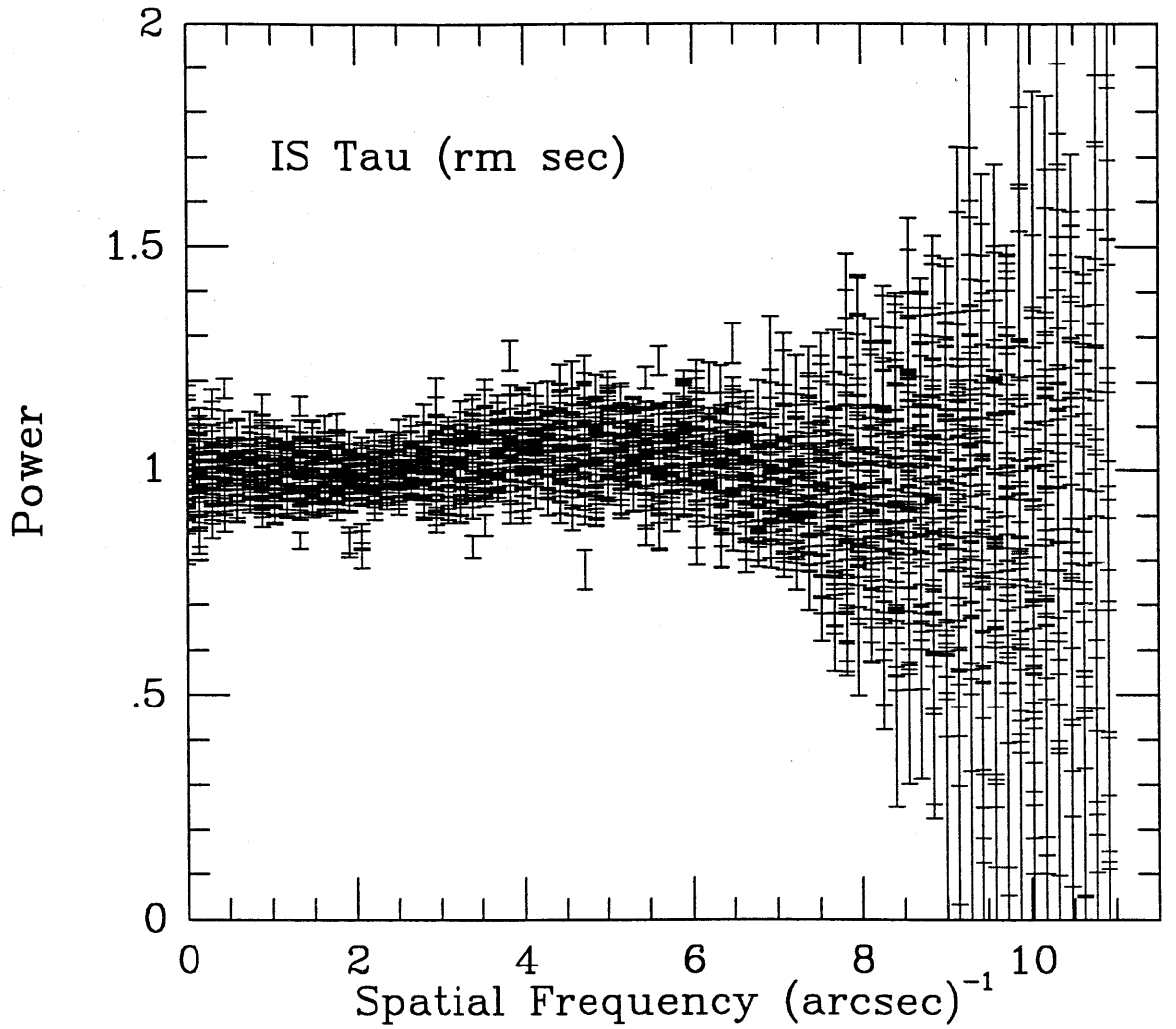
IS Tau (rm sec)
Power
2
1.5
1
.5
0
0
2
4
6
8
10
Spatial Frequency (arcsec)$^{-1}$

Figure A.104

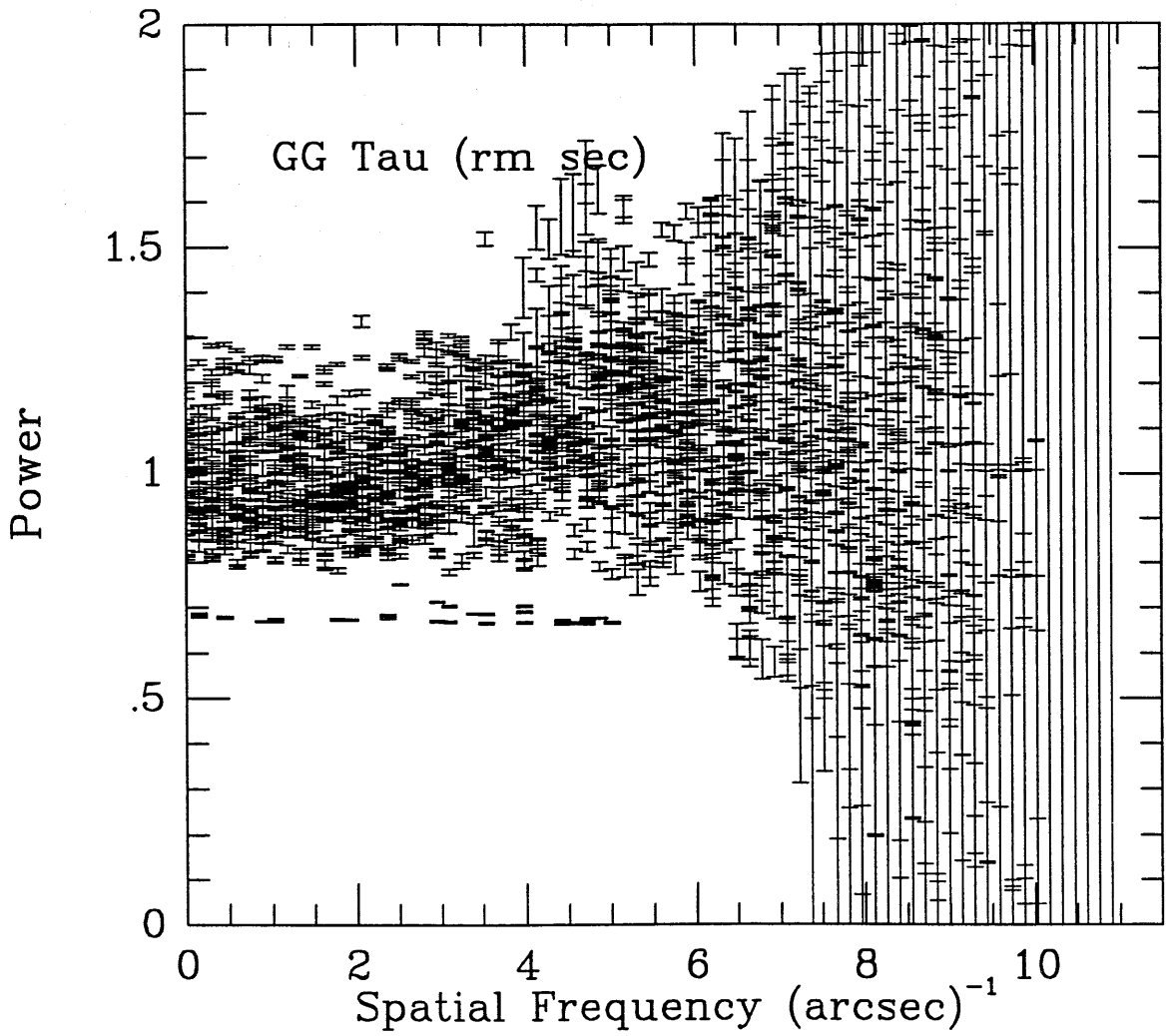
GG Tau (rm sec)
Power
2
1.5
1
.5
0
0
2
4
6
8
10
Spatial Frequency (arcsec)$^{-1}$

Figure A.105

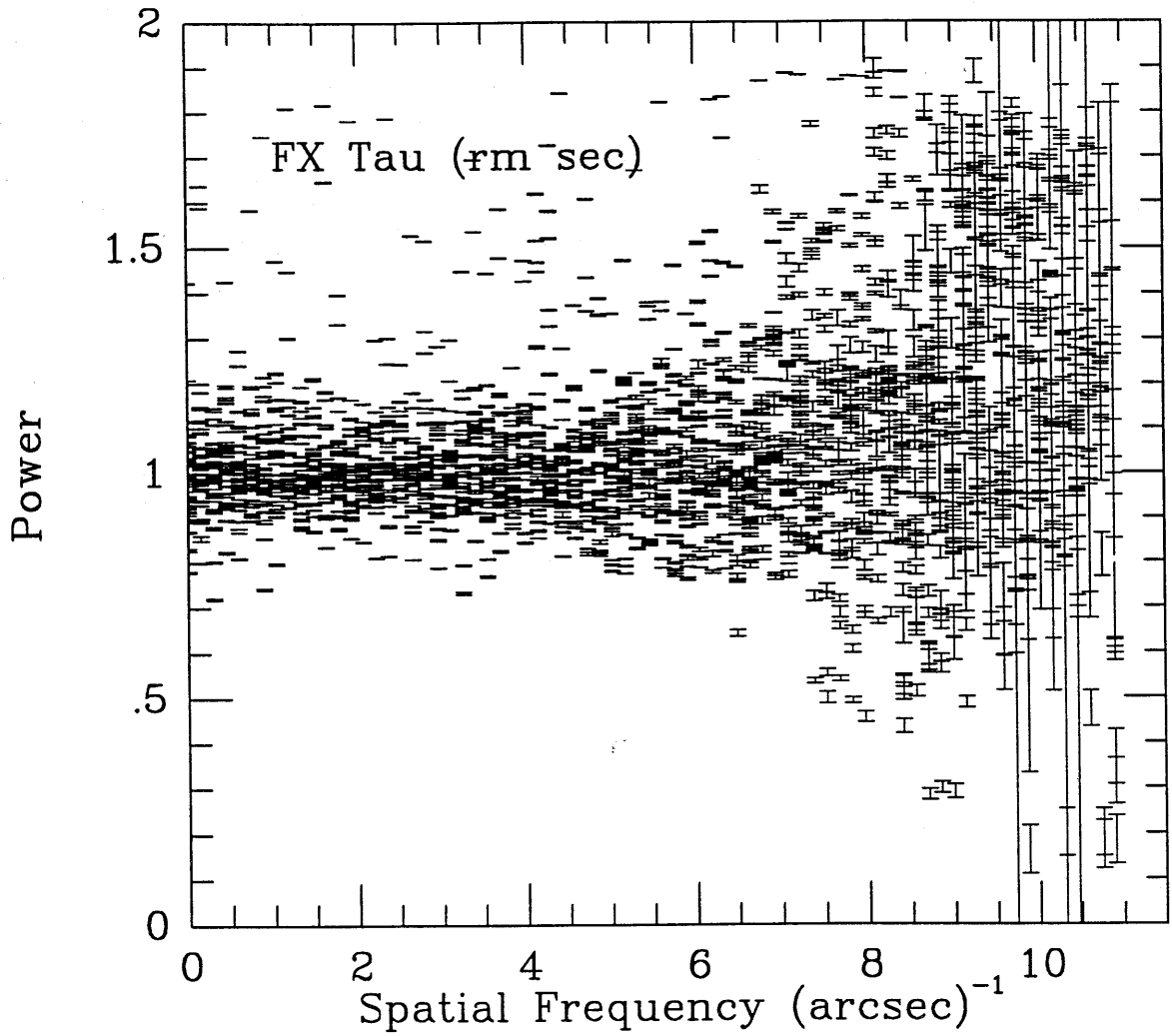
FX Tau (rm sec)
Power
2
1.5
1
.5
0
0
2
4
6
8
10
Spatial Frequency (arcsec)$^{-1}$

Figure A.106

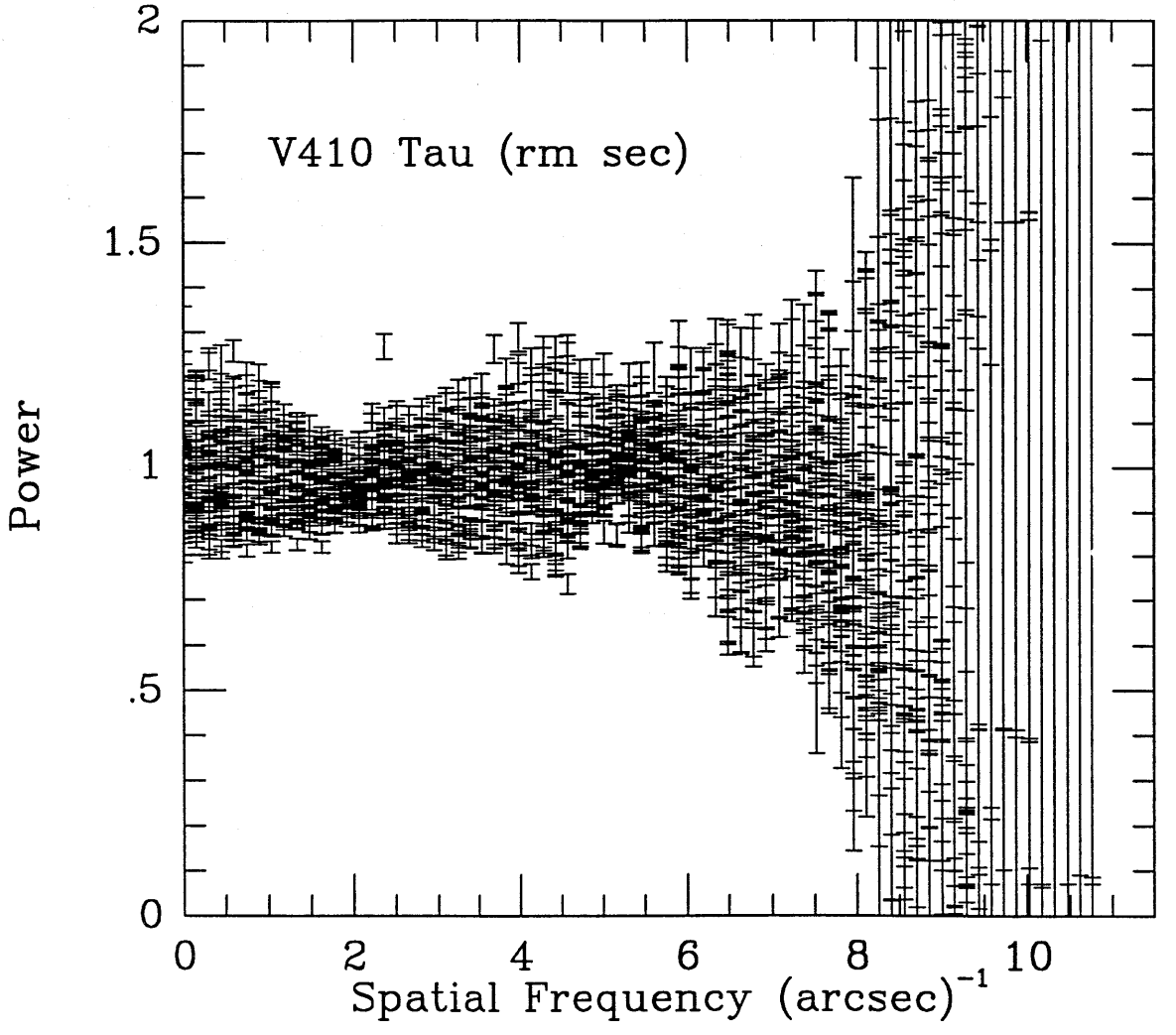
V410 Tau (rm sec)
Power
2
1.5
1
.5
0
0
2
4
6
8
10
Spatial Frequency (arcsec)$^{-1}$

Figure A.107

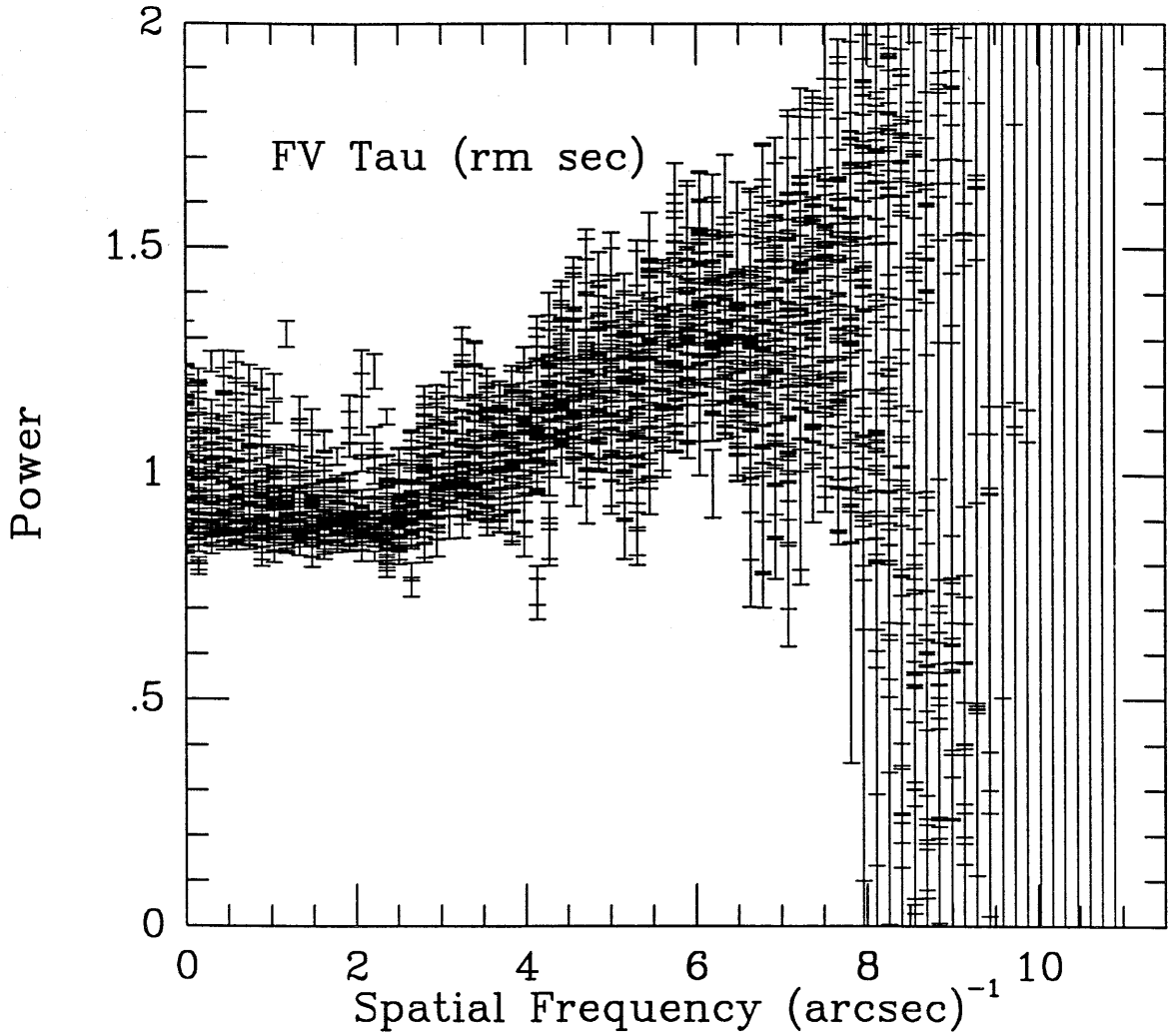
FV Tau (rm sec)
Power
Spatial Frequency (arcsec)$^{-1}$
0
.5
1
1.5
2
0
2
4
6
8
10

Figure A.108

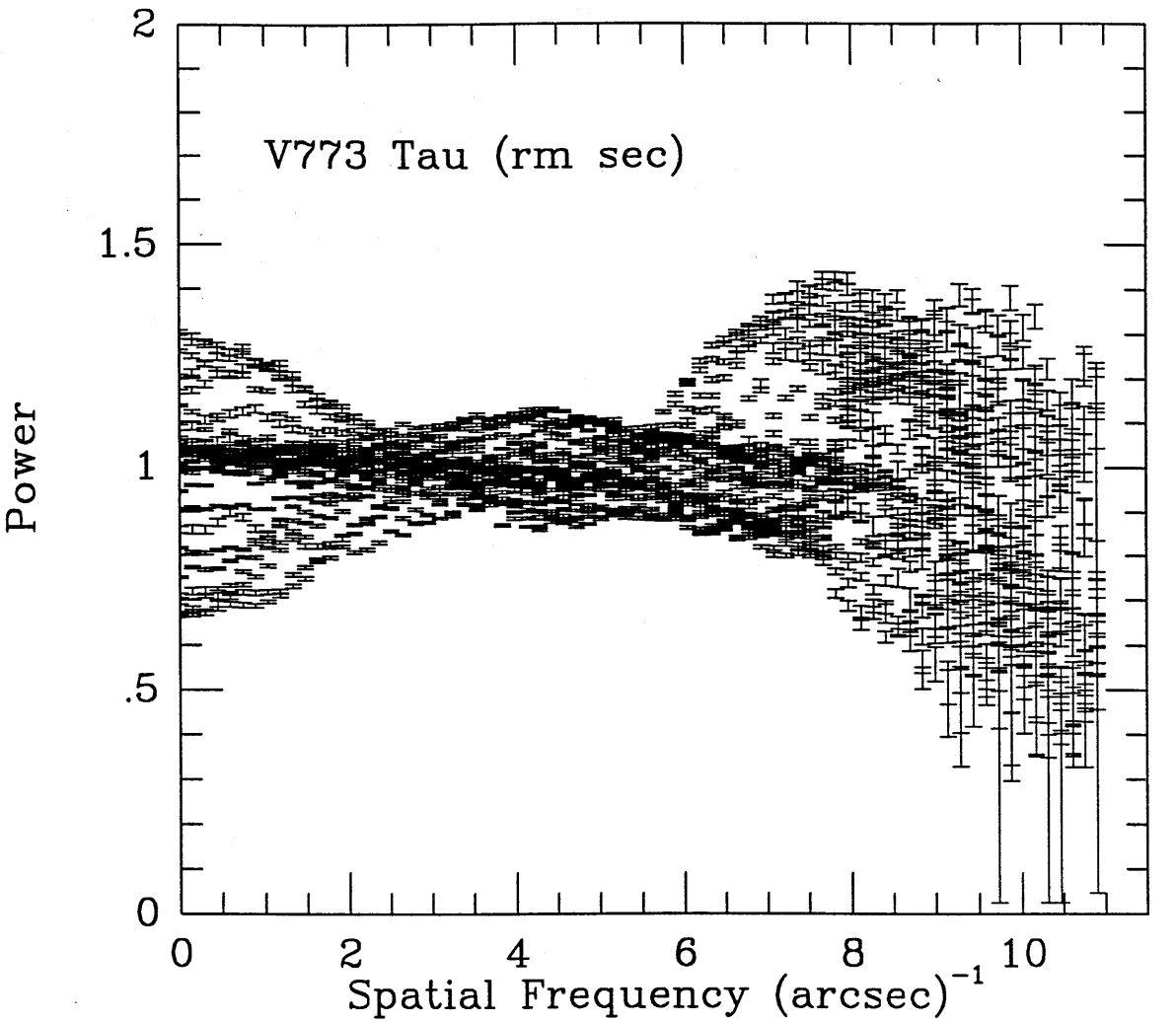
V773 Tau (rm sec)
Power
2
1.5
1
.5
0
0
2
4
6
8
10
Spatial Frequency (arcsec)$^{-1}$

Figure A.109

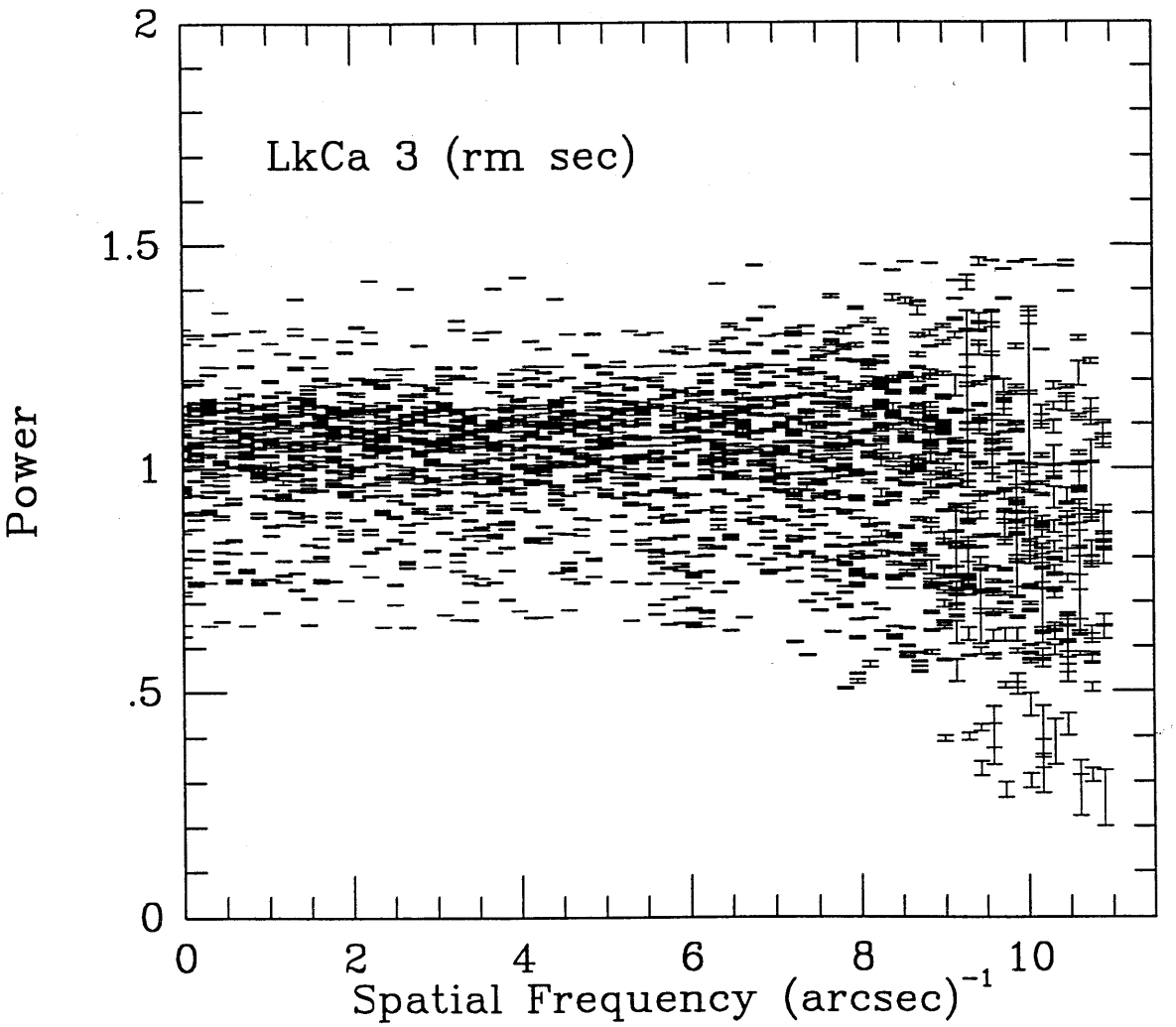
LkCa 3 (rm sec)
Power
2
1.5
1
.5
0
0
2
4
6
8
10
Spatial Frequency (arcsec)$^{-1}$

Figure A.110

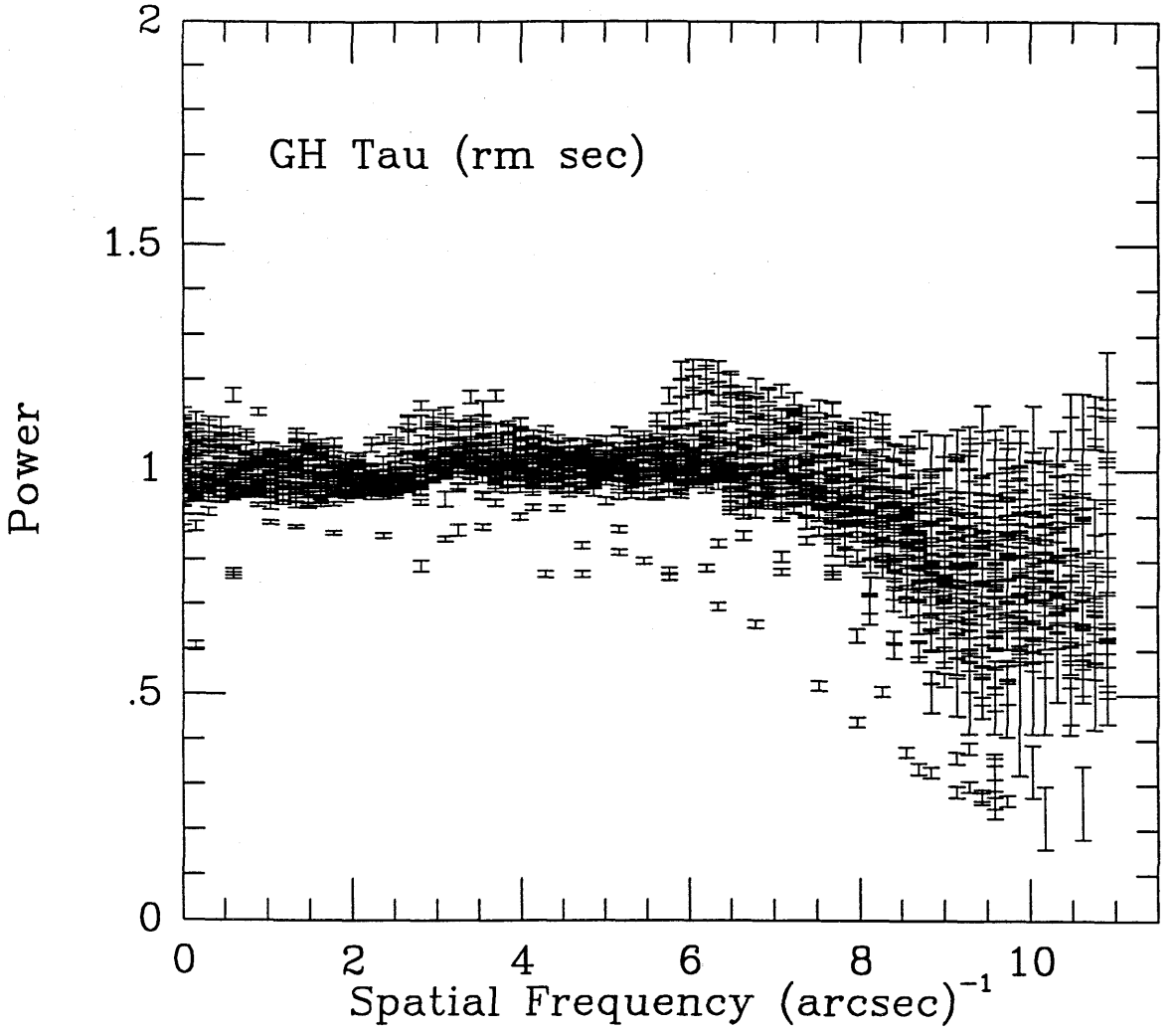
GH Tau (rm sec)
Power
2
1.5
1
.5
0
0
2
4
6
8
10
Spatial Frequency (arcsec)$^{-1}$

Figure A.111

Appendix B

B. Diffraction Limited Infrared Images of the Binary Star T Tauri

B.1. Introduction

In 1982, Dyck et al. (1982) discovered the first example of a close pre-main sequence binary in the variable star T Tauri. Using one-dimensional speckle interferometry they measured the projected north-south binary separation to be 0."6. Subsequent VLA observations of T Tau at 2 and 6 cm showed it to be a double thermal radio source (Schwartz et al. 1984; Schwartz et al. 1986); the more intense radio component corresponded to the southern infrared source, T Tau S, while the northern source, T Tau N, was identified with the visible star on the basis of astrometric studies (Hanson et al. 1983). Apart from statistical arguments (Dyck et al.), evidence for the two stars being physically related comes from the 2 cm VLA radio map (Schwartz et al. 1986), in which an emission bridge apparently connects the two sources. Nisenson et al. (1985) reported an additional optical component, T Tau O', 0."3 north of T Tau N, but Gorham et al. (1992) do not detect this component in their 1990 data.

To understand the T Tau system and its spectral energy distribution it is necessary to take into account both its variable and binary nature. This paper reports the results of an infrared study of the components of the T Tau system at high spatial resolution. The work includes two dimensional near infrared (1 - 5 μm) speckle imaging, mid-infrared (10 - 20 μm) slit scans, and 1 - 20 μm photometry. Nearly simultaneous measurements over a large range of wavelengths together with measurements at a smaller number of wavelengths over a much longer time period provide the opportunity to study both the nature of the two components as they appeared at the

end of 1990 and their behavior from 1981 to the present. The 1990 spectral energy distribution of T Tau N is fit by two components - a photosphere and a circumstellar disk. T Tau S's spectral energy distribution is dominated by luminosity from an accretion disk. The repeated measurements show a dramatic change in the brightness of T Tau S over the last two years, which we propose resulted from an increase in the accretion rate.

The observations are presented in section 2 and the results in section 3. In section 4 we examine the 1 - 20 μm spectral energy distributions of T Tau N and T Tau S separately, as well as the variation in the flux density of T Tau S between 1981 October and 1991 January. Our conclusions are summarized in section 5.

B.2. Observations and Reduction

B.2.1. Speckle Observations

Two-dimensional near-infrared speckle observations of T Tau ($\alpha(1950) = 04^h\,19^m\,04.21^s$, $\delta(1950) = +19^o\,25'05.''4$) were made between 1989 August and 1990 November at the f/415 Gregorian focus of the Hale 5 meter telescope using the Cassegrain infrared camera with a Hughes-Santa Barbara Research Center 58 x 62 InSb hybrid array. We determined the scale and orientation of the detector by observing and reconstructing images of several binaries with well known orbits (McAlister & Hartkopf 1988). Referred to the sky, the pixel scale is 0."053 x 0."053 (± 0."001) and the field of view of the array is 3."1 (E-W) x 3."3 (N-S). Thus the data were slightly undersampled for all wavelengths less than 2.6 μm.

Speckle measurements were made in the photometric H(1.6 μm), K(2.2 μm) , and L'(3.7 μm) bands, and in additional narrow bands ($\delta\lambda/\lambda$ = 0.015) at 3.3 μm and 4.8 μm. Table B.1 contains the details of the speckle observations. The observations were carried out in sets of object/calibrator "pairs." The term "pair" refers to 400

consecutive short exposure frames of the T Tau system followed by 400 exposures of a nearby calibrator star, which is assumed to be unresolved. Estimates of the errors introduced by changing atmospheric conditions between any two observations were obtained by examining multiple object/calibrator pairs. The use of two calibration stars for some of the observations ensured that at least one would be unresolved. In fact, all the calibrators for these observations were unresolved at the diffraction limit of the 5-meter telescope. At each wavelength the FWHM of integrated calibrator data provided a measure of the seeing and is reported in Table B.1.

Diffraction-limited Fourier amplitudes were recovered by deconvolving the ensemble-averaged autocorrelation (the Fourier equivalent of the power spectrum) of T Tau with that of an unresolved calibrator (c.f. Labeyrie 1970, Gorham et al. 1990). The Fourier phases of T Tau were retrieved by first calculating the bispectrum of the object (Lohmann et al. 1983) and then fitting the bispectrum phases using a global least squares algorithm (Cornwell 1987, Gorham et al. 1989). A Fourier inversion of these amplitudes and phases produced a reconstructed image of T Tau for every object/calibrator pair obtained. The final images presented in section 3 are averages of all the pairs reconstructed for each observation. Previous papers describe the application of this technique in more detail (Gorham et al. 1989, Ghez et al. 1990).

B.2.2. Slit Scans

Simultaneous north-south near-infrared and mid-infrared slit scans of T Tau were obtained at the f/70 Cassegrain focus of the Hale 5-meter telescope in 1985 December, 1990 October and 1991 January (see Table B.2) to spatially separate the two components of T Tau at mid-infrared wavelengths. The near-infrared scans delineated the optical component, T Tau N and therefore provided a reference to coadd the noiser mid-infrared scans (Matthews et al. 1987), taken with broad band 10 and 20 μm filters, as well as narrow band filters in the silicate feature (λ = 8.7, 9.5, 11.2,

and 12.5 μm). Figure B.1 shows the 1985 and 1990 coadded slit scans of T Tau at 10 μm.

At all wavelengths the slit scans of the point source α Tau, which were interspersed with those of T Tau, determined the point spread function of the telescope. One-dimensional images of the T Tau binary together with the flux density ratio of the two components were obtained at each wavelength by fitting two of the observed point spread functions appropriately separated in the north-south direction to the coadded T Tau slit scans.

B.2.3. Photometric Observations

Photometric measurements of T Tau were made in the photometric bands J (1.25 μm), H (1.65 μm), K (2.2 μm), L' (3.7 μm), M (4.8 μm), N (10.1 μm) and Q(20 μm) on 1990 October 5 and 1990 December 31 with a single element InSb detector and a Ge:Ga bolometer at the f/70 Cassegrain focus of the Hale 5 meter telescope. Beam diameters were 5" for the J, H, K, L', and M observations and 4."6 for the N and Q observations. Sky subtraction was carried out by chopping 15" north and south of the object. The stars listed in Elias et al. (1982) and α Tau were used for photometric calibration. Additional photometry of T Tau was obtained in the near infrared bands on 1991 February 24 using the InSb array at the f/70 Cassegrain focus of the Hale 5 meter telescope and at 10 and 2 μm from slit scans taken under photometric conditions on 1985 December 21. Table B.3 lists the photometric results.

B.3. Results

B.3.1. Speckle Image Reconstructions

The speckle images of the T Tau system at wavelengths between 1 and 5 μm are presented in Figure B.2 (a) - (e) and show that the system is a binary with separation 0."73 ± 0."01 and position angle $176^o \pm 1^o$ measuring the southern component, T Tau S, with respect to the northern component, T Tau N. In the images reconstructed from data obtained between October - November 1990, the northern component dominates the system at all wavelengths shorter than 3 μm. Given that the southern source becomes fainter at shorter wavelengths, it is sensible to assume that it continues to decrease in brightness at visual wavelengths, and we therefore identify the northern source with the optical star as expected from earlier astrometric results (Hanson et al. 1983).

None of the near infrared images reveal the third component, T Tau O' (Nisenson et al. 1985, Maihara & Kataza 1991). The limits for its detection in these images were set by calculating the rms noise in the region where T Tau O' first appeared; a further discussion of these limits is in Gorham et al. (1992).

B.3.2. Flux Density Ratios

The near infrared flux density ratios between T Tau N and T Tau S and the errors were determined by fitting a fringe pattern to the recovered power spectra. A binary with flux ratio R and separation s produces a fringe pattern $P(\mathbf{x}) = R^2+1+2R\cos(2\pi \mathbf{s}\cdot\mathbf{x})$ in the power spectrum (see Figure B.3). At mid-infrared wavelengths the flux density ratios and errors were obtained from fits to the slit scans as discussed in section 2. Table B.4 lists the flux density ratios at near and mid-infrared wavelengths.

B.3.3. Flux Densities of T Tau N and T Tau S

The combination of photometric data for the total system (Table B.3) and the measured flux ratios determined the absolute brightness of the separate components, T Tau N and T Tau S, given in Table B.4. If photometric data were not obtained contemporaneously with the measurements of the flux ratios, photometric observations obtained within one month were used. The near infrared flux of the T Tau system prior to 1990 October was estimated by integrating the speckle data and calculating the relative strength of T Tau to that of the calibrator. The calibrator stars are of spectral type F0 and B8, and typically remain constant over time scales of many years. Thus photometric observations of the speckle calibrators obtained in 1991 February provided a measure of the earlier 1.6 and 2.2 μm T Tau total flux densities. An interpolation between the photometric values in K and L' bands gave an estimate of the flux density of the system at 3.3 μm.

B.3.4. Silicate Measurements for T Tau N and T Tau S

The 1991 January 6 slit scans of T Tau at silicate wavelengths using narrow band filters yielded reliable flux density ratios, but due to the presence of cirrus, the photometric measurements were poor. Subsequent photometric measurements of T Tau at mid-infrared wavelengths, using both broad band and narrow band filters, were made on 1991 March 30. The 10 and 20 μm broad band photometric measurements showed a 20% decrease from the previous measurements obtained on 1990 October 5. We assumed that this change resulted entirely from a "colorless" change in T Tau S (see the discussion and Figure B.6) and derived the absolute flux densities of the T Tau system on 1991 January 6 at the silicate feature wavelengths from the 1991 March 30 measurements. Table B.4 lists the values of the silicate flux densities of T Tau N and T Tau S obtained by combining the estimated photometry and the measured flux ratios.

B.4. Discussion

At the distance to the Taurus dark cloud complex, 140 pc (Elias 1978), the projected angular separation, 0."73 ± 0."01, between the components of T Tau corresponds to a linear distance of 102 AU. The current measurement of the separation in conjunction with previously reported measurements listed in Table B.5 cannot distinguish between the two stars being gravitationally bound or simply members of the same cloud (Jones & Herbig 1979). If T Tau S is a distant background object, then it would appear stationary and the relative separation of the two stars over time should decrease (see Table B.5), reflecting the proper motion of T Tau N, μ_α=0."009±0."001 yr^{-1} and μ_δ=–0."014±0."001 yr^{-1} (Jones & Herbig 1979), as opposed to the observed increase. Thus we conclude that T Tau S is not a distant background object. We will continue to assume, as others have done, that the two components form a physical pair on the basis of statistics (Dyck et al. 1982) and the 2 cm bridge of emission connecting the two sources (Schwartz et al. 1986).

The spectral energy distributions of the components of T Tau shown in Figure B.4 were constructed by combining the photometric, speckle, and slit scan results obtained during the period 1990 October to 1991 January. Additional visual photometry from early 1990, provided by W. Herbst (private communication) and assigned to T Tau N, and limits for T Tau S at 0.6 and 0.8 μm from speckle interferometry in 1990 September (Gorham et al. 1992) are also included in this plot. Both the inferred photometry obtained from the 1990 optical speckle data and the AAVSO data base of visual observations suggest that T Tau N has remained at roughly constant visual flux densities over this period.

The spectral energy distribution of T Tau S shown in Figure B.4, indicates that it contributes a significant fraction of the overall infrared excess. T Tau N, however, still has its own infrared excess. The measured luminosity of T Tau S from 0.8 to 20 μm is 15 L_O, a factor of two greater than that of T Tau N, 7.5 L_O. An estimate of the

bolometric luminosity of the individual components is difficult since measurements made at other longer wavelengths (e.g. the IRAS observations) did not spatially resolve the system and, additionally, T Tau S's flux density has changed in the recent past (see Figure B.1 and Figure B.7).

B.4.1. T Tau N and its circumstellar material

Based on the speckle limits for the detection of T Tau S at visual wavelengths, it is reasonable to assume that an optical spectrum of the T Tau system is due entirely to T Tau N. Previous measurements of the T Tau system's optical spectrum indicated the presence of a K0 star (Cohen & Kuhi 1979, Bertout et al. 1988). We assume an effective temperature of a K0 star (Johnson 1965) and fit the visual data with a 8.8 L_O blackbody reddened by A_v=1.5 mag and the averaged extinction law given by Savage & Mathis (1979) (Figure B.5). These parameters agree quite well with what have been previously used by others (Adams et al. 1988, Cohen et al. 1989).

Adams et al. (1987) and others propose that the presence of a circumstellar disk accounts for the infrared excess observed in most T Tauri stars. T Tau N's mid-infrared data excess suggests the use of a disk model with a power law temperature distribution, $T(r) = T_o(\frac{r}{1AU})^{-q}$ plus heating from the central star (Beckwith et al. 1990). This model with T_o = 260, q = .42, and an inner disk radius of 4.3 R_O accounts for the observed infrared excess. Figure B.5 shows the blackbody representation of the photosphere, the disk model, and the sum of the two which accommodates the general shape of the spectral energy distribution quite well. The heating of the inner portions of the disk by the central star provides the extra luminosity seen at near infrared wavelengths.

The 10 μm silicate feature appears to be in emission in T Tau N's spectral energy distribution. This implies that the radiation at 10 μm is not optically thick.

Since material at temperatures of roughly 330 K contribute most to the 10 μm radiation, a corresponding location of roughly 120 R_O in the disk is found from the model temperature distribution. Thus a this distance from the central star, the circumstellar material is no longer optically thick.

B.4.2. T Tau S and its circumstellar material

T Tau S does not appear to be a clump of material heated solely by T Tau N, Over the wavelength range of 0.8 to 20 μm, the flux density measurements show T Tau S to be twice as luminous as T Tau N. Thus T Tau S must be a self luminous source.

The spectral energy distribution of T Tau S shows a 10 μm silicate absorption feature. The depth of the feature, $\tau_{9.5\,\mu m} = 0.4 \pm 0.2$, corresponds to 4.6 ± 2.5 mag of visual extinction along the line of sight (Reike & Lebofsky 1985). Since the line of sight to T Tau N is not obstructed by much dust, it is most likely that the dust is located in a relatively small zone around T Tau S alone.

If the visual extinction to T Tau S is $A_v = 4.6 \pm 2.5$ mag, then the near infrared part of the spectral energy distribution can be fit by a reddened blackbody of temperature 930 ± 50 K, radius 102 ± 6 R_O, and luminosity 7.0 ± 0.7 L_O; this fit is shown in Figure B.6. The low effective temperature supports the protostellar model previously suggested by Hansen et al. (1983) and Bertout (1983). The spectral energy distribution of a typical protostar peaks at roughly 100 μm (Adams et al. 1987), whereas that of T Tau S peaks at 3 μm. This implies that if T Tau S is a protostar it is atypical, in that it is not dominated by radiation from a mass of cold dust. This apparent lack of cold dust may stem from the binary nature of the T Tau system, since the outer part a protostellar dust shell might be disrupted by T Tau N.

The measured flux densities of T Tau S changed by two magnitudes at all wavelengths between 1 and 10 μm during the observations presented here. Figure B.7

shows these data and previous measurements taken from the literature (Dyck et al. 1982, Beckwith et al. 1984, Maihara and Kataza 1991). If the flare was both colorless and simultaneous at all wavelengths, then the well sampled K light curve, shifted by a constant, would fit the data at other wavelengths; see the dotted curves shown in Figure B.7. This interpretation works from 2 to 10 μm but fails at 1.65 μm. Either the flux density of T Tau S increased more at 1.65 μm than it did at other infrared wavelengths, or the flare occurred at a later time at 1.65 μm.

Most explanations of flares observed in young stellar sources invoke unsteady accretion from a disk surrounding the star (e.g. Bertout et al. 1988, Lin & Papaloizou 1985). If most of the currently observed luminosity comes from accretion energy, the luminosity of the disk is $L = \frac{GM_*\dot{M}}{2R_*}$. If the star has a mass of 1 M_O and a radius of 1 R_O, the accretion rate derived from the 0.8 to 20 μm luminosity is $3.6\times10^{-6} M_O\, yr^{-1}$. Using the K light curve as a crude measure of the flare, approximately $4\times10^{-6} M_O$ was accreted during the flare.

The flare suggests that T Tau S may be fit by an accretion disk model. T Tau S appears to similar to FU Ori stars, which are thought to be T Tauri stars experiencing rapid disk accretion and having spectral energy distributions that are dominated by an accretion disk. The accretion disk model discussed by Hartmann & Kenyon (1985) fits the T Tau S data with an inner disk radius of 33 R_O and an accretion rate of $6\times10^{-6} M_O\, yr^{-1}$, assuming a 1 M_O and 1 R_O central star. Furthermore the preflare data, the unfilled points in Figure B.6, are also well fitted by a similar model with an inner disk radius of 10 R_O and an accretion rate of $3\times10^{-7} M_O\, yr^{-1}$. This implies that the flare was caused by the accretion rate increasing by a factor of 20 while the inner disk radius was pushed out by $20R_O$. If T Tau S is an FU Ori star as opposed to a protostar, it could then possibly be coeval with T Tau N.

B.5. Summary

We conclude that the T Tau system consists of two stellar components, T Tau N and T Tau S, and associated disks. The optical component, T Tau N, is a 8.8 L_O K0 star, surrounded by a disk that follows a power law temperature distribution. The 10 μm emission feature in T Tau N's spectral energy distribution implies that the material located at roughly 120 R_O in the disk is not optically thick.

The cool infrared companion T Tau S is assumed to have undergone a flare due to an increase in accretion. The spectral energy distribution is fit by an accretion disk model, similar to those used to explain the young outburst sources (FU Ori stars). The measured flux densities for T Tau S imply a lower limit for the accretion rate at the end of 1990 of $3.6\times10^{-6} M_O yr^{-1}$, in agreement with the accretion disk model which predicts an accretion rate of $6\times10^{-6} M_O yr^{-1}$.

The measurements presented in this paper demonstrate the potential importance of separating close binary pairs and avoiding the confusion engendered by unresolved spectral energy distributions. In addition, the brightening of T Tau S by two magnitudes at wavelengths between 1 and 10 μm over a period as short as one year, illustrates the importance of obtaining simultaneous multiple wavelength observations.

Table B.1: Journal of Speckle Observations of T Tau

Date UT	λ_o μm	$\delta\lambda$ μm	Cal#1 SAO	Cal#2 SAO	Exp. Time sec	Pairs	Seeing (λ)[a] "
1989 Aug 16	2.2	0.4	76548	...	0.10	21	0.9
1989 Aug 17	1.65	0.3	76548	...	0.10	16	0.7
1989 Dec 9	2.2	0.4	93918	...	0.10	7	1.0
1990 Aug 7	2.2	0.4	93918	...	0.10	2	0.7
1990 Oct 3	3.7	0.64	93918	93974	0.05	4	0.8
1990 Oct 3	4.8	0.07	93897	...	0.10	7	0.8
1990 Oct 3	3.28	0.05	93897	...	0.10	4	0.9
1990 Nov 8	4.8	0.07	93897	...	0.20	5	1.1
1990 Nov 9	2.2	0.4	93918	93874	0.10	7	1.3
1990 Nov 9	1.65	0.3	93918	93874	0.07	8	1.2

(a) The seeing is reported as the FWHM of the calibrator at the observed wavelength.

Table B.2: Log of Slit Scan Observations of T Tau

Date	λ μm	$\delta\lambda$ μm	NIR Ref λ μm	Conditions
1985 Dec 21	10.1	5.0	2.2	photometric
1990 Oct 6	10.1	5.0	1.65	thin cirrus
1991 Jan 6	10.1	5.0	1.65	cirrus
1991 Jan 6	20	6.0	1.65	cirrus
1991 Jan 6	8.7	0.1	1.65	cirrus
1991 Jan 6	9.5	0.1	1.65	cirrus
1991 Jan 6	11.2	0.2	1.65	cirrus
1991 Jan 6	12.5	0.2	1.65	cirrus

Table B.3: Photometry of Total T Tau System

	1985 Dec 21	1990 Oct 5	1990 Dec 31	1991 Feb 24	1991 Mar 30
$\lambda(\mu m)$	$F_\nu(Jy)$	$F_\nu(Jy)$	$F_\nu(Jy)$	$F_\nu(Jy)$	$F_\nu(Jy)$
J(1.3)	...	2.3 ± 0.1	2.2 ± 0.1	2.2 ± 0.1	...
H(1.6)	...	3.4 ± 0.2	3.3 ± 0.2	3.6 ± 0.2	...
K(2.2)	3.5 ± 0.4	5.6 ± 0.3	5.4 ± 0.3	5.5 ± 0.3	...
L'(3.7)	...	12.2 ± 0.8	11.7 ± 0.7	11.9 ± 0.8	...
M(4.8)	...	18 ± 1	14.8 ± 0.9	...	...
N(10.1)	11.6 ± 2	28 ± 3	...	...	23 ± 2
Q(20)	...	45 ± 7	...	...	38 ± 6

Table B.4: Photometry of T Tau Components

λ	Date	Observation	Flux Density Ratio	$f_\nu(TTau\ N)$	$f_\nu(TTau\ S)$
μm	UT		$f_\nu(TTau\ N)/f_\nu(TTau\ S)$	Jy	Jy
1.6	1989 Aug 17	Speckle	80 ± 30	3.2 ± 1.3	0.04 ± 0.02
1.6	1990 Nov 9	Speckle	10.0 ± 0.4	3.1 ± 0.2	0.31 ± 0.02
2.2	1989 Aug 16	Speckle	6.2 ± 0.2	3.9 ± 0.5	0.6 ± 0.07
2.2	1989 Dec 9	Speckle	2.71 ± 0.05	3.9 ± 0.4	1.4 ± 0.1
2.2	1990 Aug 7	Speckle	2.20 ± 0.06	3.8 ± 0.5	1.7 ± 0.2
2.2	1990 Nov 9	Speckle	2.40 ± 0.05	3.9 ± 0.2	1.60 ± 0.07
3.3	1990 Oct 3	Speckle	0.43 ± 0.04	3.1 ± 0.4	7.2 ± 0.9
3.7	1990 Oct 3	Speckle	0.44 ± 0.01	3.7 ± 0.3	8.5 ± 0.6
4.8	1990 Oct 3	Speckle	0.244 ± 0.006	3.6 ± 0.3	14.7 ± 1.1
4.8	1990 Nov 8	Speckle	0.24 ± 0.02	3.2 ± 0.3	13.3 ± 1.3
8.7	1991 Jan 6	Slit scan	0.21 ± 0.02	4.5 ± 0.8	22 ± 4
9.5	1991 Jan 6	Slit scan	0.60 ± 0.03	8.7 ± 1.5	14 ± 2
11.2	1991 Jan 6	Slit scan	0.33 ± 0.07	7 ± 1	22 ± 4
12.5	1991 Jan 6	Slit scan	0.27 ± 0.03	7 ± 1	27 ± 4
10.1	1985 Dec 21	Slit scan	2.6 ± 0.06	8.4 ± 1.1	3.2 ± 0.4
10.1	1990 Oct 6	Slit scan	0.50 ± 0.03	8.5 ± 1.1	17.1 ± 2.3
10.1	1991 Jan 6	Slit scan	0.41 ± 0.01	8.3 ± 1.0	20.4 ± 2.5
20	1991 Jan 6	Slit scan	0.46 ± 0.03	14.3 ± 2.3	31 ± 5

Table B.5: Relative Separations

Measurements			Predictions for 1990.9			
Sepn	PA	Epoch	$Sepn^a$	PA^a	$Sepn^b$	PA^b
arcsec	deg	1900+	arcsec	deg	arcsec	deg
0.6 ± 0.1	N-S	81[c]	0.5 ± 0.1	N-S	0.7 ± 0.1	N-S
0.55 ± 0.07	167 ± 2	82.5[d]	0.42 ± 0.07	174 ± 2	0.6 ± 0.1	171 ± 6
0.65 ± 0.07	174.7 ± 0.7	83.75[e]	0.55 ± 0.07	180.4 ± 0.8	0.66 ± 0.09	177 ± 4
0.73 ± 0.03	176 ± 1	90.9[f]	...	...	...	...

(a) the predicted relative position of the two components if T Tau S remained stationary and T Tau N moved according to its proper motion

(b) the predicted separation if T Tau N moved according to its proper motion and T Tau S had proper motion consistent with being a member of the Taurus Dark Cloud (Jones & Herbig 1979).

(c) Near infrared measurement by Dyck et al. 1982

(d) Radio measurement by Schwartz et al. 1984

(e) Radio measurement by Schwartz et al 1986

(f) this work

Figure Captions

Figure B.1: Coadded slit scans of T Tau at 10 μm. North is to the right in both figures. (a) Data obtained in 1985, show T Tau N dominating the system. (b) In 1990, T Tau S dominates the system. These slit scans are fit with two point spread functions, determined by slit scans of a point source, to obtain flux ratios.

Figure B.2: Speckle image reconstructions of T Tau. The images shown have been centered on a point midway between the two components. North is up and east is to the left and the contour levels are -1, 1, 2, 4, 8, 16, 32, 64% of the peak value in each map. (a) The 1.6 μm image reconstructed from data obtained 1990 November 9. Although the secondary looks slightly resolved, this is most likely an artifact of undersampling. (b) The 2.2 μm image reconstructed from data obtained 1989 August 16. (c) The 3.28 μm image reconstructed from data obtained 1990 October 3. (d) The 3.7 μm image reconstructed from data obtained 1990 October 3. The increased noise at the position angle 180^o from the secondary is is the result of slightly different amplitude and phase solutions for the binary's flux ratio. (e) The 4.8 μm image reconstructed from data obtained 1990 October 3. The low frequency noise is characteristic of a seeing mismatch between the T Tau observations and those of its calibrator.

Figure B.3: T Tau's spatial power spectrum. (a) The two dimensional power spectrum obtained from data obtained at 2.2 μm on 9 Novemver 1990. (b) The two dimension visibility function is collapsed along the axis of the binary's separation. A binary separated by s with a flux ratio of R will produce a power spectrum of the form $P(\mathbf{x}) = R^2+1+2R\cos(2\pi \mathbf{s}\cdot\mathbf{x})$. The binary is clearly observed in this power spectrum out to the highest spatial frequencies obtained by the 5 meter telescope. The increased scatter at low spatial frequencies is due to seeing miscalibration (i.e., slightly different seeing conditions between the time T Tau and its calibrator were observed).

Figure B.4: The spectral energy distribution of T Tau N (square points) and T Tau S (triangular points). The filled points are data presented in this paper and the unfilled points are optical photometry measurements provided by W. Herbst. Optical speckle measurements (Gorham et al. 1992) provided limits on the detection of T Tau S, and justified the assignment of the optical photometry measurements to T Tau N. In the wavelength range 0.8 to 20 μm, T Tau S contributes twice as much luminosity as T Tau N to the total luminosity of the T Tau system. Note that the 10 μm silicate feature appears to be in emission for T Tau N and in absorption for T Tau S. The lines are drawn only to guide the eye.

Figure B.5: The spectral energy distribution of T Tau N. The dashed line is a 8.8 L_O blackbody with an effective temperature of a K0 star reddened by A_v = 1.5 mag representing the photosphere of the star. A power law temperature distribution plus stellar heating disk model (dotted line) accounts for the infrared excess. The solid curve is the sum of the photospheric blackbody and the disk model.

Figure B.6: The spectral energy distribution of T Tau S. The near infrared points are fit by a reddened blackbody of temperature 930 K and luminosity 6.9 L_O (dashed line). The visual extinction applied, A_v=4.6 mag, was obtained from the depth of the silicate feature. The solid curves show accretion disk models for both the preflare data (open triangles) and the end of 1990 data (filled triangles).

Figure B.7: The light curves for T Tau S at various wavelengths. All wavelengths show that T Tau S has undergone a 2 magnitude flare, but the K data were obtained frequently enough to map the flare in time. The curve at 2.2 μm is repeated for each wavelength to suggest that the flare was similar at all each wavelength, except 1.65 μm. The K data shown are a compilation of the data presented here and data from the literature (Dyck et al. 1982, Beckwith et al.

1984, Maihara and Kataza 1991).

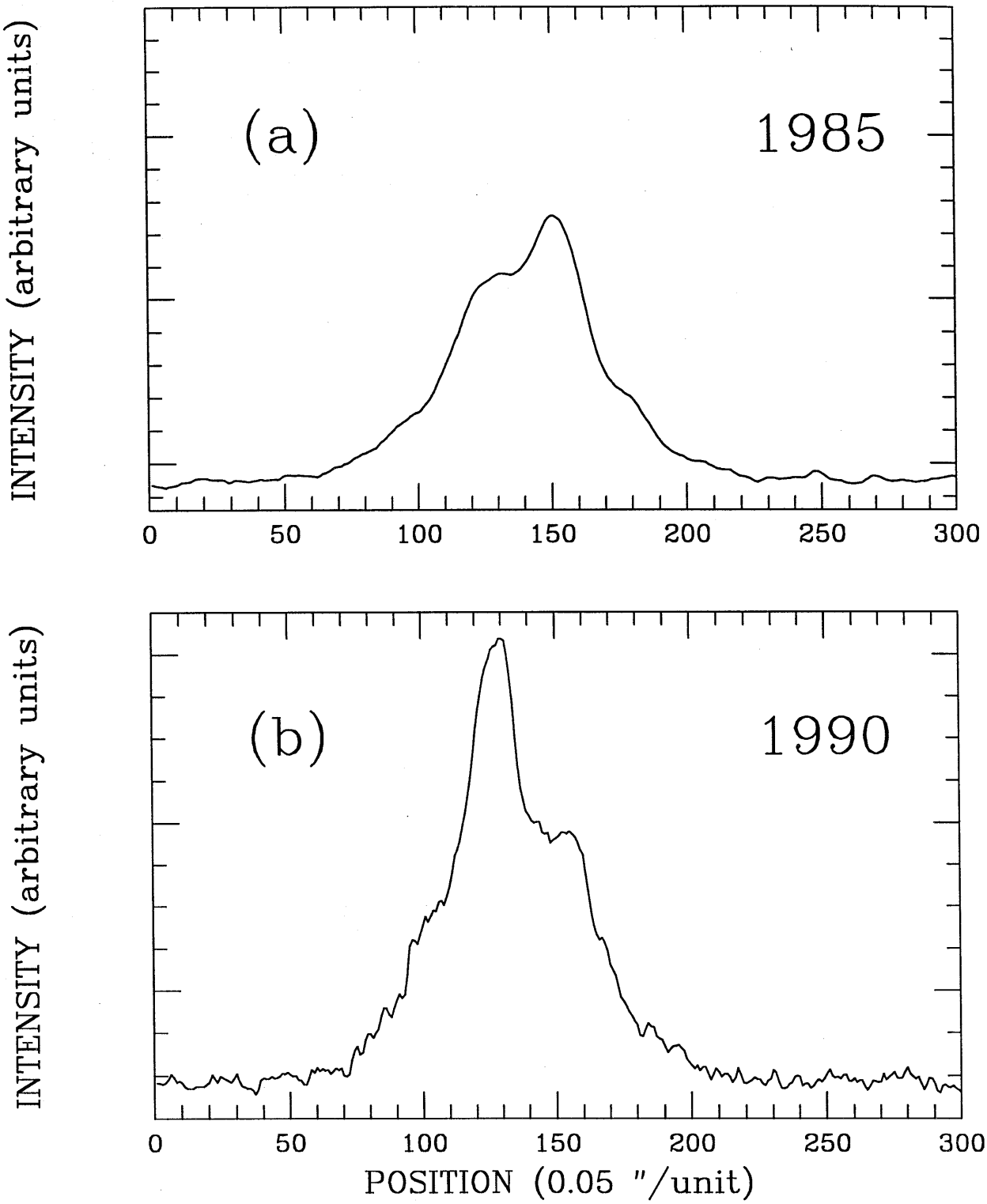
INTENSITY (arbitrary units)
(a)
1985
0
50
100
150
200
250
300
INTENSITY (arbitrary units)
(b)
1990
0
50
100
150
200
250
300
POSITION (0.05 "/unit)

Figure B.1

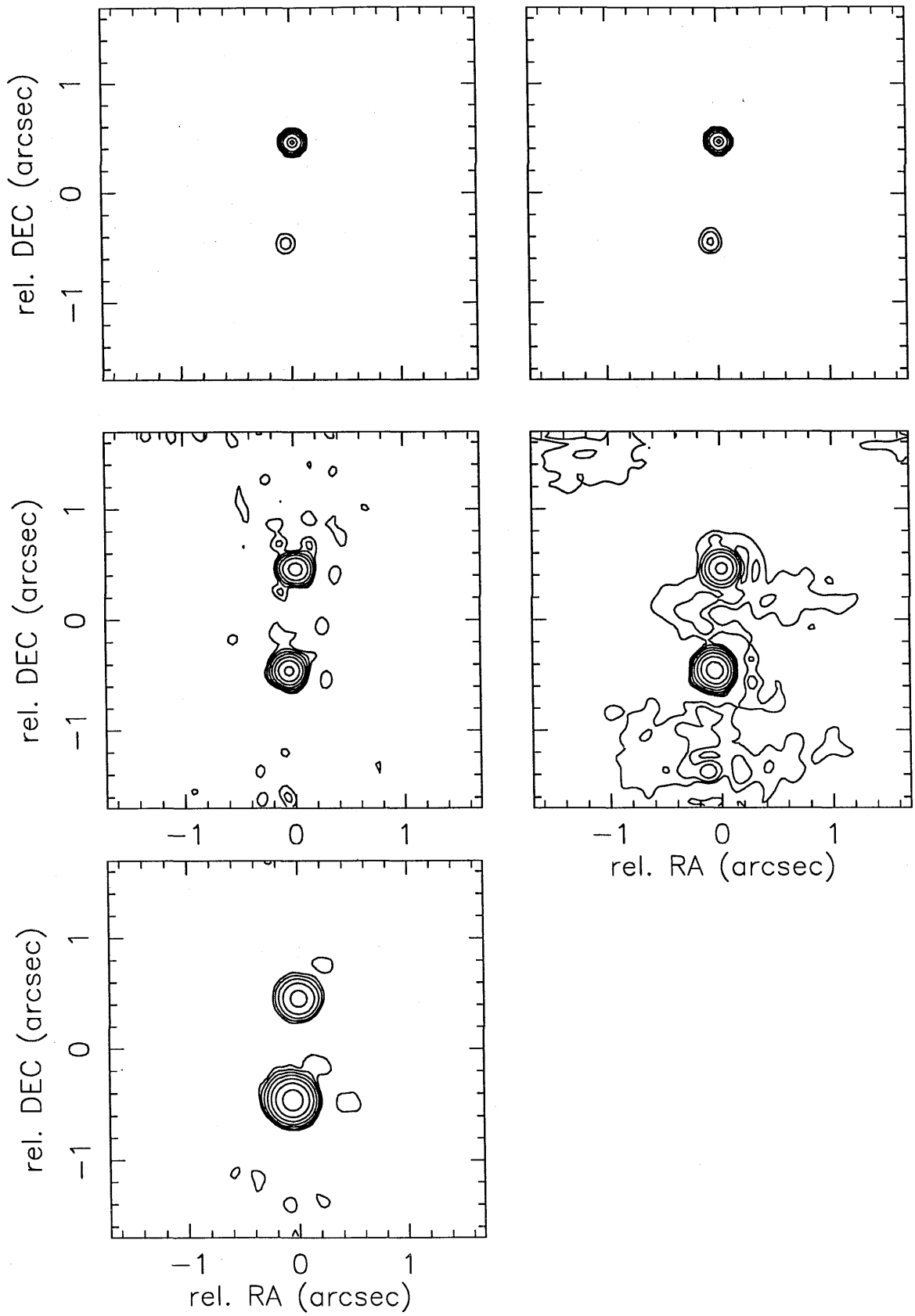
rel. DEC (arcsec)
rel. DEC (arcsec)
rel. DEC (arcsec)
rel. RA (arcsec)
rel. RA (arcsec)
−1
0
1

Figure B.2

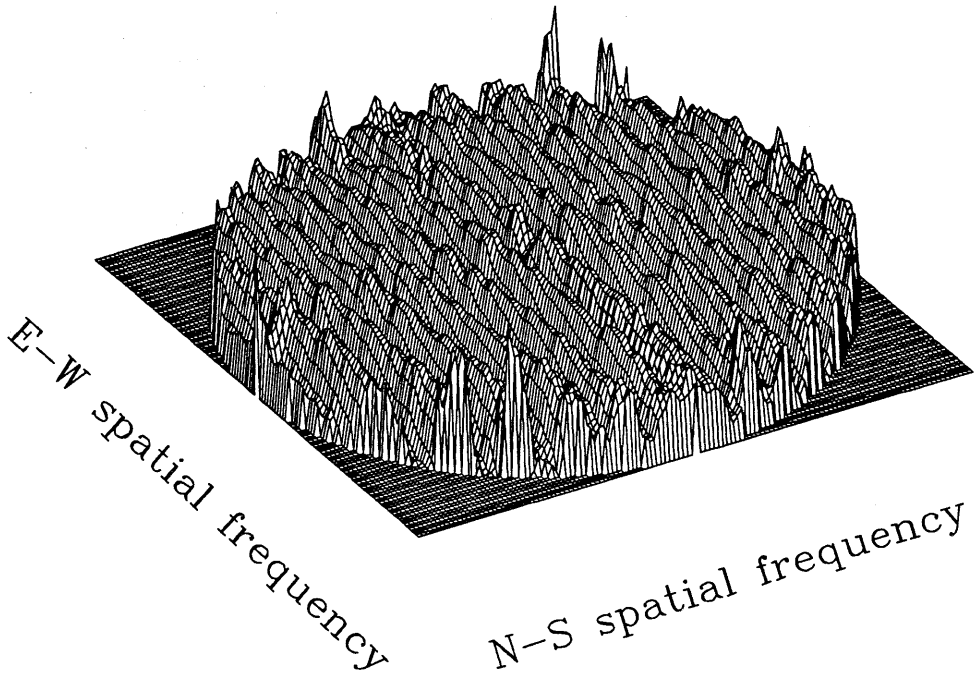

Figure B.3.a

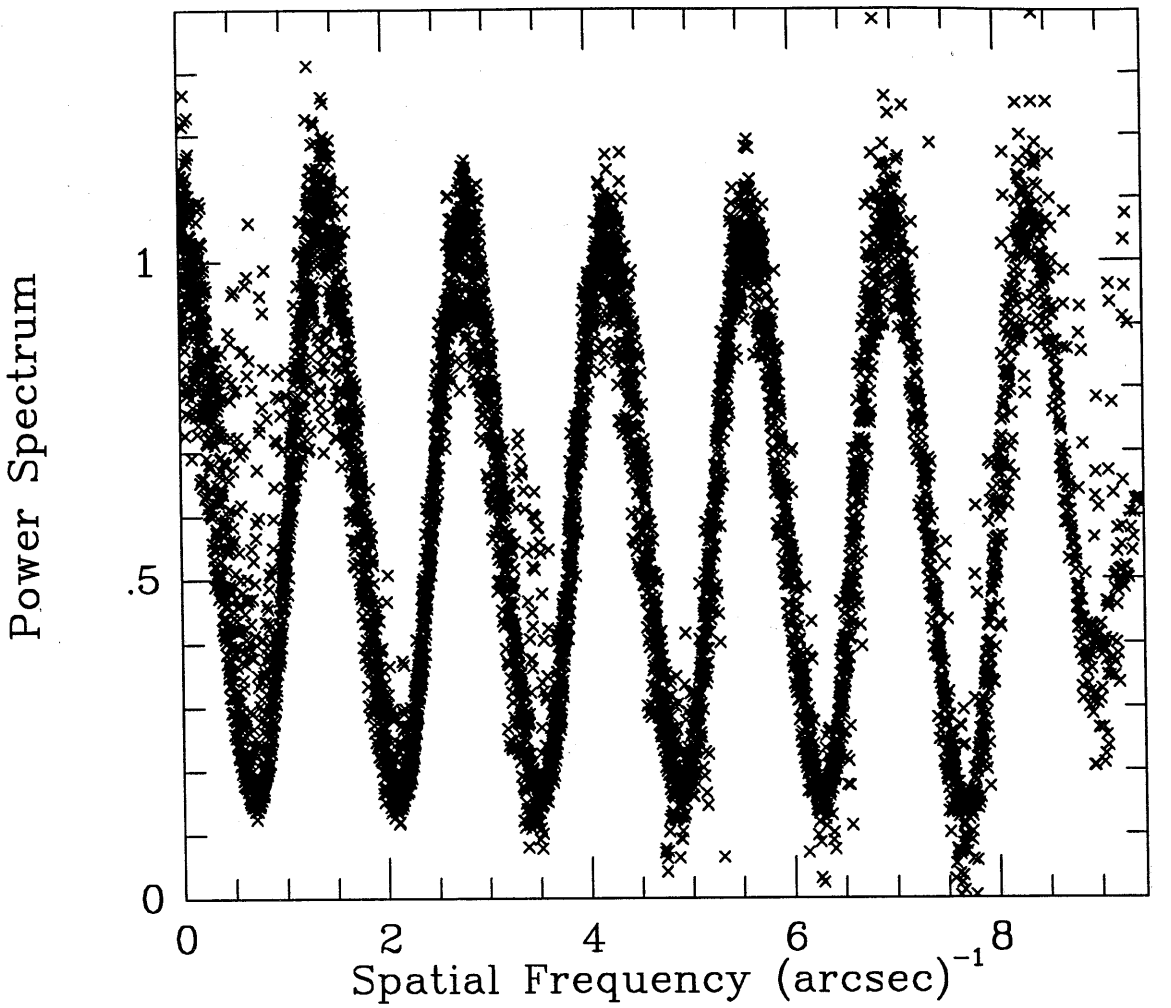

Figure B.3.b

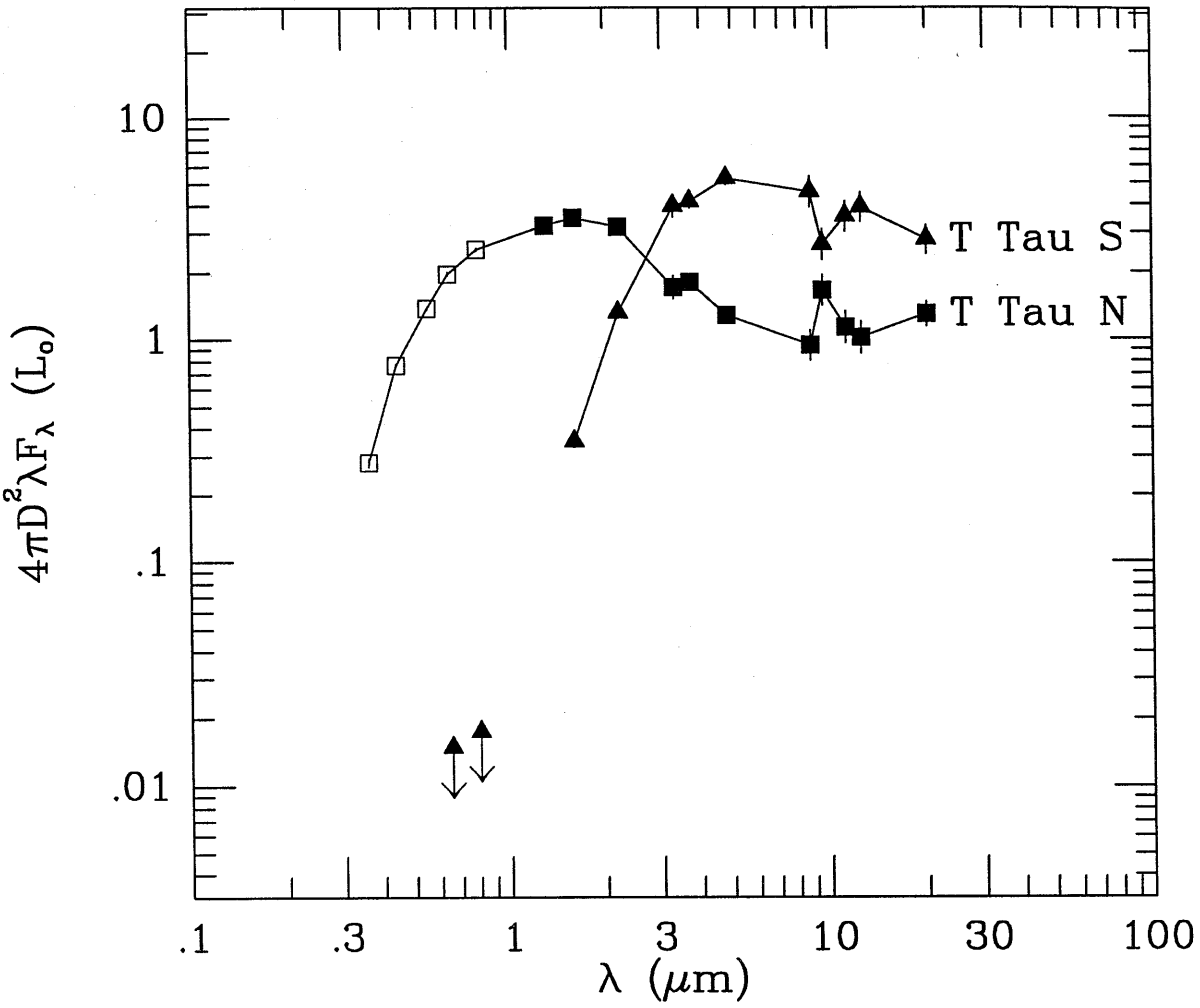
10
1
.1
.01
$4\pi D^2 \lambda F_\lambda$ ($L_\odot$)
.1
.3
1
3
10
30
100
λ (μm)
T Tau S
T Tau N

Figure B.4

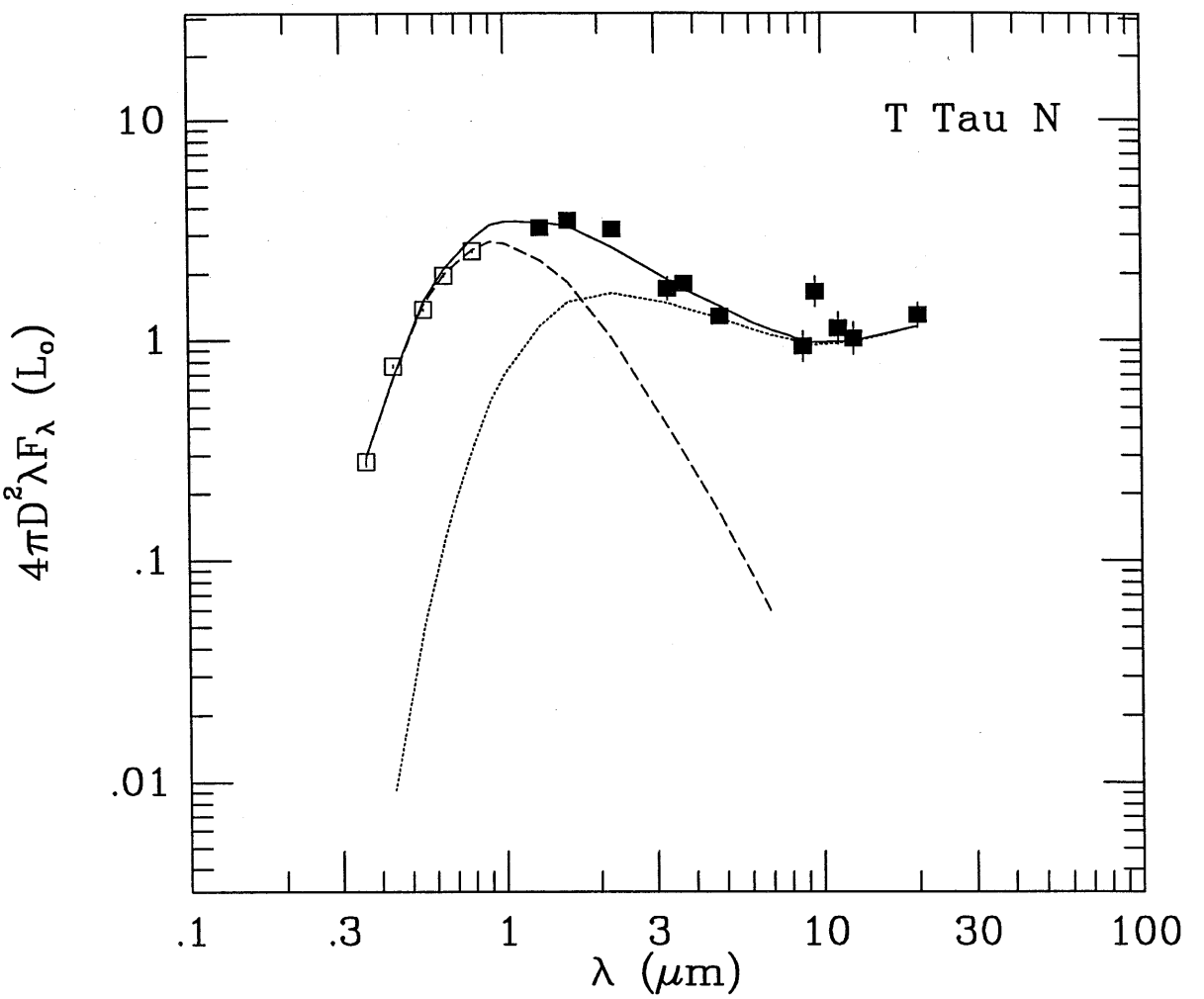

Figure B.5

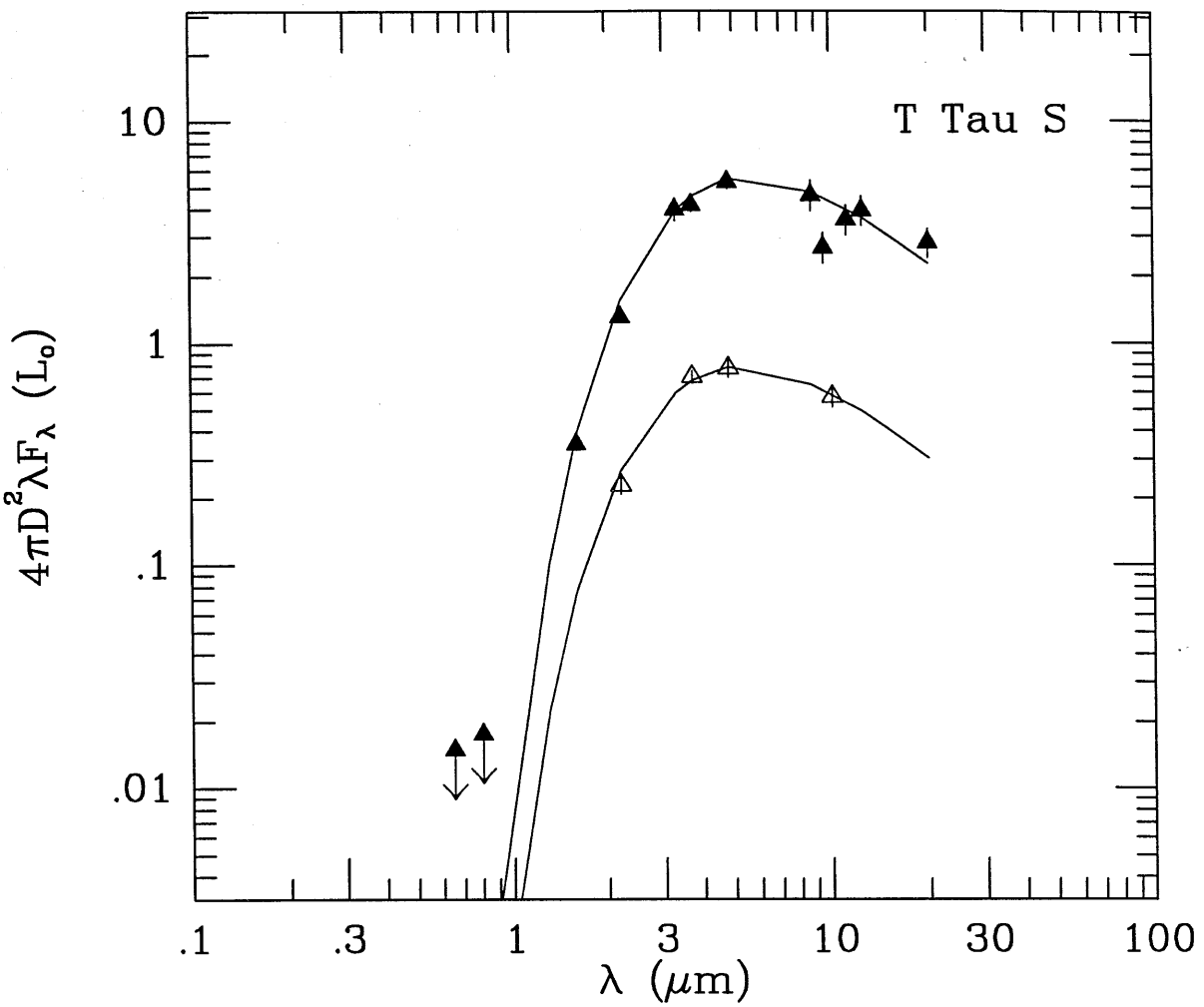
T Tau S
10
1
.1
.01
$4\pi D^2 \lambda F_\lambda$ ($L_\odot$)
.1
.3
1
3
10
30
100
λ (μm)

Figure B.6

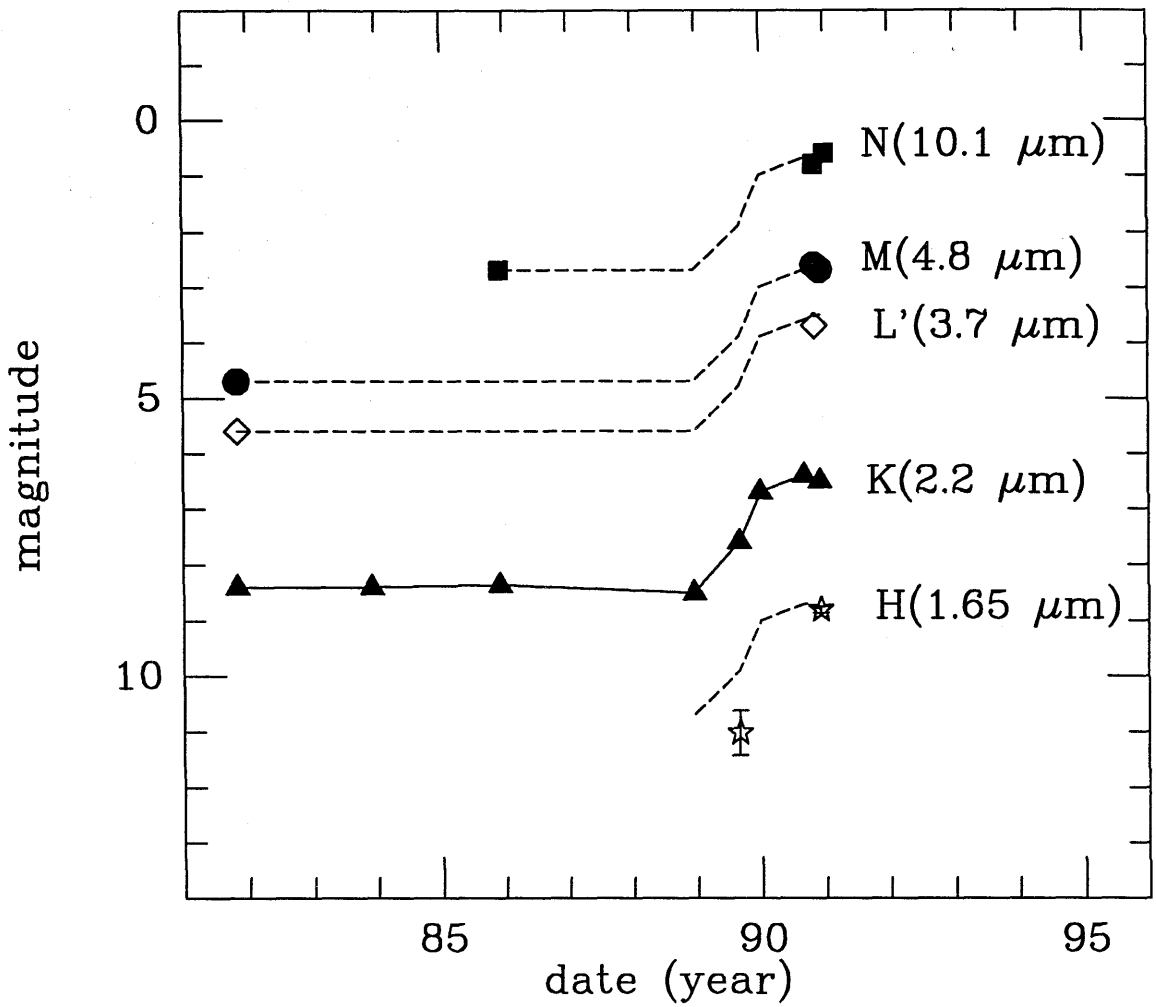
0
5
10
magnitude
N(10.1 μm)
M(4.8 μm)
L'(3.7 μm)
K(2.2 μm)
H(1.65 μm)
85
90
95
date (year)

Figure B.7

References

Abt, H. A. 1983, ARAA, 21, 343

Abt, H. A. and Levy, S. G. 1976, ApJSS, 30, 273

Adams, F. C., Lada, C. J., and Shu, F. H. 1987, ApJ, 312, 78

Adams, F. C., Lada, C. J., and Shu, F. H. 1988, ApJ, 326, 865

Ambartsumian, V. A. 1947, in Stellar Evolution and Astrophysics, Acad. Sci. Armenian SSR, Erevan

Appenzeller, I., Jankovics, I., and Ostreicher, R. 1984, A&A, 141, 108

Bartelt, H., Lohmann, A. W., and Wirnitzer, B. 1984, Appl. Opt., 23, 3121

Basri, G. and Batalha, C 1990, ApJ, 363, 654

Basri, G. and Bertout, C. 1989, ApJ, 341, 340

Bastian, U., Finkenzeller, U., Jaschek, C., and Jaschek, M. 1983, A&A, 126, 438

Bastien, P., Robert, C., Nadeau, R. 1989, ApJ, 339, 1089

Beckwith, S. V. W. and Sargent, A. I. 1992, In *Protostars and Planets III,* eds. E. H. Levy and J. Lunine, preprint

Beckwith, S. V. W., Sargent, A. I., Chini, R. S., and Gusten, R. 1990, AJ, 99, 924

Beckwith, S., Sargent, A. I., Scoville, N. Z., Masson, C. R., Zuckerman, B., and Phillips, T. G. 1986, ApJ, 309, 755

Beckwith, S., Zuckerman, B., Skrutskie, M., Dyck, M. 1984, ApJ, 287, 793

Bertout, C. 1983, A&A, 126, L1

Bertout, C., Basri, G., and Bouvier, J. 1988, ApJ, 330, 350

Bouvier, J., and Appenzeller, I. 1991, AASS, 92, 481

Bouvier, J., Tessier, E., and Cabrit, S. 1992, A&A, preprint

Cabrit, S., Edwards, S., Strom, S. E., and Strom, K. M. 1990, ApJ, 354, 687

Chelli, A. 1984, in Proceedings of IAU Colloq. 79, 309

Chelli, A., Zinnecker, H., Carrasco, L., Cruz-Gonzalez, I., and Perrier, C. 1988, A&A, 207, 46

Chen, W. P., Simon, M., Longmore, A. J., Howell, R. R., and Benson, J. A. 1990, ApJ, 357, 224

Christou, J. C., Cheng, A. Y. S., Hege, K. E., and Roddier, C. 1985, AJ, 90, 2644

Cohen, M., Emerson, J. P., and Beichman, C. A. 1989, ApJ, 339, 455

Cohen, M., and Kuhi, L. V. 1979, ApJSS, 41, 743

Cornwell, T. J. 1987, A&A, 180, 269

Dainty, J. C. 1984, in Laser Speckle and Related Topics, ed. J. C. Dainty, 255

de Geus, E. J., de Zeeuw, P. T., Lub, J. 1989, A&A, 216, 44

Duquennoy, A. and Mayor, M. 1991, A&A, 248, 485

Dyck, H. M., Simon, T., and Zuckerman, B. 1982, ApJ (Letters), 255, L103

Edwards, S., Cabrit, S., Strom, S. E., Heyer, I., Strom, K. M., and Anderson, E. 1987, ApJ, 321, 473

Elias, J. H. 1978, ApJ, 224, 857

Elias, J. H., Frogel, J. A., Matthews, K., and Neugebauer, G. 1982, AJ, 87, 1029

Fischer, D., and Marcy, G. 1992, ApJ, preprint

Fried, D. L. 1965, JOSA, 55 1427

Fried, D. L. 1966, JOSA, 56, 1372

Fried, D. L. 1979, in High Angular Resoltuion Stellar Interferometry, Proceedings of IAU Colloq. 50, ed. J. Davis and W. Tango, 4-1

Ghez, A. M., Gorham, P. W., Haniff, C. A., Kulkarni, S. R., Matthews, K., Neugebauer, G., and Weir, N. 1990, SPIE Proceedings, 1237, 249

Ghez, A. M., Neugebauer, G., Gorham, P. W., Haniff, C. A., Kulkarni, S. R., Matthews, K., Koresko, C., and Beckwith, S. 1991, AJ, 102, 2066

Glass, I. S., and Penston, M. V. 1974, MNRAS, 167, 237

Gorham, P. W., Ghez, A. M., Kulkarni, S. R., Nakajima, T., Neugebauer, G., Oke, J. B., and Prince, T. A. 1989, AJ, 98, 1783

Gorham, P. W., Ghez, A. M., Haniff, C. A., Kulkarni, S. R., Matthews, K., and Neugebauer, G. 1992, AJ, 103, 953

Gorham, P. W., Ghez, A. M., Haniff, C. A., and Prince, T. A. 1990, AJ, 100, 294

Graham, J. 1991, private communication

Haas, M. 1990, A&A, 236, 531

Haas, M., Leinert, Ch., and Zinnecker, H. 1990, A&A, 230, L1

Hanson, R. B., Jones, B. F., and Lin, D. N. C. 1983, ApJ (Letters), 270, L27

Haro, G. and Chavira E. 1974, Inf. Bull. Var. Sts., 926

Hartmann, L., and Kenyon, S. J. 1985, ApJ, 299, 462

Hartigan, P, Kenyon, S. J., Hartmann, L, Strom, S. E., Edwards, S., Welty, A. D., and Stauffer, J. 1991, ApJ, 382, 617

Henry, T. 1991, Ph.D. University of Arizona

Herbig, G. H. 1962, 1962, Adv. Astron. Astrophys., 1, 47

Herbig, G. H. 1977, ApJ, 214, 747

Herbig, G. H., and Robbin-Bell, K. 1988, Lick Obs Bull No 1111

Herbig, G. H., Vrba, F. J., Rydgren, A. E. 1986, AJ, 91, 575

Herbst, W. and Warner, J. W. 1981, AJ, 86, 885

Johnson, H. L 1965 ARA&A, 4, 193

Jones, B. F., and Herbig, G. H. 1979., AJ, 84, 1872

Joy, A. H. 1945, ApJ, 102, 168

Joy, A. H. and Van Biesbroeck, G. 1944, PASP, 56, 123

Kenyon, S. and Hartmann, L. 1987, ApJ, 323, 714

Knox, K. T. and Thompson, B. J. 1974, ApJ, 193, L45

Koresko, C. D., Beckwith, S. V. W., Ghez, A. M., Matthews, K., and Neugebauer, G. 1991, AJ, 102, 2073

Labeyrie, A. 1970, A&A, 6, 85

Lada, E. A., Strom, K. M., and Myers, P. C. 1992, In *Protostars and Planets III,* eds. E. H. Levy and J. Lunine, preprint

Leinert, Ch., Haas, M., Richichi, A., Zinnecker, H., and Mundt, R. 1991, A&A, 250, 407

Leinert, Ch., Weitzel, N., Haas, M., Lenzen, R., Zinnecker, H., Christou, J., Ridgway, S., Jameson, R., Richichi, A. (1992) IAU #135 "Complementary Approaches to Double and Multiple Star Research" preprint

Lin, D. N. C. and Papaloizou, J. C. B 1992, In *Protostars and Planets III,* eds. E. H. Levy and J. Lunine, preprint

Lin, D. N. C., Papaloizou, J. C. B., 1985, *Protostars and Planets II,* eds D. C. Black & M. S. Mathews (Univ. Arizona Press: Tucson), p. 981

Lohmann, A. W., Weigelt, G. P., and Wirnitzer, B. 1983, Appl. Opt., 22, 4028

Lynds, B. T. 1962, ApJSS, 7, 1

Maihara, T., and Kataza, H. 1991, A&A, 249, 392

Mathieu, R. D., Walter, F. M., and Myers, P. C. 1988, AJ, 98, 987

Mathieu, R. 1992, IAU Colloq. 135, Complementary Approaches to Double and Multiple Star Research

Matthews, K, Neugebauer, G., McGill, J., and Soifer, B. T. 1987, AJ, 94, 297

McAlister, H. A., and Hartkopf, W. I. 1988, *Second Catalog of Interferometric Measurements of Binary Stars,* Center for High Angular Resolution Astronomy

Moneti, A. and Zinnecker, H. 1991, A&A, 242, 428

Montmerle, T., Koch-Miramond, L, Falgarone, E., and Grindlay, J. E. 1983, ApJ, 269, 182

Myers, P. C. 1985, In *Protostars and Planets II,* eds. D. C. Black and M. S. Mathews, 81

Nisenson, P., Stachnik, R. V., Karovska, M., and Noyes, R. 1985, ApJ (Letters),297, L17

Reike, G. H., and Lebofsky, M. J. 1985, ApJ, 288, 618

Roddier, F. 1986, Opt. Commun., 60, 145

Roddier, F. 1988, Physics Reports, 170, 97

Rucinski, S. 1985, AJ, 90, 2321

Rydgren, A. E., Schmelz, J. T., and Vrba, F. J. 1982, ApJ, 256, 168

Rydgren, A. E., Strom, S. E., and Strom, K. M. 1976, ApJSS, 30, 307

Rydgren, A. E. and Vrba, F. J. 1981, AJ, 86, 1069

Rydgren, A. E. and Vrba, F. J. 1983, AJ, 88, 1017

Sargent, A. I. and Beckwith, S. V. W. 1987, ApJ, 323, 294

Sargent, A. I. and Beckwith, S. V. W. 1991, ApJ, 382, L31

Savage, B. D., and Mathis, J. S. 1979, ARA&A, 17, 73

Schwartz, P. R., Simon, T., Zuckerman, B., and Howell, R. R. 1984, ApJ (Letters), 280, L23

Schwartz, P. R., Simon, T., Cambell, R. 1986, ApJ, 303, 233

Shu, F. H., Adams, F. C., and Lizano, S. 1987, ARAA, 25, 23

Simon, M. 1992a, IAU Colloq. 135, Complementary Approaches to Double and Multiple Star Research

Simon, M. 1992b, private communication

Simon, M., Chen, W. P., Howell, R. R., Benson, J. A., and Slowik, D. 1992, ApJ, 384, 212

Simon, M., Howell, R. R., Longmore, A. J., Wilking, B. A., Peterson, D. M., and Chen, W. P. 1987, ApJ, 320, 344

Skrutskie, M. F., Dutkevitch, D., Strom, S. E., Edward, S., and Strom, K. M. 1990, AJ, 99, 1187

Strom, K. M., Strom, S. E., Edwards, S., Cabrit, S., and Skrutskie, M. F. 1989, AJ, 97, 1451

Ungerechts, H. and Thaddeus, P. 1987, ApJSS, 63, 645

Walter, F. 1986, ApJ, 306, 573

Walter, F. 1990, private communication

Walter, F. 1992, private communication

Walter, F. M., Brown, A., Mathieu, R. D., Myers, P. C., and Vrba, F. J. 1988, AJ, 96, 297

Warner, G., Strom, S. E., and Strom, K. M. 1977, ApJ, 213, 427

Weigelt, G. P. 1977, Opt. Commun., 21, 55

Weintraub, D. 1989, Ph.D. University of California, Los Angeles

Wilking, B 1989, PASP, 101, 229

Wilking, B. A. and Lada, C. J. 1983, ApJ, 274, 698

Wilking, B. A., Lada, C. J., and Young, E. T. 1989, ApJ, 340, 823

Zinnecker, H. Brandner, W., Reipurth, B. 1992, IAU Colloq. 135, Complementary Approaches to Double and Multiple Star Research